Microstructural Evolution as a Function of Cooling Rate in Rapidly Solidified Commercial Grey Cast Iron

Olamilekan Rasaq Oloyede

Submitted in accordance with the requirements for the degree of
Doctor of Philosophy

The University of Leeds
Institute for Materials Research (IMR)
School of Chemical & Process Engineering

May, 2017

The candidate confirms that the work submitted is his own, except where work which has formed part of jointly-authored publications has been included. The contribution of the candidate and the other authors to this work has been explicitly indicated below. The candidate confirms that appropriate credit has been given within the thesis where reference has been made to the work of others.

Following publications have been made based on materials contained in Chapter 5 and 6 of this thesis. The citations for these publications are as follows:

List of Article Publications and Presentations:

(*From April 2014 to date*)

Published papers / Renounced Journal article:

1. Oloyede, O., Bigg, T.D., Cochrane, R.F. and Mullis, A.M. *Microstructure evolution and mechanical properties of drop-tube processed rapidly solidified grey cast iron. Materials Science & Engineering A*. **654** (2016), pp.143-150. *http://dx.doi.org/10.1016/j.msea.2015.12.020*.

2. Oloyede O, Cochrane RF, Mullis AM. *Effect of rapid solidification on the microstructure and microhardness of BS1452 grade 250 hypoeutectic grey cast iron*. Journal of Alloys and Compounds. **707** (2017), pp. 347-350. http://10.1016/j.jallcom.2016.08.214.

Published Conference proceedings:

3. Oloyede, O., Bigg, T. and Mullis, A. *Characterization of rapidly solidified commercial grey cast iron in drop-tube*. Paper presented at *MS&T '15*. Columbus, Ohio USA: The conference proceeding of Materials Science & Technology, pp.843-849. Available at: http://matscitech.org.

4. Oloyede, O., Bigg, T. and Mullis, A. *Effect of cooling rate on drop-tube processed commercial grey cast iron*. Paper presented at ASME 2015 Houston, Texas USA: pp: V0T11A018; 8 pages ISBN: 978-0-7918-5757-1. *2015:():V014T11A018.doi:10.1115/IMECE2015-52368.* .

5. Oloyede, O., Cochrane R. and Mullis, A. *Effect of Cryogenic Quenching on Microstructure and Microhardness of Rapidly Solidified Grey Cast Iron*. Paper published in *MS&T '16*. Salt Lake City, Utah USA: The conference proceeding of Materials Science & Technology, pp.1173-1178. Available at: http://matscitech.org.

Conference Oral presentation:

6. Oloyede, O., Bigg, T., Cochrane, R. and Mullis, A. (2015). *Characterization and microstructural changes in grey cast iron by drop-tube processing.* In: 22nd International Symposium on Metastable, Amorphous and Nanostructured Materials. Paris, France: ISMANAM 2015, p301.

Conference Postal Participation:

7. Oloyede O, Bigg T, Cochrane RF, Mullis AM. *Characterization & microstructural evolution of rapidly solidified grey cast iron.* Poster session presented at: The 5th National Student Conference in Metallic Materials. 2015 June 23-24th; University of Manchester conference centre. Manchester, UK.

8. Oloyede, O., Cochrane, R. and Mullis, A. (2016). *Structure – Property correlation of grey cast iron as a function of cooling rate..* In: 23nd International Symposium on Metastable, Amorphous and Nanostructured Materials. Nara, Japan: ISMANAM 2016, P53.

Dedication

To the Almighty God, the great *I AM* ! The Lord of my life, my source of strength and my help. Thank you Lord for every season of my life. Thank you for bringing me this far. To you be praise and adoration for ever and ever, amen !

Acknowledgements

With gratitude to God, I want to express my heartfelt appreciation to Professor Andrew M. Mullis and Dr. Robert R. Cochrane for their unwavering support and supervision of this research project. This work will not have been possible without your knowledge, guidance and patience. Also, special thanks to Federal government of Nigeria for granting me scholarship and sponsorship for this project through PTDF. A big thank you for the love and support from my immediate family: Dr. Precious Iso Oloyede (my wife), King David Oluwatobiloba Olayinka Oloyede (my son), Queen Esther Oluwatosinloba Oladunni Oloyede and Her Majesty Victoria Oluwatoyinloba Oladipupo Oloyede (my daughters). Thank you for holding my hand through this adventure!

I would like to thank Lady Di (Diane Cochrane), Rob Simpson, Tim, Bigg, Mo Javed, Stuart Micklethwaite, John Harrington and all others who assisted me during different laboratory sections in the course of this research. It is important to also thank my colleagues in the Rapid Solidification group namely: Toyin Jegede, Nafis Haque, Ayems and Frank, thank you guys for all your positive criticism and friendly assistance on my project. I appreciate all the prayers and encouragement from my extended family members, all my brethren in Nigeria and United Kingdom.

I am grateful to God for My parents. To my father, *honorary emeritus professor* Alhaji S. I. Oloyede of Abokede Compound of Ilugun Asalu, Mokola Abeokuta, who taught me practical metallurgy (goldsmith) at early age! Thank you for all the great values and virtues you installed in me and the sacrifices in seeing me through my educations. You are legendary !

Again, to God be glory for His mercies endureth forever !

Abstract

The influence of post-production re-engineering of microstructure through rapid solidification processing at constant elemental composition on microhardness of low alloyed commercial BS1452 grade 250 grey cast iron has been studied. In this investigation, the effect of cooling rate on rapidly solidified droplets cooled separately in Nitrogen and Helium in a 6.5 m high drop-tube are compared against conventionally solidified as-cast alloy. Powder sample sizes obtained ranges from ≥ 850 μm to ≤ 38 μm in diameter with corresponding estimated cooling rate of 200 K s^{-1} to 16,000 K s^{-1} in N_2 and 700 K s^{-1} to 80,000 K s^{-1} in He gases respectively.

Microstructure evaluation were made by light optical and SEM, while XRD and TEM were employed for evolved phase's identification and confirmation. DTA was used to determine the onset of the evolved metastable phase and deep cryogenic treatment of the droplets further transform fractions of the retained austenite to martensite. The microscopy result shows that the as-cast bulk sample reveals extensive graphite flakes randomly distributed in a ferritic – pearlitic dendritic matrix, meanwhile the same was absent in virtually all the droplets samples. However, with decreasing droplet size (i.e increasing cooling rate); there was a progressive phase transformation from the initial ferrite (α-Fe) phase fraction decreasing to retained austenite (γ-Fe) phase which further decreases as α'-Fe increases in smaller droplets with evidence of undercooling effect.

The relationship between cooling rate ($\dot{R}$) and the individual droplet diameter (D) in measuring microhardness values in the two media are governed by a power functions $\dot{R} = 6.40 \times 10^{-3}D^{-1.45}$ in N_2 gas and $\dot{R} = 7.75 \times 10^{-3}D^{-1.60}$ in He gas. Hence, a cooling rate of ~ 200 K s^{-1} in N_2 results in approximately double the measured hardness value of the as-cast (conventionally cooled) material. Meanwhile, Helium gas has five times better thermal conductivity compared to Nitrogen.

From *me* to *you* !

"We are like dwarfs on the shoulders of giants, so that we can see more than they, and things at a greater distance, not by virtue of any sharpness of sight on our part or any physical distinction, but because we are carried high and raised up by their giant size."

@Bernard of Chartres 1130

Table of content

Chapter One: GENERAL INTRODUCTION

Chapter Two: BACKGROUND SCIENCE

Chapter Three: LITERATURE REVIEW

Chapter Four: MATERIALS & METHODS

Chapter Five: EXPERIMENTAL RESULTS

Chapter Six: DISCUSSION OF RESULTS

Chapter Seven: CONCLUSIONS

Chapter Eight: FUTURE WORK

Appendices

List of Tables

List of Figures

Abbreviations

BS – British Standard
BSD – Backscatter Detector
CE – Carbon Equivalent
CCT – Continuous Cooling Curve
D – Droplet diameter
DTA – Differential Thermal Analysis
DTP – Drop-Tube Processing
EBSD – Electron Back Scattered Diffraction
EDX – Energy Dispersive X-ray
EML – Electro-Magnetic Levitation
FIB – Focused Ion beam
HAZ – Heat Affected Zone
HPGA – High-Pressure Gas Atomization
MF – Melt Fluxing
OM – Optical Microscope
$\dot{R}$ – Cooling Rate
SAED – Selected Area Electron Diffraction
SE – Secondary Electron
SEM – Scanning Electron Microscopy
TEM – Transmission Electron Microscopy
TTT – Temperature Time Transformation
XRD – X-Ray Diffraction

CHAPTER ONE

GENERAL INTRODUCTION

Preambles

Different engineering materials respond differently to processing and post-production treatments, which actually determine or affects their microstructure, properties and eventually their performance in service. To get the best of metallic materials, appropriate processing must be employed during or after their production such that the materials will be suitable or have their properties further enhanced through modification for ultimate performance. For instance, Fe–Si–C based alloys (e.g. cast irons) are very versatile and they come in different forms and grades, depending on the alloying elements or processing route employed for their production and treatment thereafter. For clarity, the block-diagram shown in ***Fig. 1.1*** describes the interconnectivity of two standard variable features that substantially influences the desired or expected end result of these alloys i.e. output features of mostly metallic (or similar) products. Invariably, there is a general strong relationship between manufacturing/modifying processing on microstructure and consequently on mechanical properties of especially metallic alloys. In this study, emphasis is on the impact of rapid solidification processing at constant elemental composition on the microstructure and microhardness of low alloyed commercial engineering material namely BS1452 grade 250 hypoeutectic grey cast iron.

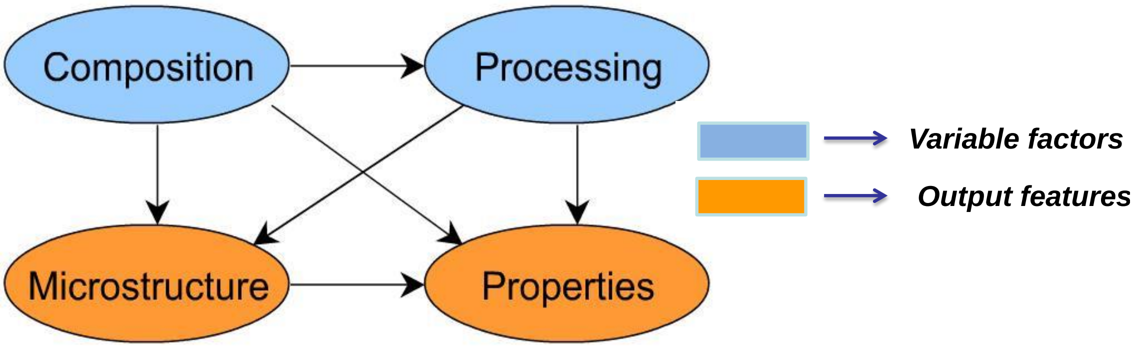

Fig. 1.1: Block diagram of basic variable factors that influence end features of metallic alloys

Basically, grey cast iron is a widely used metallic material because of its preferred properties such as good castability, formability, machinability, high damping capacity, relative low cost and good corrosion resistance. In its as-cast state, it has relatively low strength and toughness as a result of random precipitation of graphite in its microstructure which makes it brittle and limits its application.

Although standard commercial hypoeutectic grey cast iron (BS1452 grade 250) is the selected material for this study, there will be need for future research on employing this same containerless solidification processing i.e. drop tube technique; to investigate another cast iron alloy containing higher carbon content, such as hypereutectic cast iron alloy. The outcome of such research can then be compared with that obtained from this present study. Hence, with rapid solidification processing; an alloy's microstructure and by extension its mechanical property (microhardness) could be modified in a way that it becomes suitable for desired use by suppressing graphite flakes. Therefore for the proposed hypereutectic alloy experiment, it is expected that the droplets will have higher carbon percentage content in solid-solution. Certainly, the expected droplets will have evolved phases different both in morphology and % phase fraction from the kind obtained using hypoeutectic alloy presently studied here.

Basically, in most processing methods, there are standard laboratory or research techniques as well as industrial or production methods. For rapid solidification, drop tube, levitation, melt-flexing and melt-dispersion techniques are all majorly for research purposes; while salt bath-quenching, melt-spinning and high pressure gas atomization (HPGA) are largely for high quantity and quality industrial production. For instance, for research purpose; with drop-tube technique (containerless processing) a relatively small quantity in the range of ≥ 10 g to ≤ 30 g of the as-cast sample is all that is required to produce droplets for laboratory analysis as compared to large initial quantity needed for gas atomization method. In terms of basic difference in these methods, say for drop tube and HPGA; the former (drop tube) produces droplets with wider size range as compared to the later (gas atomization process) which produces largely high quantity uniform metal powders. The two methods end up in producing droplets, but with different quantity. The industrial application of this processing methods, form the basis for mass production of alloy droplets otherwise known as powder metallurgy process. Although in principle the two techniques are similar, but there is basic set up difference in that there is no dynamic flow of gas in drop tube method (although there is a considerable volume of back-filled gas). However, in HPGA, there is dynamic stream of gas flow met for shearing the molten metal into droplets which cool as they flow down the long column of the tower. Hence, alloy powders obtained by HPGA offer even spherical shaped particles with better quality and quantity. So, using drop tube method for this work is a kind of prototype research study.

The whole study is divided into **seven chapter**s with understanding that each chapter address a sequential subject of interest leading to effective understanding of the objectives and aims of the research. This has been carried out within the scope of the effect of rapid solidification processing on microstructural evolution and identification of emergent phases in relation to observed changes in the microhardness values of the control sample (as-cast) and the droplets as a measure of its mechanical properties enhancement. ***Chapter one*** serves as general prelude, as it is; describing various sections and outlining the essential theme and scope of the study with emphasis on the effect of variable factors on the outward features of the sample material even at constant elemental composition. In ***chapter two***, basic definitions, concepts and terminologies are outlined as relates to fundamental science and knowledge needed to explain the connection between set aims and the expected actual experimental results. Principles of crystal formation, science of heat transfer and various stages of solidification procedures are explained. Robust explanation on the knowledge of fundamentals of solidification as relates to nucleation and grain growth, free energy along with understanding cooling rate and degree of undercooling are included in this chapter. Meanwhile, ***chapter three*** of this thesis is focused on literary exploits of previous researchers as it relates to this study and the interest it covers. It explains with due reference to other people previous works on stable and metastable phase formation and advancement in rapidly solidified droplets with emphasis on Fe-based alloys. There is a section dedicated to explaining various containerless processing techniques and full description of drop-tube apparatus and its operation method was given in particular. The chapter outlined basic features of the cast iron generally and specifically treats grey cast iron in the light of phase diagram and other essential isothermal or transformation diagrams such as CCT and TTT diagrams. Finally, the chapter spells out the likely expected morphological changes and evolved phases and how these have been literally enhanced by further heat treatment from other earlier researchers.

Chapter four basically outlines the detailed description of the various experimental methods used in the course of this study. It starts with full description of the as-cast sample, revealing its elemental composition, microstructure and observed initial phases present. Full description of the droplets production and metallography sample preparation were outlined. Optical and scanning electron microscopic observations along with phase identification analysis such as transmission electron microscopy (i.e. TEM) and confirmation methods such as differential thermal analysis (DTA) are described. Also low temperature quenching i.e. cryogenic treatment and its effect on microhardness of all the particles sizes as well as the effect of cooling rate and resultant undercooling on this mechanical property were measured and graphs plotted for comparative analysis. ***Chapter five*** contains compilation of all the experimental results obtained in sequence and relevant micrographs and measured or derived values to substantiate the observed change in morphologies and microhardness due to evolved phases as a result of rapid solidification and deep cryogenic quenching are all tabled and graphically presented. In addition, the effect of various etchants on the as-cast and droplet samples are also outlined. ***Chapter six*** contains discussion of all presented results stating the principles and mechanism behind the observed results as well as interlinking such to the basic science that governors such interdependence. Primarily, the effect of rapid solidification on the droplets is the elimination of graphite flakes even in the droplet with modest cooling rate. Hence, as a result of increasing cooling rate the droplets experience higher fragmented dendritic structure and as the particle sizes reduces, the ferritic and retained austenite phases progressively transform to acicular ferrite or martensite.

Finally, ***chapter seven*** gives a summary of the entire study and emphasize the findings as well as providing prove that the study is worth the effort and have actually contributed to the knowledge which is one of the principal aim of the studies at this level. This is followed by valuable recommendations in light of possible implementation and upholding of the fact and findings this study has brought into limelight.

Additional information in terms of appendices and other related items are compiled for referencing purposes and all this are referred to appropriately in the mean body of the thesis.

CHAPTER TWO

BACKGROUND SCIENCE

2.0. Introduction to Background Science

There exist a confirmed strong relationship between *microstructure* and *properties* of basic engineering materials (metals, alloys and composites); and the linking factor between these two end-points depends on the "*processing*" route taken to achieve the desired feature(s) [1]. One such processing or phenomenon in metallurgical industries that has transcend generations, and acts as anchor for other derived processes in cast solidification [2]. It involves cooling of melt and its subsequent solid state modification. The microstructure obtained depends essentially on cooling rate, the cooling medium and composition of the alloy which subsequently affects mechanical properties [3]. This section focuses on the fundamental theories and concepts needed to understand basic melt solidification, crystal evolution, phase transformation and definition of thermodynamics parameters of equilibrium, non-equilibrium or undercooled metallic melts.

2.1. Basic Crystallography

The interest of this research will be guided by structure evolution in rapidly cooled Fe-based alloys, its solid state transformation and the accompanying phase formations. Derived concepts and theories based on crystal formation from melt solidification i.e. nucleation, grain formation and crystal growth will be explained in the course of this study. Although, those steps involved in solidification process may be well understood, however the emerged solidified structure and the accompanying internal cell arrangement which serves as finger prints for samples' crystallography need to be explained based on composition involvement [4]. For instance, temperature varies during solid state cooling in a typical as-cast alloy across sections as a result of difference in atoms thermal stability, rate of cooling and conductivity of cooling medium. In such cases, theories and concepts of crystal formation are needed to explain noticeable changes based on atoms re-orientation. These at times are based on acceptable variables such as temperature, pressure, entropy and other derived or assumed factors that can only be explained on the knowledge of crystal formation, lattice re-arrangement and/or phase evolution [1].

2.1.1. Description and Identity of Unit Cell.

A unit cell is simply the smallest complete portion of a matter. It is the comprehensive portion or atoms having the same orientation or symmetry which then develop into crystals, possessing well-defined lattice patterns. It has six significant quantitative parameters; three of which are identified as vector length ***a***, ***b*** and ***c***; representing the 3-D edges and the three in between angles namely ***α***, ***β*** and ***γ***; existing between (***b*** and ***c***), (***c*** and ***a***) and finally (***a*** and ***b***) respectively [4]. Hence, with ordered repetition of these unit cells in three dimensions, specific crystals are formed and named based on orientation and combination of these six variable significant quantitative parameters. The simplest crystal structure is cubic unit cell as shown in ***fig. 2.1*** from which other structures i.e. ***bcc***, ***fcc***, ***hcp*** and so on are derived.

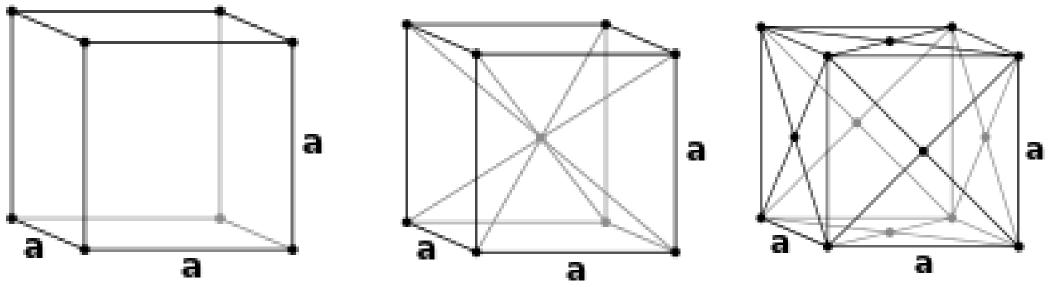

Simple cubic Body-centered cubic Face-centered cubic

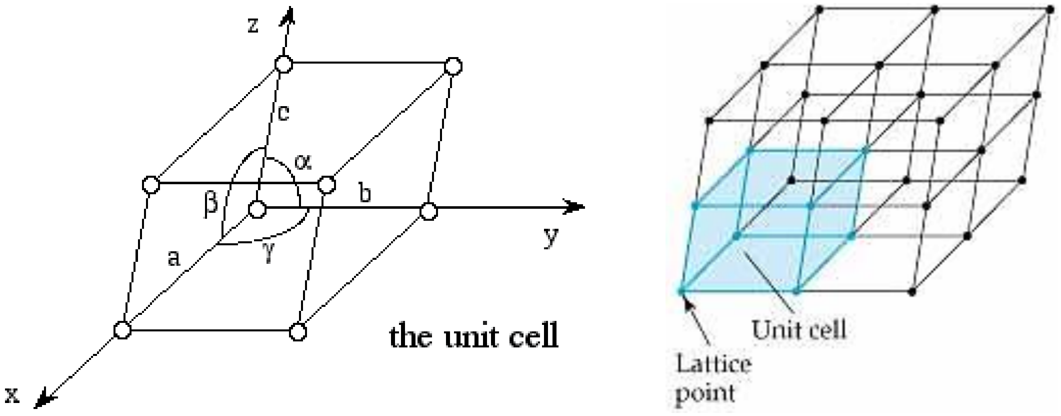

Fig. 2.1: A unit cell, types, parameters and simple crystal lattice description [1].

2.1.2. Crystal symmetry and systems.

Mirror repetition of a formed crystal produces crystallograpic units which are product of symmetry due to reflection, rotation, inversion or combination of any of these. Hence, crystals are classified based on their definite external and/or internal ordering which is peculiar to such crystal system but can be re-ordered or re-oriented resulting in the crystal system change or phase transition. Therefore, crystals are said to possess symmentry when it has more than one indistinguishable orientation in space. For instance, if a crystal has n-fold symmentry possibility about an axis, it therefore means that it can undergo $360^o/n$ rotation to bring it to self-resemblance [4]. For a cube shown in ***fig. 2.2***; different rotation about the axes will bring it to coincidence with different resultant fold axis of symmentry. Similarly, this applies to other similar crystal systems as shown in **Table 2.1**.

Table 2.1: Crystal systems: their symmentry and elemental examples

	Crystal System	Symmetry fold occurence	Typical sample
1	Cubic	Four 3-fold and three 4-fold axis	Ag, NaCl, CsCl, Diamond
2	Orthorombic	Three mutually pependicular 2-fold or $\bar{2}$-axis	I_2, $HgCl_2$
3	Tetragonal	One 4-fold or $\bar{4}$-axis	White tin
4	Monoclinic	One 2-fold or $\bar{2}$-axis	$KClO_3$
5	Rhombohedral	One 3-fold or $\bar{3}$-axis	$CaCO_3$
6	Triclinic	One 1-fold or $\bar{1}$-axis	$K_2Cr_2O_7$
7	Hexagonal	One 6-fold or $\bar{6}$-axis	SiO_2

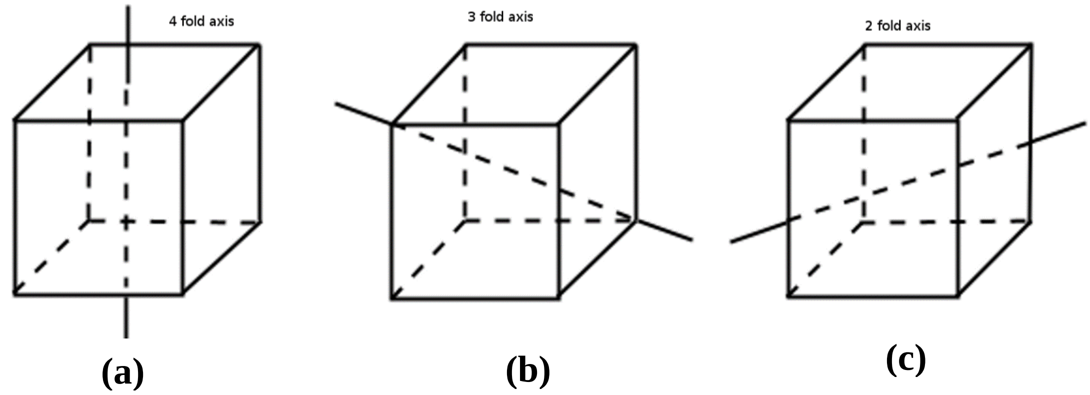

Fig. 2.2: Cube rotation and different symmentry; (a) 90^o vertical rotation and since it has 6 faces, then there is possible three 4-fold axis rotation; (b) Body diagonal rotation (120^o) and since there are four body diagonal, it has four 3-fold axis rotation; (c) Shows one of the six 2-fold rotation passing through cube edge to mass centre to edge [1].

2.2. Thermodynamics of supercooled melt

During solidification, be it conventional or containerless; rate of cooling, the degree of undercooling and cooling medium are three essential factors that influences the evolved phases and microstructures. However, irrespective of the process route, these factors must be well understood based on their relationship with thermodynamic parameters and other background science and concepts [2]. For instance, during non-equilibrum solidification processing, characterized by a very high cooling rate and increased undercooling; there is high possibility of obtaining refined microstructure, extended solid solubility, new metastable phase formation and even glass phase formation. The interesting thing is that there is need to define those parameters that control and facilitate microstructure or phase transformations. Hence, in this section; basic thermodynamic concepts and parameters that relate to rapid solidification processing such as Enthalpy, H; Entropy, S; Gibbs free energy, G and specific heat capacity, C_p; are thereby explained.

2.2.1. Heat transfer concept.

Generally, there is heat exchange during melting or solidification. Models have been built and equations developed to express the transfer of energy based on laws of thermodynamics and/or principle of energy conservation [3]. For instance, heat exchange during rapid solidification processing of undercooled spherical droplets has been analyzed using a Newtonian or non-Newtonian models [2]. Meanwhile, the estimated heat flux is actually given by Fourier's law of heat transfer which states that, there is an energy exchange from high temperature region to low temperature region [5]; which can be express mathematically as:

$$\frac{q}{A} = - \mathrm{k} \frac{\partial T}{\partial x} \qquad \textbf{(2-1)}$$

where $\frac{q}{A}$ (W) is the heat flux normal to the surface of the area A (m^2), through which the heat flows; k (W/mK); then the thermal conductivity; T (K) is the temperature and x (m) is the descriptive space parameter perpendicular to the surface. The minus sign is due to the opposite direction of the heat flow and the temperature gradient. Fourier's law is the defining equation for the thermal conductivity (k) which may be measured for each material droplet [6].

2.2.2. Gibbs Free Energy concept

A system is said to be in equilibrium when in a state of absolute rest [4]. However, the degree of metastability depends on how far a system or phase is from equilibrium. For instance, during solidification; the driving force is the difference in Gibbs free energy between the solid and the liquid states, $G_s – G_l$ [3]. Generally, this is determined by the local value of Gibbs free energy, G at temperature T and pressure P, which can be mathematically expressed as:

$$G = H - TS < G_i \qquad \textbf{(2-2)}$$

where G_i is the initial Gibbs free energy, H and S are enthalpy and entropy of the phase transformation as a function of temperature. Normally phase transformation is always favoured when Gibbs free energy decreases. Hence, there is relatively large varied G of metastable states of materials in natural occurrence [7]. The probability of their existence at ambient temperature depends on the kind of well-designed processing technique such as rapid solidification that is involved.

2.2.3. Enthalpy

It is the thermodynamic parameter that expresses the heat content of a system depending on its prevailing equilibrum status and it is defined by variable factors such as internal energy, pressure and volume. Hence, the change in enthalpy, ΔH; of liquid - solid transistion during rapid solidification processing is in two parts namely; libration of latent heat of fusion, ΔH_f and the experienced undercooling. This can be expressed mathematically as:

$$\Delta H = \Delta H_f - \int_T^{T_m} C_p \, dT \qquad \textbf{(2-3)}$$

where C_p is the heat capacity difference between the liqiud and solid state. Hence, to achieve high activation energy expressed in **equation 2-3**, for phase transformation to occur; all the thermodynamics parameters must be well defined.

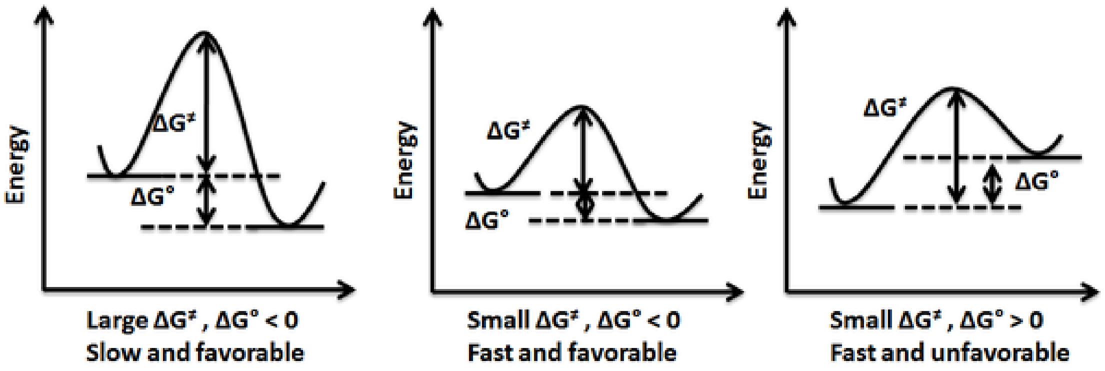

Fig. 2.3: Schematic variation in Gibbs free energy with different configuration of stability.

2.2.4. Entropy

This is the thermodynamic parameter that describes the degree of disorder in a system. Change in entropy measures the heat exchange that takes place during thermal process such as during solidification or melting based on the relation:

$$dS = dQ_{rev} / T \qquad \textbf{(2-4)}$$

where Q_{rev} is the quantity of heat exchanged and T is the temperature of the exchange. For a system in equilibrum, the entropy at microscopic point of view is given by:

$$S_m = k_B \ln W \qquad \textbf{(2-5)}$$

where k_B denotes the Boltzmann constant and W, the occurrence or frequency.

2.3. Nucleation: Theory and Concept

Nucleation is simply the initiation of solidification. It is the foundation on which solid phase transistion depends [8]. For instance, when a liquid is cooled below its equilibrum melting temperature (T_m) i.e. $T < T_m$ there is normally a driving force for Gibb's free energy (G) of solidification given as $G_L - G_S$ as described above, the sequence of nucleation and crystallization concept is as illustrated in ***Fig. 2.4(a-c)***. It shows different stages of equilibrium solidification from nuclei to grain boundaries formation. However, cooling rate among other factors has the most outstanding influence on metals microstructure and properties during solidification processing especially at constant composition. For example, rapidly solidified Fe-based droplets with constant elemental composition in drop-tube apparatus will produce microstructure and phases depending purely on the degree of superheat, rate of cooling and conductivity of the cooling medium [9].

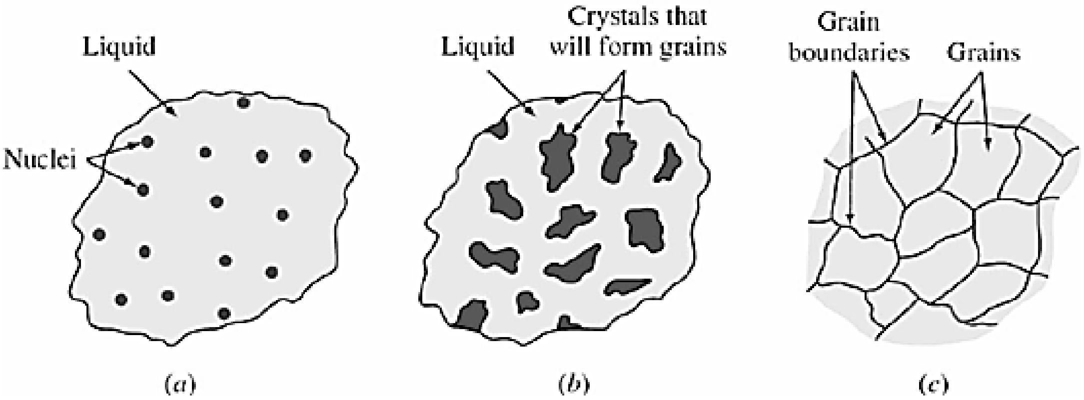

Fig. 2.4: Solidification sequence: (a) Nucleation, (b) Crystal formation and (c) Grain Growth.

2.3.1 Homogeneous Nucleation

Homogenous nucleation is the simplest nucleation event but of extremely rare occurrence mainly because of the presence of container's wall and impurities that act as nucleant in most systems. It applies to solidification of very pure metal crystals. Such pure metallic substances differ widely in the likelihood that they will crystallize under conditions in which the crystalline state is inherently stable [4]. The fact remains that; a system will always strive to be in thermodynamic equilibrium. For example, glycerol is a confirmed example of a compound prone to supercooling. Hence, the degree of undercooling, ΔT is approximately proportional to the driving force that exist for solidification to take place below the equilibrium melting temperature, T_m. Kurz [2] stated that, this driving force is actually the difference in the Gibbs free energy, ΔG, which exist for transition from liquid to Solid state. Again, when a melt is cooled below T_m, thermal changes enables tiny clusters of crystallised solid to emerge within the molten metal; which eventually lowers the free energy of the entire system thereby enhancing solidification process as outlined in previous main section. The free energy volume, ΔG_v, concerned with the formation of the solid cluster is proportional to the volume and therefore varies with radius as r^3; where r is the emergent solid cluster radius. These terms are expressed and related mathematically as shown in **equation 2-6** through to **equation 2-10** [2, 3]:

$$\Delta G_v = \frac{\Delta H_v \Delta T}{T_m} \qquad \textbf{(2-6)}$$

where ΔH_v is the enthalpy change of phase transition. It is assumed at this point that the emergent solid nucleates as spherical clusters having a critical-size nucleus of radius, r^*; normally, the net free energy, $\Delta G_{(r)}$of a singular nucleus of radius r, can be expressed as:

$$\Delta G_{(r)} = V\Delta G_v + \mathrm{A}\gamma_{SL} \qquad \textbf{(2-7)}$$

where: V = $\frac{4}{3}\pi r^3$ *(volume)* and A = $4\pi r^2$ *(Area)*; which can be express as:

$$\Delta G_{(r)} = \frac{4}{3}\pi r^3 \Delta G_v + 4\pi r^2 \gamma_{SL} \qquad \textbf{(2-8)}$$

where γ_{SL} is the solid/liquid interface energy. The relationship between T_m, r^*, ΔG_v, γ_{SL}, ΔH_v and ΔT is given by differentiating **equation 2-7** with respect to r (i.e. $\frac{\Delta G_v}{dr}$) to obtain r^*:

$$r^* = -\frac{2\gamma_{SL}}{\Delta G_v} = -\frac{2\gamma_{SL}T_m}{\Delta H_v \Delta T} \quad \textbf{(2-9)}$$

Meanwhile, the critical radius r^* only exists when $\Delta G_{(r)}$ is maximum; hence the associated free energy difference for homogeneous nucleation ΔG^* can be derived by simply substituting r^* , *(i.e. equation 2-9)* into **equation 2-8** which then becomes:

$$\Delta G^* = \frac{16\pi\gamma_{SL}^3}{3\Delta G_v^2} = \frac{16\pi\gamma_{SL}^3 T_m^2}{\Delta H_v^2 \Delta T^2} \quad \textbf{(2-10)}$$

Hence, ***fig. 2.5*** shows the relationship of radius, *r* with free energy for a phenomenon of nucleation. However, **equation 2-8** and **2-9** show that change in free energy and critical nucleus size decrease with ΔT, thereby confirming the tendency of homogeneous nucleus growth with increasing undercooling.

2.3.2. Heterogeneous Nucleation

Heterogeneous nucleation is a common liquid–solid transformation system as it allow nucleation at preferential sites such as the container's wall, inclusions or inherent impurities [3]. Therefore, when solidification is allowed with such conditions or factors, such that the activation energy required for nucleation is actually reduced as compared to that of without them such as in homogeneous nucleation. Hence, at lower temperature, T, significant undercooling will be noticed for heterogeneous nucleation as a result of replacement of part of the solid – liquid interface with a solid–solid

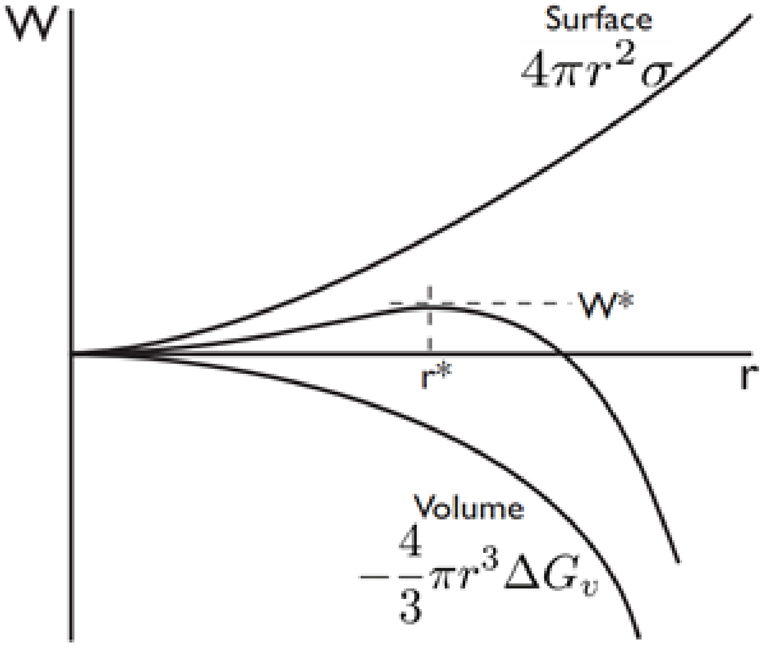

Fig. 2.5: Relationship between nucleus radius, *r* & the free energy barrier, ΔG^* [2].

interface, leading to a smaller energy barrier ΔG^* to nucleation; which have been substantially reduced. Hence, assuming that the solid–liquid interface energy is isotropic, it can simply be proven that the total interfacial energy of the system for a given volume of solid will be reduced to lowest value if the embryo has spherical-cap like shape with a wetting angle of θ and radius r as illustrated in ***fig. 2.6***. However, taking into consideration all the existing interfacial tensions, such as between: (1) the mould and the liquid, (2) the solid and the mould and (3) the solid and the liquid; then the equation for the Gibbs free energy change $\Delta G_{(r)}$, of a system having heterogeneous nucleation will be the algebraic sum of the homogeneous nucleation activation energy of the system and that of *each* interface present in the system given as:

$$\Delta G_{het} = \{\mathrm{V}\Delta G_v + A_{SL}\gamma_{SL} + A_{SM}\gamma_{SM} - A_{SM}\gamma_{ML}\}S(\theta) \quad \textbf{(2-11)}$$

where $A_{SL}\gamma_{SL}$, $A_{SM}\gamma_{SM}$ and $A_{SM}\gamma_{ML}$ are the interfacial energies (ΔG_i) for (1) solid – liquid, (2) solid – mould, and (3) mould – liquid interfaces present in the system as illustrated in **equation 8**. Where V is the volume; A is the area and γ is interface tension or force in the system. The term $S(\theta)$ as expressed in **equation 2-12** is known as the shape factor with value ≤ 1, depending on the wetting angle and is given as:

$$S(\theta) = \frac{(2+\cos\theta)(1-\cos\theta)^2}{4} \quad \textbf{(2-12)}$$

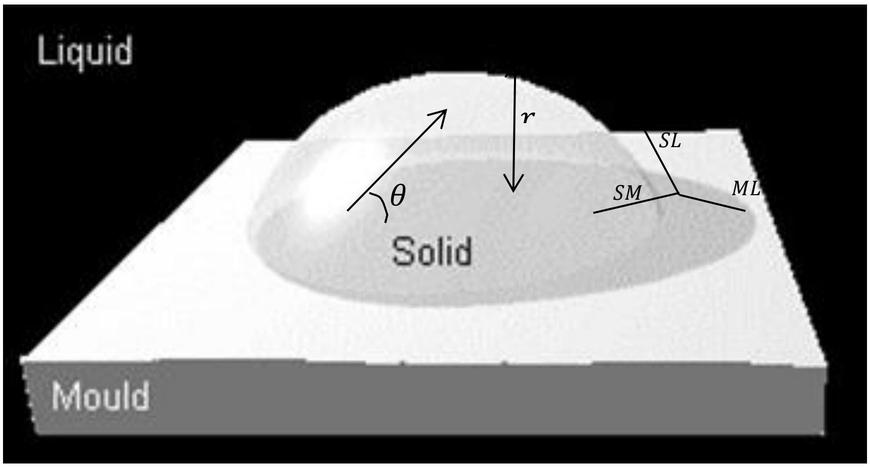

Figure 2.6: Heterogeneous nucleation of a spherical-cap like melt on a flat mould wall [10].

However, the critical radius r^*; is not affected by nucleant i.e. the mould wall; hence it is the same for both homogeneous and heterogeneous systems as shown in **equation 2-13** which if substituted in **equation 2-10** gives the associated ΔG^* as expressed in **equation 2-14**.

$$r^*_{het} = \frac{-2\gamma_{SL}}{\Delta G_v} = r^*_{hom} \tag{2-13}$$

$$\Delta G^*_{het} = \frac{16\pi\gamma^3_{SL}}{3\Delta G^2_v} S(\theta) = \Delta G^*_{hom}\, S(\theta) \tag{2-14}$$

Therefore it can be easily deduced from **equation 2-13** above that ΔG^*_{hom} barrier to nucleation is greater than ΔG^*_{het} by $S(\theta)$. In summary, the relationship shows that nucleation occurs more readily in heterogeneous systems than in homogeneous system as illustrated in ***fig. 2.7.***

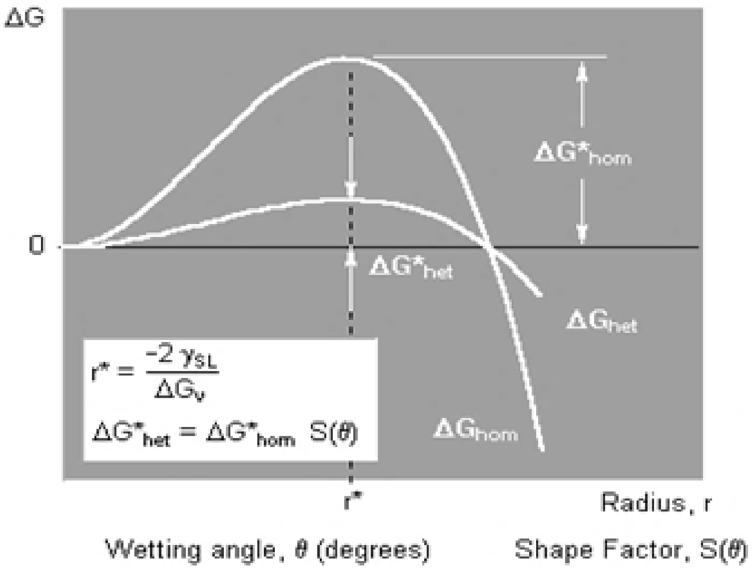

Figure 2.7: Shape factor effect on ΔG^*_{het} againstΔG^*_{hom}; making the former easier [10].

2.3.3. Nucleation Rate

It refers to the estimation of the number of grains initiated within a given volume of melt and time. It establishes a relationship between the emergent cluster size, nuclei number, associated free energy and the degree of undercooling involved [2]. Now consider an ideal mixture of homogeneous nucleation that contains an overall number of liquid atoms, N_L in the metallic melt and let N_n represent the atoms in the various varieties of small crystalline clusters formed; then assuming that $N_n \ll N_L$, (which is normally the case prior to crystal growth) and that each isolated cluster is in equilibrium, then the probability that the cluster will grow or dissolve back is the same [11]. Therefore, if we assume that clusters of all sizes and structures are presumed to be in equilibrium, then the equilibrium distribution, that is the solubility of the clusters can be estimated by **equation 2-15** [12]:

$$\frac{N_n}{N_L} = exp^{\left(-\frac{\Delta G_n}{k_b T}\right)} \qquad \textbf{(2-15)}$$

where ΔG_n is the energy of a nucleus containing n atoms and k_B is the Boltzmann's constant. Meanwhile as the number of clusters formed in the melt increases, the value of ΔG_n needed for nucleation decreases. Hence, at the point of nucleation; critical free energy barrier ΔG^* must have been produced by a cluster of critical radius r^*; along with associated energy ΔG_d required for the diffusion of atoms across the cluster–liquid interface. Therefore, taking into consideration these two related energies (ΔG_n and ΔG_d); the rate of nucleation I, can be expressed as shown in **equation 2-16** and consequently summarised in **equation 2-17**, [13].

$$I = N_L v_0 \, exp\left(-\frac{\Delta G^*}{k_B T}\right) exp\left(-\frac{\Delta G_d}{k_B T}\right) \qquad \textbf{(2-16)}$$

$$I = I_0 \; exp\left(-\frac{1}{k_B T}\right)^{(\Delta G^* + \, \Delta G_d)} \qquad \textbf{(2-17)}$$

Where ΔG^* is as described in **equation 2-14**, $\Delta G_d = A_{SL}\gamma_{SL}$, which is the cluster-liquid ($s - l$) interface energy and $N_L v_0 = I_0$ (known as pre-exponential factor, but v_0 is the atomic vibration frequency). Therefore, at constant nucleation rate the probability for occurrence of stable nucleation is inversely proportional to time via an exponential.

2.3.4. Methods for obtaining high degree of undercoolings

Section 3.3 contains more details on various methods i.e. containerless experimental techniques for obtaining bulk undercooling. These processes are carried out under ultra pure environment which provides the opportunity of achieving high undercooling as they avoid heterogenous nucleation by circumventing the effect of container walls and greatly minimize surface induced nucleation [14]. Examples of notable techniques for achieving high undercooling include: melt fluxing, levitation and drop-tube techniques. Each of these techniques provide means of monitoring and investigating different stages of rapid solidification behaviour and possible undercooling of metals and alloys [15]. For example, Table 2.2 displays various maximum undercooling values for some notable metals using selected specific or suitable containerless solidification processing techniques.

Table 2.2: Maximum undercooling values of some metals obtained using different containerless processing techniques such as: (EML-electromagnetic levitation,, Melt-flux and drop-tube processing) [14].

Metal	Undercooling °C	ΔT/Tm	Experimental Technique
Ag	227	0.184	MF
Co	350	0.198	EML
Ta	650	0.198	DTP
W	530	0.144	DTP
Pt	380	0.186	DTP
Cu	271	0.200	MF
Zr	430	0.232	DTP
Ni	480	0.278	EML
Nb	525	0.191	DTP
Ti	350	0.180	DTP
Mo	520	0.180	DTP
Fe	420	0.232	EML
Ge	520	0.352	EML

CHAPTER THREE

LITERATURE REVIEW

3.0. Introduction to Literature review

This chapter gives an overview of relevant theoretical concepts, literature survey as well as highlights of previous studies that are related to the fundamental interest of this research. It begins with explanation of terms and processes that are peculiar to equilibrium and non-equilibrium solidification. It contains literature extractions that show that there have been increasing interest among researchers over the years to understand and improve alloys properties especially as it relates to rapid solidification of some alloys through microstructure evolution via high cooling rate rather than elemental composition alterations [16-18]. It also showcases notable structural evolutions that occur during non-equilibrium transition of basic Fe-C alloys especially cast irons, based on different solidification conditions [2], which have their origin in the established principle of conventional and non-equilibrium solidification [3, 12]. Equilibrium solidification of molten metals involving two fundamental stages namely nucleation and grain growth has been explained in relation to overall microstructure formation [19].

The emphasis in this study is on microstructural characterization of grey cast iron and its different morphologies and phases that evolved as a result of different solidification condition employed. It is important to know that with appropriate solidification conditions of undercooled alloys, the parameters that allow directional or dendritic growth are deliberately favoured [20], however, many non-conventional solidification processing (not all) are diffusionless in nature with accompanying unique morphologies and characteristic mechanical properties. The last section of this chapter gives a brief summary on selected previous non-equilibrium solidification studies of cast iron and similar alloys with particular interest in grey iron; their relevance to this research and how the evolved microstructure influences property, but virtually none has really address rapid solidification of this very commercial grey cast iron, which formed the basis for this investigation.

3.0. Solidification

Solidification is simply a phase transition phenomenon which occur when there is a definite change from liquid to solid state as a result of temperature reduction. Such phase change in materials as shown in ***fig. 3.1***, occurs when factors that influences stability in a chemical system of a material such as composition, pressure, temperature etc., changes; thereby causing definite shift in such equilibrium stability. This and similar phase changes caused specifically as a result of composition variation or temperature reduction as illustrated above and as such referred to as transition diagram [21]. Hence, a phase diagram is an essential diagram that shows thermodynamic transition conditions against factors that can result in distinct phase occurrence or coexistence of such in equilibrium.

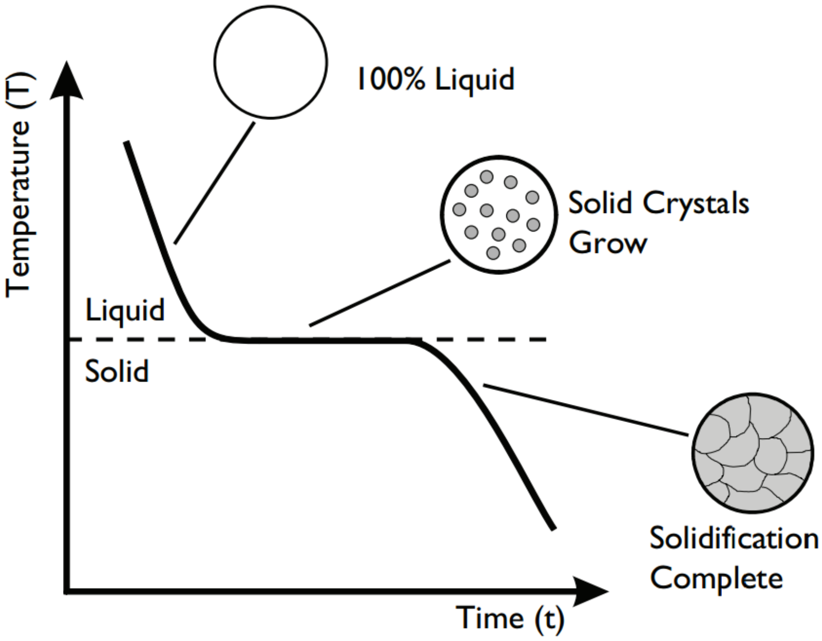

Fig. 3.1: Solidification sequence of a pure metal with accompanying phase formation.

3.1. Rapid Solidification

Rapid solidification is simply the process by which molten metals are either undercooled or completely cooled to a solid state in a very fast manner using a convenient technique in an appropriate cooling medium. It has been “loosely” defined in literature as the quick extraction of both superheat and latent heat during the transformation from molten (high temperature) to solid state (room or ambient temperature). This fast evolution of thermal energy that occurs during rapid solidification processing permits considerable deviation from equilibrium, which gives it the following general advantage as a unique method: (a) It gives an extended solid solubility, often by high magnitude; (b) It provides detailed information on microstructure changes even at constant elemental composition; (c) It explains transformations in non-equilibrium or metastable phases; and (d) It gives insight into intrinsic microstructural refinement and phase morphological changes. Rapid solidification processing includes various set of techniques ranging from high pressure gas atomization specifically for the production of metal powders and laser welding for repair to plasma-spray processes for thin film coatings [22].

There are 3 different ways of achieving rapid solidification namely: (1) fast cooling at high rate during solidification processing; (2) favouring a high degree of undercooling prior to solidification and (3) ensuring high advancing speed during continuous solidification procedure (deep undercooling). However, deep undercooling has more to do with the suppression of nucleation rather than rapid heat extraction [22, 23]. Rapid solidification processing has received tremendous attention from researchers in recent times [11, 24, 25] and the end microstructure is usually martensite as show in ***fig. 3.2***. Undercooling itself is a phenomenon whereby liquid metal is retained and sustained far below its freezing/melting point so avoiding heterogeneous nucleation [15, 26]. It is more pronounced in magnetic levitation, melt-fluxing, pendant drop and other notable containerless solidification processes [27]. Meanwhile, rapid quenching on the other hand, involves fast heat extraction from a sample through conduction, convention or radiation. The principle and application of this can be clearly understood in the use of vacuum atomization, melt spinning, arc spray, splat and other quenching processes.

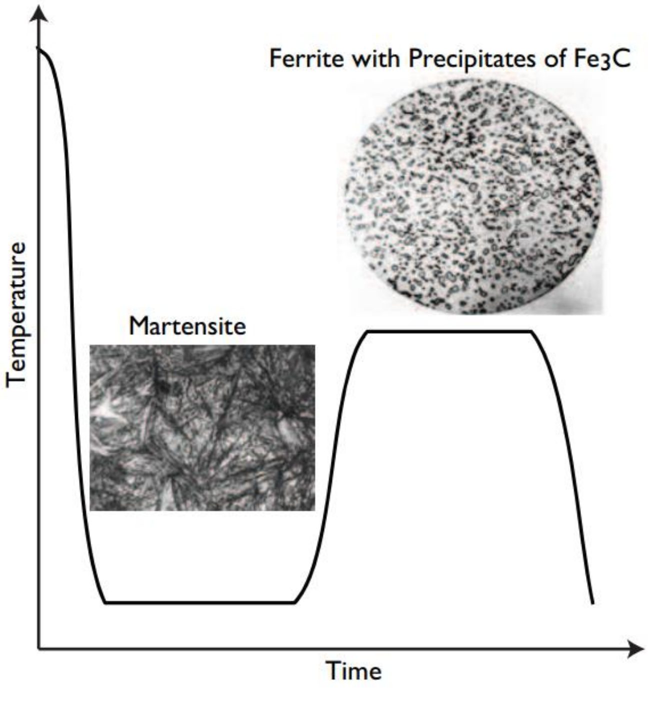

Fig. 3.2: Effect of rapid cooling on microstructures evolution of Fe-based alloys.

Generally, rapid cooling can be achieved using different methods relative to a cooler surface or medium to control the cooling rate. However, non-equilibrium solidification in comparison with conventional solidification, has intrinsic mechanisms which circumvent nucleation, supresses the kinetics of grain growth, promotes undercooling and finally retained metastable phase(s) at ambient temperature [28]. The following outlined concepts of rapid solidification are explained in different sections that follow.

3.2. Undercooling Concept.

Undercooling, otherwise known as supercooling, is a concept of drastically reducing the temperature of a melt below its freezing temperature without it necessarily becoming a solid. Containerless solidification processing provides solidification experts the possibility of attaining a high degree of undercooling, due to avoidance of heterogeneous nucleation on the wall of the container. However, with sufficient undercooling, at high cooling rate; ΔG^*, the energy barrier to nucleation must be overcome and this will then be followed by growth that favours the evolved solidified morphologies [29, 30]. Hence, depending on the degree of undercooling, nucleation can either be heterogeneous or homogeneous. Although in most cases, the latter is unlikely since very high undercooling is required for it to occur. ***Fig. 3.3*** [31] gives a schematic illustration of undercooling concept. From this illustration, we see the alloy of composition Co being undercooled into a single-phase.

However, with temperature increase and recalescence, i.e., release of latent heat of solidification; the reverse is also possible, i.e. the alloy's composition returns to its stable two-phase ($\alpha + L$) region. Hence, recalescence helps to bring the temperature of the alloy back to precisely the solidus temperature (T_S). This is indeed a special case of undercooling as illustrated in ***fig. 3.3(b)***. This condition, where $T_S = T_R$ is known as "critical undercooling";

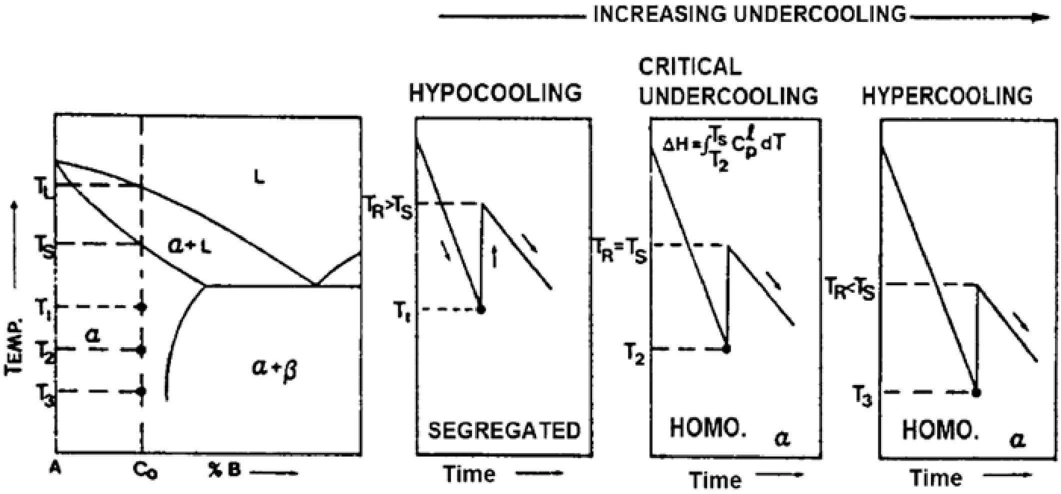

(a) (b) (c)

Fig. 3.3: Schematic illustration of undercooling & hypercooling concept; following the direction of increasing cooling, the undercooling temperatures for Co of this alloy are T_1, T_2 and T_3; while T_R is the recorded recalescence [31].

while ***fig. 3.3(c)*** shows a quite rare condition termed “hypercooling” in which $T_R < T_S$ which require $\Delta T > L/C_p > 400$ K. This further illustrate how the recalescence helps in reversing the single-phase. In practice, there are some basic techniques that have been developed over the years to manage cooling rate and consequent range of undercooling prior to solidification. Examples of common and widely used techniques include: (i) Droplet emulsion technique (DE), [27]; (ii) the drop tube technique (DT) [32] and (iii) magnetic levitation [27]. The common underlying feature of these and other rapid processing techniques is to minimize the probability of heterogeneous nucleation by eliminating crucible and nucleant induced nucleation.

Therefore, if these conditions are satisfied, then the only primary limiting factor for high undercooling extensions will be surface-induced nucleation processes [33]. Hence, the retention of intrinsic features of evolved rapidly solidified microstructures usually require a fast post-recalescence cooling rate. In summary, undercooling concept require non-equilibrium conditions resulting in some interesting metastable or anomalous phases [34]. For example, dendrites are branched substructure networks which in case of heterogeneous nucleation, grow continuously into the molten liquid-metal laterally from the mould wall or any inclusion in the melt or in the case of homogeneous nucleation whereby it extends radially from the stable nucleus formed during extensive undercooling [35, 36].

3.2.1. Stable and Metastable Phases: Formation, Illustration and Advancement.

Metastable phases abound in the natural world. Diamond is a typical common example, formed as another crystals of graphite at high pressure but which retain all its intrinsic metastable features even at ambient conditions[1]. This is possible because the rate of conversion to its equilibrium state, graphite is eternally slow at room temperature and pressure [37]. So, metastable phases generally form and survive without ever becoming stable. Based on this, researchers over the years have created desirable metastable phases by capitalizing on kinetic differences as illustrated in ***fig. 3.4*** [38]; using novel processing techniques such as containerless rapid solidification. Hence, the concept of rapid solidification promotes specific metastable transformation or phase evolution as illustrated in ***fig. 3.5*** [39].

However, for conventional solidification, nucleation is usually followed by gradual crystallization and grain growth as a result of slow cooling over time. The formation and growth of dendrites in such cooling is due mainly to the diffusion and heat transfer along the solid – liquid interface as a result of predominant temperature gradient [30]. Negative (or positive) temperature gradient is dictated by the direction of heat transfer relative to solidification front. It is said to be negative when the solidification front built advances in the direction of decreasing temperature interface [38]; otherwise it is said to be positive temperature gradient is the direct inverse. Hence, the formation of metallic glass is a good example of metastable phase formation [40]. During rapid liquid – solid transition, many factors contribute to the formation, advancement and stability of the emergent metastable phase(s). Such basic parameters are kinetic, thermodynamic or physical factors that work together to contribute to

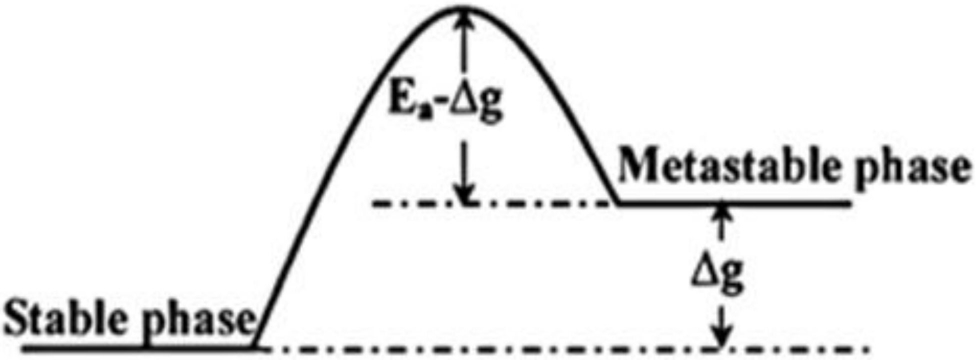

Fig. 3.4: The illustration of Gibbs free energy as cooling rate increases[38].

undercooling [2, 34]. Hence, at high undercooling; the solidification front is favoured as a result of projected negative temperature gradient build up ahead of it at high cooling rate [41].

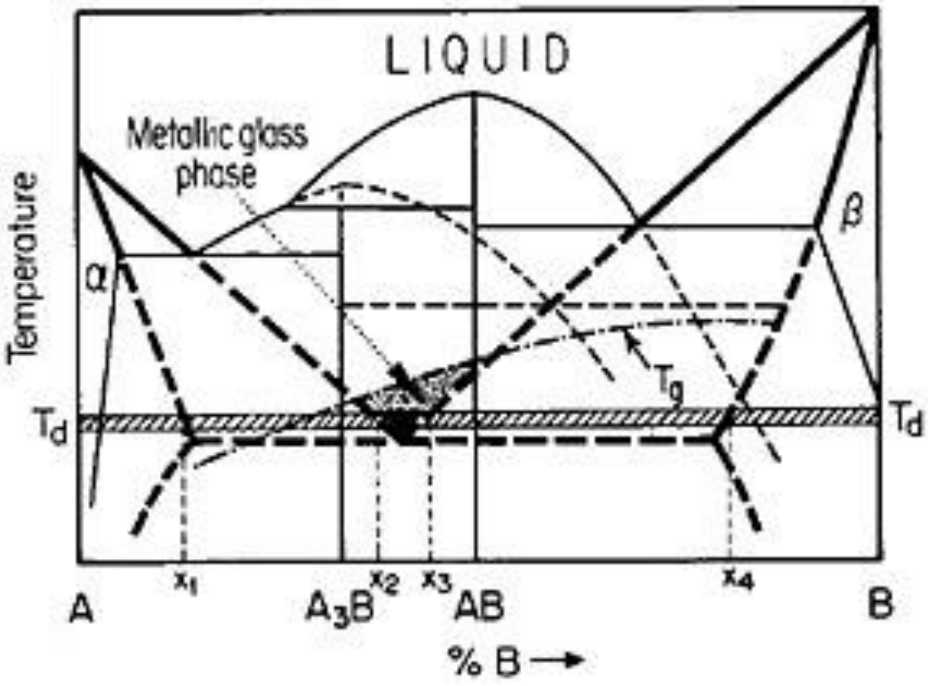

Fig. 3.5: Metastable isothermal metallic glass formation by inter-diffusion at temperature T_d existing between phases A and B. The evolved stable phases A_3B and AB do not nucleate. T_g is referred to as glass transition temperature [39].

3.2.1.1. **Temperature gradient and Interface Stability.**

Consider for instance a solidification front of a melt as illustrated in ***fig. 3.6***; the temperature ahead of the interface will decrease into liquid as heat is being taken away through the solid by the cold mould walls. In this case the interface will be advancing into a cooler region. The direction of growth is opposite to the heat flow resulting in negative temperature gradient. The front view of the advancing interface or perturbation determines the resultant structure or morphology of resultant crystal, the small perturbation just ahead of the interface will experience a higher temperature and will therefore tend to re-dissolve into the interface ahead which results in negative temperature gradient [39]. A planar interface is stable and dendritic solidification is

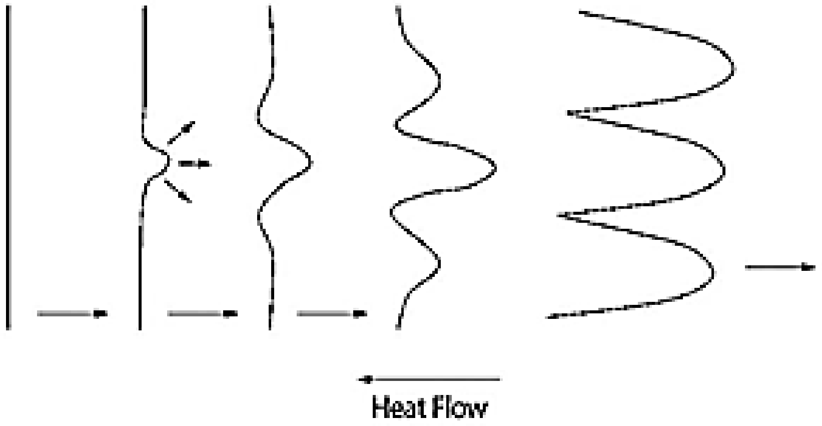

Fig. 3.6: Interface transition from planar to multicellular growth [2].

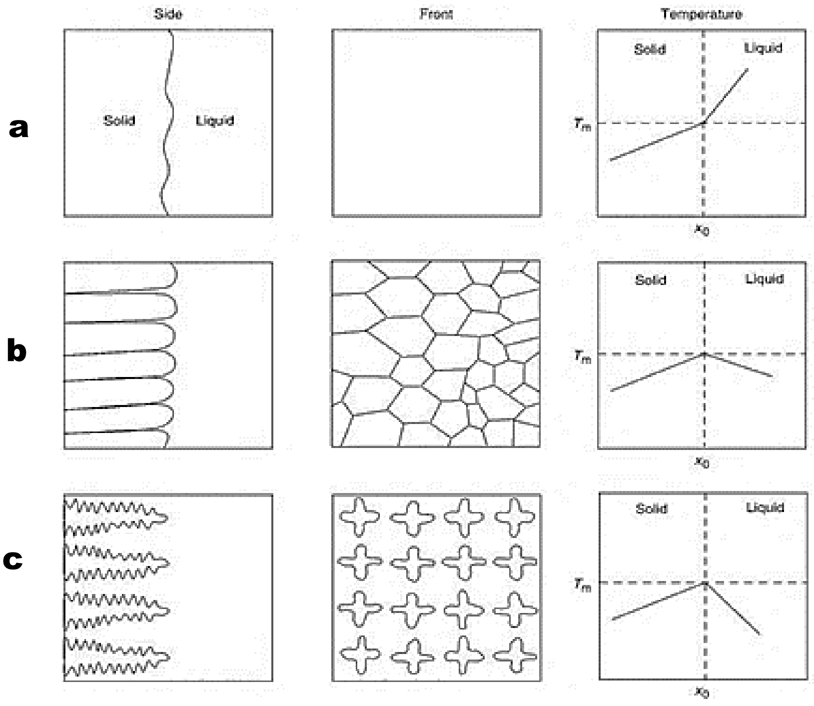

Fig. 3.7: Effect of undercooling on solidification structures. The perturbation tip condition defines the specific type of structure formed: (a) Planar interface, (b) Equiaxed growth and (c) dendritic growth [39].

therefore not favoured as it is in ***fig. 3.7(a)***. On the other hand, during sufficient undercooling; the solid grow into the melt. The release of latent heat of fusion as the solidification front advances result in a temperature increase in the newly formed solid advancing into lower temperature region of the melt (negative temperature gradient). However, since the bulk part of the melt is still undercooled and the small perturbation just ahead is at higher temperature; therefore as it advances to cooler region further solidification is favoured and growth is enhanced dendritically as shown in ***fig. 3.7(c)*** and eventually a well-defined microstructure then emerges.

3.2.1.2. **Microstructure formation and Phase transformation.**

As solidification proceeds, there are two main possible types of structural formation that can emerge depending on the conditions applied during the phase transition. Structural growth can either be free or constrained [42, 43]. For instance, on free or unconstrained microstructure formation such as in dendrite formation; free dendritic growth occur as a result of unrestricted growth of a nucleus into very highly undercooled melt forming a network of primary, secondary and even tertiary arms; while constrained dendrite growth out from development of many solid clusters. In ***fig. 3.8***, if we consider a free growth of a nucleus advancing towards an opposing front disturbance in the interface; the growth will experience perturbation ahead of it [44]. Actually free dendritic growth can be easily applied to multi-direction expansion and this gives more realistic insight into factors influencing dendritic branches formed [45]. Hence, the refinement of any evolved microstructure is governed by the spacing between the primary, secondary and tertiary arms. The closer these are, the finer the emerged final microstructure; meanwhile, the more distant the spacing the less coarse the emerging microstructure [2].

A constrained growth interface proceeds from a chill surface during rapid solidification. For instance, a pure melt solidifying under confined condition will exhibit a stable, planar solidification front due to the positive temperature existing ahead of the interface [46]. Normally the stability of constrained growing cluster depends on both the thermal and the solutal gradients which usually lead to higher undercooling and subsequently the de-stabilisation of the interface [39]. This leads to side branching with increased undercooling. It is simply a phenomenon in which the immediate solidification front is at lower temperature than the actual melt temperature thereby arm propagation is encouraged [2, 34]. The undercooling was caused by negative temperature gradient, which is what leads to dendrites formation, branched arm stability and propagation as illustrated in ***fig. 3.7(c)*** with its schematic diagram displayed in ***fig. 3.8 (a) & (b).*** Under these conditions the primary, secondary and higher order branches tend to grow in the easiest permissive direction favoured by the alloy constituent as indicated in ***fig. 3.9***; for purely binary system. Meanwhile, with higher solidification velocities such as in rapid solidification; gradual transformation from dendrites will be noticed. This is often characterized by sharper tips, broader trunks with more oriented side branches like interlocks as shown in ***fig. 3.7 (b)*** and ***3.8 (b)*** [42].

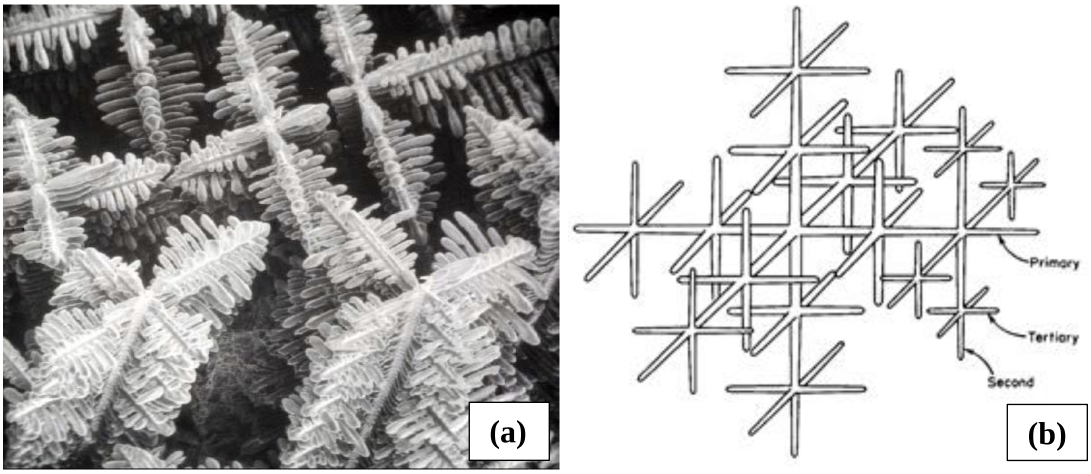

Fig. 3.8: (a) Micrograph and (b) Schematic diagrams of dendritic growth [2].

3.2.1.3. **Eutectic System: Solidification and Stability**

Eutectic is the most common phase system where two principal constituent elements of an alloy cause a lowering of the liquidus lines from both melting points of these pure elements involved. It is a state of evolution of two separate solid phases at a point from a completely liquid phase.

$$\text{Liquid} \xrightarrow[\text{cooling}]{\text{eutectic temperature}} \alpha \text{ solid solution} + \beta \text{ solid solution}$$

Hence, a eutectic solidification depends majorly on the composition of the alloy on a given eutectic isotherm. Therefore at the eutectic point, there is a definite transformation from liquid phase (L) to a solid phase with two distinct phases (α and β) **(*fig. 3.9*)**. Any shift from this point affects the alloys composition and the element that form first will have an enriched solid that is determined by the nearness of such to either side of the eutectic point, this is usually expresses in percentage as shown in ***fig. 3.9***. There are various solid form of eutectic alloys; it could be lamellar with its appearance often containing two distinct phases such that may, or may not be distinguishable by metallography. ***Fig. 3.10*** shows some eutectic structures. The basic underlying feature in all these structure is the concept that there is regular well patterned segregation of atomic species during eutectic solidification; and the stability of these depend mainly on the percentage of constituent elements and the processing temperature under consideration. It therefore means that for any eutectic microstructure, there will be distinct phase difference on the microscopic scale across the sample as observed in each structure shown in ***fig. 3.8***. Any inhomogeneity can significantly affect the final properties of the solidified alloy; as the microstructure produced from a process affects its performance [39].

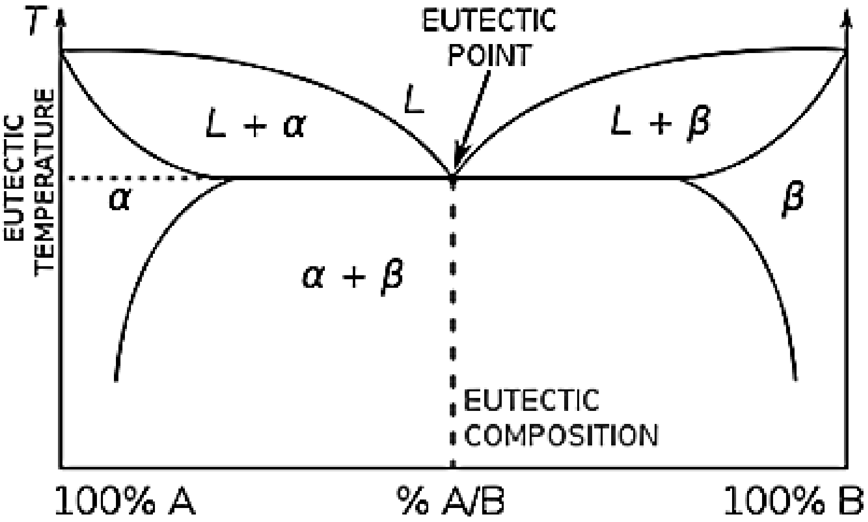

Fig. 3.9: A phase diagram for a fictitious binary chemical mixture (with the two components denoted by A and B; used to depict the eutectic composition, temperature and point [1].

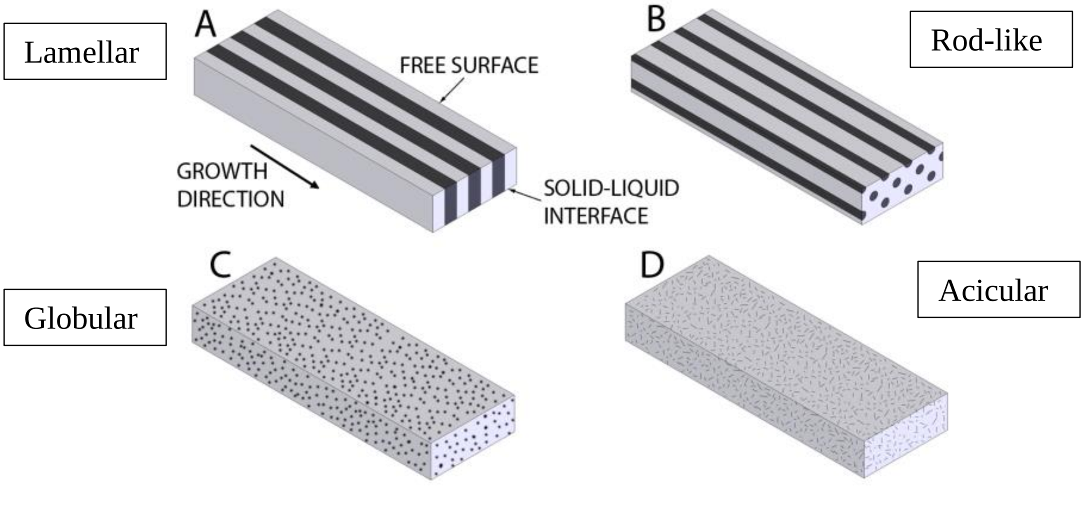

Fig. 3.10: Different typical examples of common eutectic microstructures [1].

3.2.1.4. Microstructure transformation dependence on time and temperature.

Microstructure evolution generally depends not only on transformation temperature but also on the period of occurrence. Typical example is isothermal transformation in eutectoid reaction or martensitic formation. These transformation which leads to interesting microstructures as a function of cooling rate, time and specific temperature cannot be expressly explained using equilibrium phase diagram. Hence, the progression of transformed phase and the expected microstructure at various cooling rate can be conveniently represented on time, temperature transformation curve [1]. The curve gives graphic description of the cooling rate required and the exact temperature at which a phase transformation will occur. ***Fig. 3.11*** shows the schematic TTT diagrams for eutectoid plain carbon steel. The curves show the different possible phases that can be formed in ***fig. 3.11(a)*** in accordance with different cooling rate path as shown in ***fig. 3.11(b)***. The diagram has S or C shape and it is indeed a very useful tool for interpreting and understanding the basic features of metastability of eutectoid microstructures [47]. TTT curves will provide information on the nature, type and rate of transformation; as well as the temperature-time and stability of transformed phases. The reason for the S or C shape is primarily due to the fact that near to the eutectoid temperature, the transformation driving force is minimal as a result of very

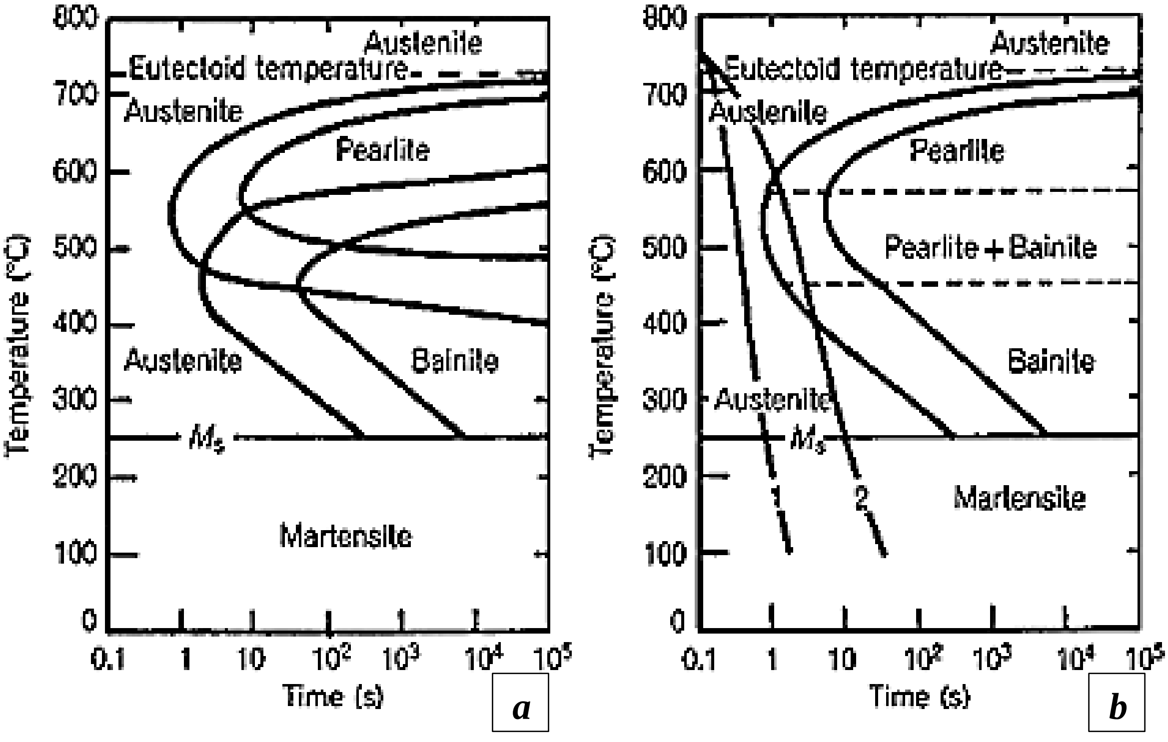

Fig. 3.11: (a) TTT curves showing pearlite, bainite and martensite phases in eutectoid (0.8 wt.% C) plain carbon steel; (b) derivative of (a) with superimposed cooling rate paths 1 and 2 [47].

low undercooling. However, the transformation increases with higher undercooling reaching maximum rate at the “nose” of the curve. Meanwhile below this temperature, the transformation driving force continues to increase but then the reaction get hindered by slow diffusion despite the rapid transformation.

3.3. Containerless solidification processing methods:

This section focuses on experimental methods for obtaining high degree undercooling. It addresses the fundamental science behind the formation of metastable phases and other non-equilibrium solidification phenomena [21, 22]. For instance, containerless processing techniques are rapid solidification methods for obtaining high degree undercoolings [22]. Commonly employed containerless facilities include: (a) free fall apparatus such as drop-tube; (b) levitation apparatus which can be acoustic, electrostatic or electromagnetic and (c) dispersion or fluxing technique involving emulsification in suitable oil. These techniques are relevant in preventing the possible effect of container wall during solidification [24]. They provide means of circumventing the effect of catalytic sites during liquid-solid transition which are essential to obtain extensive undercooling. In other words, these techniques consist of special melting/ejecting unit. The complete elimination of impurities and non-contact with the chill wall of the container in all of these techniques is important to the study of undercooling and rapid solidification of any alloy melt so as to clearly understand the phase changes and to characterize the emergent metastable phases formed during liquid to solid transformation.

The non-interference of the chill wall of the container during these processes in near ultrapure environment has eventually opened up the possibility of achieving large degree of undercooling of the melt, resulting in several non-equilibrium metastable phases not achievable by other methods [12, 48]. Subsequently, samples obtained from these non-equilibrium processing techniques are then examined; and these have been of keen interest to researchers as a result of extraordinary microstructural, physical and mechanical properties evolved. Indeed, containerless processing techniques are useful means of understudying rate of undercooling and rapid solidification but these are usually deduced *post-mortem* from the rapidly solidified end product by metallographic examination. In all these, the droplet size refinement is influenced by the extent of undercooling; other factors that governs undercooling potential of a melt include its composition, ejection pressure and the melt superheat.

3.3.1. Melt-dispersion techniques

Although this method is referred to as containerless it has carrier fluid for particles dispersion and cooling medium. Otherwise called melt sub-division or inert solid emulsification. It involves dividing certain volume of a molten metal into tiny dispersions in relatively large volume of suitable inert fluid as illustrated in ***fig. 3.12***. With sufficient rigorous dispersion effect, the majority of the material will be tiny and nucleant-free. Therefore, large degree of undercooling can be achieved [49]. So to ensure effective emulsification of this process, powered high-speed inert shearing fluid under non-reactive conditions must be employed. This can produce very fine metal droplets for microstructural investigation. Therefore, the small metal droplets produced in the inert liquid are free of internal and surface nucleation sites thereby resulting in extensive undercooling of the melt. Hence, for metals which have their melting point below 500 ^{o}C, organic emulsification fluids can be used; while molten salt or inorganic glass slags are used for melts having higher melting temperature such as ferrous alloys. However, as a result of temperature range limitation, this method is limited for powder metal droplet production; notwithstanding it can be extended to related metals with higher melting temperature by using alternating carrier fluids in sequence [50]. For this method, the significance of the melt sub-division is as provided by the tiny sample particles as shown by the increasing levels of undercooling with

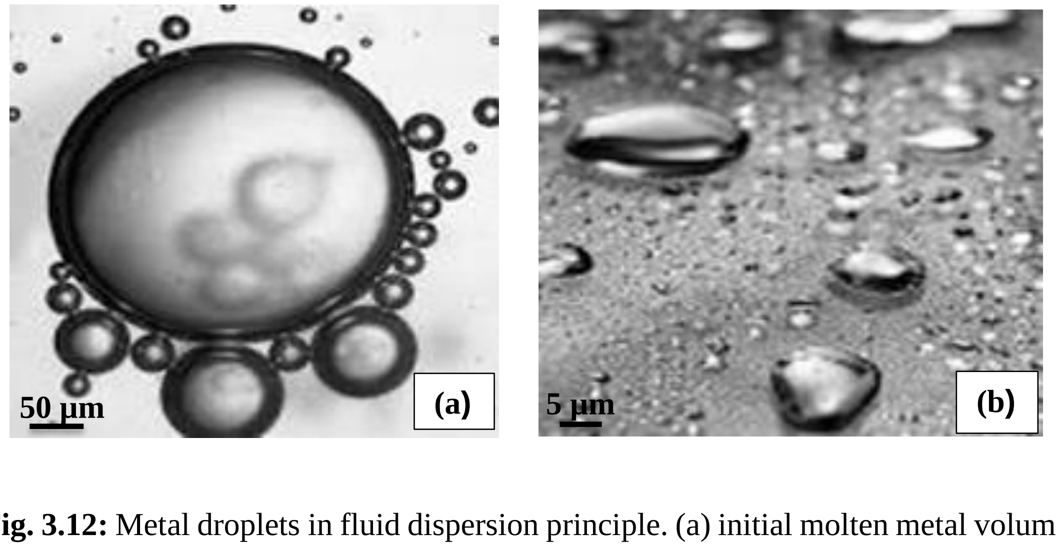

Fig. 3.12: Metal droplets in fluid dispersion principle. (a) initial molten metal volume and (b) tiny droplets formed after melt dispersion or emulsification inert suitable liquid [50].

decreasing particle sizes; powered by ultrasonic agitation of the carrier fluid. Therefore, the nucleation motes, otherwise called clusters are dispersed within the cooling medium and this are usually uniformly distributed within therein.

3.3.2. Short Drop-tube: features and droplets production

A typical short drop tube is basically a segmented tightly-fitted stainless steel enclosure in which droplets are produced from pieces of bulk metal that are melted, ejected, cooled and solidified through free fall in an inert low pressure atmosphere. Short drop-tubes are only few metres high; generally between 1.5 and 6.5 m tall. In very high drop-tubes, droplets experience free fall as if in a vaccum, i.e. near zero gravity experiences. The vacuum pumping system comprises of an oil sealed rotary pump and a turbo-molecular pump for purging the entire apparatus. ***Fig. 3.13***, show a schematic illustration of a typical short drop tube. This apparatus is a 6.5m ultra-high vacuum drop-tube situated in the Institute for Materials Research, University of Leeds. Due to the aerodynamic breaking effect of the gas, short drop-tubes do not produce micro-gravity (free-fall); but like any other typical drop-tube facilities, they are evacuated by high powered vaccum pumps to ensure very low pressure throughout the tube.

All drop tubes have very similar structural geometry that allow for melting, easy ejection and cooling of droplets in a controlled environment while falling freely down the appartus long segmented shaft in a relatively high vaccum or low pressure condition. This technique have been in used since it was invented by Prince Rupert around 1650. It was used for many years for the production of lead shots before its modification for producing other alloy droplets. It is a containerless technique and was first used for reseach purpose by Turnbull [26], who used this technique to examine and reveal different evolved metastable phases in Fe-35 at.% Ni alloy. This pioneering experiment by these duo, triggered other researchers interest in the usage of drop-tube as a research apparatus ever since. The concept of a typical drop-tube apparatus is that a material is melted in an inbuilt furnace situated at the top of the tube, at the appropriate temperature; the melt is then pressured ejected (not atomized) down the tube by and in an inert back filled gaseous medium (in this case), Nitrogen and/or Helium. The droplets rapidly solidify as they fall through the inert gas atmosphere and are then collected at the bottom of the apparatus. The resulting powder can then be collected, sieved and separated into size fractions, each of which represents a different solification velocity or cooling rate. One distinguishing feature of a short drop-tube is the need for back-filled gas to slow the fall of the droplets such that solidification will occur in-flight [27, 51].

3.3.2.1 **Long Drop-tube: Description and Usage.**

These apparatus are so called based on their height and the degree of undercooling that can be attained using such. It is said to be long, if it’s total vertical hight is approximately 50 m and above. There are tubes that are as high as 150 m, giving ~ 4.3 s microgravity or free fall. Typical example is the 105 m high long drop-tube at the NASA Marshall Space Flight centre in United State. So, these are employed to estimate the effects of microgravity on alloy droplet in earthbound labouratories at relatively low costs [52]. This long tubes are mostly used to study and analysis single droplets falling in vacuum and are applied in special studies as mentioned above; while short drop tubes are mostly employed for sprayed or pressurized droplets falling in a gas-backfilled controlled cooling medium [53]. In long drop tube, the heating and

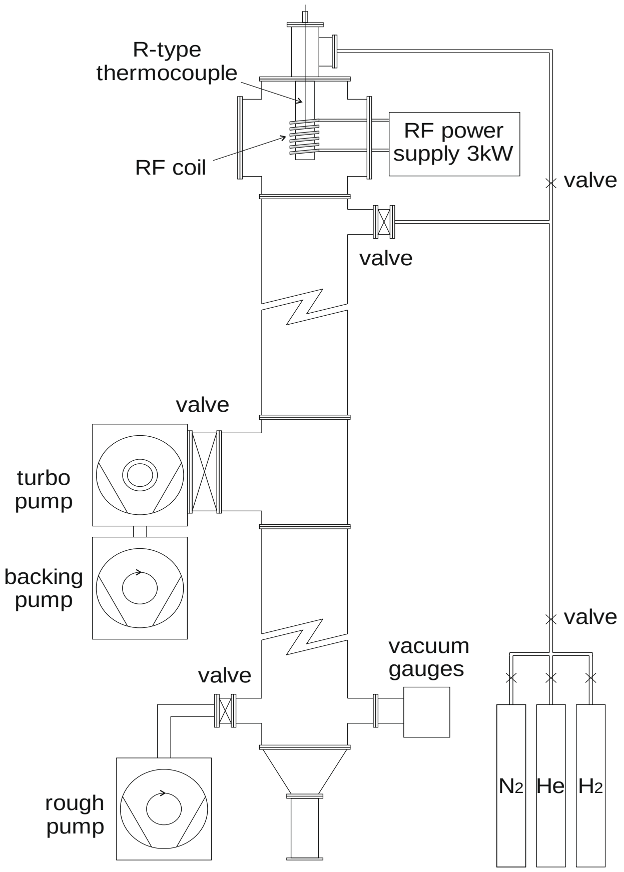

Fig. 3.13: Schematic diagram of the 6.5 m high drop-tube used for this study. [32].

ejection of the droplets are monitored by Si or InSb photodiodes or photodetecteor arranged at regular interval along the entire length of the equipment which enable the recalesence event and thermal history of the droplets to be recorded using in pyrometer as it falls down and releases latent heat [54]. They are mostly for research purposes.

3.3.2.2 Drop-tube purging, back-filling, monitoring and effect on cooling rate.

When required pressure is attained, thorough purging of the entire tube is then follows. The time taken for complete undercooling in a drop-tube varies with the sample as well as the nature and pressure of the back-filled gas used. Using the heat transfer equations during a free fall of a droplet prior to recalesence, a direct analysis of the cooling rate before and after nucleation can be estimated but due to the stochastic nature of nucleation an equivalent analysis of undercooling can not be elevated. This calculation gives a clue on effects of solidification velocity on microstructure formation, which can be inferred with the droplets sizes produced. Meanwhile, even if cooling rate is the same for say certain size fractions, the undercooling will be slightly different within such. The only variable factor on which cooling of each droplet depends is their size which is a function of the thermal properties of the cooling medium i.e. the back-filled gas [55]. So, the cooling rate experienced by a falling droplet can be increased substantially by back filling the tube with inert gas of high thermal propeties.

The effective cooling influence of inert gases employed in short drop-tubes with height ranging from 1.2 to 6.5 m to investigate metastable phases have made these apparatus suitable for research purposes. For example, there are recent studies on the effect of containerless rapid processing and high undercooling of many novel alloys [56, 57]. Method of droplet formation is one major difference between short and long drop tubes. For melting, solid bulk samples are loaded into the RF furnace; but droplets in short drop-tubes are pressure ejected through very tiny needle-eye holes at the bottom of the crucible and as these droplets fall downward different metastable morphologies or phases evolved [28]. The ejection pressure, inert gas environment and the small ejection holes contribute to much higher cooling rates of the droplets [53, 58]. Meanwhile, this is at the detriment of detecting the recalescence except for melts of alloys with higher melting temperature that are visible during ejection. One notable limitation to the usage of drop-tube is mainly in the fact that it is applied to rapid solidification studies of droplets of short experimental time frame unlike magnetic levitation. Also direct diagnosis of the undercooling in short drop tubes is very unlikely [40]. As mentioned earlier, experiment performed using this apparatus depends majorly on the post-mortem statistical and microstructure analysis of small spherical droplets of different diameter (x) of 38 μm $\leq x \leq$ 850 μm as per the apparatus used in the course of this experimental study. This is a very useful technique for the collection of large amount of data in one single study to investigate formation of possible metastsble transitions and the effect on mechanical property.

3.3.3. Levitation techniques

Levitation technique focuses on effective undercooling of single bulk sample melt instead of droplets formed using drop-tube. The concept is usually to suspend the droplet in a quiescent state and make it stable (in position) by suitable levitation field application [24]. Bulk melt levitation generally provides direct observation and means of undercooling the whole sample and step to step monitoring of how this solidification can be model or stimulated. Common levitation methods include: acoustic, aerodynamic, electrostatic and electromagnetic levitations. These methods were developed depending on the field used to levitate and set single bulk samples in the earthbound and space laboratories under various conditions [59].

3.3.3.1. **Acoustic levitation** This is based on the generation and application of high ultrasonic levitation field intensity to counteract the effect of opposing gravitational pull such that a sample can be kept in a steady state in-between the two forces. When this is achieved, the levitated object is maintained within standing wave pattern [52]. Therefore, the dimensions of any sample for suitable acoustic levitation must be far less than that of sound wavelength. Meanwhile, to obtain effective counteracting levitation force, high mass density gases such as Benzene, Krypton or Toluene rather than helium or argon is used. Based on this, a range of sample size in submillimetre can be effectively suspended against gravity in any of the above gas medium with resonant field frequency bewteen 1 and 100 kHz. In summary; acoustic levitation provides containerless rapid solidification for metals, alloys and non-metal samples and it is mostly for samples with small mass densities [40].

This method is in great use in fluid dynamics researches in both earthbound and space laboratories experiments [54].

3.3.3.2. **Aerodynamic levitation** is another example of containerless suspension technique based on the application of dynamic gas flow or fume positioning. It involves samples being levitated by regulating the fast flow rate of gases via different shaped nozzles [24]. The resultant stable suspension of any specimen in the generated field is actually as a result of levitation field intensity of the jet air flow, to keep the sample in stable positioning, and this is then heated up by subjecting the entire system to isothermal furnace heating [60, 61]. Meanwhile, certain features such as the number and geometry of nozzles, mass density and flow rate of gas determine to certain extent the stability of levitated sample. One other way this levitation is achieved is by means of sets of collimated holes through which gas is blown to keep the sample suspended in the field intensity [62]. Hence, shaping of liquid melts in gas layers as such emerge from crucibles is possible by this technique. The downside of aerodynamic levitation is the high gas consumption. Also, due to the high gas flow impurities in the gas tend to nucleate solidification, which limits undercooling [63].

3.3.3.3. **Electrostatic levitation** is a concept based on the principle of charged particle placed within an electrostatic field [29]. This effect is made possible by the Coulomb laws of electrostatics. This combined effect allows suspension of particles within directly opposite well-positioned charged plates. However, within these electrodes, the right suspension of the specimen can only be monitored by means of control system feedback. This can be achieved by combined effect of optical examination and computer monitoring to keep the suspended sample in position by means of capacitance field generated as a result of voltage applied to the end electrodes [64]. The major challenge of this method is the means of keeping the sample electrically charged at elevated temperature and under a vacuum [65].

3.3.3.4 **Electromagnetic levitation** is a suitatable technique for metallic materials especially for levitating sphere of up to 10 mm diameter. It is based on the principle of alternating current flowing through a coil of a conically shaped wire of single loop [66]. So, with right parameters; the electromagnetic field produced will induced eddy current in the electrically conducting sample. The eddy current produced in such electrical sample leads to opposing force against the primary field intensity and this leads to heating effect by induction [36]. Meanwhile, the concept of electromagnetic levitation allows definite analytical calculation of the field intensity distribution which is independent of the sample size and induction coil diameter. Hence using this technique, considerable undercooling have been recorded [67]. Therefore, electromagnetic levitation under specified conditions will produce extensive undercooling achievable with the potential to reach the critical phenomena in the solidification behaviour of the sample [68, 69].

3.3.4. Melt Fluxing technique

In this processing technique, samples are isolated from solid container walls and the numbers of potent heterogeneous nucleation points are significantly reduced [70]. It involves melting, undercooling and solidification of a suspended metallic sample in an inorganic glass flux [71]. Generally, the procedure for melt fluxing involves heating the sample by RF induction coil and the rate of melting depends on the intensity of the generated flux in the vacuum or inert environment [72]. However, to monitor the temperature of the droplets, thermocouple or two-colour pyrometer can be used. These are usually connected to an out-put device such as chart recorder to keep track and estimate the time – temperature profile of the experiment. This method provides a number of advantages in the sense that, firstly it prevents mould wall nucleation. Secondly, the generated flux aids in the removal of oxides and impurities from the melt; particularly with cycling i.e. repeated melting-undercooling cycles which are believed to progressively purify the sample, and so high undercooling is achieved. With this technique, high speed imaging of the recalescence front can be recorded and it also allows direct measurement of the sample’s temperature at intervals. Hence, this method is specifically useful in microstructure evolution investigation of melts as a function of undercooling [73].

3.3.5. High Pressure Gas Atomization technique

Generally, high-pressure gas atomization (HPGA) is a close-coupled discrete jet atomization method. It is one of the most effective industrial rapid solidification processing methods. Others include, metal injection molding, thermal spraying and melt spin chill casting techniques. These methods are used for mass production of very fine metal/alloy powders [30]. Meanwhile, HPGA stands out and it is the most used industrial rapid solidification technique. This is because better powder size and refinement can be achieved with it especially with right nozzle and appropriate atomization pressure. When compared to other methods, it is reasonable to assume that the increased gas flow kinetic energy associated with HPGA is in part (along with the gas thermal conductivity) responsible for the result it gives as an effective method. Its background principle is based on the kinetics of the melt and gas flow associated it. However, the energy transfer mechanism leading to the resultant melt break-up and the droplets formation is still undergoing investigation.

Meanwhile, the science behind its viability and stability is thought to be brought about by the interaction between the liquid stream and the shearing force of the gas at the melt-gas interface. The momentum of this rapidly growing internal surface tearing wave are amplified within the pressure ejected liquid. The wave thereby continue to grow in amplitude until a critical size is achieved and this generates its dispersion into fragmented ligaments and subsequently into large quantity of highly purified droplets [50].

3.4. Phase Transformation Systems.

Rapid solidification usually results in microstructures re-engineering that are very different from that obtained during normal or slow cooling. This change in morphology, usually alters the basic inherent properties of materials such as magnetic, electric, optical, thermal and mechanical properties of the evolved metal or alloy [13]. All rapid solidification methods including various containerless processing techniques offer controlled access to novel and advantageous metastable states which lie far from equilibrium. The degree of rapid solidification leads extensively to sequentially metastable supersaturated solid solution, non-equilibrium crystalline phase, metallic glasses and spontaneous grain refinement depending on the rapid solidification conditions [10].

3.4.1. Supersaturated Solid Solution and metastability.

Supersaturated solid solutions have been described as an example of compositional metastability [40]. This has attracted many researchers’ attention because of notable improved properties at room temperature and the potential for solid solution strengthening and age hardening it offers in metallic transformation to produce desired metastable phases. Typical application of supersaturated solid solution was described in rapidly solidified Al-12 wt.% Si which was cooled at a rate of up to 10^6 K s^{-1} in order to obtain a nano-dispersion of Si particles within a supersaturated Al matrix [74]. An example of this is age hardened 7xxx series Al-alloys which has extensive application in aerospace. The resultant microstructure produced an increased hardness value of more than double that of the original or equilibrium alloy [75, 76]. For this sample, the solid solution could be retained up to a temperature of about 523 K, beyond which the precipitation of Si and microstructural coarsening leads subsequently to a substantial reduction in hardness. Meanwhile, for proper understanding of the fundamentals of supersaturated solid solution, attention must be given to the basic science behind this kind of rapid cooling techniques. Therefore as noted earlier in section 3.2.1, the release of latent heat upon recalescence can destroy the metastable state and large degrees of undercooling are required in order to retain it. However, Lora et. al. [76] provided a solution to this challenge by applying the combine effect of a melt-fluxing and quenching technique. The same could be true of any technique that uses high undercooling with high cooling rate, i.e. drop-tube technique; which allows the non-equilibrium structure to be frozen, retained and made stable at ambient temperature. The combined achievement of having a metastable phase in a saturated solid solution (undercooling and cooling rate) with or without noticeable recalescence permits the retention of the transformed metastability [55].

3.4.2. Stable - Metastable Crystalline Phase miscibility.

Metastable crystalline phase formation requires a certain degree of undercooling which must be kinetically favoured or preferred. To understand this concept requires adequate knowledge of phase formation, identification of emergent phase with corresponding metastable phase diagrams and providing metastable phase evolution pattern from the melt to the solid state. Hence, the knowledge of the factors that influences nucleation and increase of metastability of phase is very important [77]. Also, it is important that prior understanding of the features and identities of expected phase are compared with reference in a data base [78]. Various containerless solidification techniques provide useful ways of evolving and promoting the formation of any desired metastable crystalline phases. In their pioneering work, Gao et al. [79]; showed that external triggering of preselected phase is possible and could be used to produce BCC metastable phase in Fe–B alloys by encouraging solidification at moderate undercooling using a BCC Fe-Nd-Zr-B alloy. Most often, the confirmation of metastable phase formation are obtained through the observation of re-melting at a temperature below the equilibrium melting temperature. This method provides useful way of obtaining experimental data for metastable phase diagram determination [80]. Below are different types of such phase miscibility:

3.4.2.1. **Quasicrystalline Alloys**

Quasicrystalline alloys are formed as a result of non-periodic ordering of clusters of atoms exhibiting local symmetry, where non-periodic repetitiveness is expected. These alloys are a class of intermediate compounds that exhibit diffraction patterns that are somewhat rare in crystals [81, 82]. There are two types of quasicrystalline symmetry, namely I-phase and T-phase quasicrystals. The difference between them is in their crystal orientation. The I-phase is the most common form of quasicrystalline symmetry, so called because of its icosahedral configuration, which is quasi-periodic in three dimension or more [46]. However, the T-phase is quasi-periodic in two dimensions and exhibits point group symmetry. The ability of these phases to change orientation arises from the regular spacing of indeterminately large number of elements, which can be simply described as long range ordering. Meanwhile, many other quasicrystalline phases have been discovered and are mostly formed in peritectic phase transformations [82, 83]. These are mostly metastable although some stable quasicrystalline phases have been observed [82]. Therefore, a proper understanding of the formation of these intermetallic phases will definitely leads to future designs of better high performance alloys.

3.4.2.2. **Metallic Glass**

Generally, metallic glass is formed when crystallisation is avoided during rapid cooling, leading to the evolution of amorphous solid [84]. This is probably the most researched metastable structure so far. During rapid solidification, the structure of the melt is essentially frozen into congealment solid; giving a non-crystalline phase characterised by a total absence of long range crystallographic order [41]. This definite transformation is achieved by a sufficiently very fast cooling. The rapid cooling rate circumvents the growth of nuclei by reaching the glass transition temperature, T_g rapidly before any appreciable crystalline growth can occur. In simple terms, it means the viscosity will increase continuously as the temperature decreases. However, above T_g the properties of the melt such as volume and fluidity depend mainly on temperature owning to the mobility of the atoms in the melt which allows configurational changes. Meanwhile, below T_g, mobility of atoms in the melt becomes so slow that changes are no longer possible and a rigid glass structure will be formed [85]. Therefore, no appreciable changes in the structure and properties of the metal will be noticed even with further cooling. In conclusion, the kinetic consideration of atomic mobility is rather the determining factor for T_g than the thermodynamic factors [86].

Other outstanding factors than influences metallic glass formation include the degree of relaxation, retendering atomic diffusivity, using negative heat alloying elements and narrowing down melt–solid temperature gap; will definitely enhance rapid metallic glass formation [86]. Such alloys possess great desirable properties. In a way, the structural and mechanical properties of glasses and metals therefore combine to give: strength which are around twice that of steel and yet they are lighter, have good hardness and possess better wear resistance. However, at elevated temperature, like any other fluid; metallic glasses viscosity becomes greatly reduced thereby revealing their potential for hot-forming. Also, the formation of metallic glass is favoured by a deep eutectic [87].

3.5. Cast Irons: History, Features and Types

Cast iron was invented in the 5th century BC in China. Then, it was primarily used to make pots and weapons, but it came to limelight in the western world when in 15th century it was being used for making cannon and shot [88]. The then King Henry VIII initiated its usage for making of military arms for England Navy, though it was heavier but it provided better cheaper protection. Thereafter, in 1712, steam engine was developed with cast iron by one Thomas Newcomen and by 1770s; this material was already being used for structural purposes. Since then, it has been used in various ways and its application continues even till day. Cast iron has become prominent in the heavy construction industry, in car and truck manufacturing industries. It belong to a family of ferrous metals with wide varieties of properties.

Like steel, they are versatile and are primarily made up of iron, carbon and silicon [89]. It is said to be the first man-made "composite" with over 2500 years of existence. Beside its relative low cost, longevity in service, availability and formability; it has a range of desirable and adjustable physical and mechanical properties. While steels contain less than 2% carbon (practically less than 1%), cast irons generally contain more than 2% carbon which is about the upper limit of carbon solubility in Fe-C alloy. The undissolved free carbon content remains in solution with single phase iron, retained austenite. Therefore, cast irons normally solidify as heterogeneous solid solution with more than one stable or metastable phase constituent depending on the solidification condition which affects the evolved microstructure [90, 91].

There are different types of cast irons with microstructures and distinct percentage composition. **Table 3.1** shows the elemental composition ranges of non-alloyed and or relatively low alloyed common cast irons. They are basically; Gray, Spheroidal and White cast irons [92]. Meanwhile, low alloy BS1452 GRADE 250 commercial grey cast iron is being used for this research study.

3.5.1. Grey Iron

As the name implies, grey cast iron appears greyish when sectioned or fractured as a result of its high graphite content. Iron is the principal constituent with % carbon content in the range of 2.5–4.0 percent; majority of which are present in graphite flakes randomly distributed in the stable iron BCC phase matrix. The size, amount and distribution of these graphite flakes influence and dictate the microstructure, physical and mechanical properties of this very important alloy [91]. Silicon content is another major influence of cast iron feature. It acts as carbon stabilizer and precipitant for graphite flakes formation. It is relatively cheaper than steel, it has good formability, castability and many other desirable properties that distinguished it as the most commonly used cast iron. Grey iron are brittle mainly because the graphite propagates cracks. However, when properly alloyed and processed; it often provide desired properties. Naturally grey iron has good compressive strength, wearability and damping effect.

3.5.2. White Iron

White cast iron differs from grey iron basically because it has less silicon content, hence the matrix is iron carbide saturated; which gives its distinguishing reflective whitish surface when sectioned or deeply scratched due to its silicon deficiency [89]. Hence, with lower silicon content, the carbon is precipitated not as graphite flakes but as cementite. Therefore, iron carbide formed, precipitate in quite high rate and this makes the evolved sample much more brittle in nature than grey cast iron [91]. It occurs as Fe_3C phase and can coexist with other phases as part of the eutectic. It is a hard intermetallic material which exhibits mixed metallic/covalent bonding. Also, carbide sometimes occurs along with other stable or metastable Fe phases mostly at higher carbon content. For example, it forms solid solution with austenite to produce what is known as ledeburite. The more the cementite that is formed, the more brittle the alloy; which is the reason the fractured surface is very reflective. White cast iron has higher cooling rate compare to grey cast iron, making it possible to have hard cementite outer layer with softer grey inner part [93]. This allows its application where high abrasion is required.

3.5.3. Spheroidal Iron

This is similar to grey cast iron in the sense that they both have graphites. However, it has its distinctive peculiarity as the flakes are somewhat noddle-like and less common. In fact, the carbon distribution in its matrix appears in spheroidal (spherical-like graphite) form rather than in flakes, hence sometimes referred to as nodular iron [94]. To form this structure, inoculants such as cerium or magnesium must be added along with sufficient silicon to precipitate the carbon as graphite nodules. Often called ductile iron, it has better mechanical properties compared to other cast iron types. Its peculiarity include a high tensile strength, high toughness and no notch effect [95].

Table 3.1: Chemical composition of typical un-alloyed cast irons [89].

Iron Type	**Carbon**	**Silicon**	**Manganese**	**Sulphur**	**Phosphorus**
Gray	2.5-4.0	1.0-3.0	0.2-1.0	0.02-0.25	0.02-1.0
Ductile	3.0-4.0	1.8-2.8	0.1-1.0	0.01-0.03	0.01-0.1
Compacted Graphite	2.5-4.0	1.0-3.0	0.2-1.0	0.01-0.03	0.01-0.1
Malleable (Cast White)	2.2 -2.9	0.9-1.9	0.15-1.2	0.02-0.2	0.02-0.2
White	1.8-3.6	0.5-1.9	0.25-0.8	0.06-0.2	0.06-0.2

3.6. Grey Iron: Graphite morphology, types and shapes.

Graphite formation and distribution is a characteristic feature of grey iron microstructure due primarily to the nature and properties of carbon. Most stable phase of solid-state carbon is graphite. It has two distinct phases; a dihexagonal dipyramidal and a ditrigonal disphenoidal. The latter is metastable as compared with hexagonal phase. Based on this, the carbon content add up with other alloying elements to determine the iron-carbon equivalent value **(**see ***equation*** *3-2***)**. Hence, carbon equivalent (CE) is the summation of the carbon percent and one third of that of Silicon and Phosphorus in the alloy. It is mathematically expressed as:

$$\text{Carbon equivalent (CE) value} = \%\,C + \%Si/3 + \%P/3 \quad \ldots\ldots\ldots\ldots\ldots \quad \textbf{(3-2)}$$

The graphite appears and grows in form of flakes which is basically a worm-like structure with more growth in length than in thickness. There are two typical kinds of graphite growth depending on the growth mechanism. There is the primary flakes, which grow freely within the melt and the eutectic flake which grow side by side along with any other phase(s) in solid solution [96].

3.6.1. Primary Flakes Formation

Typical morphology of primary graphite is mostly found in slowly cooled as-cast grey irons. It is randomly distributed and appears as long trunk of dendrite with non-directional network of flaky morphology. ***Fig. 3.7(c)***, gives progressive growth of a typical primary flakes front. This form of graphite is otherwise classified as type C or Kish graphite with a few hundred micron in length but few 1/10 microns in width. The random arrangement of this graphite flakes justify its formation just before and after the eutectic point. Hence, these flakes grows more steadily within the slow cooling alloy of iron -carbon rich hypo- & hyper- eutectic alloys [89].

3.6.2. Eutectic Flake Solidification

The formation of eutectic flakes occur during eutectic solidification and this graphite appears in layers or plate-like form known as lamella along with another phase usually cementite in austenite matrix. The schematic growth of these flakes is shown in ***fig. 3.14(a)***. From this figure, we see graphite nuclei formed in the melt; these then branches into flakes which then continue to grow by consuming the carbon atoms within their immediate vicinity and what is left is matrix of near pure Fe; i.e. ferrite in alternating layers as sandwich [97]. The final morphology is in the form of lamella that grows side by side as plate-like interconnected or spherical eutectic cells. Such network of flakes in a eutectic cell whose metallic phase has been etched away is as showed in ***fig. 3.14(b)***. The obvious difference between primary and eutectic flakes is that the eutectic flakes are finer and more convoluted than the primary flakes.

This is as a result of lower growth temperature of eutectic flakes as well as restriction imposed by the alternating harder metallic phase forming simultaneously. Normally as the cooling rate raises, the Fe-Fe_3C eutectic forms more fine pearlitic phase. Hence, based on their morphologies graphite flakes can be further classified depending on their solidification conditions and composition [13].

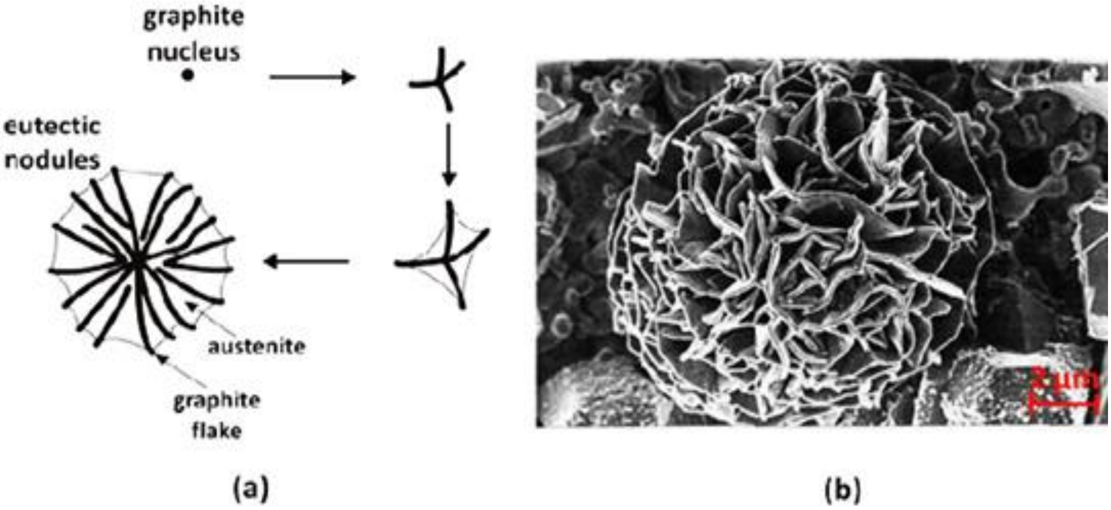

(a)

(b)

Fig. 3.14 (a) Schematic and (b) micrograph of Fe – C eutectic cells formation [89].

3.6.2.1. **Type A flakes**

This type of graphite flake is shown in ***fig. 3.15 (a)***. It can be observed that the flakes are inter-woven and possess a compound strand of morphology arranged in a randomly oriented pattern. They are normally formed in cast iron with slow cooling or minimum undercooling. Generally undercooling promotes high chilling tendency, hence the addition of inoculant such as Al or

Ca and more of Si content will favour the formation of this type of graphite flakes as a result of increased graphitization potential.

3.6.2.2. **Type B flakes**

Type B graphite flakes is commonly found in grey cast iron at near eutectic composition which cools faster than the rates associated for type A flakes. ***Fig. 3.15 (b)*** shows a typical type of this graphite flake which appears in form of rosette or clusters and grow in a mechanism similar to the one shown under normal eutectic graphite flakes. This type of graphite flakes are found in thin-walled castings or on the surface of thicker section of as-casts.

3.6.2.3. **Type C flakes**

This is the most common or otherwise called normal graphite flakes. It is a typical graphite flake that forms when cooling of as-cast is allow at ambient temperature. It appears as thread-like and randomly distributed in saturated solid matrix of either ferrite or pearlite phase. The network of this flakes are worm -like needle structure that are non-directional. It is often referred to as Kish graphite as described in primary eutectic flake formation in section 3.6.2.

3.6.2.4. **Type D flakes**

The morphology of type D flakes is as shown in ***fig. 3.15 (d)***. The distinguishing feature of this type of graphite flakes is that, it possesses very smooth morphologies with a preferred orientation with predictable repeated unique pattern. They are usually formed in-between the metallic dendrites at the final stage of normal solidification. Its formation require medium cooling rate but higher than that needed for Type A and B, yet it is lower compared to the one needed for cementite formation.

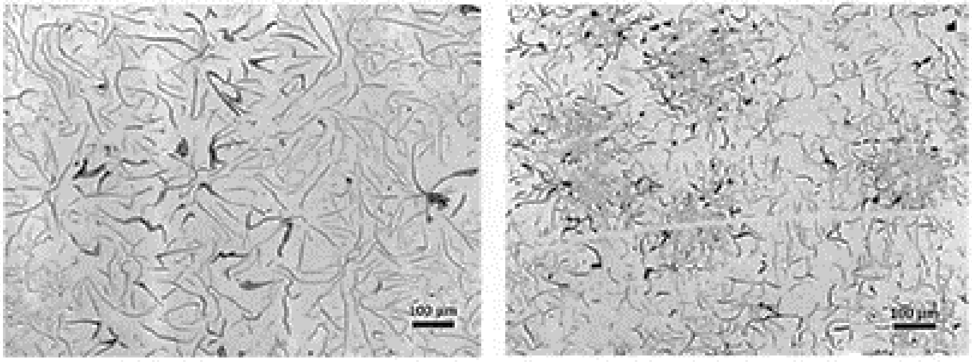

a) Flake type A b) Flake type B

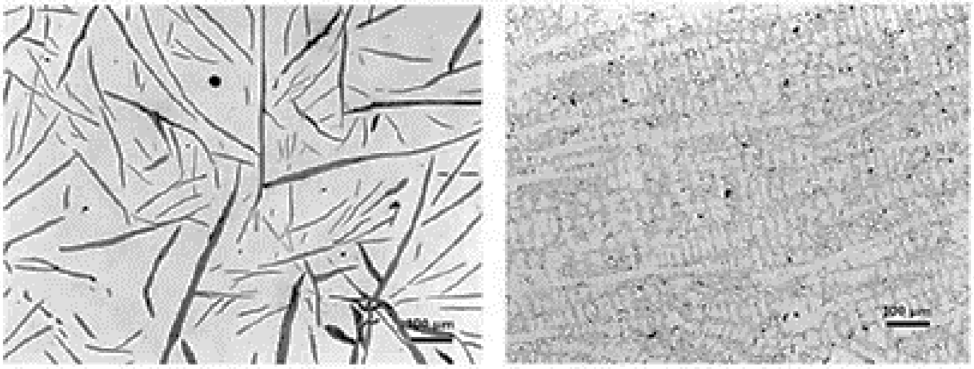

c) Flake type C d) Flake type D

e) Flake type E

Fig. 3.15: Possible graphite flakes depending on cooling rate and % C content [98].

3.6.2.5. Type E flakes

A typical Type E flake is shown in ***fig. 3.15 (e)***. It is coarser, more fibrous-like flaky morphology than the Type D flakes. One can easily notice that it has preferred interdendritic distribution and more pronounced traceable patterns.

3.6.3. Non-flaky graphites in cast irons:

3.6.3.1 Spheroidal or nodule graphite.

Nodular graphite is as shown in ***fig. 3.16***. It appears as spheres or nodules in iron matrix hence the name spheroidal or nodular graphite. When formed in grey cast iron, such becomes more ductility with better mechanical properties close to that of mild steel. Previous studies [99, 100] has shown that Mg or Ce promote sphere graphite growth in Fe-C alloys. Such elements that enhance spheroidisation are referred to as nodulizers.

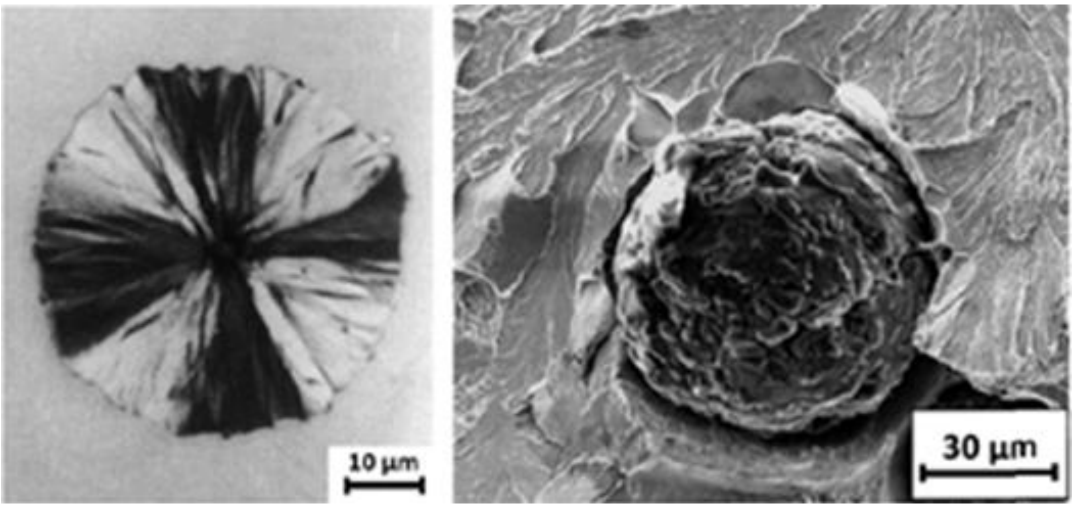

Fig. 3.16: Isolated sphere graphite with (a) Optical microscopy & (b) SEM [89].

3.6.3.2. Coral (fibrous) graphite.

This class of graphite has very fine semi-fibrous morphology which is an intermediate type between flake and sphere graphite. In ***fig. 3.17,*** (a) and (b) show the light optical and SEM micrographs of coral graphite. This derived or distorted graphite structure normally forms during rapid solidification of iron melt with low sulphur content of less than 0.001%. The schematic diagram shows that the fibres have branched irregularly and form a highly convoluted and interconnected three-dimensional framework.

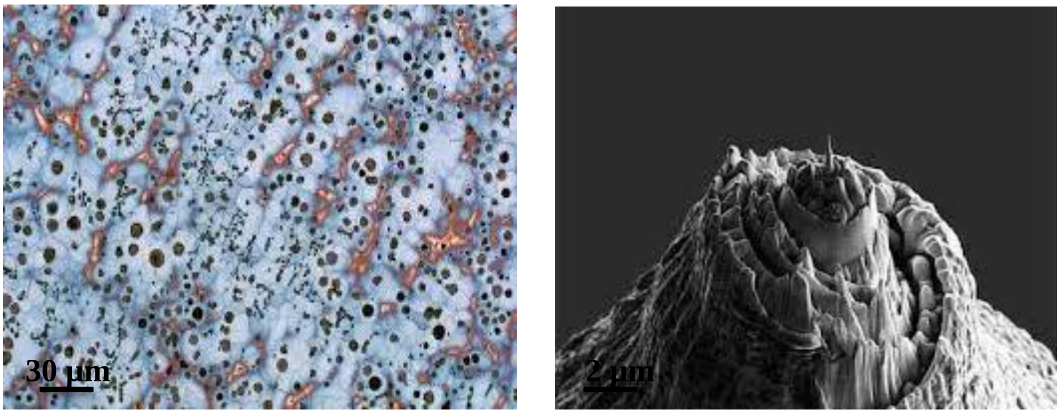

Fig. 3.17: Coral graphite observed with: (a) Optical & (b) SEM microscopy [19].

3.7. Phase Transition and Representation in Fe-C based alloys.

Generally, phase transition in alloys occur along lines of equilibrium and these determine the kind and nature of thermodynamic transformation that is eventually followed [101]. Carbon is considered as an interstitial impurity in Fe. Actually, it forms solid solution with α, γ, δ phases of iron. The Fe–C phase diagram is fairly complex. However, there are stable and metastable portions of the Fe – C phase diagrams. Like any other Fe-based alloys, cast irons exhibit mechanical properties which depend on the evolved microstructure as a result of processing employed and the % carbon content in the alloy.

3.7.1. Iron – Graphite (Fe – C) and Iron- Cementite (Fe – Fe_3C) Phase Diagrams.

A typical superimposed Fe – C and Fe–Fe_3C phase transformation diagram is as shown in ***fig. 3.18*** [1]. The understanding of the different part of this diagram is important to knowing the expected phase(s) as the percentage of carbon content increase with rise in temperature in any iron-based alloy. The steel portion of the diagram ranges from 0 to 2.08 wt.% C, while the cast-iron part is represented by 2.08 to 6.67 wt. % C [89]. The diagram shows one eutectic reaction at 4.30 wt.% C and 1147 ^oC temperature as illustrated in the *expression* ***3-3***. An eutectoid reaction occurs at 0.76 wt. % of carbon and temperature of 727 ^oC; above this point is a phase referred to as austenite or the gamma (γ) iron which when cooled, forms two new phases called ferrite (alpha), α-Fe and cementite, Fe_3C. This decomposition is commonly referred to as austenite decay as shown in *expression* ***3-4***. The principal sections within the steel region of this iron rich phase diagram can be subdivided into: hypoeutectoid (0

< wt. % C < 0.68 wt. %), eutectoid (C = 0.68 wt. %), and hypereutectoid (0.68 < wt. % C < 2.08 wt. %).

$$\textit{Liquid Iron} \leftrightarrow \textit{austenite} + \textit{cementite} \quad \ldots\ldots\ldots\ldots\ldots \textbf{(3-3)}$$

$$\textit{Solid} \rightarrow \textit{Solid}\ \alpha + \textit{Solid}\ \beta \quad \ldots\ldots\ldots\ldots\ldots \textbf{(3-4)}$$

Where solid γ is austenite, solid α is ferrite, and the solid β is cementite.

3.7.2. Possible evolved phases in Fe – Fe_3C Phase Diagram.

Again, steel and cast iron are generic families of metals with very interesting microstructures and alterable properties. For example, towards the low-carbon side of the iron – cementite phase diagram shown in ***fig. 3.18 (a & b)***; one can easily distinguish ferrite (α-Fe), which dissolve at most 0.028 wt. % C around 738 °C and austenite (γ-iron), capable of dissolving up to 2.08 wt.% C at 1154 °C. Hence, carbon steels hardening as well as many other steel alloys, is based on the solubility of carbon in the various iron phases namely α-iron (ferrite) and γ-iron (austenite) [92]. However, at the carbon rich end of the Fe–C phase diagram we find cementite (Fe_3C). The stability of these phases depend on the percentage of carbon along the horizontal axis and temperature along the vertical axis. Critical analysis of iron-carbon diagram shows that the following stable and metastable equilibrium phases have certain features or peculiarities depending on the combination factors.

3.7.2.1. **Austenite**

The austenite phase otherwise known as gamma-phase (γ-Fe) iron is a metallic solid solution comprising carbon in FCC iron. It is a non-magnetic allotrope of iron and only exist between 727 and 1493 ^oC with maximum carbon solubility of 2.14 wt.%. However, at 1395 °C, γ-Fe transforms to δ-Fe with body centered cubic structure. This phase is not stable below 727 ^oC but can be retained at room temperature when rapidly cooled [69]; and its transformations are apparently along the left vertical axis of the Fe – C phase diagram; but its stability can be extended or shortened by alloying elements such as Silicon [1, 102, 103].

3.7.2.2. **Ferrite**

This is the BCC phase structure of solid solution of carbon in iron at ambient temperature and pressure as well as at higher critical temperature before it melts. It contains only very small concentration of soluble carbon of ~ 0.022 wt.% which is the highest solubility of carbon in it. Otherwise known as alpha-ferrite (α-Fe), it is very stable up to 912 °C, after which it transforms into FCC austenite. However, at higher temperature, specifically at 1394 ^{o}C; it becomes delta ferrite (δ-Fe), which is stable up till 1538 °C before it melts [95]. This high-temperature ferrite has similar crystal structure (BCC) as alpha-ferrite.

3.7.2.3. **Cementite**

This is formed in the much rich carbon portion of the Fe–C phase diagram. Iron carbide, as it is often called; contains up to 6.7 wt.% C. It is a very hard intermetallic metastable compound of iron. When cooled slowly it then produces coarse pearlite which is a lamella of ferrite and carbides. Meanwhile, cementite will slowly decomposes to form α-Fe and C (graphite) between 650 - 700 °C; over many years otherwise it will remain as indefinitely a compound at room temperature.

3.7.2.4. **Bainite**

This is a fine non-lamellar plate-like microstructure that forms between 250 to 550 ^{o}C as a result of the decomposition of austenite (γ) phase to form carbide (Fe_3C) and dislocation rich ferrite (α) phases. Bainite is often classified into upper bainite which appears predominately below pearlite and lower bainite which forms just above martensite transition temperatures with little or no overlap on either side. In terms of hardness value, bainite is between pearlite and martensite.

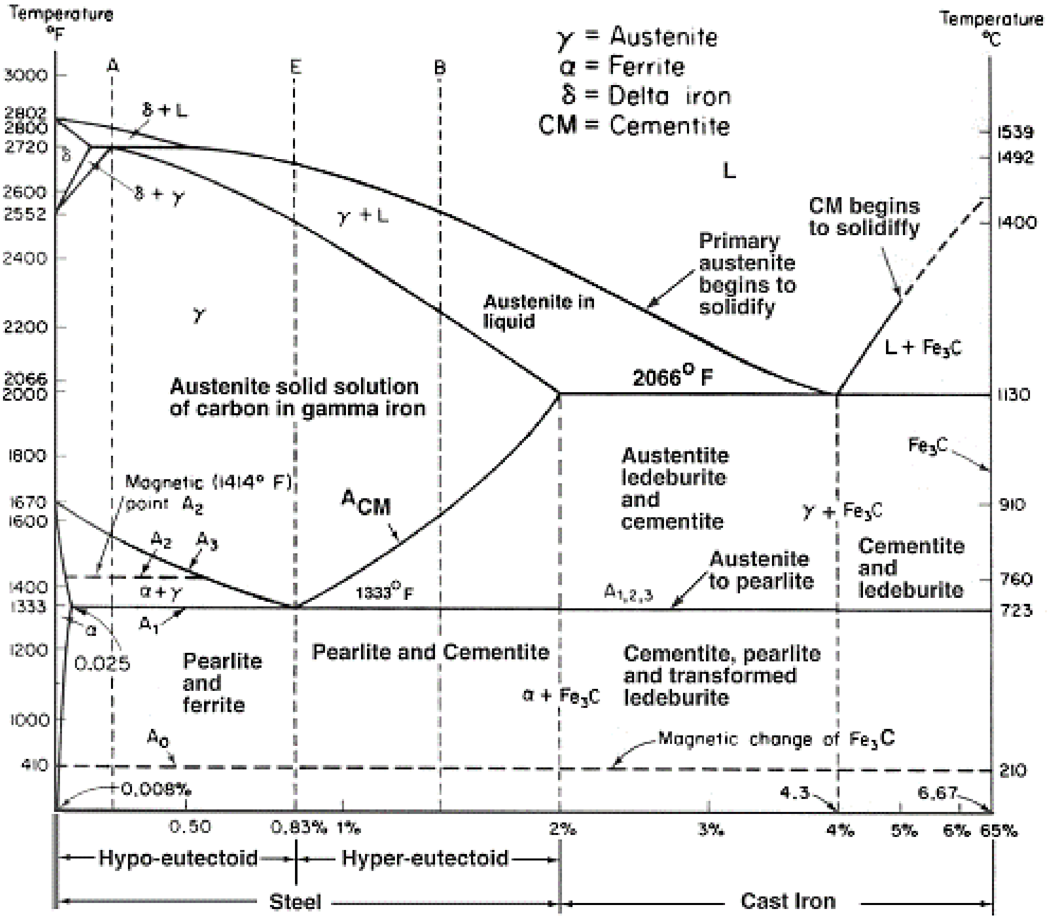

Fig. 3.18 (a): Iron – Carbon and Iron – carbide phase diagram [1].

3.7.2.4. **Pearlite**

This is a two-phased mixture of alternating plate (lamellar) structure composed of ferrite and cementite that occur in some steel and cast iron. The alternating thickness of the lamella formed (88 wt.% α-Fe and 12 wt.% Fe_3C); depends on the cooling rate of the sample which consequently affects the mechanical properties of the sample. For example, faster cooling rate results in finer microstructures and the stronger the Fe-C based alloy. Therefore, a fully pearlitic structure which often occurs at 0.8 wt.% C, has high toughness and machinability.

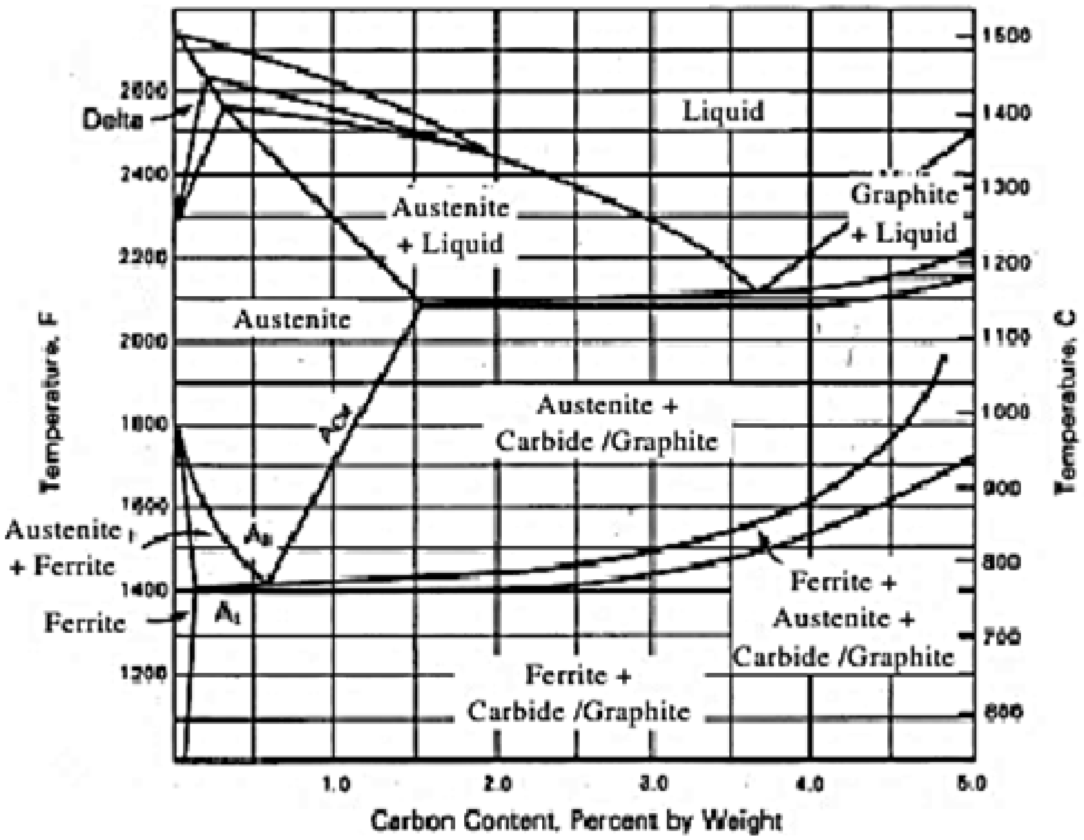

Fig. 3.18 (b): Iron – Carbon – Silicon (2%) ternary phase diagram [104].

3.7.2.5. **Martensite**

Martensite is the metastable end product of rapid quenching of austenite. This diffusionless or athermal transformation, changes the Fe – structure from face-centred cubic (FCC) to body-centred tetragonal (BCT), which occur largely due to insufficient amount of time to enable the formation of pearlite from the carbon-saturated austenite because of the rapid solidification. The overall mechanical properties of martensite such as hardness depend on its carbon content, cooling rate and medium of transition [103]. However, this non-equilibrium metastable phase, martensite can co-exist with other phases, but cannot be represented on the equilibrium Fe–C phase diagram.

3.7.3. Kinetics of phase transformations.

Phase transformation do not occur instantaneously and it involves morphological or structural rearrangement. Many of the significant materials' processes such as solidification or heat treatment involves change of phase or phase transformation without composition alteration. In the previous chapter, brief explanation on the basic background science of heat transfer phenomena and rate of phase transition during solidification has been outlined. In the next major sub-heading (section 3.8), consideration is given to the effect of time and temperature on phase transformation using Fe – C alloy as an example. However, this sub-section explains how phase transformation affects microstructure as a result of kinetic ordering and it can be divided into two categories:

3.7.3.1. **Diffusion-dependent phase transformations.**

This could be either with change or no change in the number of phases or amount of phase compositions. Normally, phase transformation that is diffusion-dependent is usually slow and the evolved microstructure is often depend on the rate of its transition. Typical example of diffusion controlled transformation process with no change in either number of phases or composition include: melting, solidification of pure metal, allotropic transformation, recrystallization and so on. In the case of solidification, it is based on: (1) Nucleation and (2) Growth. Meanwhile, eutectoid transformation is a good example of diffusion-dependent transformation with noticeable change or evidence in phases formed or compositional changes. Such a change is most often notice as evolution of second phase [101].

3.7.3.2. **Diffusionless phase transformations**.

It is simply the kind of phase change that occur without the long-range displacement of atoms but rather by some form of cooperative, homogeneous movement of many atoms that results in crystal morphological change [105]. Such non-equilibrium conditions, due to substantial undercooling and high cooling rate, favour but not necessarily producing supersaturated solid solution, grain refined microstructures, metallic glasses, quasicrystalline alloys and metastable crystalline phases. The most common diffusionless phase transformation of this type is the martensitic transformation. This is actually the most studied non-diffusional transformation. Martensitic transformation is identified by the very unique re-arrangement of Fe-C atoms in the solid solution of γ-Fe (austenite) FCC structure to a body-centered tetragonal (BCT) solid solution (martensite) as mentioned in *3.7.2.5.*

3.8. Transformation Diagrams (CCT & TTT).

There are basically two types of transformation diagrams the TTT (Time Temperature Transformation) and the CCT (Continuous Cooling Transformation) curves. The two plots are diagrams of temperature against the logarithm of time for alloys of definite composition such as Fe–C system. TTT diagram measures rate of transformation at constant temperature; while, CCT diagram gives the extent of transformation as a function of time for a continuously decreasing temperature. For example, these graphs can be used to determine among other things, the transformation rate and time of an isothermal (constant temperature) heat treatment of a previously austenitized alloy to determine a phase transformation starts and when it ends. From the explanation given in the previous section, temperature and cooling rate play very significant role in the eutectoid reaction as illustrated in austenite to pearlite transition [106]. To explain this, we have to consider the temperature – time dependence of system like Fe–Fe_3C eutectoid reaction of austenite to various possible phase products. For instance, transformation of austenite as illustrated in ***fig. 3.19*** and expression by the *reaction in **3-5***.

$$\gamma\ (0.76\ \text{wt.\% C}) \quad \leftrightarrow \quad \alpha\ (0.022\ \text{wt.\% C}) \quad + \quad Fe_3C\ (6.70\ \text{wt.\% C}) \qquad \ldots\ldots.. \ \mathbf{(3\text{-}5)}$$

When cooled, the austenite phase with high solid solubility of carbon concentration will transform to ferrite phase with very little carbon content and cementite which has high carbon concentration. The faster the cooling of the austenite, the quicker the formation of ferrite and the finer the pearlitic phase that may be formed. All these depend on the degree of temperature changes (ΔT) and time which are essential to the mechanism of the emergent pearlite lamella; with bainite forming at higher C content and martensite at much lower C %.

3.8.1. Isothermal/Athermal Transitions: The Evolved microstructures & their properties.

To properly understand evolved microstructures, their morphologies, grains size, phase % and the accompanying mechanical property changes, we need to connect the various factors that leads to the observed changes. For example, in analysing phase boundary crossing on either CCT (Continuous Cooling Transformation) or TTT phase diagram; the resultant equilibrium or non-equilibrium transition will be induced depending on the chosen process and conditions. The change in question could be due to supercooling or superheating and/or wt.% of C as in the case of Fe–C phase diagram. However, metastable states are often enhanced by fast (TTT) change and this strongly affects the evolved microstructure and consequently the properties.

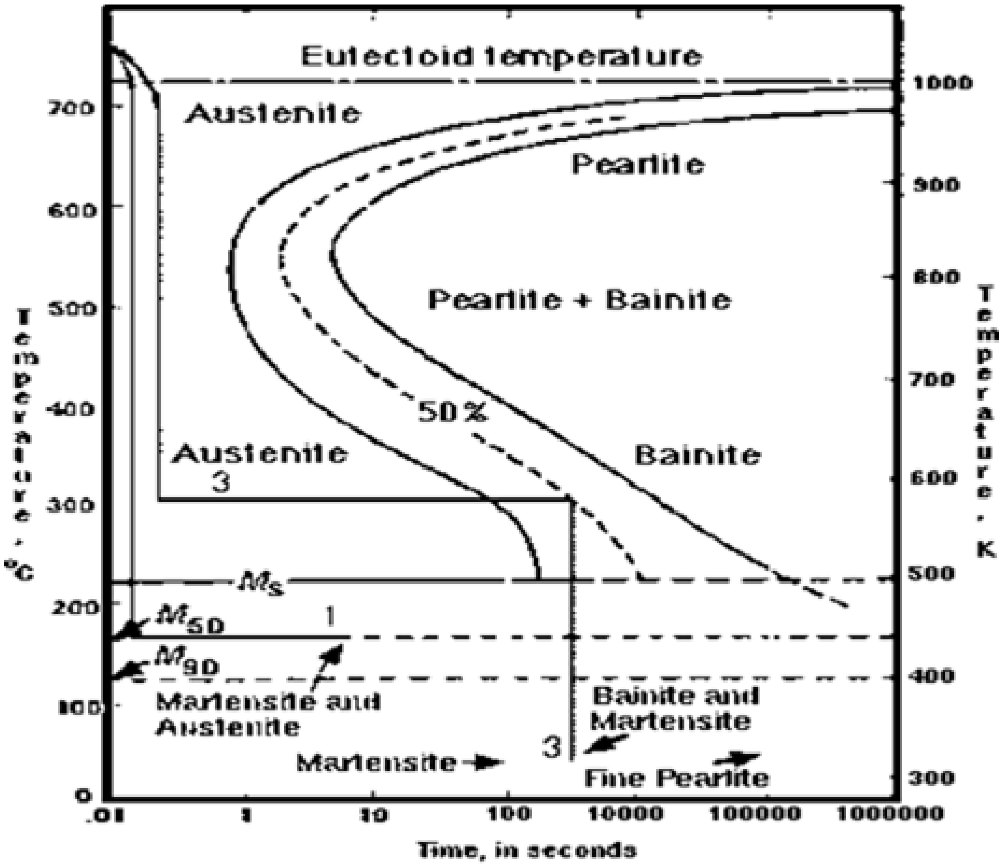

Fig. 3.19: TTT diagram of Fe–C transition showing its various variables, [1].

Considering the TTT diagram, the nose-shaped curves are shifted to shorter times at higher temperature; indicating that transition is dominated by nucleation (which increases with supercooling) and not by diffusion (which occurs faster at higher temperature). Hence, possible microstructure that are obtainable from any of the transformation paths predicted by Fe–C phase diagram or TTT diagram are as described in section 3.7.2. Meanwhile, the martensitic transformation depends only on temperature. Consequently, the inter-relationship between process – structure – properties of a metallic alloy apply not minding the transformation path taken. For example, any process that favour formation of more cementite in Fe–C diagram; will make the material less ductile, since it is harder and relatively more brittle compare to ferrite. Similarly, we can compare the mechanical properties (strength and hardness) of other microstructures (phases) such as bainite, pearlite, spheroidite and again even martensite. In terms of strength and hardness, spheroidite is the most ductile, fine pearlite is harder and stronger than coarse pearlite; bainite is harder and stronger than pearlite while martensite is the hardest, strongest and the most brittle of these phases as indicated in ***fig. 3.20***. Hence, the martensite strength observed is not related to microstructure, but rather to the interstitial arrangement of C atoms within the matrix of the prevailing Fe-rich phase. Meanwhile, it is important to note that there is not a single fixed all TTT or CCT diagram for a particular alloy, but these changes

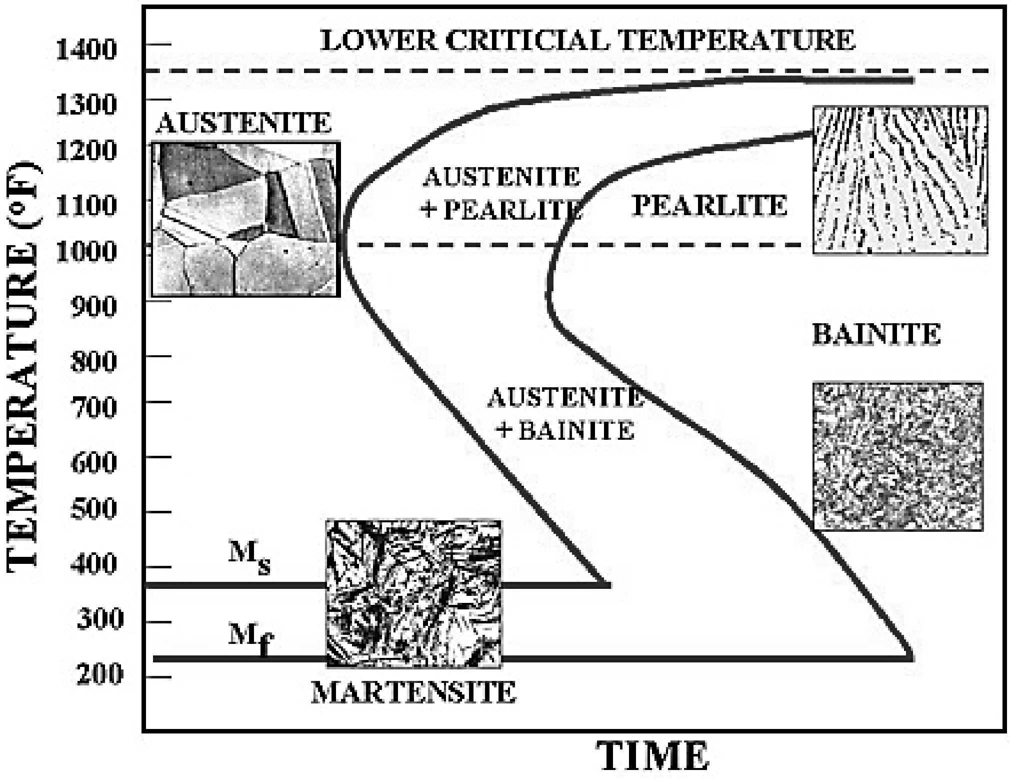

Fig. 3.20: Detailed TTT diagram with microstructures obtained at different transformation in Fe–C alloy system. It shows cooling path (process) in relation to evolved microstructure that determines the properties of emergent phases shown in Figure 3.17 [103].

with composition which affects its structure and influences its properties such as dislocation (resulting in solid solution hardening) and by limiting the number of its existing slip planes.

In conclusion, processing, microstructure and properties inter-relationship of various possible evolved structures as it relate to martensite, it needs process modification.

Meanwhile, for practical application; martensite needs further heat treatment. This can be achieved through a process known as tempering which involves heating it within a temperature range of 250 – 650 ^{o}C to obtain fine or tempered martensite, which is an extremely refined and well dispersed cementite phase in a ferrite matrix. The resultant tempered martensitic phase is therefore, less brittle with enhanced ductility as compared to regular martensite microstructure [103].

3.9. Previous progresses on rapid solidification of cast iron.

The understanding and knowledge of cast iron as an engineering material in the earlier years of its discovery was very limited for quite a long time as a result of its crude processing methods and resultant properties. However, attempts has since been made to reveal its different microstructures and accompanying properties under various possible processing paths. The first recorded publication on cast iron was in 1896 in the old Journal of American Foundry-men's Association [2]. The inability of early blacksmiths to understand cast iron properties in terms of shrinkage, brittleness, strength and hardness drove the people like Andreas, Daniel and Wazzan [91] to research the discovery of softer (ductile) iron through local heat treatment which made it less brittle and more machinable. However, in the 1970s, more investigation led into the discovery and recognition of compacted graphite (CG) iron. This singular art of science brought graphite (grey) cast iron into limelight of research for better improvement on its properties, application and performance.

One early source that propelled cast iron discovery was proposed by Piwowarsky's famous monograph that shown segregation that can be altered, and that was published in 1942 [107]. Subsequent to this, in 1892, Ledebur and his fellow workers recognised silicon's role in the solidification structure of ferrous cast alloys; thereby they proposed carbon equivalent (CE) correlation [96]. By late 1924, Maner designed a famous structural diagram that shows relationship between cast iron carbon content and microstructure. In furtherance of this, D. M. Stefanescu [108], presented critical discoveries in understanding the solidification of cast iron; in which he revealed that cast iron solidification has advanced to the point that few areas are actually in needs of investigation these include metastable phase retainment during undercooling. In the same vein, Kiani-Rashid [109] presented strongly the assessment of thermal analysis of grey cast iron under different cooling rate to establish the effect of undercooling on varied elemental compositions. These researchers, among others did not provide sufficient correlation between the recorded undercooling in relation to the resultant microstructures of grey cast iron. While considering the characterisation of cast iron using x-ray diffraction, Roviglione et al. [110], emphasised the eutectic transition of flake graphite to compacted graphite as an evidence of radical transformation due to rapid solidification of the cast iron. This was considered too general, hence, very little on microstructural evolution of especially rapidly solidified grey cast iron has been done so far.

However, considering an earlier study by Yang et al. [111], on the high pressure gas atomization of grey cast iron powder; their XRD analysis shows that with increasing cooling rate (particle size reduction) the amount of retained γ-Fe and cementite increased relative to decreasing α-Fe phase; even as the random flake morphology changed to oriented with no other phase detected. To explain the thermodynamic properties of the phases formed during the rapid cooling, [104] gave significant insight assessments on the Fe-Si (binary) and Fe-Si-C (ternary) system to establish the difference in the evolved stable and metastable phases with emphasis on Si role to supress the eutectic temperature during rapid solidification processing of these or similar systems. Therefore, they estimated that during rapid cooling the addition of about 2.83 wt.% in any of these Fe-C or Fe-Si-C systems will significantly lower the eutectic temperature of these binary or ternary system. Hence, for an alloy composition as we have in BS1452 Grade 250; Cao et al., [23] explained in their recent study that the combined effect of melt undercooling and high cooling rate on the various sample droplets as a result of melt sub-division especially on the smaller droplets. They established that at high undercooling, the γ-Fe primary dendrites formed will increase relative to the $\gamma + Fe_3C$ eutectic.

Relating the mechanical properties of possible evolved phases during rapid solidification of any Fe-C based alloy system, Yi et al. [112] using laser fusion welding technology based on rapid cooling repair processing, discovered that the entire crack toughness around a sample’s laser repaired zone can definitely be improved. In line with this, Ebrahimnia et al. [113] stated in their study on the effect of cooling rate on the soundness of heat affected zone (HAZ) that crack initiation can be stopped in especially ductile cast iron powder by controlled welding. They established that cracking in HAZ can be prevented based on the compatibility between the thermal coefficient of expansion of the welded metals. Wei et al [114]; further confirmed that cast iron weldability can be generally improved using laser cladding whereby graphite precipitation will be inhibited between mean metal and the weld zone thereby stopping its propagation.

However, many more attempt have been made on the study of the effect of rapid solidification on cast iron in the laboratory and industries, but one thing stands out, a comprehensive investigation on the effect of rapid cooling on commercial grey cast iron using drop-tube in an inert environment have not been specifically treated. Even though solidification of grey cast iron was thoroughly investigated by G. L. Rivera et.al [96], the actual microstructural changes that occur as a result of large undercooling which is the focus of this research work was scarcely touched. Close in thought to this work is an outstanding investigation by Eiselstein et. al. [93], which was based on structural characterization of rapidly solidified white cast iron powders by gas atomization technique; in which emphasised was placed on white cast iron and not grey cast iron as it is in this case. Also the two processes have different particle size distribution.

3.10. Aim and objectives of this research.

The primary aim of this research study is to show how processing (rapid solidification) at constant composition (hypoeutectic) affects microstructure which in turns determines mechanical property (microhardness) due to morphological and phase transformation. The target is to produce rapidly solidified droplets of commercial grey cast iron BS1452 GRADE 250 using the drop-tube technique in two separate cooling medium of nitrogen and helium; and to characterize, analysis and understand the phase formations, microstructure evolutions and the microhardness values (at high cooling rates) in comparison to its conventionally cooled as-cast or bulk sample obtained from the industry in accordance with predicted structures by the phase and TTT diagrams. Hence, the target is to classify these evolved droplets microstructures as a factor of their cooling rate in relation to their decreasing particle sizes and to explain their thermal behaviour and its effects consequent to different phase transformation observed. Finally, all these put together will help in the understanding of effect of containerless rapid solidification processing on microstructure and mechanical property of this very important engineering material.

CHAPTER FOUR

MATERIALS AND METHODS

4.0: Introduction to Experimental Methods

In line with the objective of this study, this chapter is dedicated to the description of materials, the various methods and techniques used to carry out this research. The control sample (as-received) was supplied by West Yorkshire Steel Company Limited, Wetherby, Leeds UK; while the rapidly solidified powder particles were produced using drop tube apparatus in the University of Leeds. Hence, this section explain the choice of sample cut-out from the conventionally cooled as-received (25mm x 300mm) rod and the non-equilibrium conditions required to obtain high undercooling during the rapid solidification process which invariably leads to various droplet sizes that determine their cooling rate. It also gives details on droplet separation by sieving followed by thorough metallographic sample preparation (i.e. mounting, grinding, polishing, etching) and characterization of the various size particles using Optical Microscopy (OM), Scanning Electron Microscopy (SEM), Energy Dispersive Spectrometry (EDX), X-ray diffractometry (XRD) and Differential Thermal Analysis (DTA).

4.1: Sample "as-received" and Description

The supplied bulk as-received sample is simply a round bar of 0.25 m diameter which needed to be cleanse to removed scales and grease. The needed pieces for the droplets production were cut-out from this rod near surface (to avoid scales or oxide inclusion) to the inner core (centre point) of the conventionally cooled bar specification as shown in ***fig. 4.1 (a-c)***. As a continuous slowly cooled cast iron bar, this bulk sample has fine graphite flakes and dense homogeneous microstructure at a relatively low magnification. It has a nominal tensile strength and hardness values of 250 MN/m^2 and 145-240 HB respectively as specified by the supplier (West Yorkshire Steel Co. Ltd.). These nominal values for this sample grade are suitable for application where good wearing characteristics and strength are required. It is widely used in the making of plastic and glass industrial equipment. It also has established applications for but not limited to the production of piston-heads, metallic moulds, bearings, bushes, connecting rods, brake callipers, brake pads, rotors, gear box and engine block etc.

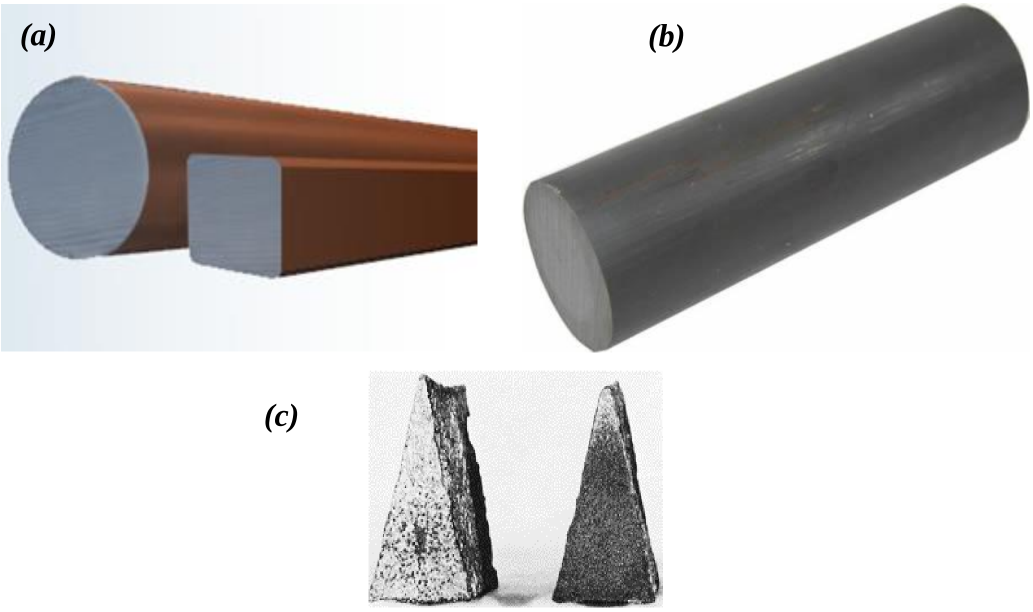

Fig. 4.1: Bars of as-cast commercial BS1452 Grade 250 grey cast iron (Yorkshire Steel)

4.2: Specimen Selection for droplets production

The as-received sample bar (3m long in supply form) has its outer layer covered with oxide scale as shown in ***fig. 4.1(a)***; which was completely removed by gentle grinding and wire brushing to expose the very fresh layer of the sample as shown in ***fig. 4.1(b)***. Thereafter, small pieces of triangular prism of roughly 1-2 cm^3 sections were cut out of the properly cleaned rod using hacksaw which resulted in yet smaller pieces as shown in ***fig. 4.1(c)***. These cleansed pieces are obviously free from scale, grease (having been rinsed with methanol) and then weighed; ready for loading into drop-tube RF furnace using special graphite crucible which 1-3 holes drilled into the base.

4.3: Droplets production procedure

Rapid solidification via drop tube technique in two different protective inert gases (Nitrogen and Helium) were used in this study as described in Sections 3.3.2. Hence, to obtain the droplets in N_2 and He cooled environment, the as-received cut-out pieces weighing approximately 17.6511 g, 16.2686 g, 18.7603 g and 16.4724 g were respectively loaded inside a small cylindrical graphite crucible that has three laser drilled (300 µm) holes at its base. The crucible was enclosed in graphite susceptor with an open ends outer alumina shield. The alumina shell acts as a radiation shield to reduce heat loss from the susceptor and to separate it from the heating copper coil, made from 5 mm diameter copper tube, which is then connected directly to the RF-generator. Pressure tight clamp was then used to fix the whole of the furnace assembly securely to the top of the drop-tube so that the crucible could be pressurised to eject the melt down-wards using nitrogen or helium at desire ejection pressure which in this case is 3 bars. ***Fig. 4.2*** shows an enlarged schematic description of the drop-tube furnace top section, the full diagrammatic illustration of the drop-tube apparatus is as shown in ***fig. 3.13***. The graphite susceptor is actually fixed under the air-tight steel lid by clamping both end ports of the lid and the susceptor together to avoid leakage. There is also a 10 mm hole in the base of the susceptor, targeted at providing a path for spraying melt spot as it proceed downward in the drop-tube shaft with edge to hold the crucible. The furnace temperature was monitored using an R-type thermocouple and the targeted ejection temperature was 1450 ^{o}C to ensure that the entire sample inside the crucible melted before pressure ejection. This R-type thermocouple was fixed to the top of the drop-tube steel lid and it extends into the crucible, which hung up just above the melted sample inside the crucible without touching the molten alloy; while the other end of the thermocouple was connected to the digital screen monitor to provide temperature output. The RF melting unit is

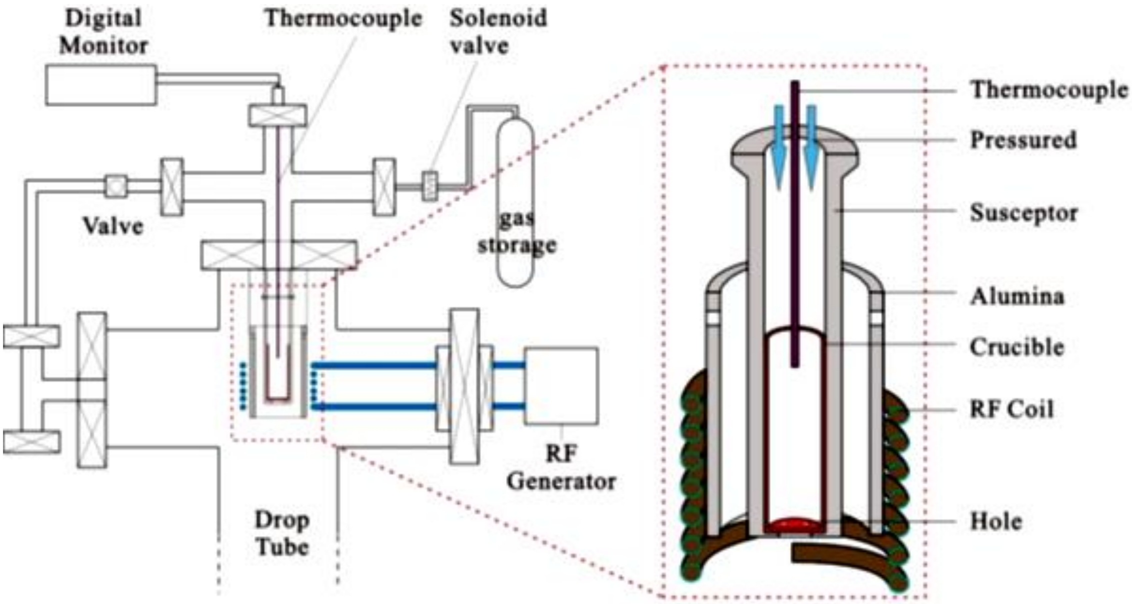

Figure 4.2: Schematic description of drop-tube furnace top section with ejection details [115].

located at the top-most part of this apparatus and after loading the sample, this section was tightly sealed and the entire equipment was then purged 3 times consecutively using rough pump until a pressure of 0.02 mbar was achieved inside the tube. Firstly, the oil-sealed rotary-vane pump was used to reduce the tube pressure inside to low vacuum level of (~10^{-4} Pa); beyond which the pump strength is redundant, hence turbo-molecular pump was then used to keep the pressure down to (~10^{-7} Pa). The entire tube was then immediately backfilled to 3 x 10^{-5} mbar using Nitrogen/Helium (as the cooling medium). After a period of systematic heat up monitored by the R-type thermocouple and the targeted ejection temperature achieved; the molten metal in the crucible was then pressure ejected via a solenoid valve connected to the crucible from a reservoir which was pre-pressurised (with either Nitrogen or Helium) to the desired ejection pressure (in this case 3 bar). As the melted sample flows down inside the drop-tube shaft; it solidifies with the smaller droplets cooling faster. Once the ejection is completed, the solenoid valve is immediately switched off. With the ejection pressure applied from the tube top, the sprayed melt fall downward through the tube column to the collection pot in the lower part of the tube. After gradual and proper monitored controlled cooling of the entire equipment and when the whole system has cooled to room temperature and the tube pressure has normalised with that of the surrounding atmosphere, the collection pot at the bottom of the tube was then opened and the near spherical sample droplets and needles of the sprayed grey cast iron was collected for sieving, storage, identification and analysis. Consequently, the cooling rate can be expressed as shown in **equation 4-1**.

$$\frac{dT}{dt} = -\frac{6}{\rho C_p^1 d}\left[h(T - T_0) + \sigma_{SB}\,\varepsilon(T^4 - T_0^4)\right]$$ **....…………….(4-1)**

where h (as given in **equation 4.2**) is an empirically determined heat transfer coeffient given for $Re < 10^5$ by

$$h = \frac{K_g}{d}(2.0 + 0.3Pr^{0.33}Re^{0.6})$$ **…..…..……….(4-2)**

where K_g is the thermal conductivity of the gas and Pr and Re are the Prandtl and Reynolds numbers for the falling droplet. Then the equation of motion for the droplet can be expressed as shown in **equation 4-3**.

$$\frac{dV}{dt} = g\frac{\Delta\rho}{\rho_g} - \frac{3}{4}D_r\rho\left(\frac{V^2}{\rho d}\right) \qquad \text{……….………..(4-3)}$$

where g is the gravitational acceleration, ρ_g the gas density, $\Delta\rho = \rho - \rho_g$, V the relative velocity between the droplet and the gas, and D_r the drag coefficient (a function of Re) usually taken as the empirically determined value for a hard sphere.Nine different sample sizes ranges i.e. ≥ 850 µm; 850-500 µm; 500-300 µm; 300-212 µm; 212-150 µm; 150-106 µm; 106-75 µm; 75-53 µm; 53-38 µm and ≤ 38 µm were obtained based on the set of sieves used. These were then prepared for microscopy examination and other characterizations techniques.

4.4: Metallography:- Specimen Preparation and Etching

The as-received and drop-tube samples were hot mounted in Buehler phenolic resin using 30 mm diameter automatic mounting press. This provided good handling for the next stage which was wet grinding. Coarse and fine grinding of the samples were done in sequence using series of silicon carbide grinding papers ranging from 240, 400, 600, 800 and 1200 grit. During this process, some of the SiC grinding papers were not needed especially for the smaller droplets. For example, for the particle of diameter ≤106 µm, 1200 grit SiC paper was enough to avoid losing the sample. Throughout the preparation, samples were constantly washed with diluted detergent in running water, cleansed in ethanol, dried in hot blowing air and then examined using optical microscope to ensure progressive clean and smooth surface before proceeding to the next stage. After noticeable satisfaction and confirmation on the fine grinding status of the samples surfaces using optical microscope for each stage, the samples were finally washed in running water, cleansed in ethanol, dried and polished to mirror-like surface using 6µm, 3µm, 1µm and 0.25µm diamond polishing paste respectively on polishing cloths on a rotating wheel. Like grinding, good polishing was carried out in sequence from higher microns size to the finest microns size. These ground and polished samples were then ready for etching. To etch the samples, cast iron ASM standard (PN-61/H-503) recommends three etchants. They are namely: Nital solution (2% nitric acid in 98% ethanol), Picral solution (4% sodium picrate in deionized water) and Murakami reagent. These etchants were selected for use to observe their effect on the samples by immersion. **Table 4.1;** shows the composition and effect of these etchants on cast iron generally. Each etching section was followed by thorough washing in running tap water, then cleansed with ethanol and dried in a stream of dry blowing air before optical and scanning electron microscope examination.

Table 4.1: Some etchants for cast iron samples as specified by PN-61/H-503.

Etchant name	***Composition***	***Comments***
Nital	96 – 98 mL ethanol 2 – 4 mL nitric acid	Common etchant for ferrous alloys including steels and cast irons. It reveals alpha grain boundaries and constituents. Duration up to 60s
Picral	4g picric acid in $\{(NO_2)_3C_6H_2OH\}$	Commonly used for structures consisting of 100 mL ethanol ferrite and carbides. Does not reveal ferrite grain boundrries and Martensite as quenched.
Murakami reagent	10g $\{K_3Fe(CN)_6\}$ 10g KOH or NaOH in 100 mL distilled H_2O	Reveals chromium carbide by tinting it brown but leaves Fe_3C un-attacked or barely attacked. Immersion can take up to 3mins.

4.5: Characterization techniques employed

The following techniques were employed for microstructural characterisation of the samples. These include: Optical Microscopes (OM), Scanning Electron Microscopes (SEM), Energy Dispersive x-ray Spectrometry (EDX), X-ray Diffraction (XRD), Differential Thermal Analysis (DTA), Focused Ion Beam (FIB) and Transmission Electron Microscopy (TEM).

4.5.1: Light Optical Microscope (OM)

The Olympus BX 51 light microscope used for this study has a range of objectives lenses (5, 10, 20, 50 and 100 times) to magnify objects and an inbuilt Carl Zeiss Axiocam MRc5 Zeiss digital camera to take images. This unit is attached to a computer system for micrograph display, adjustment and storage. The samples were handy enough to go under the microscope for examination and the surfaces were kept flat and free of scratches; while plasticene was used to hold the samples on glass-slide by means of levelling press.

4.5.2: Scanning Electron Microscopes with EDX

Characterization of the samples involves high resolution microstructural examination and elemental analysis using Scanning Electron Microscopy (SEM) with Energy Dispersive Spectroscopy (EDX). This is an important tool for microstructural evaluation at very high magnifications operating at 10 – 20 kV. The two principal modes: Secondary Electrons (SE) and Back-Scattered imaging (BS) were used in the cause of this project. These two imaging modes have distinctive features in term of electron – material interaction volume and the consequent effect on the micrographs resolution. There are two main factors that affect their resolution; these are: (1) the electron beam spot size and (2) the current in the electron beam. While the SE gives information on the topographical nature of the sample, the BS images reveals the atomic contrast as a result deeper interaction volume by the back scatter electrons. To obtain a clear measurable signal for three-dimensional appearance of the sample image there are principal parameters (along with other in-built features) that must be well set or adjusted. These include the probe diameter or spot size (d_p), (it is the final beam size at the surface of the specimen); probe current (i_p), (which is the current that impinges upon the specimen and generates the various imaging signals) and the beam accelerating voltage (kV), (which is the voltage with which the electrons are accelerated down the column). Proper adjustment of these parameters are essential for good imaging. The detailed features and operating principle of Evo-SEM used for this study is as outlined in Section 4.5.2.1.

4.5.2.1: ***EVO Scanning Electron Microscopy***

A Carl Zeiss Evo® MA 15 SEM, capable of imaging at magnification as high as 1, 000 000 was used for this study. The source of electron for this instrument is normally a tungsten (W) filament known as lanthanum hexaboride (LaB6) or commonly called Schottky emitter. The emitted electrons are focused using electron lenses to a beam with diameters ranging from 1-1000 nm which has effect on the sample by the resolution, and then the focused electrons scanned across the sample surface by the deflecting or scanning coils as shown in ***fig. 4.3 (a-c).*** The electrons paths are usually under vacuum because electrons are absorbed in air. Unlike optical microscopy, it has higher resolution which can be explained by the Rayleigh criterion, as shown in **Equation (4-4)** [116].

$$r_1 = \frac{d_1}{2} = \frac{0.61\lambda_w}{\mu sin\alpha} \qquad \textbf{................(4-4)}$$

where d_1 is the limit distance travelled by the emitted electron, λ_w is the wavelength of the electron beam, μ is the refractive index of the medium between the object and the objective lens. Meanwhile, the product, μsinα is normally refers to as the numerical aperture. Hence, the limit of resolution or the smallest distance between two separate positions (i.e. the smallest r_1) is directly related to the incident wavelength. It should be noted that both wave and particle properties can be applied to light and electrons having wavelength of 400-700 nm and 0.001-0.01 nm respectively. The general resolution limit of light optical microscopy is about 150 nm (0.15 μm) using green light (λ_w = 400 nm for example), whereas that of electron is approximately 20 nm using reasonable values of λ_w = 0.0037 nm (the wavelength of 100 kV electrons) and α = 0.1 radians [115].

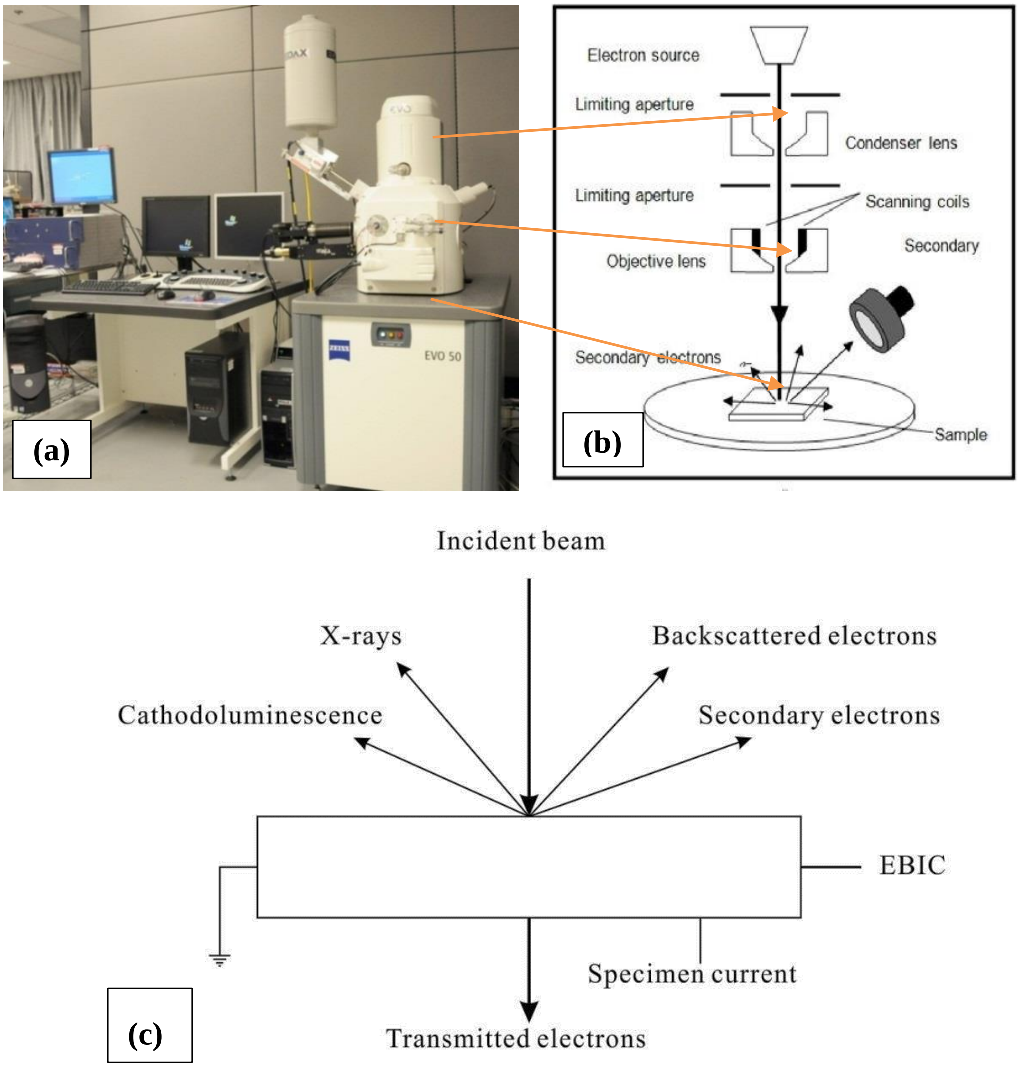

Fig. 4.3: (a) Picture, (b) Schematic and (c) Operation principle of Evo-SEM

However, because they are more strongly scattered by gases than ordinary light, complete evacuation is required in using scanning electron microscopy such as the Evo used for this study. Normally, all scanning electron microscopes have facilities for detecting secondary and backscattered electrons. The former are emitted by atoms excited by the incident electron beam with low energies (< 50 eV), and they are from short distance just below the specimen surface. Hence, secondary electrons (SE) are most widely used in SEM for studying surface features. However, the later, back scatter electrons (BSE) are reflected electrons from sample obtained by elastic scattering. Therefore, BSE micrographs provide information about the distribution of different phases using different average atomic numbers in the sample. Using this instrument, there is no problem obtaining good micrographs for any samples, provided such is clean and conductive. However, if the sample or the resin used is not conductive enough, there will be charging due to electron aggregation and coating but with a thin conducting coating layer (like gold, platinum or carbon) the charging effect of the electrons can be resolved. This same instrument was used to confirm the chemical composition of the control sample using the inbuilt characteristic X-ray emitted as electrons interacts with the sample. For example, if one electron of inner energy state has been displaced from an atom shell and then a single outer electron jumps into this inner shell vacancy, a characteristic X-ray is emitted. The energy of the emitted X-ray is the difference of the energies between the two excited electron states. Since, the energies and wavelengths are different for individual atomic species; this information is used by the SEM-EDX inbuilt programme to determine the different elements in the specimen. This eventually translates to chemical analysis by SEM.

4.5.3: Phase Identification by XRD.

The technique used here is X-ray diffraction (XRD). It is a well-known atomic scale non-destructive characterization technique used for qualitative and quantitative analysis of crystalline materials. It provides information that cannot be easily obtained through microscopic observation. The result obtained includes; phase identification, quantification and composition analysis via determination of the lattice parameters.

4.5.3.1: ***XRD working principle***

X-rays are high-energy electromagnetic radiation and the wavelength used in diffraction is approximately in the range of 0.05-0.25 nm. They have energies ranging from about 200eV to 1 MeV, which puts them between ɣ-rays and ultraviolet (UV) radiation in the electromagnetic spectrum. It is important to know that there are no sharp boundaries between different regions of the electromagnetic spectrum and that the assigned boundaries between regions are arbitrary. X-ray and gamma rays are essentially identical, ɣ-ray being somewhat more energetic and shorter in wavelength than x-rays. They differ mainly in how they are produced in the atom. X-rays are produced by interaction between an external beam of electrons and the electrons in the shell of an atom. Meanwhile, ɣ-rays are produced by charges within the nucleus of the atom; it has better penetrative signal [110]. X-rays are produced in an x-ray tube consisting of two metals electrodes enclosed in a vacuum chamber as shown in ***fig. 4.4*** below. Electrons are produced by heating the tungsten filament i.e. the cathode, which is at high negative potential and the electron are accelerated toward the anode, which have a very high velocity, collide with the water-cooled anode. The loss of energy of the electron due to the impact with the metal anode is manifested as x-rays. Actually, only a small percentage (less than 1%) of the electron beam is converted to x-rays; the majority is dissipated as heat in the water-cooled metal anode. It is this continuous spectrum produced due to electrons losing their energy in a series of collision with the atoms that make up the target peaks which are called characteristic lines. These peaks are most useful in x-ray diffraction work. Hence, the energy of the x-ray photon is characteristics of the target metal.

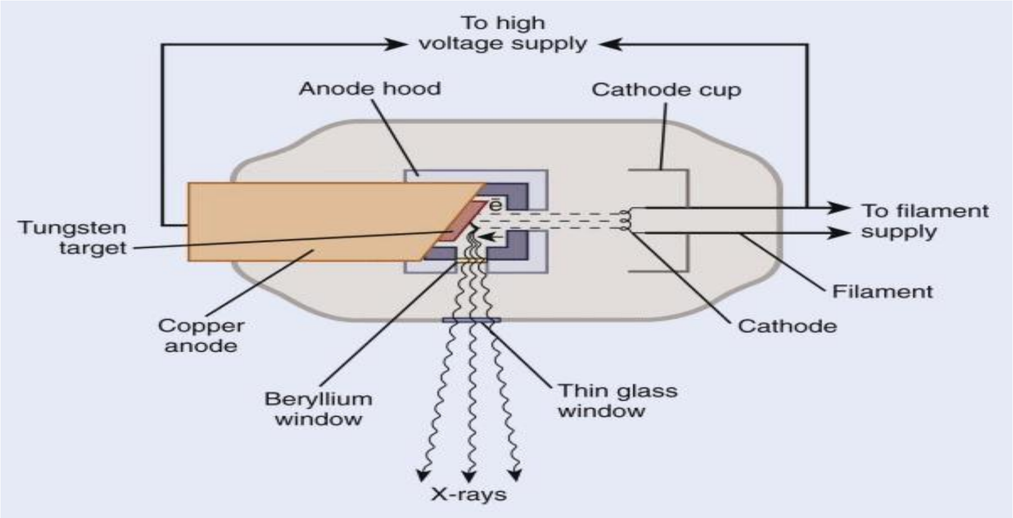

Fig. 4.4: Schematic showing the essenatial components of a modern x-ray tube [117]

4.5.3.2: ***Identified Phases analysis***.

In this study, phase analysis was carried out using the software X’Pert HighScore Plus (PANalytical B.V., Almelo, The Netherlands), which is packaged as part of the X’Pert MPD X-ray diffractometer used in Institute For Materials Research, University of Leeds. For this experiment, the quantities of particles for each size group are limited, hence the samples were first mounted in transoptic resin and then prepared as described in Section 4.4. Then the polished samples were fixed on the bracket which was thereafter fixed on the XRD machine for scanning as shown in ***fig. 4.5.*** Meanwhile due to characteristic iron florescence in the Cu K-alpha x-ray beam and in order to drastically reduce the scanning noise level, the scanning rate was programmed for a duration of 16 hours, for better distinctive peak profile results especially for smaller droplets. Beside phase identification based on crystal structure, x-ray diffractometry also reveals the crystallographic parameters, structure and peak position of the various identified phases. ***Fig. 4.5*** gives an illustration of the XRD application as used in this study. When X-ray beam with wave length, λ is incident on a crystalline material at angle θ, the constructive interference (diffraction) occurs only when the distance travelled by X-ray beam reflected from adjacent atomic planes in the material differ by an integer number n of the wavelengths ($n\lambda$) as illustrated in ***fig. 4.6***. The relationship between these terms known as Bragg’s [law $n\lambda = 2d \sin(\theta)$]; was discovered by W. H. Bragg and his son, W. L. Bragg where λ is the wavelength of the ray; θ is the angular position of a certain reflection; d is the spacing between layers of atoms and constructive interference occurs when n is an integer.

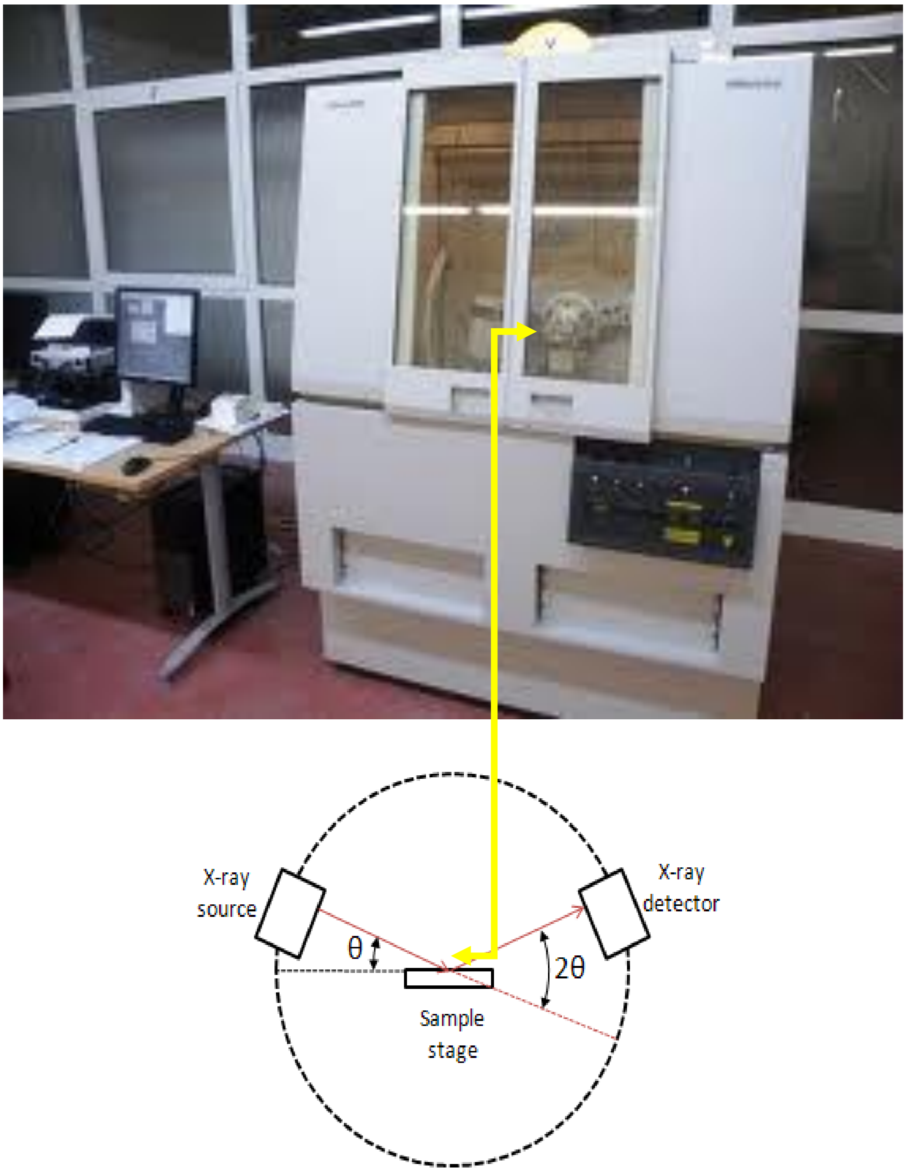

Fig. 4.5: PAnalytical X’pert Diffractometer and typical x-ray beam reflection.

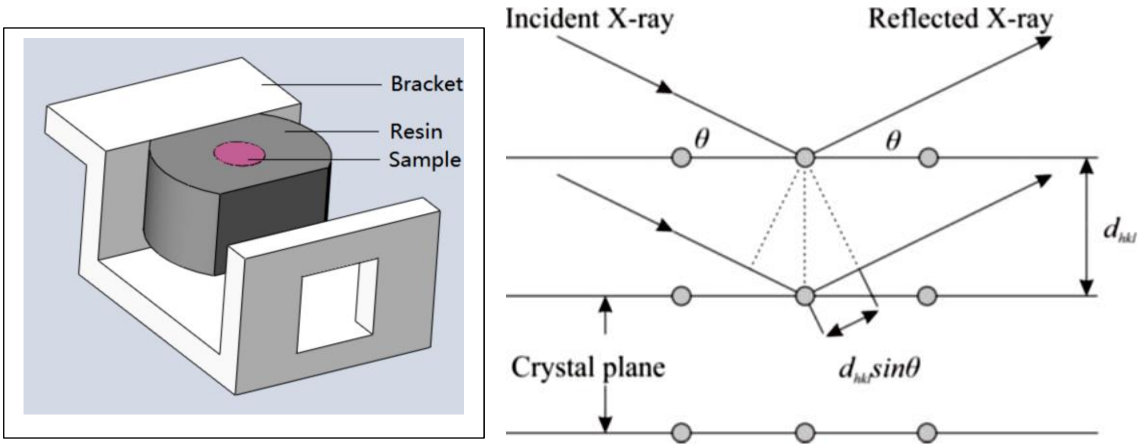

Fig. 4.6: Schematic of X-ray bracket sample holder and X-ray diffraction by a crystal [118].

4.5.4: Transmission Electron Microscopy (TEM)

The transmission electron microscope has much higher magnification than SEM and is more advantageous being capable of providing both image and diffraction information from a single sample. It works with the principle of electron diffraction/scattering like the scanning electron microscope, but in its case; images are obtained via transmitted electrons (TE) as opposed to secondary and backscattered electrons used by scanning electron microscopes.

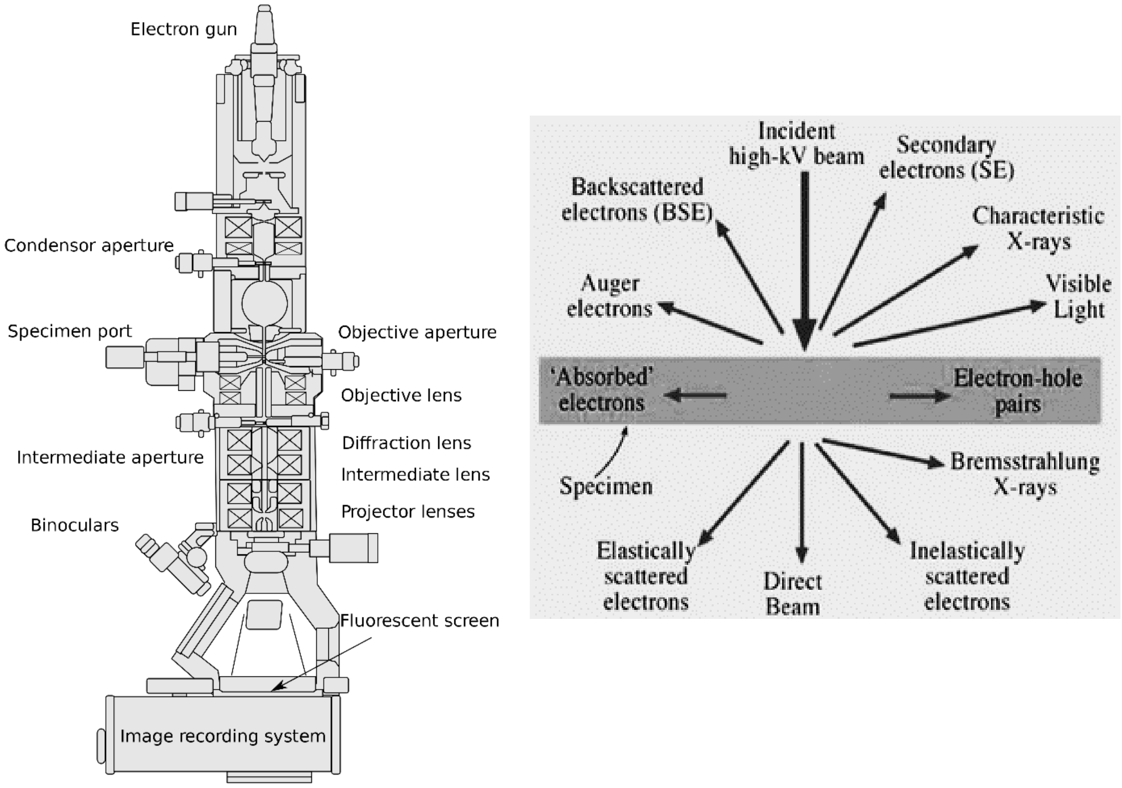

Fig. 4.7: Schematic of a typical TEM and possible emitted electrons for interaction [119].

As a result, the sample needs to be electron transparent, i.e very thin. Details of specimens preparation using the precise Focus Ion Beam (FIB) linked to the FEI Nova 200 NanoLab FEGSEM is as outlined in section 4.5.4.1. The final dimension of each specimen used as stated is 15 µm in length and 8 µm width with the thickness of about 100 nm. ***Fig. 4.7*** shows a schematic diagram of the TEM equipment along with different possible electron interaction/scattering mode from its incident beam. These accelerated electrons passes through the thin specimen by means of condenser lens systems and are either deflected or undeflected [120] to form dot patterns otherwise called selected area diffraction pattern (SAD). The various signals produced from the interaction of these accelerated electrons with the sample are used to obtain some useful information from the internal structure of the sample such as atomic arrangement, phase composition, crystal structure and defects. An advanced TEM system (Philips CM200 FEGTEM) picture, shown in ***fig. 4.8*** operated at 200kV fitted with an ISIS EDX system was used for this research to take samples' bright-field images and to obtain selected area electron diffraction (SAED) patterns for further analysis to determine the different crystallographic phases present in each sample examined. However, one major limitation of transmission electron microscopy is the fact that only a small identified sample representative area of interest can be analyzed at a time. Also samples must be very thin and electron transparent and this involves special procedures such as high precision milling (using Focused Ion beam, FIB) technique. Specimen preparation is as described in section 4.5.4.1.

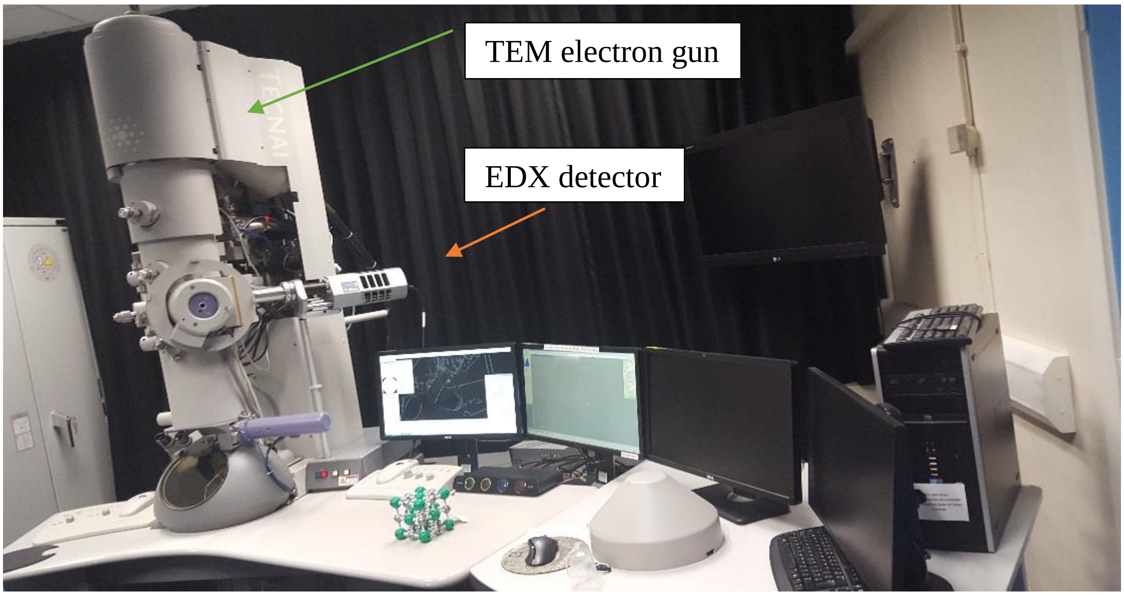

Fig. 4.8: Philips CM200 FEG-TEM with Oxford control instruments; LEMAS, Leeds

4.5.4.1: ***TEM sample preparation and preservation***.

The samples are droplets with diameters in the range of ≥ 53 to ≤ 850 µm and these were mounted and prepared as for SEM to reveal their microstructures. However, in order to make the TEM specimen from the interest area accurately, highly Focused Ion Beam (FIB) connected to the FEI Nova 200 NanoLab FEGSEM operated at 30 kV with different beam currents (2 nA for bulk removal and 50 pA for polishing) used. The final dimension of the TEM specimen is roughly 15 µm x 8 µm in size with a thickness smaller than 100 nm. ***Fig. 4.9*** shows a brief sequence of FIB sample preparation technique on a selected droplet. The first step in the process illustrated in

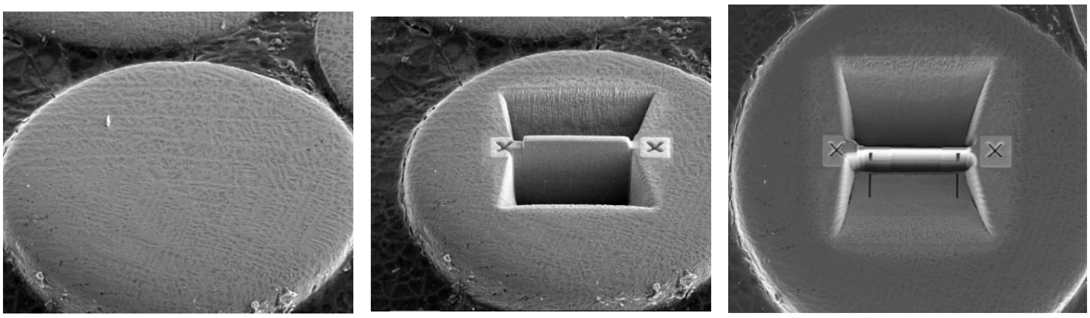

[1]. Selected target area. [2]. Sectioned lamella portion. [3]. Milled portion cut-out.

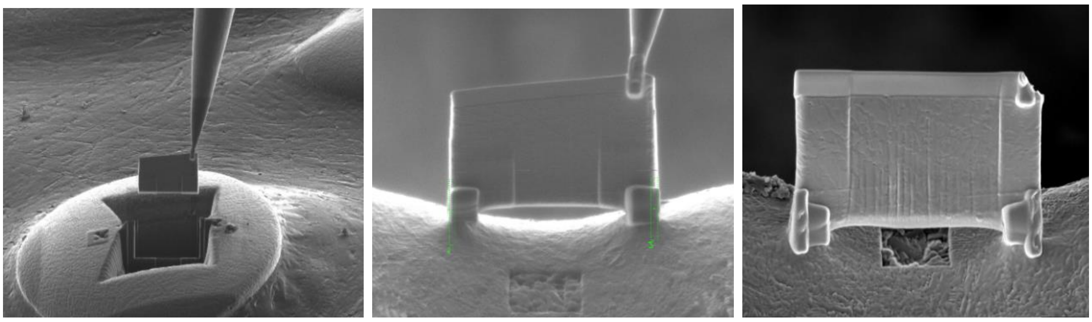

[4]. Thin lamella picked by needle. [5]. Specimen welded on TEM grid. [6]. Further slicing of specimen using Ga ion beam

Fig. 4.9: Sequence of TEM sample preparation by SEM-FIB operation technique.

the figure is the selection of area of investigation. The whole portion was then coated with Pt to protect the surface during the cutting operation. Then marking, miling and cutting out of the selected area of interest was done on both sides to allow easy removal of this very thin rectangular specimen using tungsten micro-manipulator welded to it to lift it out carefully and fix it on the TEM grid (Cu). At this point, specimen slicing continues using the parameter stated earlier until the thickness was ensured to be less than 100 nm. The well prepared specimens were then stored in vacuum vessel before the TEM analysis.

4.5.5: Differential Thermal Analysis

Differential Thermal Analysis (DTA) is a widely used standard thermal analysis technique for characterizing materials to determine their tranformation temperature using comparative calibration with a standard inert reference under the same thermal conditions or programme. This technique is used to detect the release or absorption of heat, which is associated with chemical and physical changes in materials as they are heated or cooled. Using Perkin-Elmer STA-8000 simultaneous thermal analyzer, the primary aim is to determine the presence of metastable phases and the actual melting point of the sample at a steady heating and cooling in each pan to prevent potential contamination during the heating and cooling pre-set thermal double cycle runs from initially 50^{o} C to 1450^{o} C and reverse; which resulted in loss

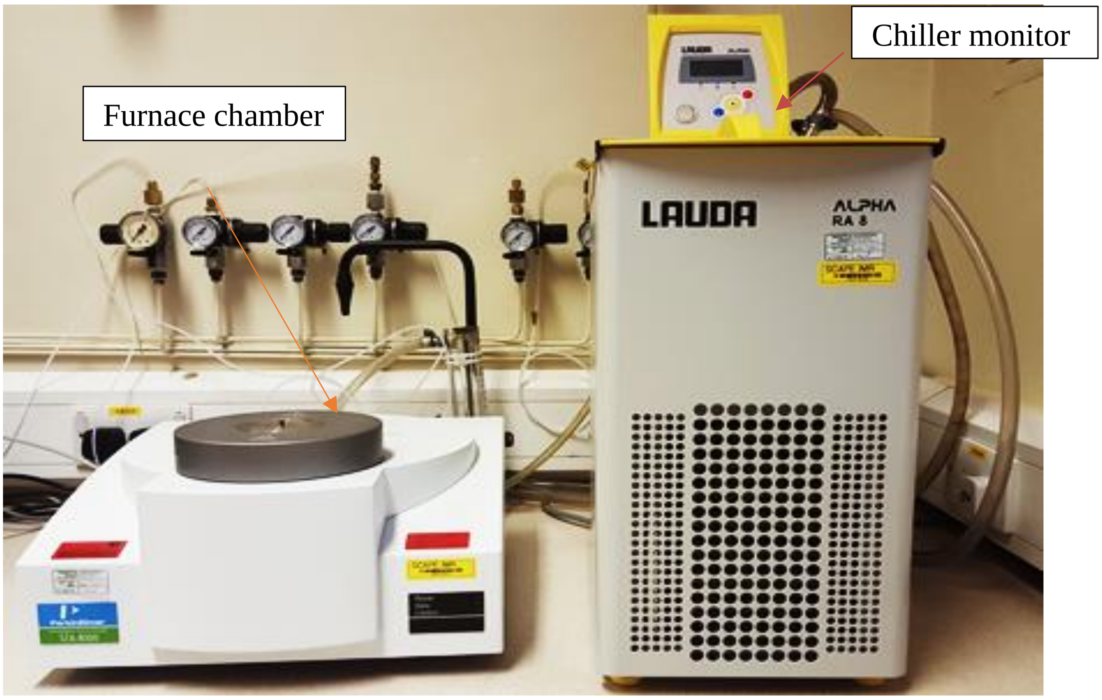

Fig. 4.10: The Perkin Elmer STA 8000 and Lauda Alpha RA 8 Chiller unit at IMR

of reproducibility due to the fact that the sample melted and there was lost of carbon, hence the temperature range was subsequently adjusted to 50^{o} C to 1050^{o} C double run at 10^{o} C/min heating rate in a constant Nitrogen atmosphere of 0.4 MPa. ***Fig. 4.10*** shows the STA 8000 and ***fig. 4.11*** reveals set up of a typical magnified DTA furnace. The detected temperature difference against constant temperature increase output is then displayed on computer screen. Generally, there is usually a series of peak in a DTA curve, such as phase transformation and melting. ***Fig. 4.12*** shows a schematic view of a typical DTA curve where the differential temperature due to endothemic reaction such as melting transition occurs to form a negative peaks and any opposite of such is exothermic which is cooling. Finally, in any DTA curve, the position is determined by the properties of the detected materials and the heating rate, while the area is related to the energy involved in the corresponding reaction [121].

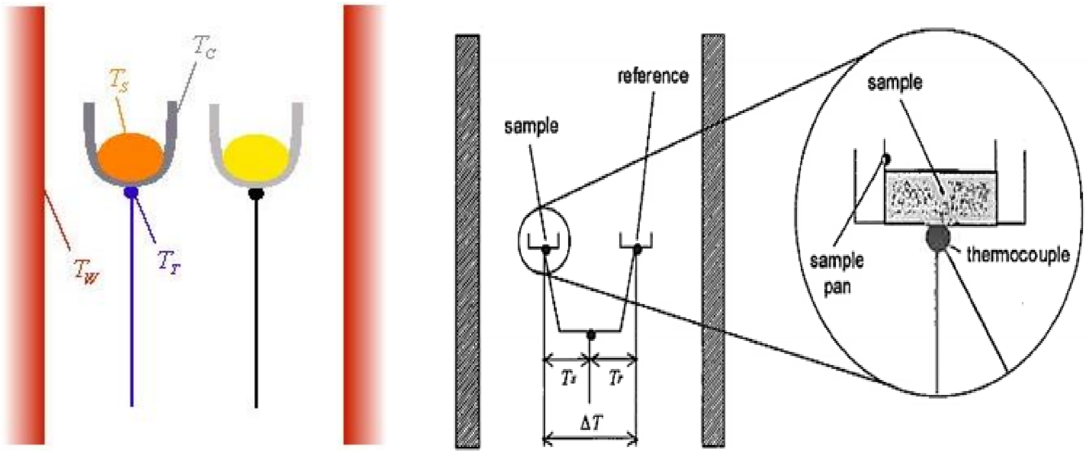

Fig. 4.11: Schematic of DTA cell arrangement of sample & reference in the furnace [122].

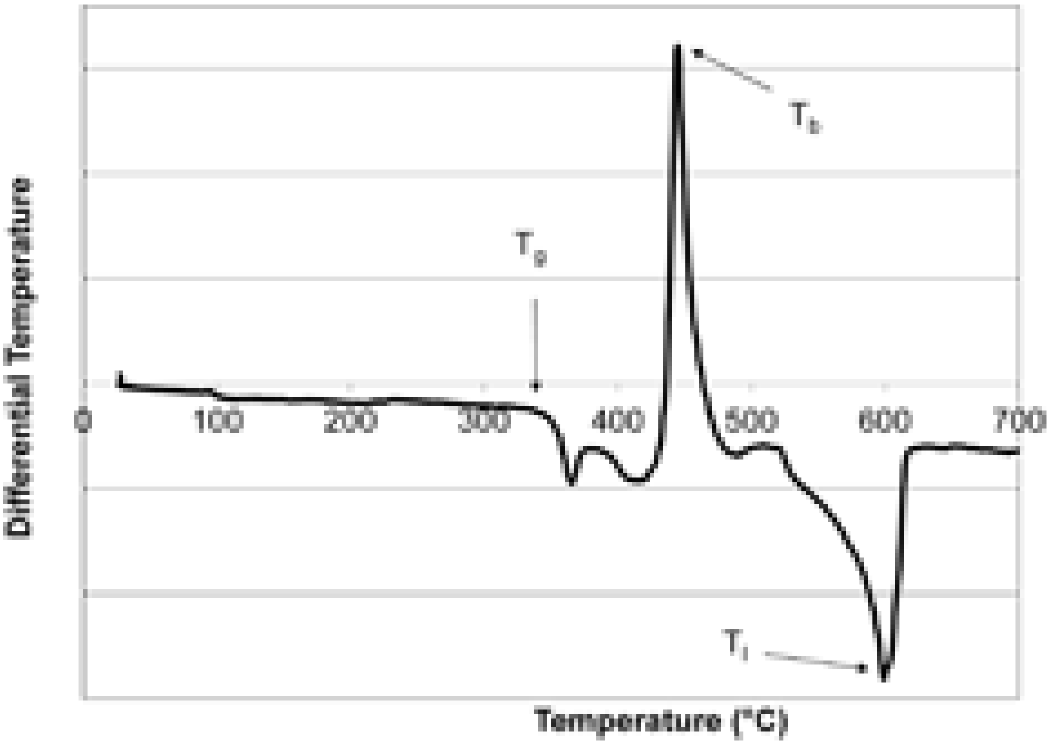

Fig. 4.12: Typical DTA Thermogram as outcome of sharp melting of sample [121].

4.5.6: Cryogenic Treatment

Cryogenic quenching involves deep freezing of materials to very low liqiud nitrogen temperature (–196 ^{o}C) [123]. Previous related studies on grey cast iron [124] and tool steel [125], have shown that cryogenic treatment promotes the complete transformation of retained austenite into martensite in Fe–C based alloys at very low temperature [126], which is normally evident in the materials microstructure, morphology and consequently in the mechanical properties such as hardness and wear resistance [124, 127, 128]. The material sample under consideration here are rapidly solidified droplets. Countainerless rapid solidification is a quenching process and there is an obvious presence of retained austenite in most of the droplets which actually decreases with increasing cooling rate i.e. particle size reduction; but with slow cooling rates the austenite may not be retained but rather it is transformed instead to ferrite. Hence, to evaluate the extent of the complete phase transformation of the rapid quenching experinced by especially the bigger droplets and to be sure the process is complete; cryogenic treatment was carried out to evaluate the volume ratio of retained austenite that will transform to martensite in the biggest samples, 850 µm droplet size particles. The cryogenic treatment was perfomed by soaking the droplets mounted in transcopis resin in liquid nitrogen for about 30 minutes. The cryogenically treated samples were then given gentle 1 µm diamond paste polishing and re-etched and the exact marked region was re-examined using SEM and XRD. For comparison, both the cryogenic treated and non cryogenic treated samples were analyzed to see the extent of microstructure changes and phase variation and how these affect mechanical property (microhardness).

4.5.7: Microhardness measurements

To fully understand the mechanism behind Processing – Structure – Properties as it affects grey cast iron, microhardness testing was carried out on the control sample and each droplet size group. The hardness of a material is usually described as a measure of its resistance to permanent deformation or damage. However, true hardness value varies according to the characterics of the material the indentor is made of, it's force, shape, the applied load and duration of application of the load on samples. Therefore, indentation measurement or hardness values are not strictly comparable unless certain conditions of similarity are followed strictly during the experiment. To assess the effect of evolved phases and the consequent change in microstructure upon the mechanical properties of the droplets as compared to the control sample (as-received); microhardness measurement and analysis was conducted using load in the range of 0.01 – 0.05 Kg. A TUKON^{TM} 1202 Wilson Hardness (Vickers) analyser (shown in ***fig. 4.13***) was used for this task on mounted metallographically well prepared samples at ambient conditions. In order to be sure that the measurement were characteristic of the sample material only and not influenced by that of the resin material, measurements were made on samples mounted on different resin materials (such as Transoptic, Bakelite and Cu loaded bakelite). As no significant difference was observed between the different mounting media, it was concluded that the values obtained are indicative of the droplets' microhardness and are not influenced by the resin material used. Each measurement was repeated at least 10 times minimum with clear reading taken from the indents on clean well polished droplets.

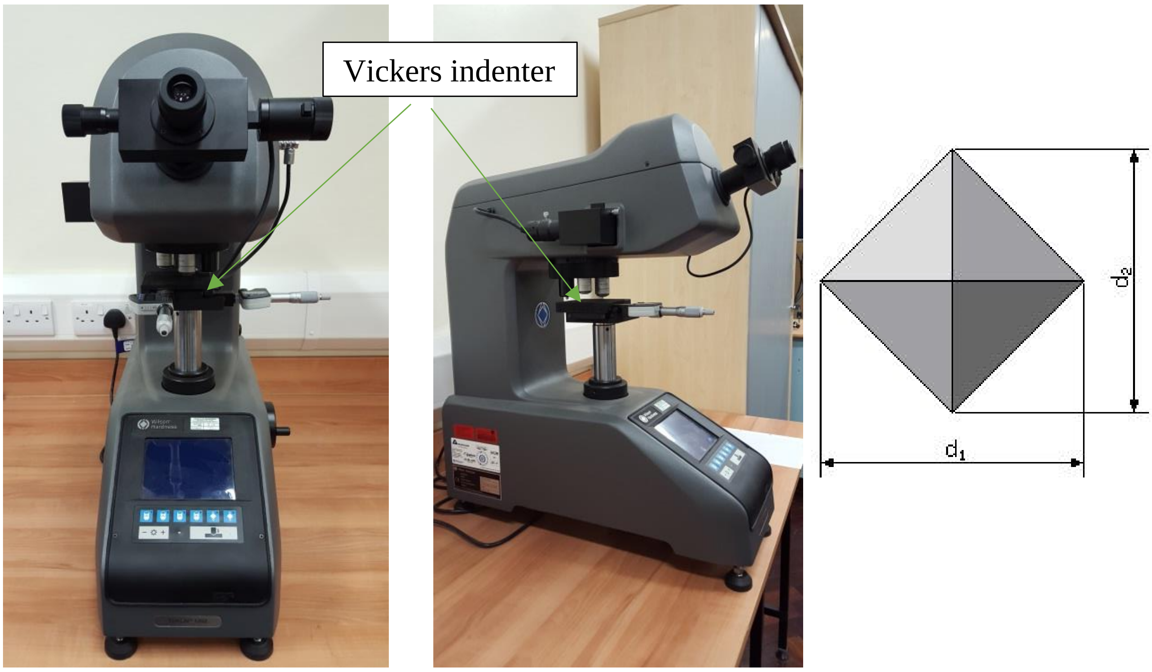

Fig. 4.13: TUKON^{TM} 1202 Wilson Hardness (Vicker) analyser with resultant measurement.

CHAPTER FIVE

EXPERIMENTAL RESULTS

5.0. Introduction to Experimental Results.

This section covers investigation results on the microstructure evolution, phase analysis, percentage volume fraction transformation and the consequent effect on the microhardness of the “as-cast” and that of rapidly solidified BS 1452 Grade 250 grey cast iron droplets. The details obtained were from two different cooling media used during the drop-tube experiment, namely: Nitrogen and Helium. The as-cast alloy serves as the control sample, with which the evolved microstructure and phases in the rapidly solidified droplets in the two environments were compared. The emphasis here is on the results from light optical microscopy, scanning electron microscopy observations, x-ray diffraction analysis, transmission electron microscopy, differential thermal analysis and Vickers microhardness measurement conducted on all the sample sizes. Meanwhile, the effect of cooling rate as a function of the droplets sizes and the impact of undercooling (as influenced by both the cooling rate and the particle diameters via melt sub-division effect) at higher rate of cooling are also presented in sequence.

The volume fraction percentage of the of the initial and evolved phases were calculated based on the comparative peak intensity of the phases. Hence, the progressive phase changes from randomly distributed graphite-ferrite matrix in the as-cast to noticeable quantity of retained austenite in the relatively big and (plus more cementite) in the medium size droplets and more dominating martensitic or acicular-ferrite like phase in the smaller droplets are hereby presented. The big droplets are considered to be those within the range of $850 \geq x \leq 300$ µm; medium size are those in the range of $212 \geq x \leq 106$ µm and the small size droplets ranges from $75 \geq x \leq 38$ µm. These droplets are so loosely grouped based on close similarities noticed in their microstructures in the two cooling environment. However, the quantitative phase volume fraction analysis is based on individual droplet sizes although differential thermal analysis emphasis will be on the 850 µm for big droplets, the 150 µm for middle size and the small 53 µm droplets cooled separately in the two gases as they show distinctive microstructural and hardness properties. Also, the identified XRD peaks for the emerged phases confirmed by TEM analysis are hereby presented and the consequent effect on the mechanical property (as reflected on the measured microhardness values against droplets diameters/cooling rate) is outlined. Hence, discussion and conclusions will be drawn based on the outlined findings in this section.

5.1. Composition analysis of the alloy.

Generally, chemical composition and cooling rate are two principal factors that affects metallic alloy microstructure evolution; the later depends majorly on solidification route employed. In this study, the former is constant as stated earlier in section 4.2. Meanwhile, ***Table 5.1*** shows the comparative elemental composition of this sample; a low alloy commercial grey cast iron BS1452 GRADE 250; analysed using XRF and EDX methods. The XRF elemental analysis was done externally by AMG Analytical Limited (former London & Scandinavian Metallurgical) laboratory using fully quantitative XRF bead fusion thermal infra-Red analyser. This technique is ISO17025 accredited. While the EDX a semi-quantitative and surface biased technique was carried out using Carl Zeiss EVO MA 15 SEM equipped with elemental composition spectroscopy. Hence, the XRF served as complementary test and was so used not only because it is more accurate but to give credibility to the EDX used mainly on the droplets.

Table 5.1: Composition of commercial grey cast iron BS1452 grade 250 as analyzed by LECO using XRF as compared to that obtained from EDX analysis using LEMAS SEM .

Element	**C**	**Si**	**Mn**	**P**	**S**	**Fe**	**CE**
As analyzed using XRF (wt.%)	2.70	2.83	0.58	0.148	0.054	93.34	3.70
As analyzed using EDX (wt.%)	2.59	2.30	0.59	0.23	0.25	93.04	3.40

Therefore, using ***equation 3-5***, in section 3.6; the calculated carbon equivalent (CE) for this sample is 3.70 wt. %C maximum; making it to be classed as hypoeutectic; because the CE is below the eutectic value which is 4.3 wt. % C; while hypereutectic values are above the eutectic value.

5.2. Cooling rate estimation of rapidly solidified grey cast iron droplets.

There are basically two means of evaluating the cooling rate of rapidly solidified droplets obtained using drop tube technique. Although these are like "post-mortem" analysis; they are indeed mathematical models found to be efficient and adequately dependable. These models are so used because it is often very difficult to record or measure accurately the thermal history of the droplets while in flight during rapid cooling in the drop-tube. The first of these is based on mathematical differential of thermal fluxes in the system [129], while the second is based on similar parameters using measurement of secondary dendrite arm spacing in the various microstructures of the free-fall rapidly cooled droplets [2, 32]. In this study, the heat transfer model used to estimate the cooling rate of each droplet is based on their thermal fluxes as the droplets move downward in the tube according to ref. [32]; which can be mathematically expressed as:

$$\frac{dT_d}{dt}\left[c_l(1-f)+ c_s f - L\frac{df}{dt}\right] = \frac{6h}{\rho d}\left(T_d - T_g\right) + \frac{6\varepsilon\sigma_b}{\rho d}\left(T_d^4 - T_g^4\right) \quad \text{………} \quad \textbf{(5-1)}$$

in which T_d refers to the instantaneous temperature of the particle, while c_l and c_s respectively denote the specific heat of the droplet in the liquid and solid state; the solid fraction is given as *f*; while ρ is the density, the droplet diameter and surface emissivity are given as d and ε; while the Stefan-Boltzman constant is σ_b and T_g is the temperature of the gas. Meanwhile, the heat transfer coefficient, h can be derived as:

$$h = \frac{K_g}{d}\left(2 + 0.6\sqrt{Re}\sqrt[3]{Pr}\right) \quad \text{…………………} \quad \textbf{(5-2)}$$

K_g is the gas thermal conductivity, Re and Pr are the Reynolds and Prandtl numbers for the flow, which are respectively given as:

$$\text{Pr} = \frac{C_{pg}}{K_g}\,\mu; \quad \text{Re} = \frac{\rho_g d}{\mu}\left|V_d - V_g\right| \quad \text{…………………} \quad \textbf{(5-3)}$$

where C_{pg} is the gas specific heat capacity, μ is the kinematic viscosity and $\left|v_d - v_g\right|$ is the differential velocity between the droplet and the gas, otherwise known as terminal velocity, v_T (only if gas velocity is zero); for the particle having d diameter subjected a the prevailing tube condition. However, for a spherical droplet, having buoyancy effects given by:

$$\left|v_d - v_g\right| = v_T = \sqrt{\frac{4gd}{3C_d}\left(\frac{\rho-\rho_g}{\rho_g}\right)} \quad \text{……………………} \quad \textbf{(5-4)}$$

Where ρ_g is gas density, g is the acceleration due to gravity while C_d is the drag coefficient given as

$$C_d \mathrm{Re}^2 = \frac{4mg\rho_g}{\pi\mu^2} \qquad \text{.................................} \qquad \textbf{(5-5)}$$

in which, m is the droplet mass. Hence, employing the thermophysical properties of the two cooling medium (N_2 and He) used separately in the drop tube as shown in ***Table 5.2*** and considering the obtained sample's composition, the estimated liquidus temperature (at 1521 K)

Table 5.2: Thermophysical properties of N_2, He and commercial grey cast iron, [76, 90].

Material	Parameter	Value
Nitrogen gas [130]	c_{pg}	1039 J kg^{-1} K^{-1}
	μ	1.78 x 10^{-5} N s m^{-2}
	k_g	2.6 x 10^{-2} W m^{-1} K^{-1}
	p_g	1.16 kg m^{-3} (at 0.1 MPa)
Grey cast iron [89]	c_l	495 J kg^{-1} K^{-1}
	L	1.26 x 10^5 J kg^{-1}
	p	7050 kg m^{-3}
Helium gas [131]	c_{pg}	443 J kg^{-1} K^{-1}
	μ	2.0 x 10-5 N s m^{-2}
	k_g	1.422 x 10^{-1} W m^{-1} K^{-1}
	p_g	0.179 kg m^{-3} (at 0.1 MPa)

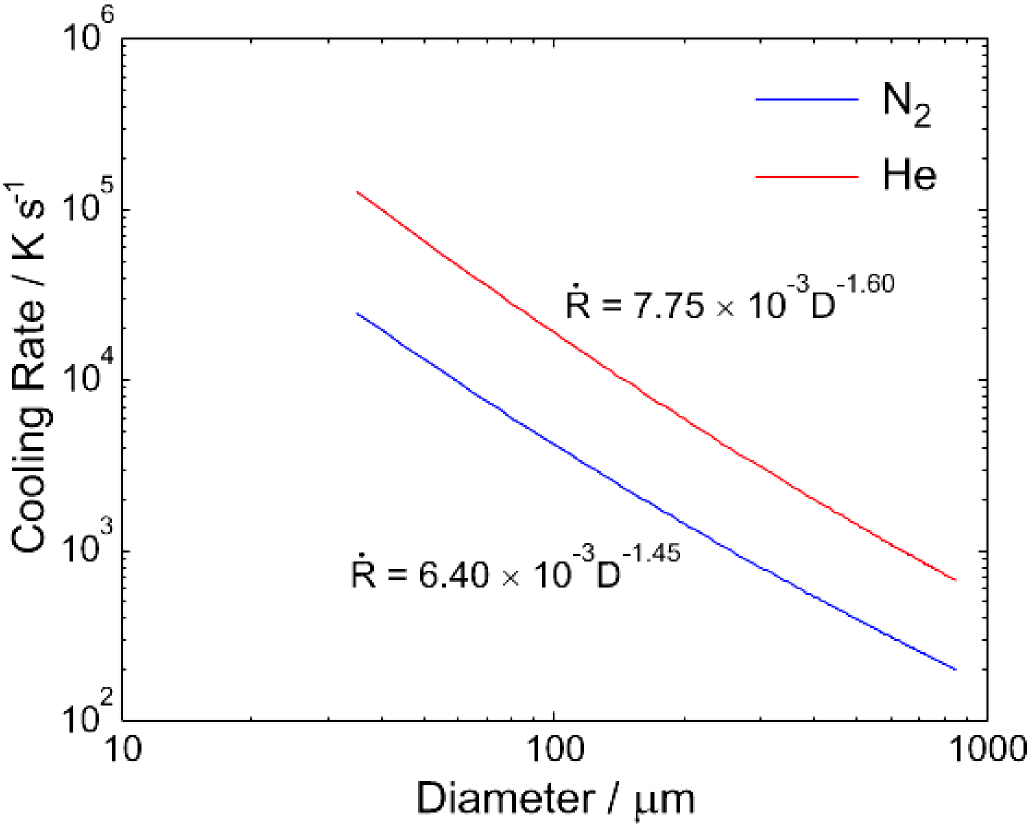

Fig. 5.1: Droplets estimated cooling rate in N_2 and He against their diameter, [90].

using Calphad calculation, hence the cooling rate for each droplet size was determined based on average cooling rate between liquidus and the Fe-C-Si metastable eutectic temperature (approximately at 1353 K). ***Fig. 5.1*** shows the comparative cooling rates estimated in the two cooling medium as a function of droplet diameter. Hence, the estimated cooling rates in the two cooling media for the specific droplets sizes are as outlined in ***Table 5.3*** range from 200 K s^{-1} (for the 850 μm size droplet) to ~23,000 K s^{-1} (for a 38 µm droplet) in Nitrogen and from 700 K s^{-1} (for 850 μm) to 80,000 K s^{-1} (for a 38 μm size droplet) in Helium, which has better thermal conductivity than Nitrogen [32] (see ***Appendix A*** for full list of droplets sizes against cooling rate in the two media) . Meanwhile, it was observed that cooling rate increases with decrease in droplet diameter irrespective of the cooling medium, while undercooling depends on both cooling rate and droplet size (irrespective of cooling rate, as a result of melt sub-division). Even so, droplets of the same size may experience different levels of undercooling as nucleation is stochastic whereas droplet cooling is deterministic in nature.

Table 5.3: Droplet sizes and the estimated cooling rates in the two media in the drop-tube.

d (µm)	d (mm)	R_N (K s^{-1})	R_{He} (K s^{-1})	Ratio
38	0.038	22951.03	90677.91	3.95
53	0.053	12852.34	50087.26	3.90
75	0.075	7146.41	26960.39	3.77
106	0.106	4062.75	14544.20	3.58
150	0.150	2354.32	7828.68	3.33
212	0.212	1396.60	4223.30	3.02
300	0.300	844.62	2273.27	2.69
500	0.500	418.07	913.85	2.19
850	0.850	210.20	354.61	1.69

5.3. Phases analysis

5.3.1: Identification and confirmation.

The procedure for x-ray diffraction (XRD) analysis along with SEM and EDX as described under ***section 4.5*** were used to identify and classify the different phases observed in the as-cast and various sizes of rapidly solidified droplets in the two media (N_2 and He gases). The resultant diffraction pattern solely for the as-cast sample is as shown in ***fig. 5.2***. It reveals predominately ferrite (α-Fe) peaks which is typical of hypoeutectic grey cast iron as shown by micrograph in ***fig. 5.6*** with randomly distributed graphite flakes (see section 3.5.1). Meanwhile, ***Fig. 5.3(a)*** and ***(b)*** show the full plotted diffraction peak patterns of all the droplets cooled in N_2 and He respectively. These offer a quick glance on the emerged phases from each droplet size. However, ***fig. 5.3(c)*** shows some selected 'group representative' of droplet sizes; i.e. 500 µm (for big sizes), 150 µm (for medium size) and 53 µm (for small size) droplets cooled in the two media (*see* ***Appendix B(1 & 2)*** for the as-received sample peak-traces (showing graphite peaks position) and *details of various phase peaks for each droplets in the two medium*). The effect of the cooling rate experienced by the droplets in the two media can be easily noticed from these figures. They show comparative difference in the evolved phases' intensity in each droplet cooled in N_2 and He respectively. Hence, these XRD patterns reveals steady progressive transformation from the ferrite (α-Fe) in the 'as-cast' to retained austenite (γ-Fe) with cementite (Fe_3C) matrix in the relatively 'big/medium' droplets to emerging martensite (α'-Fe) with less cementite (Fe_3C) in the 'smaller' droplets. The morphological changes observed in the as-received as compared to the various droplets cooled in the two media are as outlined in the light optical/SEM micrographs shown in ***fig. 5.4*** through to ***fig. 5.31*** in ***section 5.4***. These revealed microstructural changes are with respect to decrease in droplets size. This is mainly as a result of cooling rate difference and consequent undercooling which are anchored on thermal conductivity of cooling media (with Helium having 5 times better conductivity than N_2).

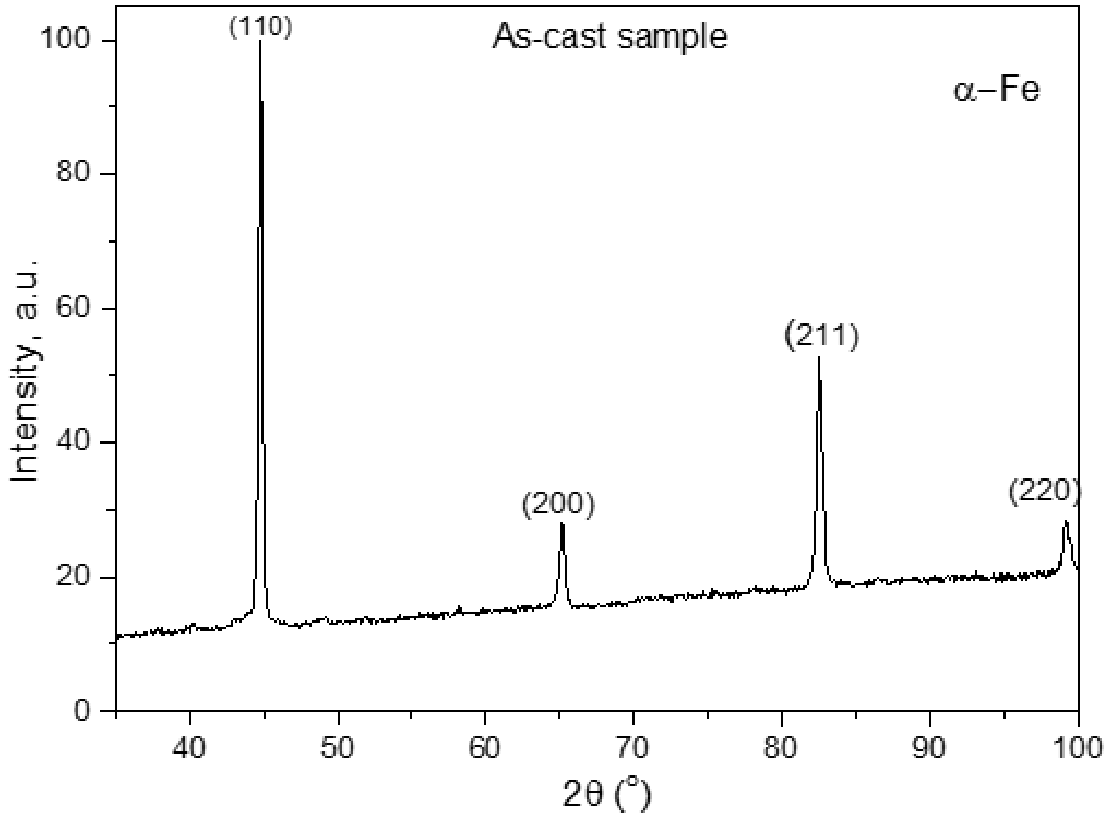

Fig. 5.2: XRD peak pattern of the 'as-cast' commercial grey cast iron sample showing four principally ferrite (α-Fe) peaks. Graphite peaks occur between 20-30 deg. *See Appendix B1 for carbon peak at lower 2θ.*

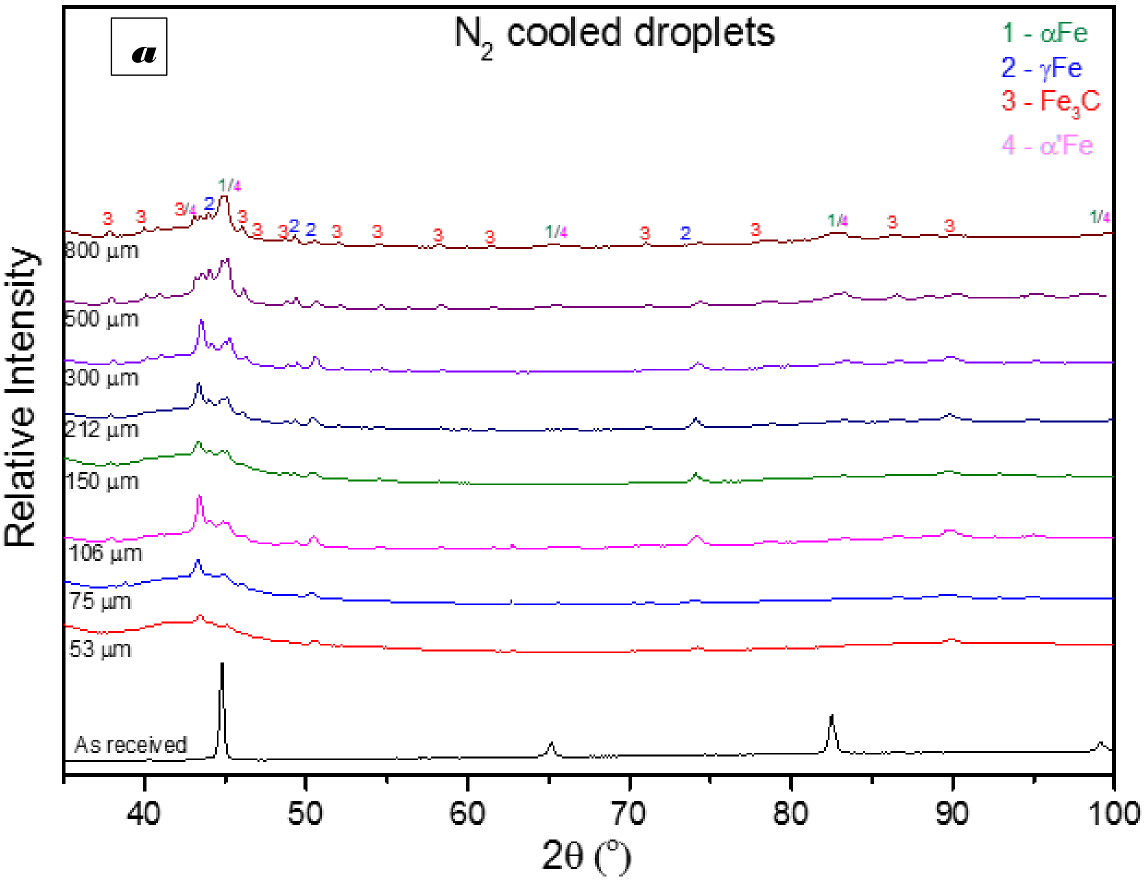
a
N$_2$ cooled droplets
1 - αFe
2 - γFe
3 - Fe$_3$C
4 - α'Fe
800 μm
500 μm
300 μm
212 μm
150 μm
106 μm
75 μm
53 μm
As received
Relative Intensity
40
50
60
70
80
90
100
2θ (°)

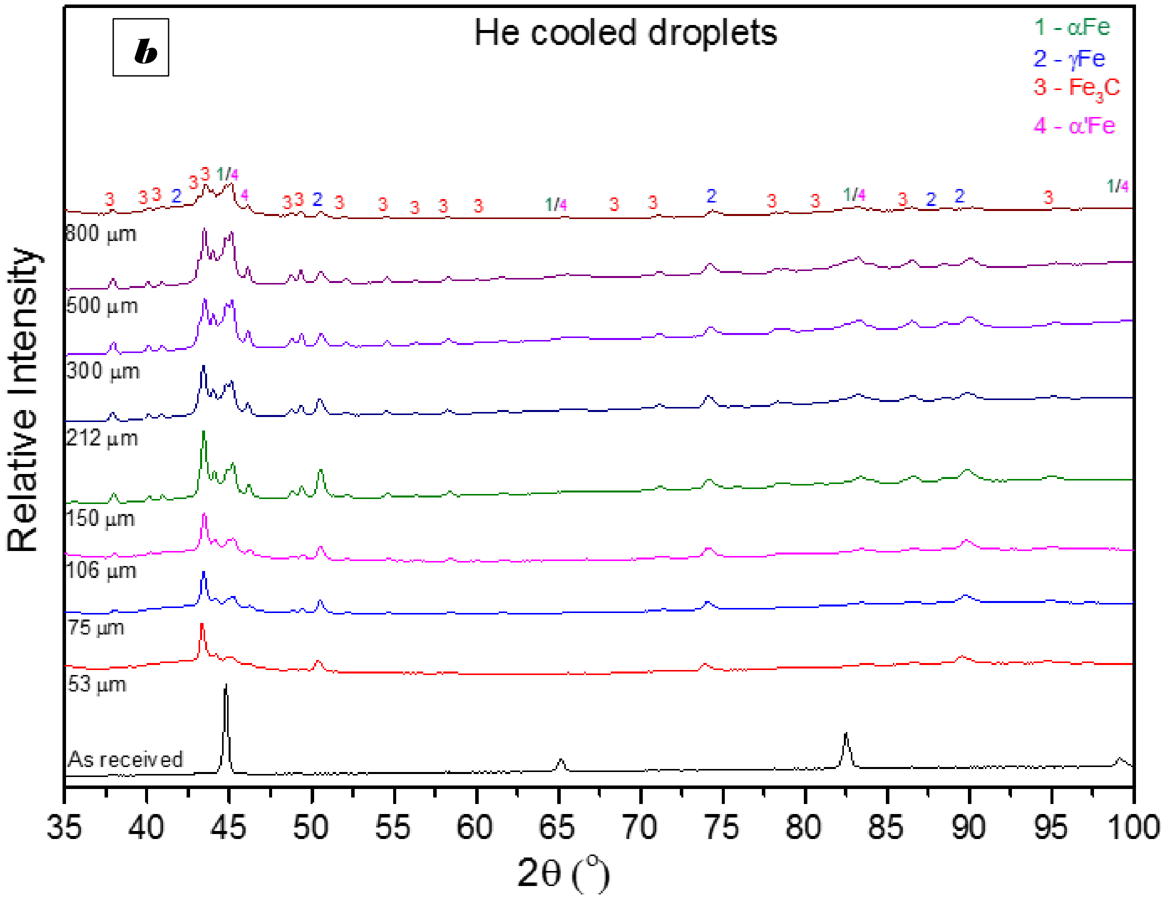
b
He cooled droplets
1 - αFe
2 - γFe
3 - Fe$_3$C
4 - α'Fe
800 μm
500 μm
300 μm
212 μm
150 μm
106 μm
75 μm
53 μm
As received
Relative Intensity
35
40
45
50
55
60
65
70
75
80
85
90
95
100
2θ (°)

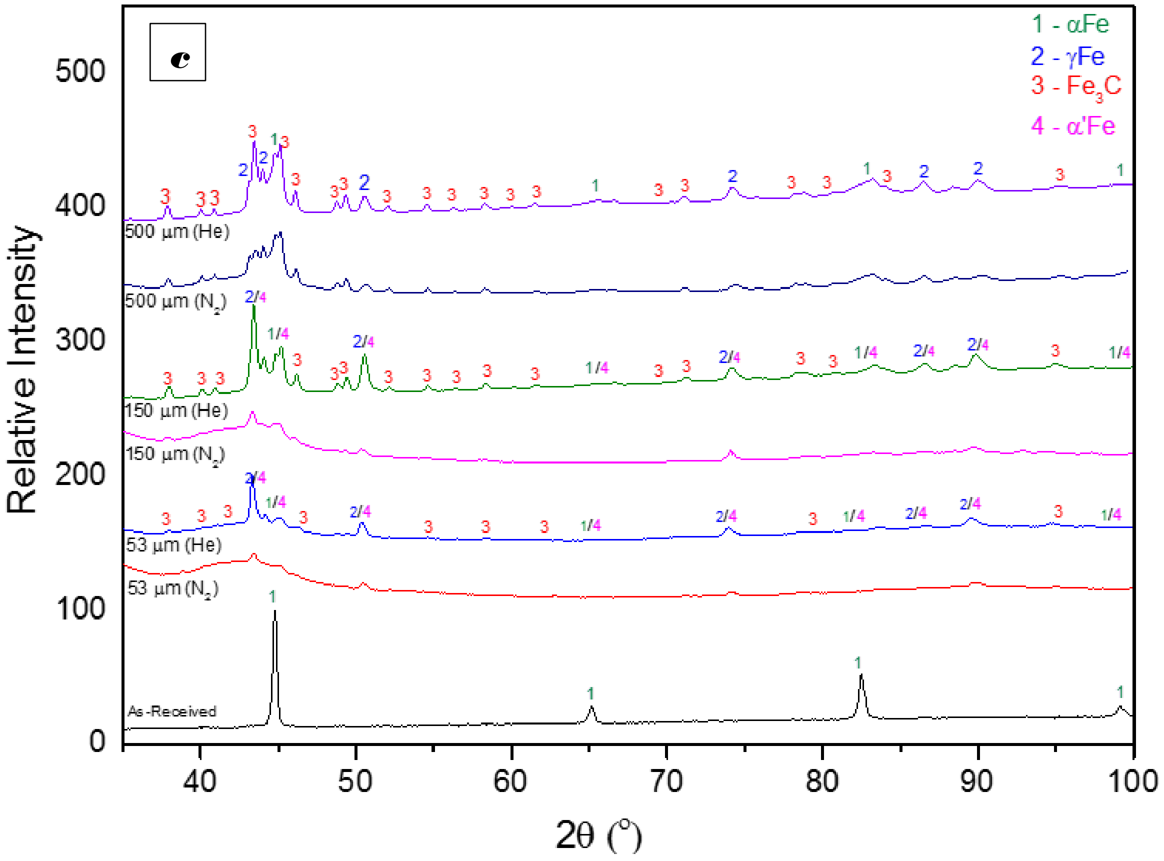

Fig. 5.3: XRD pattern s for all **(a)** N_2 and **(b)** He cooled droplet sizes with identified evolved phases; **(c)** Selected XRD patterns for the ‘as-cast’, 500, 150 and 53 µm droplets cooled in N_2 and He with corresponding evolved phases peculiar to each droplet size as shown. The as-cast is predominately ferritic (α-Fe), while the big and medium size droplets (500 & 150 µm) are mostly retained austenite (γ-Fe) plus cementite (Fe_3C) and the very small droplets are majorly martensitic (α'-Fe) with cementite.

5.3.2: Phase volume fraction analysis

The identified phases in each droplet size vary in quantity based on cooling rate and medium. However, progressive increase or decrease tread of these phases was observed as reflected in the morphological quantitative analysis of the dendritic and interdendritic transformation. Also the percentage phase fraction analysis shows transformation of the inherent ferrite and retained austenite phases reducing while emerging metastable (cementite) martensite phases increases. These semi quantitative phase separation and analysis was done using High Score software. The separation was done based on peak intensity in each size fraction corresponding to the droplets decreasing sizes as obtained in N_2 and He cooled samples. Table 5.4 and 5.5, show the estimated percentage phase fractions for each droplet size cooled in N_2 and He respectively. An average of 5 trial per droplets size was considered to get mean values.

Table 5.4: Showing % phase volume fraction of the different evolved phases in N_2 environment with their corresponding cooling rate.

N_2 cooled samples: Phase volume fraction					
Size (µm)	$\dot{R}$ (Ks^{-1})	α-Fe	γ-Fe	Fe_3C	α'-Fe
850	200	28.3	48.2	17.8	2.7
500	397	26.5	43.3	22.4	7.8
300	799	24.3	41.6	24.7	9.4
212	1318	21.4	37.3	27.5	13.8
150	2216	21.0	35.5	25.2	18.3
106	3814	20.2	25.4	26.8	27.6
75	6692	15.9	21.2	18.6	44.3
53	12006	10.6	18.3	19.3	51.8
38	21396	9.3	17.4	20.1	53.2

Table 5.5: Showing % phase volume fraction of the different evolved phases in N_2 environment with their corresponding cooling rate.

He cooled samples: Phase volume fraction					
Size (µm)	$\dot{R}$ (Ks^{-1})	α-Fe	γ-Fe	Fe_3C	α'-Fe
850	667	15.2	52.3	25.1	7.4
500	1423	13.1	49.2	26.1	11.6
300	3087	11.4	44.5	28.7	15.4
212	5366	9.3	38.7	31.5	20.5
150	9498	7.6	25.3	34.2	32.9
106	17177	6.2	22.3	26.3	45.2
75	31548	5.1	16.5	23.5	54.9
53	58983	4.2	13.5	22.5	59.7
38	108804	3.4	10.2	18.3	68.1

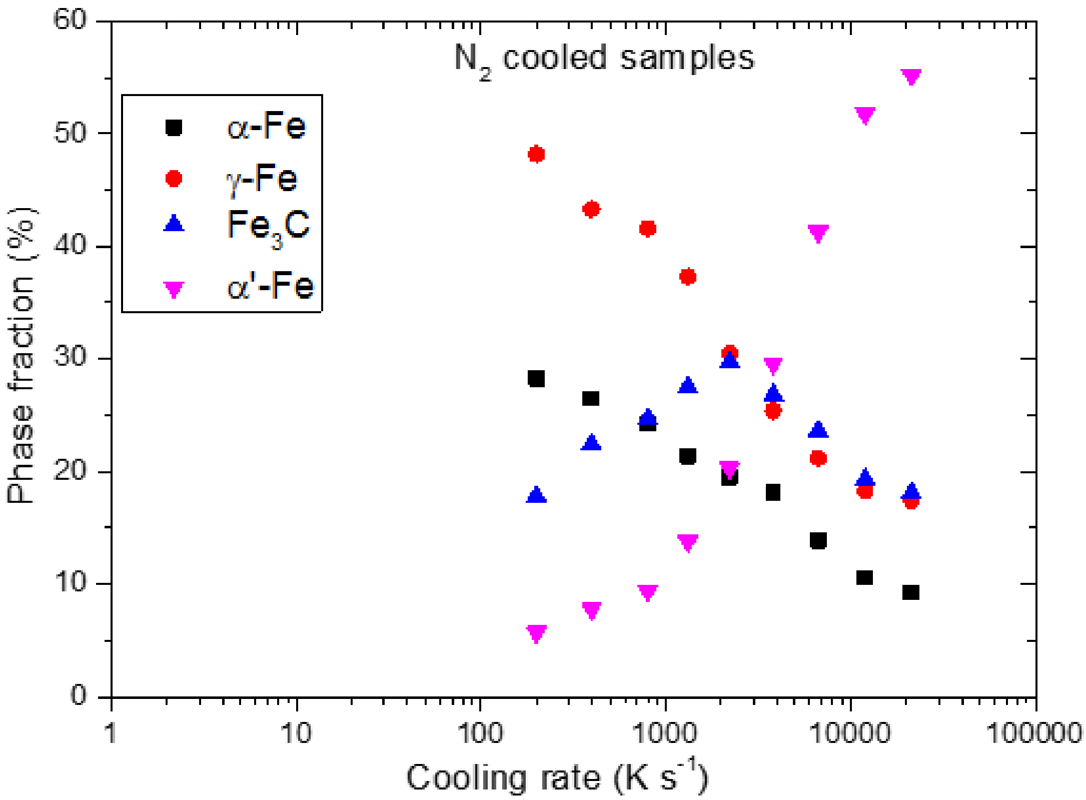

Fig. 5.4: Showing % weight fraction of all evolved phases against cooling rate in N_2 environment based on values in Table 5.4.

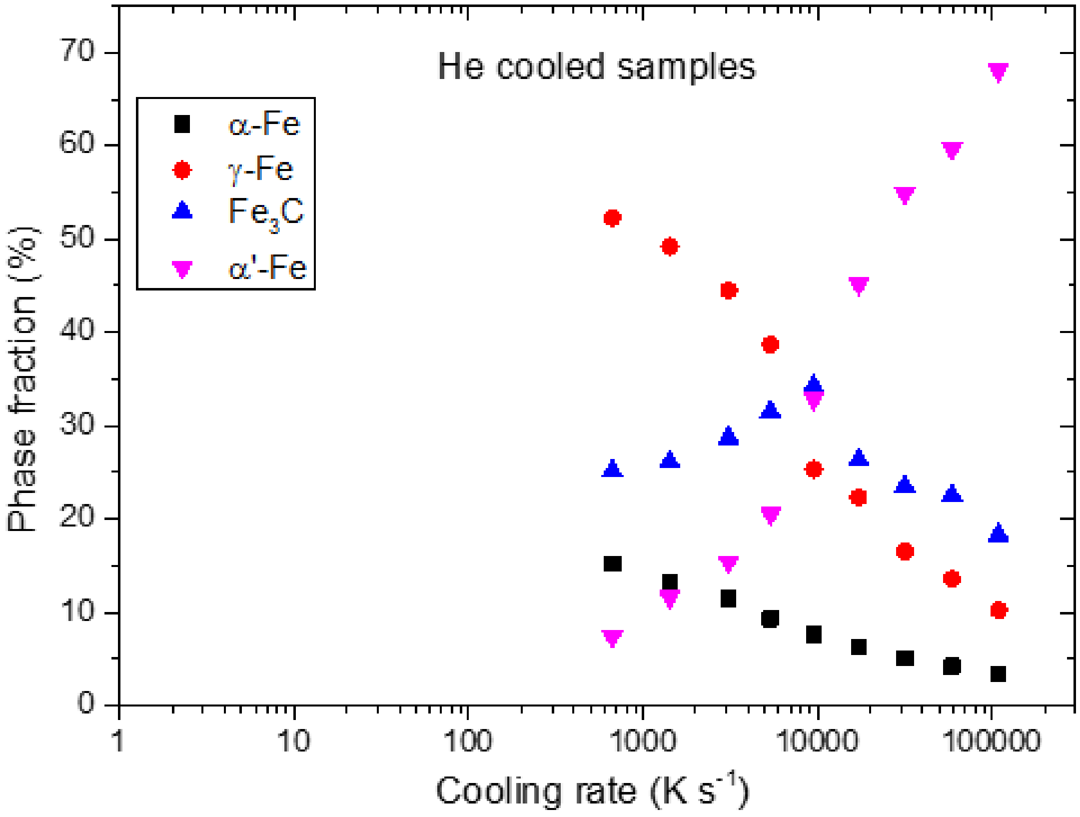

Fig. 5.5: He cooled fashion of % weight fraction of all estimated evolved phases against calculated cooling rate as displayed in Table 5.5.

5.4. Morphology and microstructure characterization.

After careful metallographic preparation of the samples as described in section 4.4, they were initially examined using optical light microscope and for more details at higher resolution, scanning electron microscopy was employed. The micrographs presented here are typical of the droplets, showing the specific characteristic of each sample sizes.

5.4.1. Light optical microscope investigation.

Fig. 5.6 and ***5.7*** show unetched optical micrographs of ‘as-cast’ and ‘crucible residue’ (drop-tube furnace remnant after rapid pressure ejection) samples respectively. As expected, the two have high level of resemblance, with characteristic flake graphite randomly scattered across the microstructures. The obvious reason for this is that both experienced slow cooling rate. The crucible residue actually solidified much more slowly inside the furnace enclosure after the ejection of the droplets. So, the observed structure looks more like the initial as-cast sample with thicker or chucks graphite flakes site appearing randomly in the microstructure [76]. The two micrographs are classified as Type C and A graphite shapes respectively as previously illustrated in ***fig. 3.15 (c)*** and ***(a);*** in ***section 3.6.2.3*** and ***3.6.2.1***. The furnace cooling (inert annealing) encourages more ‘chucky’ graphite segregation in the ferrite matrix. Meanwhile, ***fig. 5.8*** shows the dendritic structure of the ‘as-cast’ sample after it was etched in 2% Nital solution. This reveals the characteristic primary and secondary dendritic arms of the α-Fe as expected of a conventionally cooled grey cast iron. Also similar microstructure was seen in the crucible residue sample as shown in ***fig. 5.9(a);*** although with more fragmented dendrites after applying the same etchant and conditions. At higher magnification, ***fig. 5.9(b)*** clearly reveals two distinct morphologies seen both in the as-cast and crucible residue samples. The section M1 (whitish) is single phase imbedded in M2 (which is darker and comprises of lamellar layers of 2 distinct phases). The choice of Nital solution as the best etchant for this study is based on careful consideration among other etchants. ***Fig. 5.10***, ***5.11*** and ***5.12*** *{**(a)*** and ***(b)**}* respectively present the effect of two other known etchants for cast iron, namely Murakami and Picral reagents. Murakami reagent has the least effect on the microstructure of this sample. It is meant to reveal the presence of Chromium Carbide by tinting it dark brown, and because no Cr is present in this alloy, so no tangible effect could be seen from this etchant (***fig. 5.10a***). However, with very long exposure, it darkens the entire microstructure as seen in ***fig. 5.10b*** compared to that of Nital etched sample shown in ***fig. 5.11***. Meanwhile, the Picral etchant distinguishes the grain boundaries by attacking the core (matrix) and revealing the grain boundaries as shown in ***fig. 5.12 (a)*** and ***(b)*** under different picral solution percentage concentrations. The same effect could be seen on ***fig. 5.13 (b)*** and when compared to unetched in ***fig. 5.13 (a)***, the picral shows clearly the grain boundaries better than other etchants. Meanwhile, the main interest here is on microstructure evolution as a function of different cooling rate experienced by the samples under investigation, therefore the morphology and phases revealed are the main concern in this study. So even with higher concentration and longer exposure, Murakami reagent did not really make tangible difference on the samples microstructure as shown in ***fig. 5.14 (a)*** for as-cast and ***(b)*** for crucible residue; except the general attack on the matrix without further information. Hence, Nital solution is preferred for this study in the sense that it provides expected phase contrast and reveals the needed microstructure morphologies readily and clearly. (see some attached micrographs in the Pictures attachment section).

Fig. 5.15 shows the morphologies of spherical or near spherical unetched different droplets sample sizes common to both cooling media. These selected droplets shown in ***fig. 5.15 (a)***, ***(b)*** and ***(c)*** are big enough to be viewed under optical microscope at different magnifications. However, the 850+ µm droplet micrograph shown in ***fig. 5.16*** and ***5.17*** provide better morphologies of this N_2 cooled unetched big droplet from the drop-tube process. Actually, the morphology is the same for all droplets cooled in either of the medium, since no visible structural changes can be seen without etching at this level. However, the effect of rapid solidification (even on this droplet with modest cooling rate) was obvious as the graphite flakes have completely disappeared when compared to the unetched ‘as-cast’ or ‘crucible residue’ samples previously presented in ***fig. 5.6*** and ***5.7***. Therefore, when etched in 2% Nital solution, the 850+ µm size droplet (as shown in ***fig. 5.18***) reveals interesting morphologies similar to but not the same as that of as-cast sample as shown in ***fig. 5.8***. Basically the morphologies M1 and M2 are conspicuous in the microstructures and M1 clearly seems homogeneous with single phase P1 while M2 is heterogeneous and lamellar in nature comprising of two distinct phases P2 and P3; these are more noticeable when viewed at high magnification as shown in ***fig. 5.9(b)*** and ***5.19***. However, M1 in the “as-cast” sample connotes a well-defined dendritic structure, but it becomes fairly more fragmented in the 850+ µm droplet sample. It can be noticed that the dendrites are still very visible in the upper right hand of the biggest particle (as indicated in the ***fig. 5.19*** around the section labelled P1.); again this is because this sample (850+ µm size droplets) as shown in ***fig. 5.20***, experienced the least/modest cooling rate among the droplets cooled in He gas. Hence, ***fig. 5.18*** and ***5.19*** provided significant microstructure difference compared to the same unetched forms in ***fig. 5.16*** and ***5.17*** of the same 850+ µm particle. As a result of this, the observed morphology of this big droplet is quite different from that of conventionally cooled as-cast or crucible residue samples shown in ***fig. 5.8*** and ***5.9***; although still under the same etching conditions their morphologies and evolved phases differs as a result of rapid solidification experienced by the droplets. Hence, within the possible magnification capacity of the optical microscope used, the samples' morphologies show that the smaller the droplets, the more fragmented the dendrites that will be forms. Consequently, the optical microscopy results show that there is huge difference in the microstructure of the droplets and that of the control "as-cast" sample (or the crucible residue sample). Hence, the slowly cooled as-cast or furnace cooled samples revealed flake graphite in the α-iron matrix, while the drop-tube products microstructure display two distinct morphologies one seems to be single phased (γ-Fe) which is dendritic in nature while the other is a lamellar comprising of two alternating layers of α-Fe and Fe_3C (pearlite) as shown in ***fig. 5.21*** (which is an enlarged version of fig 5.20).

In conclusion, it was observed that all the droplets have distinct dendritic and interdendritic phases. The dendrites decrease with increasing cooling rate. Hence, with particle size reduction the dendrites fragment and effectually this transform more interdendritic metastable phases (i.e. Fe_3C and α'-Fe) as shown in the identified XRD peaks in fig. 5.3. Meanwhile, Table 5.6 in Section 5.4.3 displays the evidence of the progressive transformation of dendrites to interdendritic fragmentation. This calculated morphology quantitative % volume fraction analysis shows that the transformation is predominant as the particles size reduces or increased cooling rate. Hence, the smaller the droplets the less dendrite and the more metastable phases formed because of the increasing accompanying undercooling effect.

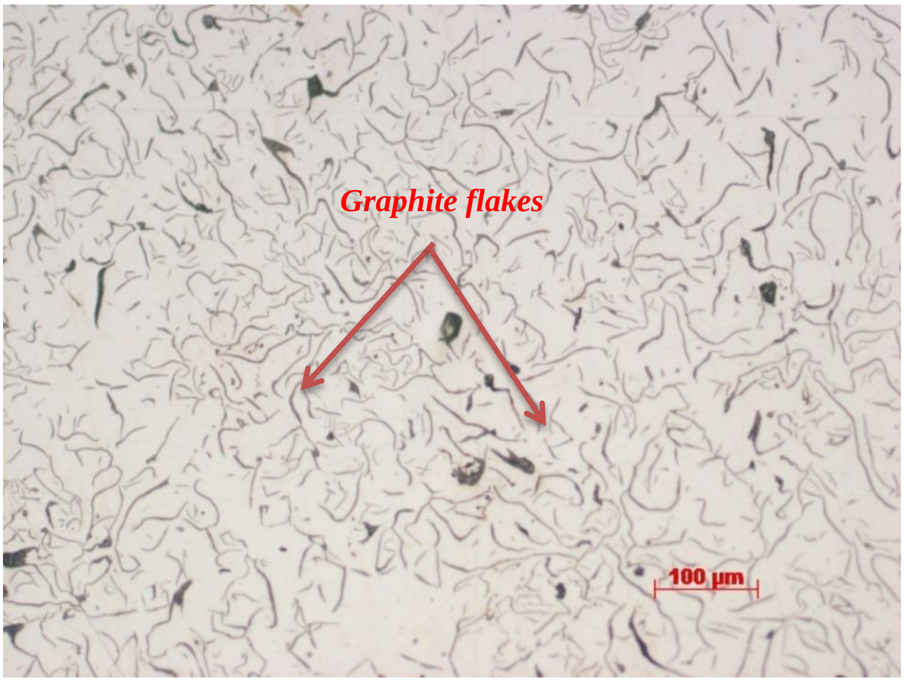

Fig. 5.6: Unetched "as-cast" grey cast iron sample (*close to the middle section*), classified as coarse flake graphite Type C in ferrite (α-Fe) matrix. The flake graphite seen here are peculiar characteristic microstructure of slowly cooled grey cast iron.

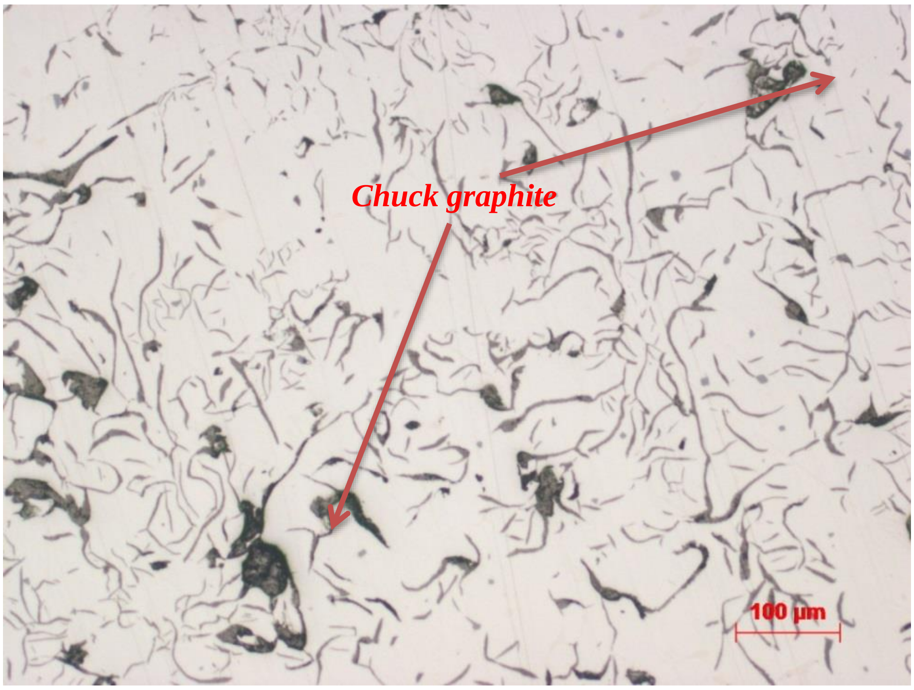

.

Fig. 5.7: Unetched microstructure of "crucible residue" sample, classified as Type A graphite. The gradual cooling of the crucible residual in the furnace is similar to that of the as-cast sample, in that there is enough time for flake graphite formation &

growth with some chucks as a result of re-melt and very slow cooling rate in the inert atmosphere.

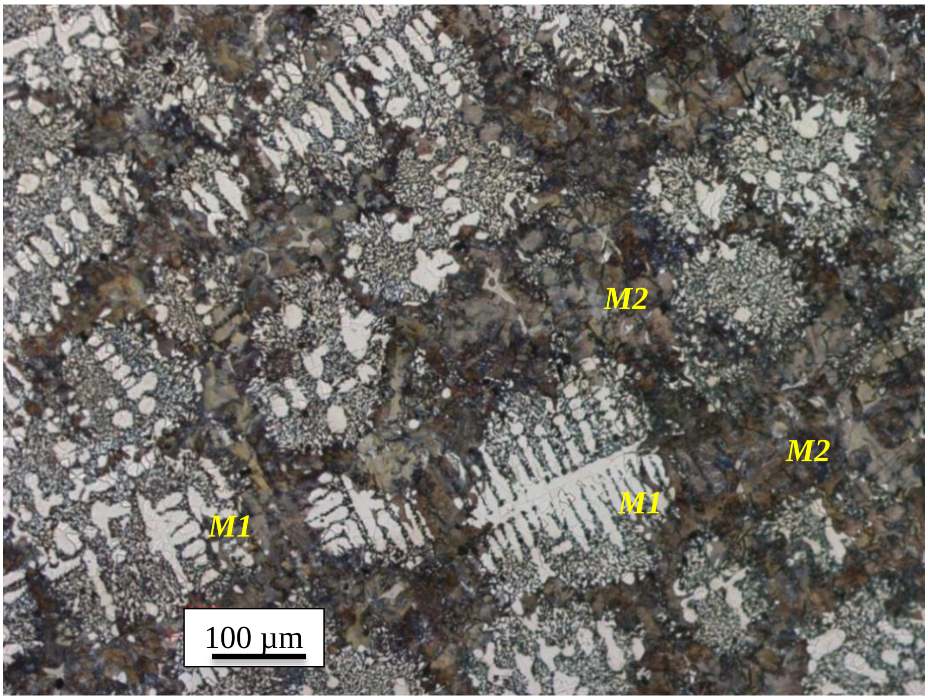

Fig. 5.8: Dendritic structure of the as-cast sample revealed after etching with 2% Nital (20 sec.) which stands out to be the best etchant for grey cast iron as compared to other etchants since it provides morphologies contrast and reveals clearly the phases contrast in the microstructure.

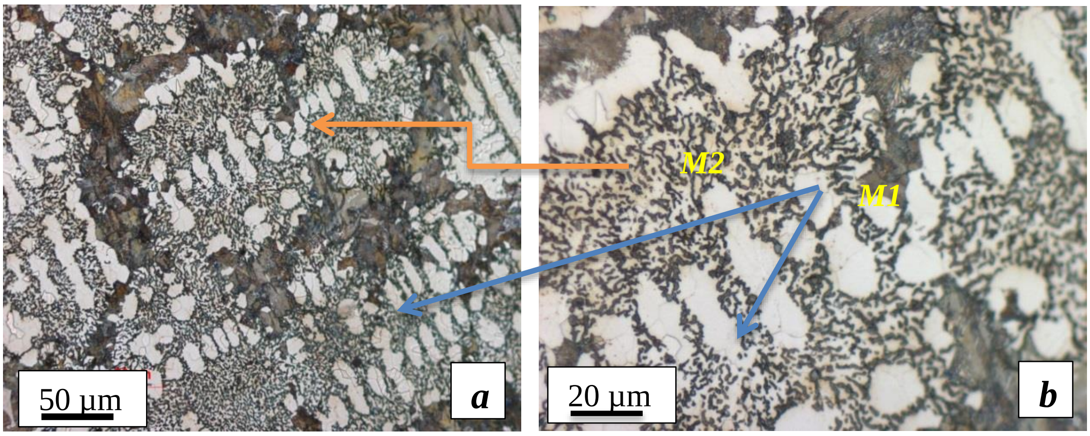

Fig. 5.9: Crucible residue microstructure morphologies with clearly revealed phases.

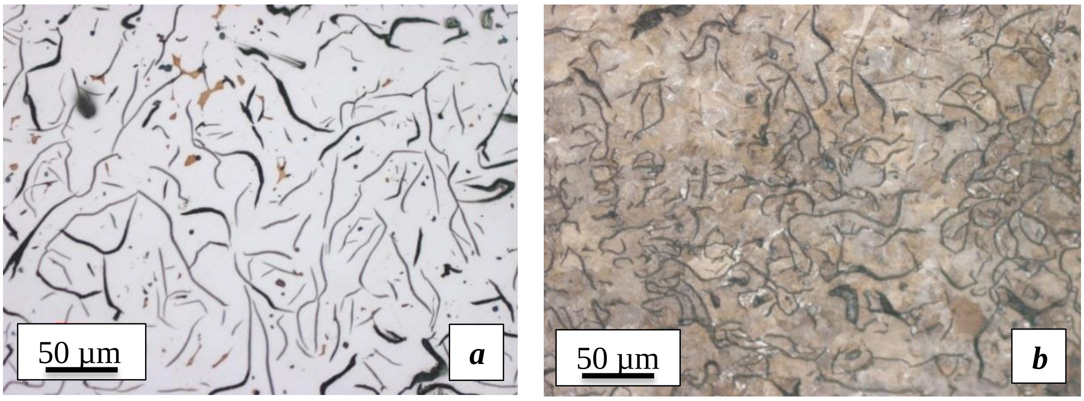

Fig. 5.10: Effect of Murakami reagent on the “as-cast” after (a) 90 secs & (b) 3mins.

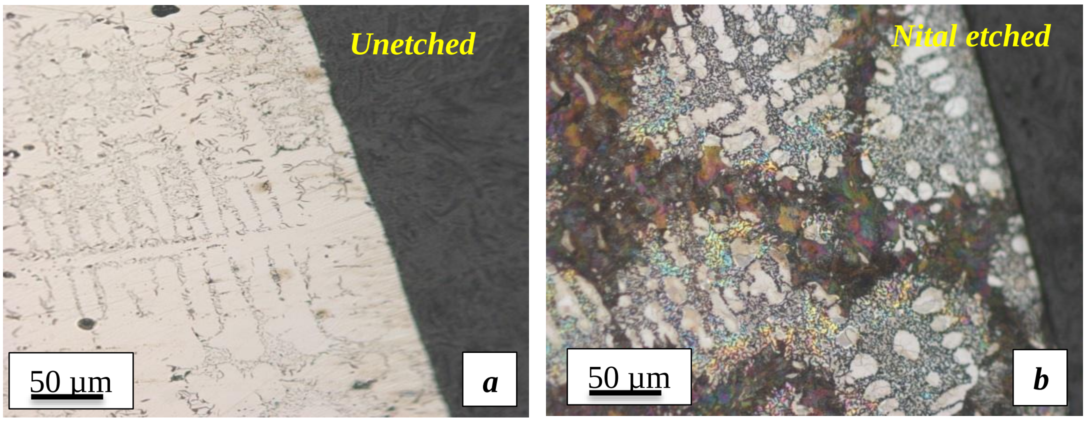

Fig. 5.11: (a) Unnetched and (b) 2% Nital etched microgrph of “as-cast” dendritic structure (after 20 sec.).

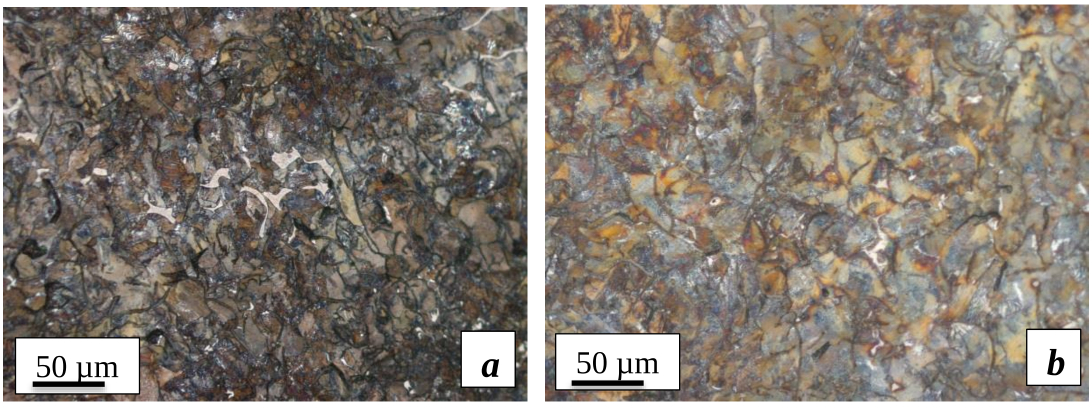

Fig. 5.12: Picral etched microstructures (a) 4% and (b) 2% of “as-cast” showing the grain boundaries (20 sec.)

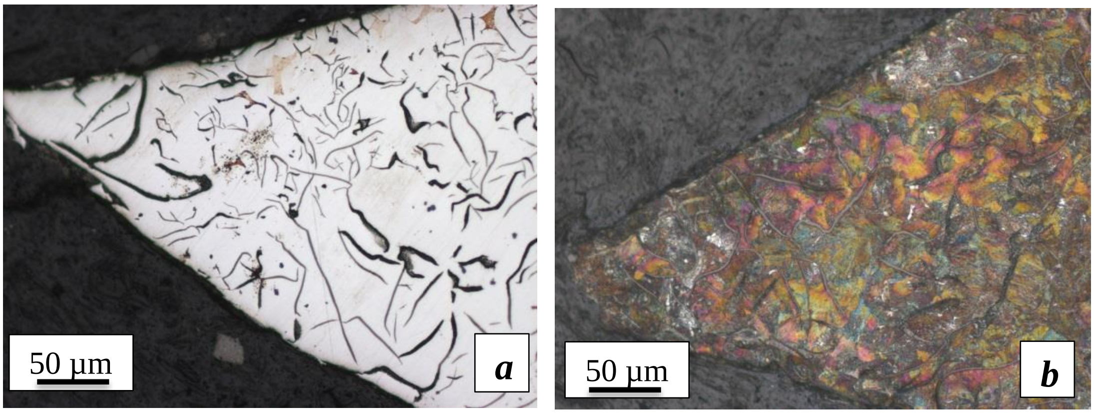

Fig. 5.13: (a) Unetched & (b) 2% Picral etched (30 s) microstructure of "mid-centre" tip of "as-cast" sample.

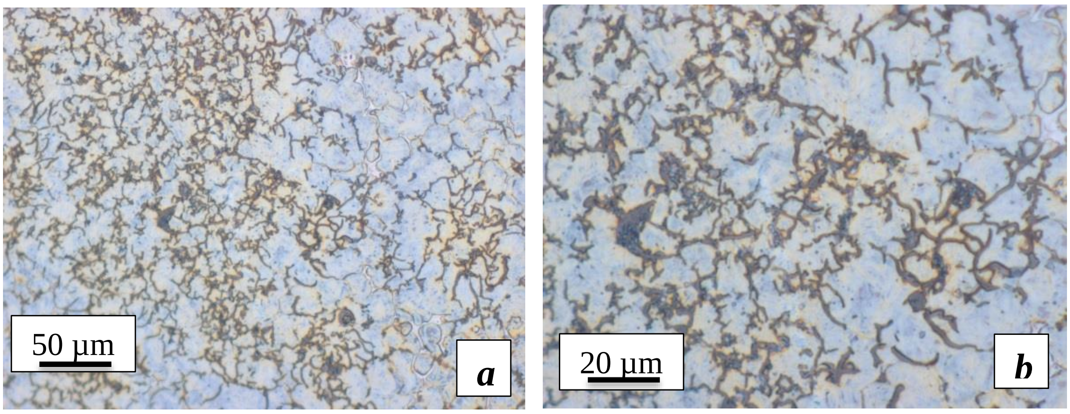

Fig. 5.14: Murakami etched microstructure of slowly cooled (a) "as-cast" and (b) "crucible residue" (2 mins.)

(a) 212 – 300 µm; ***(b)*** *300 – 500 µm;* ***(c)*** *500 – 800 µm*

Fig. 5.15: Morphologies of different unetched droplet (in either medium) after metallography section.

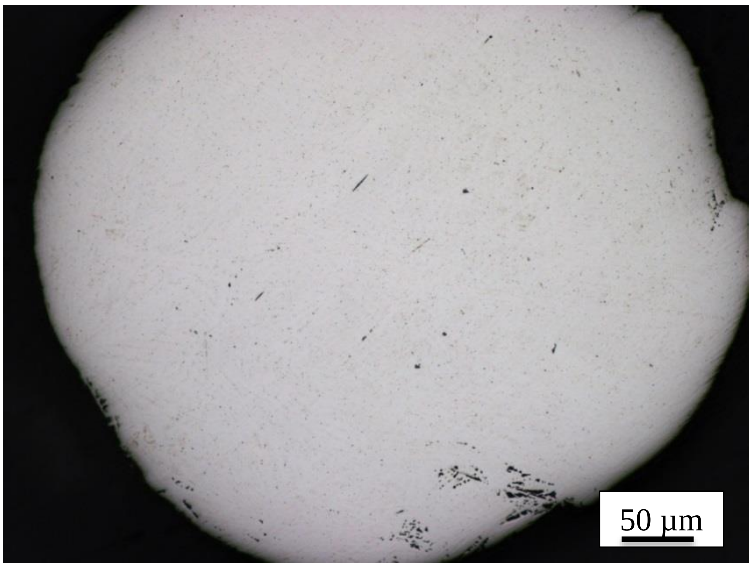

Fig. 5.16: Typical unectched 850+ µm droplet (in either medium) after basic preparation.

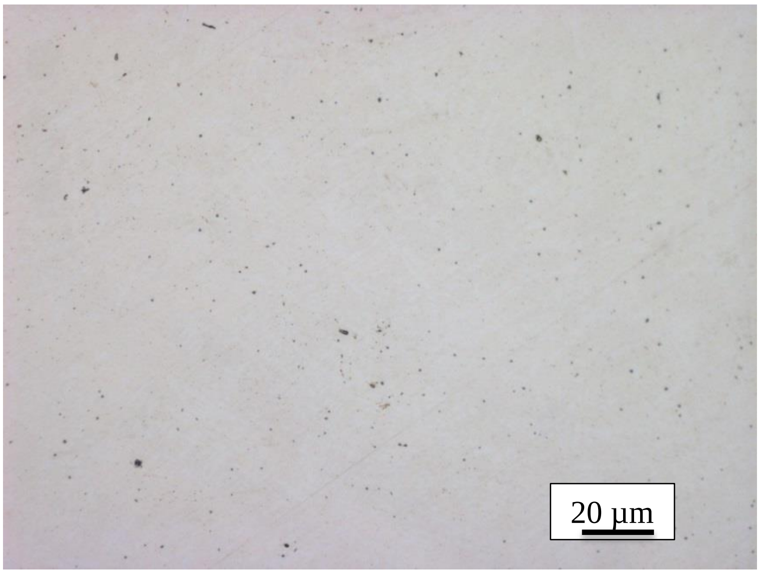

Fig. 5.17: Enlarged (*fig. 5.16*) optical micrograph of well prepared unetched 850+ µm sample. Without etching nothing meaningful could be seen even from the micrograph of the biggest drop-tube product, it is evident that the graphite flakes have all disappeared.

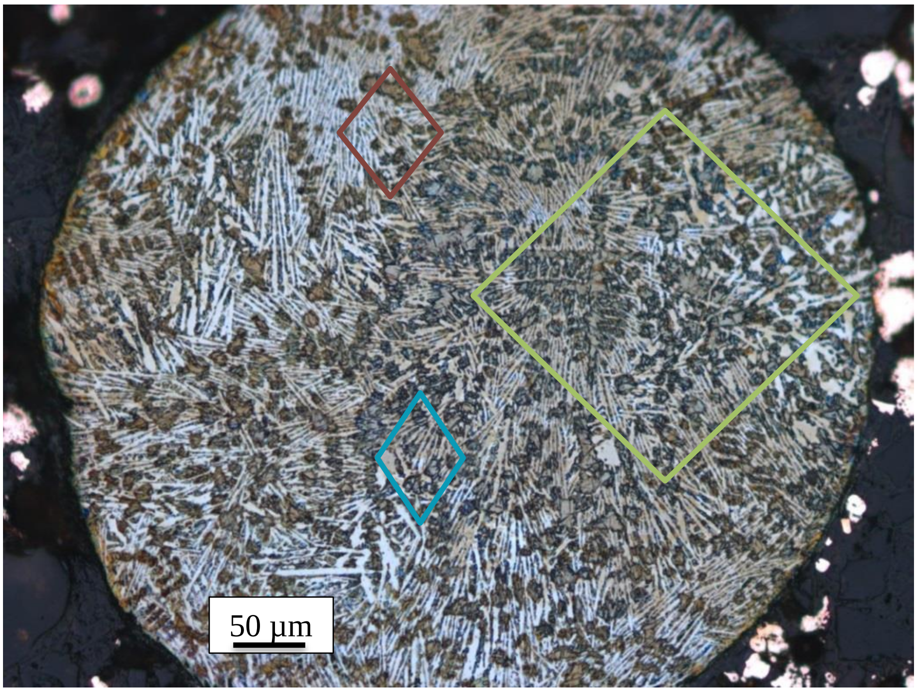

Fig. 5.18: Etched N_2 cooled 850+ µm droplet with modest cooling rate (similar to Helium cooled). This microgrph reveals the samples's microstructure after etching in (2%) Nital. The effect of the etchant can be clearly seen as it reveals the dendritic microstructure and showing the phase constrast clearly.The isolated dendritic structures in colours can be compared to that observed in the as-cast in ***fig. 5.8***.

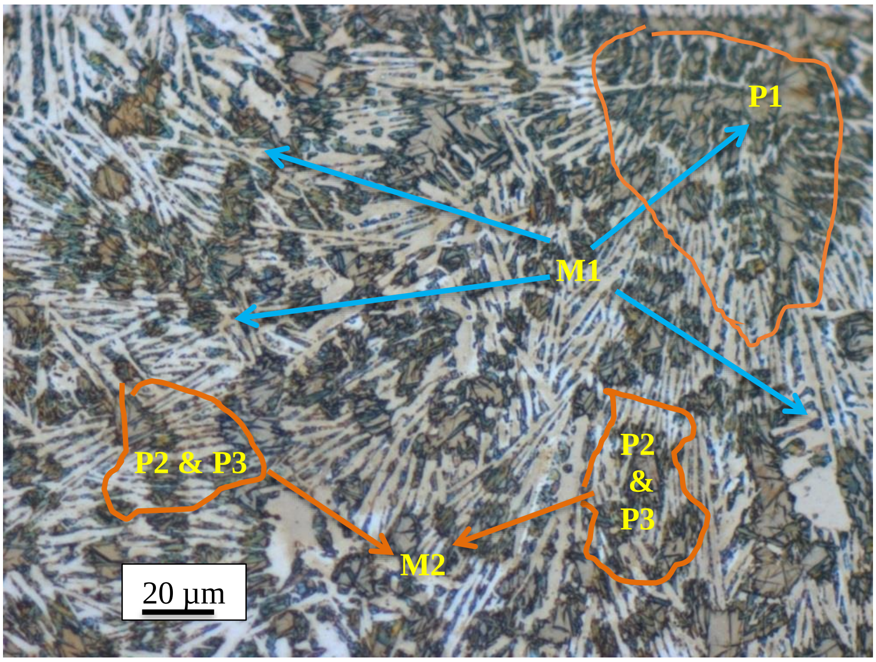

Fig. 5.19: This enlarged microgrph of ***fig. 5.18***, reveals a single dendritic phase P1with a distinctive morphology M1 embedded in a matrix displaying lamellar morphology (M2) comprising of two alternating lamella morphologies (P2 and P3) i.e. the light and dark portions. The primary and secondary dendritic arms can still be clearly seen in the upper right hand corner of the micrograph.

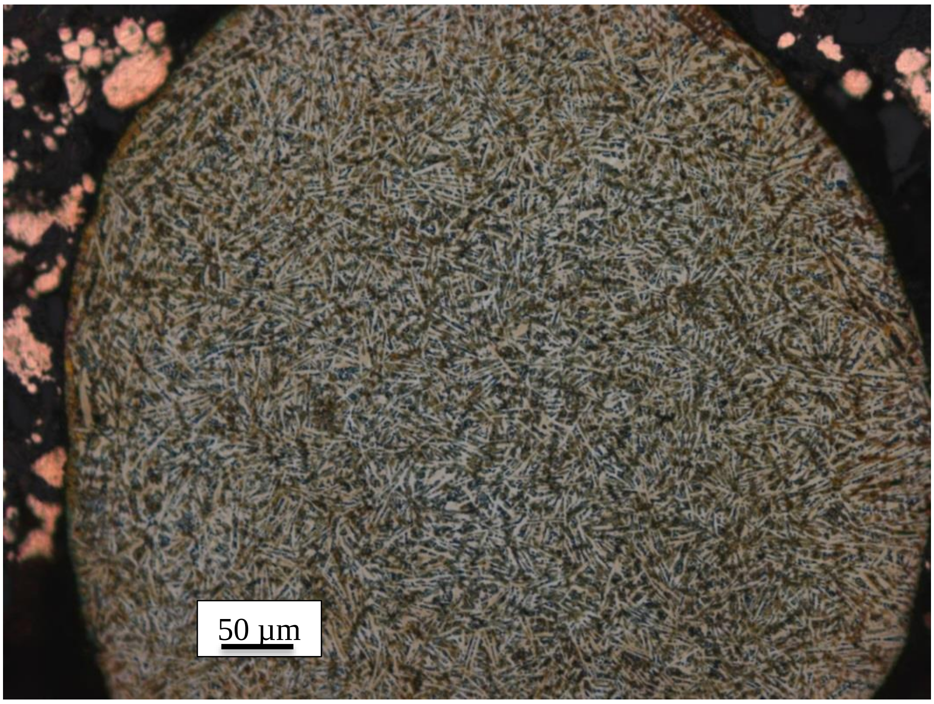

Fig. 5.20: Optical micrograph of He cooled 850+ µm size droplet sample; its morphology when compared to ***fig. 5.10*** of the as-cast sample shows high supression of the flake graphite which has been replaced by less fragementation here. Eventually the dendrites merges into plates and laths in much smaller droplets as the cooling rate increases in Helium gas.

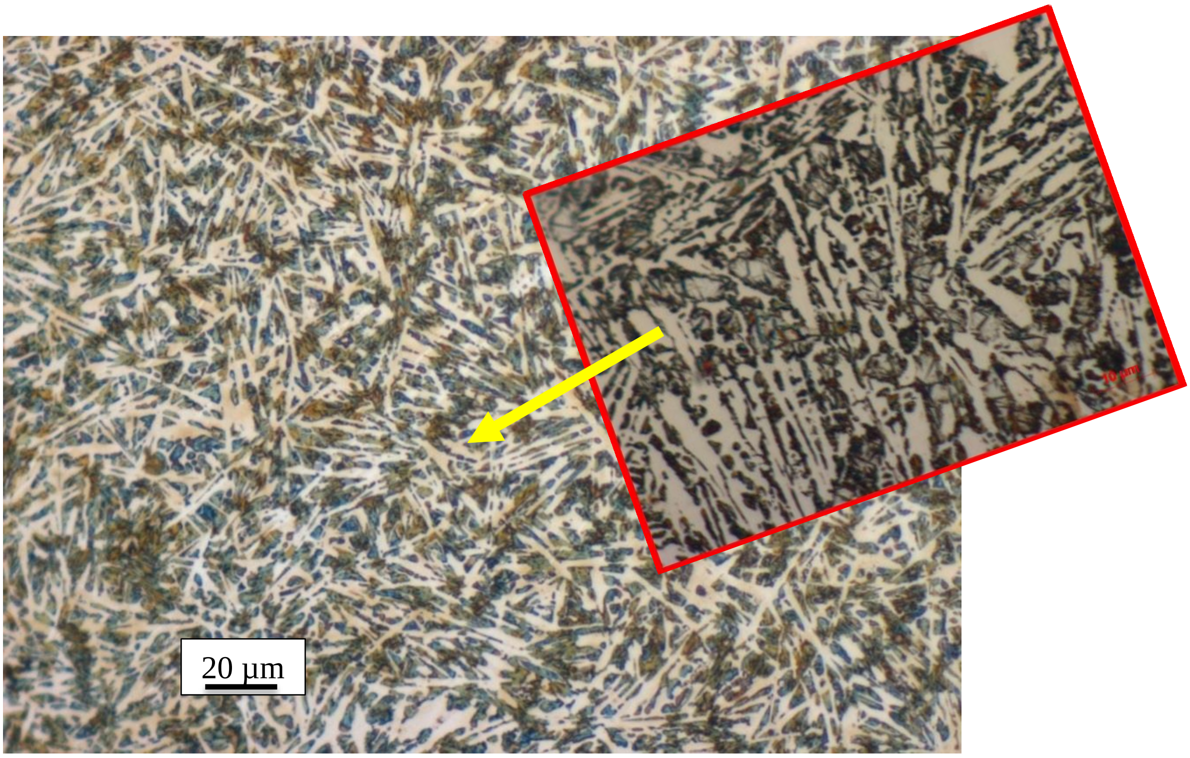

Fig. 5.21: Showing an enlarged light opitcal microstructure of ***fig. 5.20***, shows two fine distinct morphologies of M1 (comprising of a homogeneous phase P1) and M2 (with emergent phases P2 and P3 being more visible in the inserted magified portion). The dendrites are less fragemented when compared to that of ***fig. 5.19***.

5.4.2. Scanning Electron Microscopy observation

High resolution micrographs that are not possible with light optical microscope examination were obtained using scanning electron microscopy (SEM). This was to further scrutinize the identified morphologies at higher resolution. The methodology behind this characterization technique was described in ***section 4.5.2*** and the evolved microstructures are hereby presented. ***Fig. 5.22*** shows the secondary electron (SE) detector micrographs of the same as-cast sample in sequence of magnification to reveal the microstructure clearly. Flake graphite which is a typical characteristic feature of slowly cooled grey cast iron is as revealed at different magnification of this same sample shown in ***fig. 5.22 (a)***, ***(b)*** and ***(c)*** respectively. This same sample was viewed using back scatter detector (BSD) and similar micrographs but with better morphologies contrast was observed as shown in ***fig. 5.23 (a)***, ***(b)*** and ***(c)***. Based on the equivalent carbon measurement, the alloy is a hypoeutectic sample and one thing that is obvious at higher magnification is the distinction of the graphite and the lamellar nature of the matrix as can be clearly seen in ***fig. 5.22(c)*** and ***5.23(c)***. Meanwhile, ***fig. 5.24*** shows the SEM micrograph of crucible residue sample with visible shorter flake and some chunk graphite as compared to the as-cast but yet signifying that the two samples were slowly cooled. At low magnification similar to that of optical microscopic observation, ***fig. 5.25*** reveals dendritic nature of the as-cast with two distinct morphologies M1 and M2 similar to the unetched sample of the as-cast in ***fig. 5.6*** and ***5.11(a)***. Also, ***fig. 5.26*** shows the high resolution micrographs of crucible residue (see ***fig. 5.7***) with similar microstructure morphology to that of the as-cast has shown in ***fig. 5.22*** but with relatively shorter flake and some chuck graphites as well.

However, for the rapidly solidified samples, ***fig. 5.27 (a)*** and ***(b)*** are micrographs of the 850+ µm (a) N_2 and (b) Helium cooled droplets respectively. These particles show slightly different dendritic microstructure from that of as-cast or crucible residue samples shown in ***fig. 5.22(a)*** and ***5.24*** respectively. A closer look at ***fig. 5.27(a)*** and ***(b)***, show that the micrographs also exhibited more of binary morphologies with clear contrast of the single phase dendritic structure M1 (*light section:* dendrites) and M2 (the dark matrix section: interdendritic). For M1, it is obvious that it is a single phase with dendritic morphology just as seen in the as-cast in ***fig. 5.25***; while the M2 is the matrix (at slightly higher magnification). However, as the particle size reduces to say

300 µm as shown in ***fig. 5.28***, the dendrites % volume fraction reduces as a result of higher cooling rate which is a function of the thermal conductivity of the cooling medium. This tread was the observed in all the droplet samples cooled in either media as shown in Table 5.6. Hence, whether cooled in N_2 or He, one common thing to all the micrographs is that they all reveals contrast morphologies, one of which is considered to be an homogeneous dendritic phase and the other is made up of at least two (or more metastable) phases with various degree of fragmentation even though the elemental composition (see ***fig. 5.29***) remain the same in the droplets. Although there seems to be some resemblance in the morphologies of the similar droplet size cooled in the two media, yet the microstructure obtained will definitely be different and this will be more obvious with evolving lath-like or plate-like metastable phase in the microstructures of these droplets. For instance, ***Fig. 5.30 (a & b)*** show micrographs of the 150 µm droplet cooled in the two media. These give a mid-point view between the big and small droplets. A closer look at this micrographs show clear distinction as the combined effect of cooling rate and sub-division partitioning becoming evident. The micrographs are indeed different from the two extreme end micrographs of 850 and 53 µm droplets cooled respectively in same two media. Therefore, it is obvious that the thermal conductivity of a cooling medium along with other inherent factors (such as volume of back-filled gas) influenced the evolved microstructures for a particular droplet size even at the same magnification. So, the smaller the droplets, the more resolution needed to clearly reveal the morphology of such particle. Therefore, with further decrease in size of the particles such as shown in ***fig. 5.31*** for 53 µm size droplet, the microstructure become distinct from the bigger ones. In the case of ***fig. 5.32(b)***, it show much more resemblance to martensitic microstructure as expected due to higher cooling rate experienced. Details of microstructures for each droplet size in each medium are presented in ***Appendix C***. This gives the more honest reason for confirmation of the evolved identified phases using TEM to confirm the phases in the observed microstructures.

In addition to the revealed microstructures, the elemental composition obtained using an in-built dispersive X-ray analyser (EDX) that goes with the LEMAS Evo scanning electron microscope as shown in ***fig. 5.29*** which serves as a guide to a more accurate composition analysis externally obtained as shown previously in ***Table 5.1***. However, to confirm the microsegregation distribution of the constituent elements in the samples, EDX point spectrum (insert in ***fig. 5.29***) and smart mapping for as-cast (***fig.***

5.35) and a typical droplet (***fig. 5.33***) were carried out on a randomly chosen interest sites as shown. The consistency of the results in the case of the as-cast and all the droplet samples, validate the quality of the composition analysis. The localisation of elements in the as-cast can be seen to have been redistributed more uniformly after drop-tube processing as seen in the ***fig. 5.33***; although some of the element quantity are very small. The approximate carbon equivalent (CE) of these specimens is 3.70.

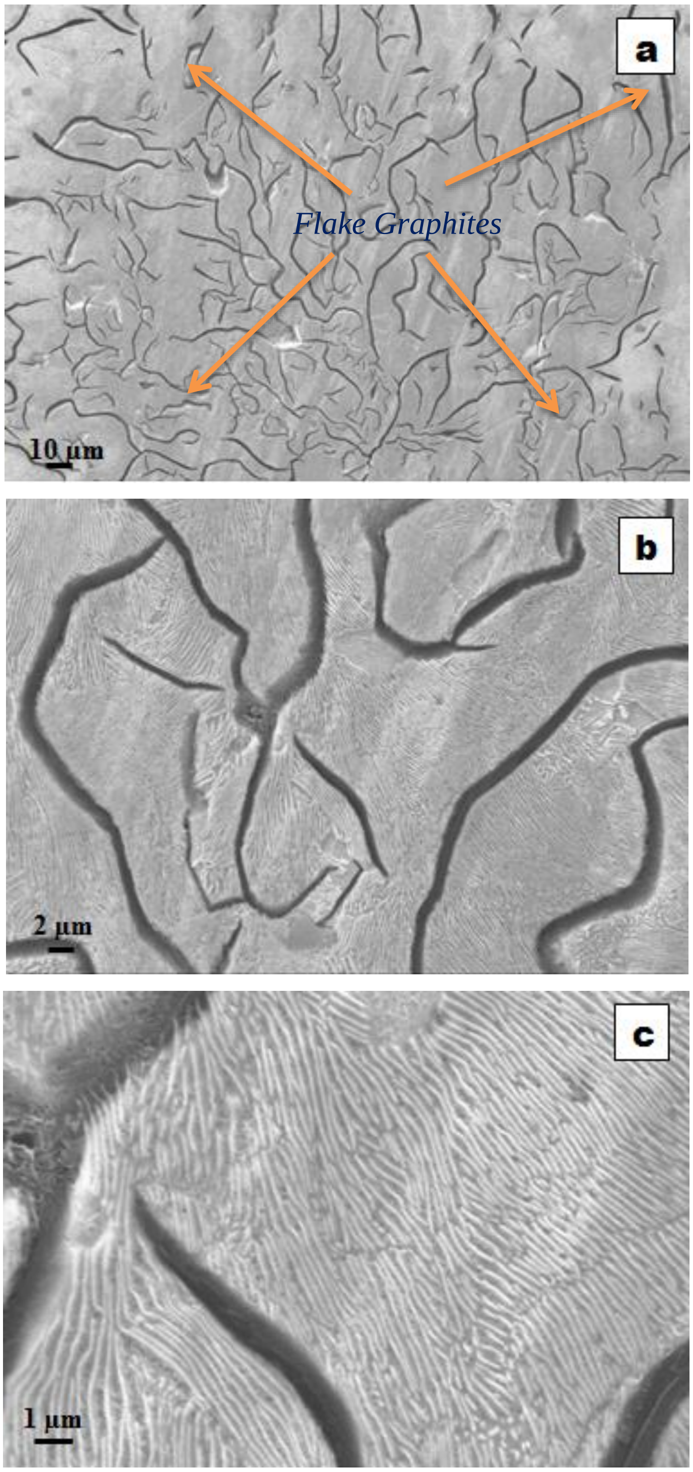

Fig. 5.22: SEM micrographs of as-cast sample revealing randomly distributed flake graphite in the hypoeutectic ferrite microstructure using secondary electron detector.

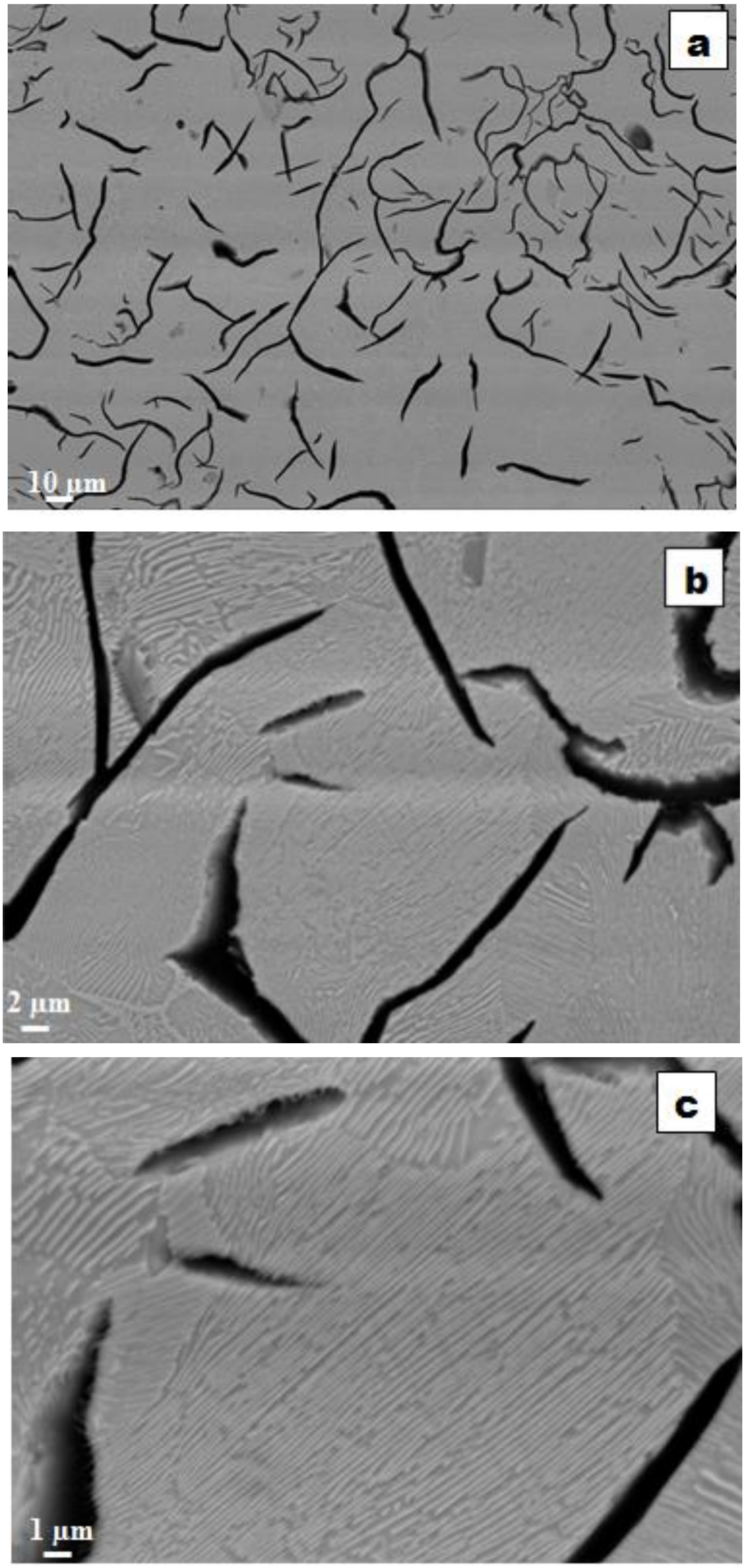

Fig. 5.23: SEM-Back Scatter Detector mode micrographs of as-cast sample with better morphologies contrast as compared to Secondary Electron detector microgrphs in ***fig. 5.22***.

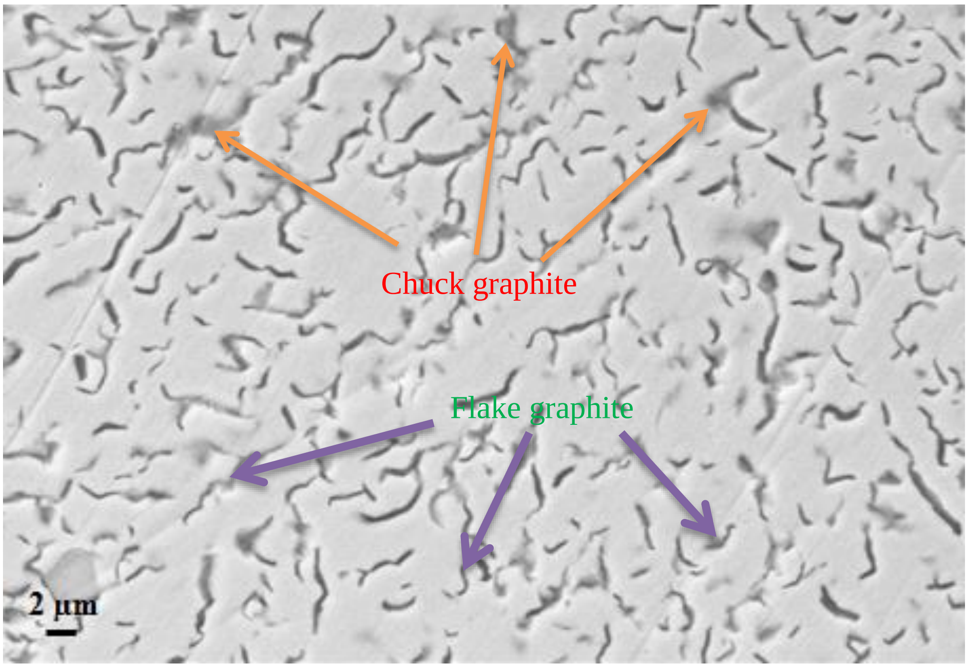

Fig. 5.24: SEM micrograph of crucible resdue sample with flake and some chuck graphites.

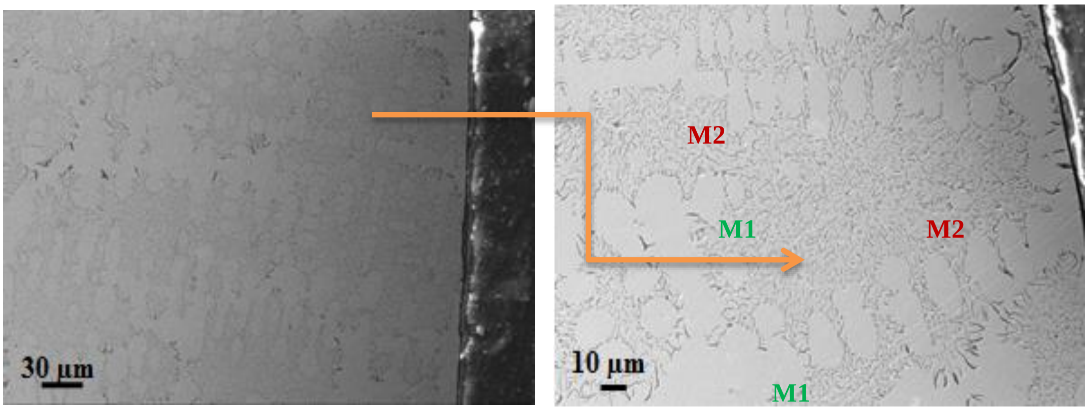

Fig. 5.25: Hypoeutectic as-cast sample with dendritc flake graphite type D at sample's edge.

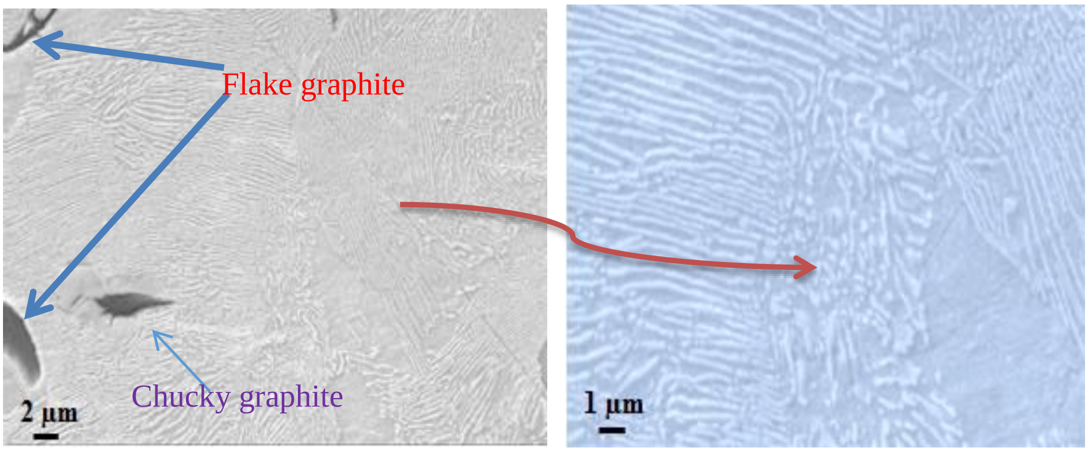

Fig. 5.26: Lamella structure of pearlite matrix in the as-cast sample microstructure.

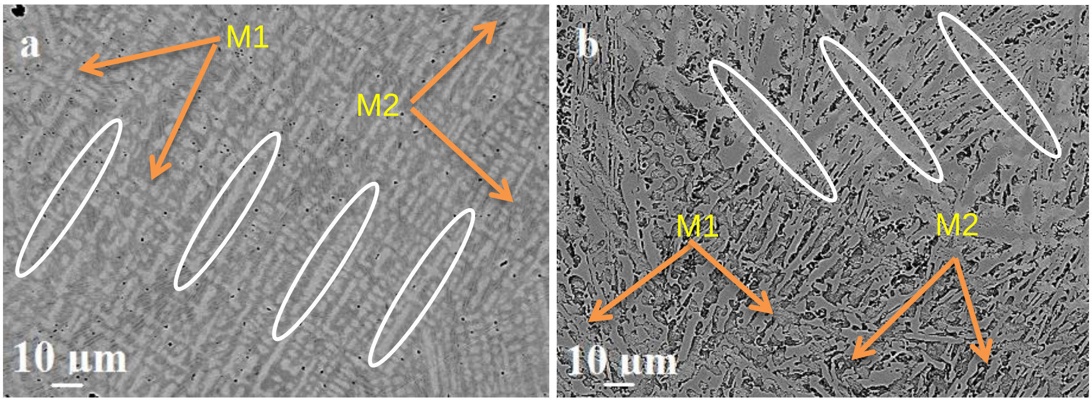

Fig. 5.27: Shows the morphology of 850 µm droplet cooled in (a) N_2 and (b) in He (with area of particular fragementation highlighted within the ellipses as indicated). The micrographs in BSE mode give better contrast, hence it reveals 2 distinct morphologies comprising M1 and M2. The morphologies reveals presences of at least 2 different phases. These droplets have the least or modest cooling rate in the 2 medium; hence, they are distinct from the as-cast microstructure as shown in fig. 5.22 – 5.26 above.

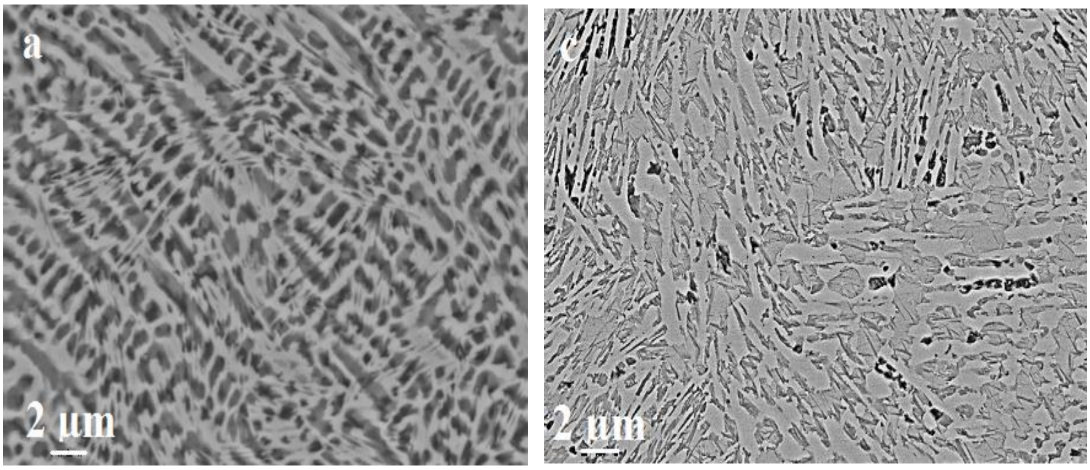

Fig. 5.28: Show morphologies of the ‘big size’ droplets representative, i.e. the 300 µm cooled separately in the two media; (a) is the N_2 cooled, while (b) is He cooled.

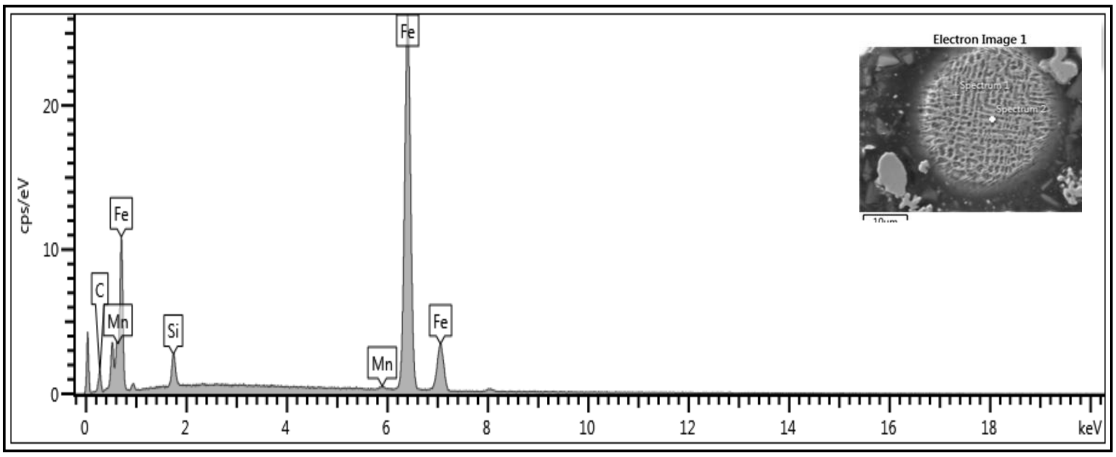

Fig. 5.29: Typical spectra of Gray cast iron droplet as observed using SEM/EDX.

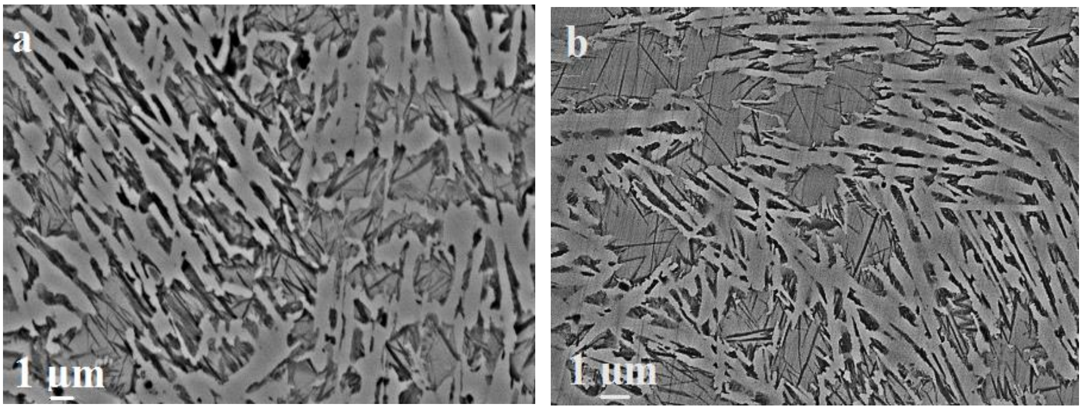

Fig. 5.30: Mircographs of 'medium size' droplet respresentative i.e. the 150 µm droplet cooled in (a) N_2 and (b) Helium. The microstructures reveal distinctive morphologies comprising of fragmented dendrite/lath embbeded in the matrix of another phase.

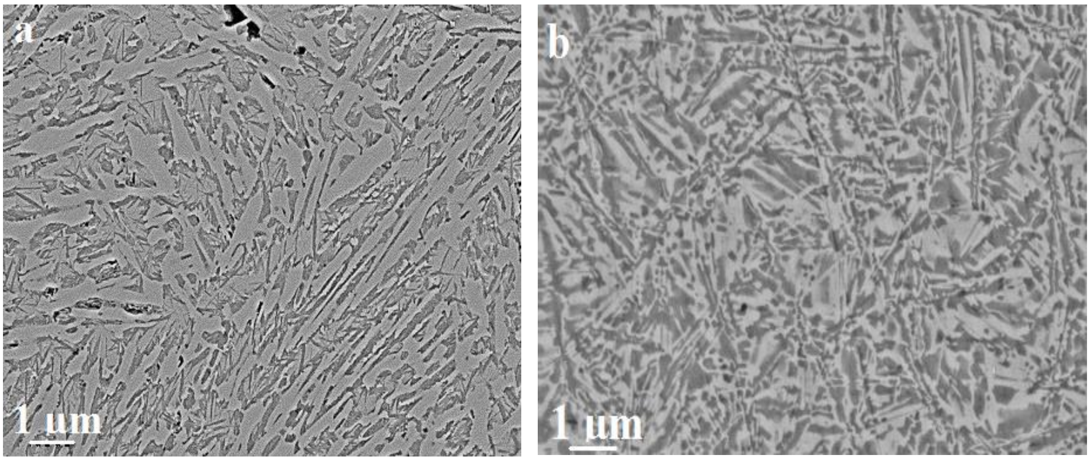

Fig. 5.31: Microgphs of evolved morphologies of 53 µm droplet denoting the 'small size' samples. Carl Zeiss EVO-SEM in BSD mode is used here to provide better contrast of the emergening microstructure which can be compare to previous sample sizes though at much higher resolution with much less fragemented evolved plates or laths as identified by XRD indexing; (a) N_2 cooled and (b) He cooled.

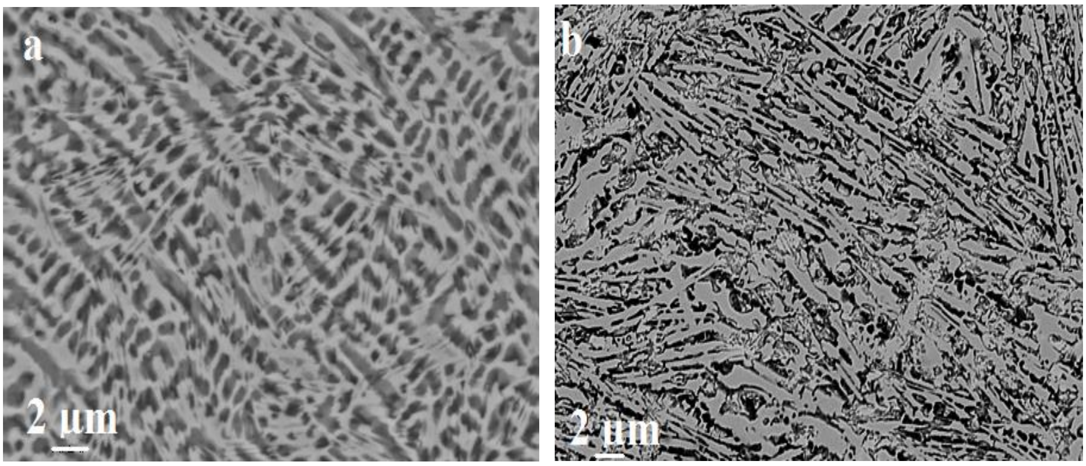

Fig. 5.32: Cooling rate and undercooling influence on the morphologies of particles with similar rate of cooling; (a) 300 µm N_2 cooled and (b) 850 µm He cooled droplets

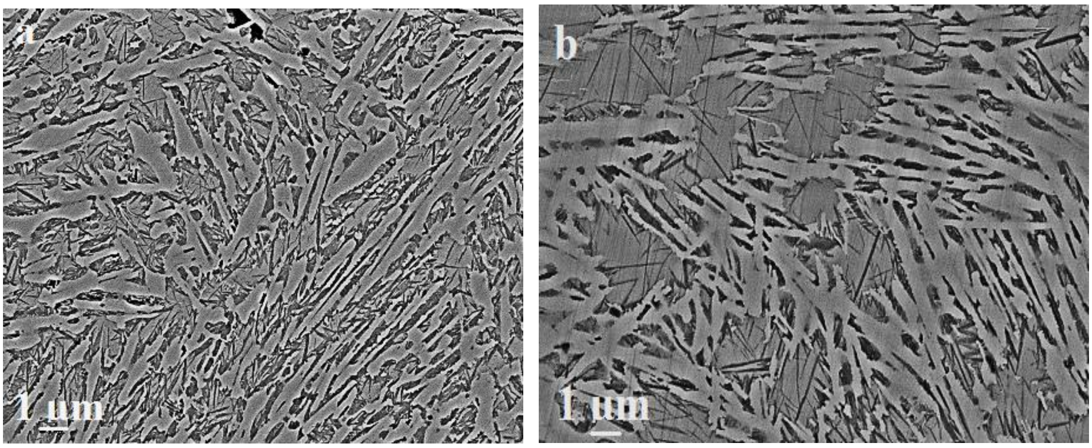

Fig. 5.33: Showing morphological resemblance between (a) 53 µm N_2 cooled and (b) 150 µm He cooled droplets having similar cooling rate but different undercooling due to size difference.

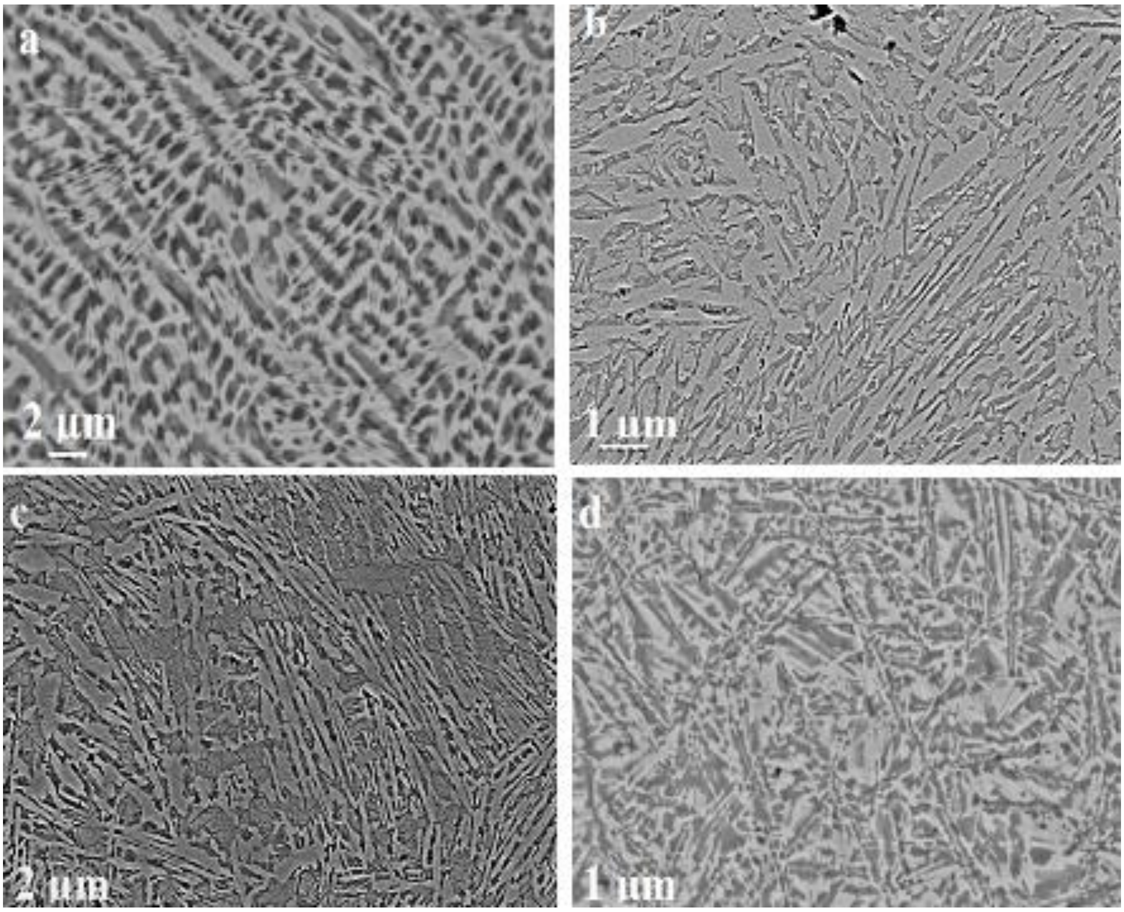

Fig. 5.34: Micrographs of (a) 300 µm N_2 cooled, (b) 53 µm N_2 cooled, (c) 300 µm He cooled and (d) 53 µm He cooled droplets showing the effect of similar cooling rate in the two media.

5.4.3: Quantitative metallography

The microstructural observations show that the as-cast material is graphitic – pearlitic in nature while the droplets progressively exhibited γ-Fe to metastable (combined varying mixture of Fe_3C and α'-Fe) phases. Besides revealing the random distribution of the graphite flakes, fig. 5.35 shows the concentration of the minor elements found in this control sample. However, as a result of rapid solidification effect, even the droplet with moderst cooling rate has no elemental segregation or graphite flakes as found in the as-received sample. This shows that the excess carbon (which appear in form of graphite flakes in the as-received sample) is now in solid-solution within the droplets and it is evident as shown in fig. 5.36 that there is perfect distribution of all the alloying elements.

Meanwhile, the quantitative analysis result of the dendritic and the inter-dendritic phase fraction was measured using imageJ analysis software for each droplet sample size in order to show how this is affected by the cooling rate i.e. the particle size reduction. The results were obtained on the basis of measurements performed on SEM images and an average of 10 measurement were taken per each droplet size. Fig. 5.37 shows the stages of the micrographs and the procedure of measurement. With this method applied, the relative error of the volume fraction evaluation of phases and structural components in each droplet size did not exceed 5 %. Hence, the average area fractions values as measured for each droplet sample sizes are as listed in Table CC. From this, the area fractions of the γ-Fe phase decreases with increasing cooling rate while that of the metastable acicular ferrite (α′-Fe) was proportionally increasing.

Table 5.6: Area fraction of dendrite and interdendritic phases measured by imageJ.

Area Volume Fraction, A % (N_2 cooled samples)									
Sample, µm	850	500	300	212	150	106	75	53	38
Dendritic, %	89.4	78.6	64.7	56.9	51.2	48.5	45.1	36.5	26.8
Interdendritic, %	10.6	21.4	35.3	43.1	48.8	51.5	54.9	63.5	73.2

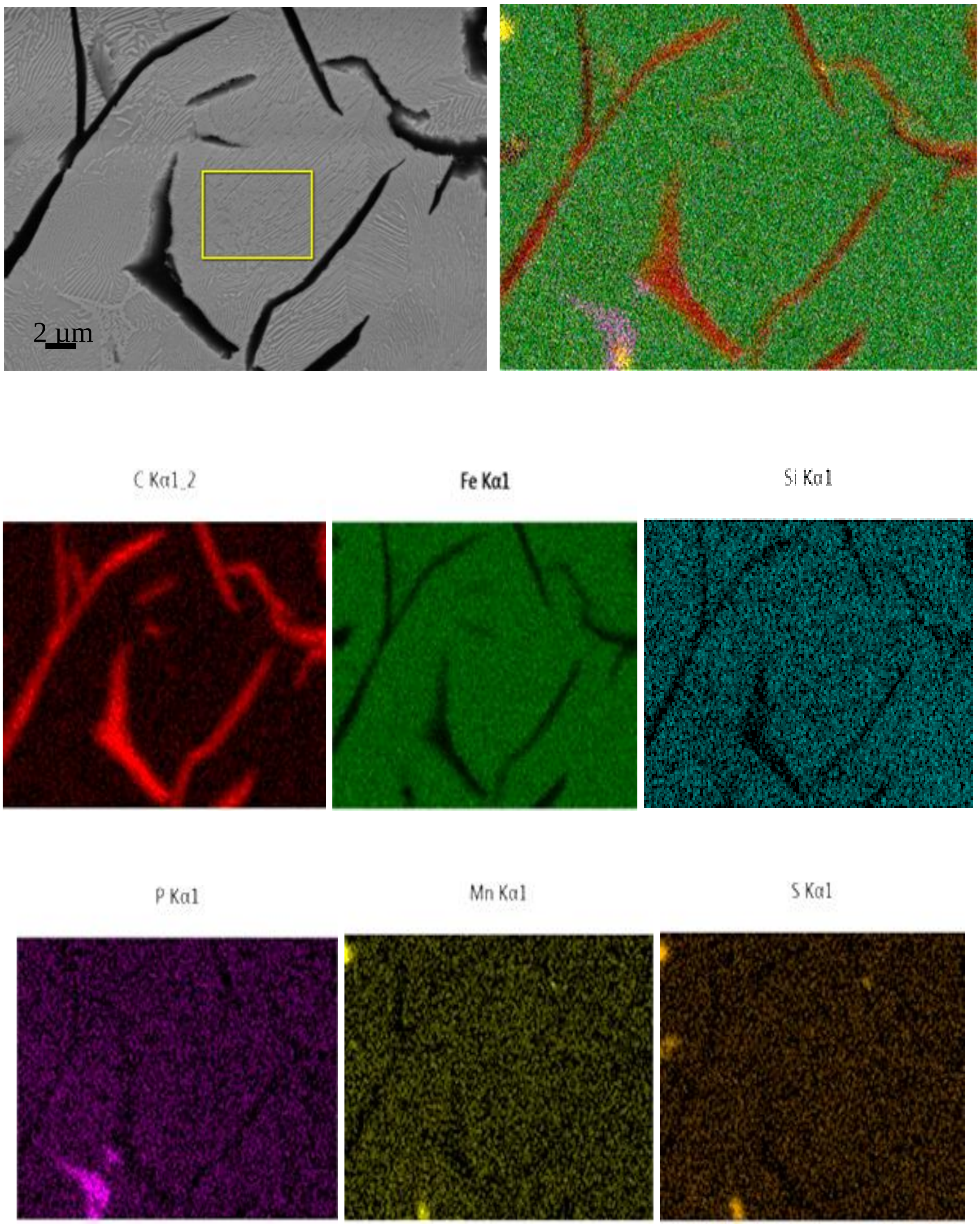

Fig. 5.35: SEM-EDX smart mapping microsegregation of elemental composition of as-cast sample. This shows the localised distribution of the elemental composition in the as-cast sample especially with the minor alloying elements such as P, Mn and S as can be seen in the microphgraphs. The constitutent elements are point-segragated before drop tube processing.

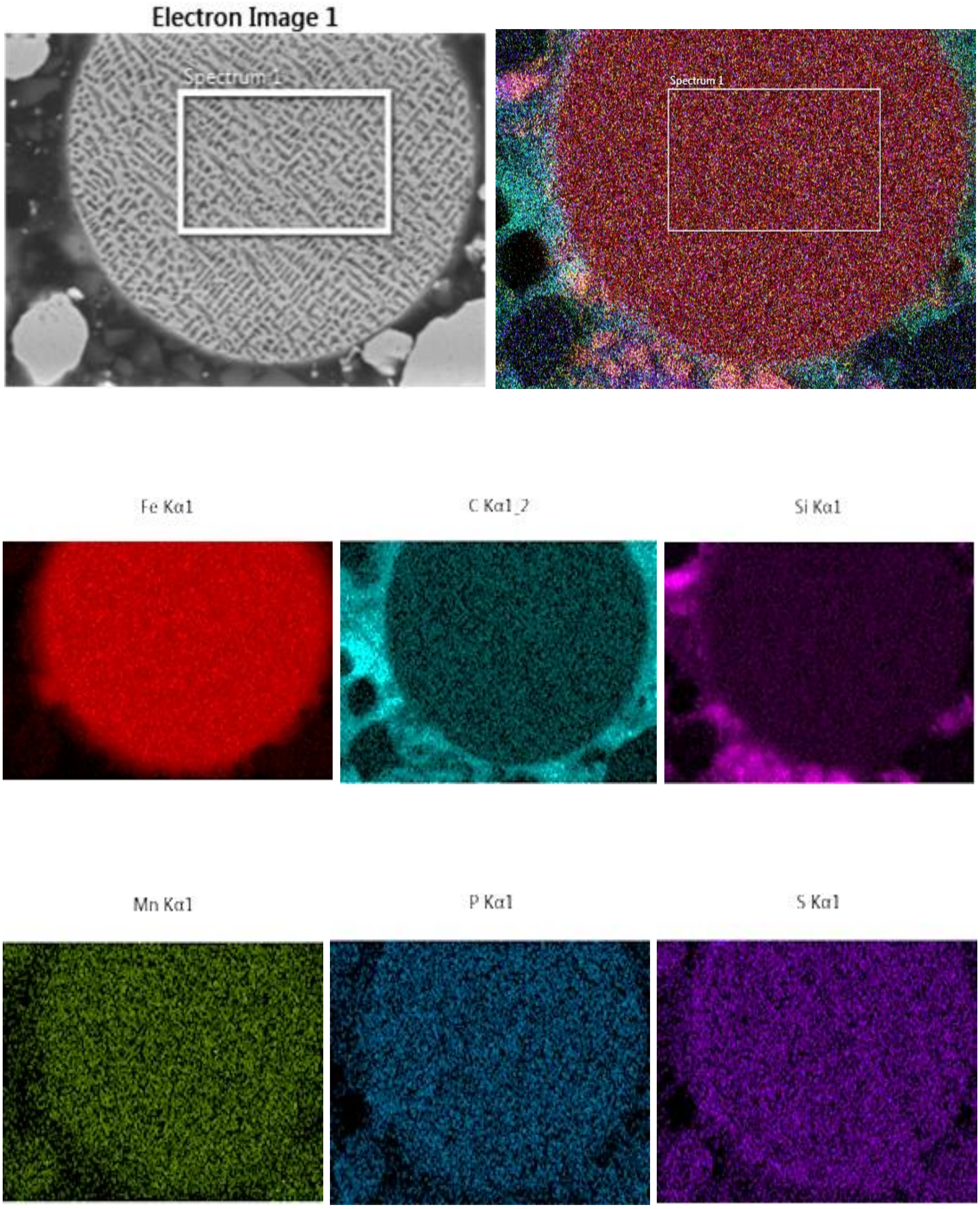

Fig. 5.36: SEM-EDX smart mapping of elemental composition of 850+ µm droplet sample. When compared to ***fig. 5.35***, of the as-cast sample, it can easily be seen that the distribution of the minor alloying elements are more even (i.e. no microsegregation) and well dispersed as a result of uniform redistribution (refinement of the segregation pattern) due to rapid solidification processing which was the case in all the droplets. Also there is better refined grain size with reduction in particle size or increase in cooling rate.

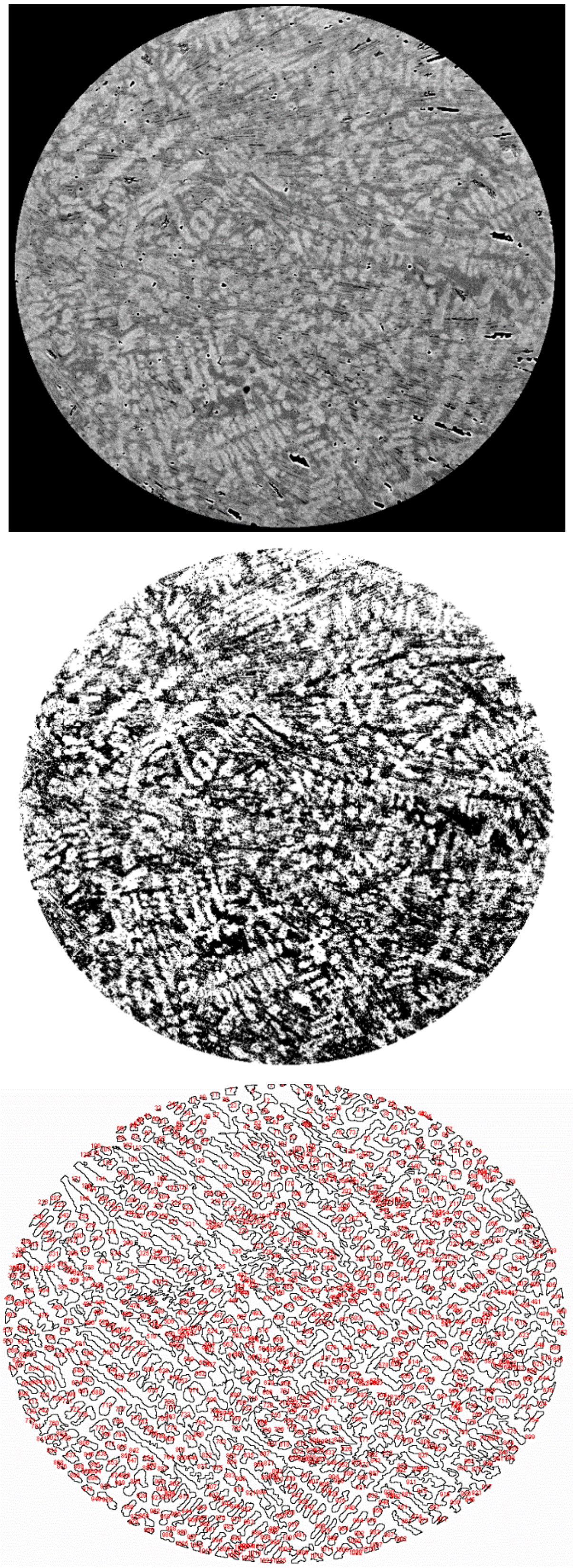

Fig. 5.37: Showing estimated phase volume fraction in each particle size. It reveals good contrast between the primary dendrites and the eutectic matrix, hence giving the ratio of the dendrites fragmentation with reduction in particle sizes. (a) uploading of the image; (b) binarisation of the chosen phase in the image and (c) measurement of the detected surface.

5.5. Confirmation of Metastable Phase.

5.5.1 Results from DTA analysis

The as-cast and all the droplets samples cooled in either of the medium were subjected to DTA double loop analysis as described in ***section 4.5.5***, to observe or monitor any metastable phase using heating/cooling rate initially set at 10 K min^{-1}. The result traces plotted for each droplet size look very much the same, irrespective of the cooling medium. Hence, to avoid repetition, emphasis is on the analysed DTA results mainly for some selected droplets size representatives, namely 500 µm for the big (850, 500, 300 µm) sizes; the 150 µm for the medium (212, 150, 106 µm) and the 53 µm droplet for the small (75, 53, 38 µm) particles sizes in each medium. Meanwhile, considering the alloy's melting point, the heating/cooling temperature range was initially set at 50 ^{o}C for start and 1450 ^{o}C finish for the double loop (re-run) for all the samples including the as-cast material. However, the challenge observed was that in the course of the 1st heating/cooling loop for as-cast sample using this initial temperature range of 50 ^{o}C for start and 1450 ^{o}C finish, the graphite flakes (C) were noticed to have diffused outward as shown in ***fig. 5.38(a)***; making the 2nd loop starting material ***fig. 5.38(b)***; entirely different from the 1st loop (i.e. the initial as-cast) material. To avoid this, the stop temperature for the as-cast sample only was re-set to much lower temperature of 1050 ^{o}C, hence the starting materials for the 1st loop (***fig. 5.39***) and that of 2nd loop (***fig. 5.40***) are quite similar and good repeatability for the two loop was ensured as observed. The plotted results traces show all the droplets in the two media exhibited similar exothermal and endothermal peaks for the double loop irrespective of the cooling (N_2 or He) medium (detail is as outlined in ***Appendix D*** for some selected droplet sizes). However, there is an exothermic peak in the 1st heating traces of each droplet size cooled in each media which is obviously absent from that of the control sample, i.e. the as-cast sample as shown in ***fig. 5.41(a)***. Actually, ***fig. 5.41*** (a) and (b) show the 1st and 2nd heating traces of relatively big, medium and small samples (i.e. 53, 150, 500 µm droplets) along with that of the as-cast sample within the same temperature range (50-1050 ^{o}C) and similar result was obtained irrespective of the cooling medium. Hence, ***fig. 5.41(a)*** displayed an exothermic reaction at ~ 485 ^{o}C in the 1st heating run for each droplet sample, which is absent in 1st and 2nd heating traces of the control sample as well as in the repeated 2nd heating traces of the droplets. This clearly shows an unrepeatable (metastable) phase transformation about this temperature in the droplets. To further, scrutinise the tempered metastable reaction noticed in the N_2 and He cooled droplets in details; slower but longer scan at heating/cooling rate of 5 K min^{-1} (which took ~20 Hours) were conducted on equal mass of the He cooled big (500 µm) and small (53 µm) size droplets respectively from 50 - 1450 ^{o}C as this temperature range is suitable for the droplets. The result of the 1st and 2nd heating traces of the slow scan for the 53 and 500 µm samples are as shown in ***fig. 5.42*** with some identified temperatures peaks. Relating these with observed transformations in Fe-C/Fe_3C phase diagram in ***fig. 3.20***; gives an understanding of the various phases evolved, the temperature at which they occurred and the composition at such temperature. With this understanding, a summary of the different range of solidification and solid state phase transformations that occurred during the full thermal characterization of the droplets is as outlined in ***table 5.7***. It gives information on possible event, observed temperature and likely reactions which reflect the different phase evolution of the drop-tube particles. Hence, the onset for the noticed exothermic peak (metastable phase) occurred at ~ 460 ^{o}C as shown in the enlarged ***fig. 5.42***.

Table 5.7: Significant reactions and temperatures as compared to phase diagram basic ranges

Observed Tempt (^{o}C)	Event	Suspected Reaction	Phase trans. Tempt (^{o}C)
460	$\alpha' + Fe_3C$	Martensitic Transformation	0 – 550
715	α + Fe3C	Eutectoid Transformation	0 – 723
798	$\gamma + Fe_3C$	Eutectic Transformation	723 – 1163
1150			
≥1200	L	Peritectic Transformation	1163 – 1325

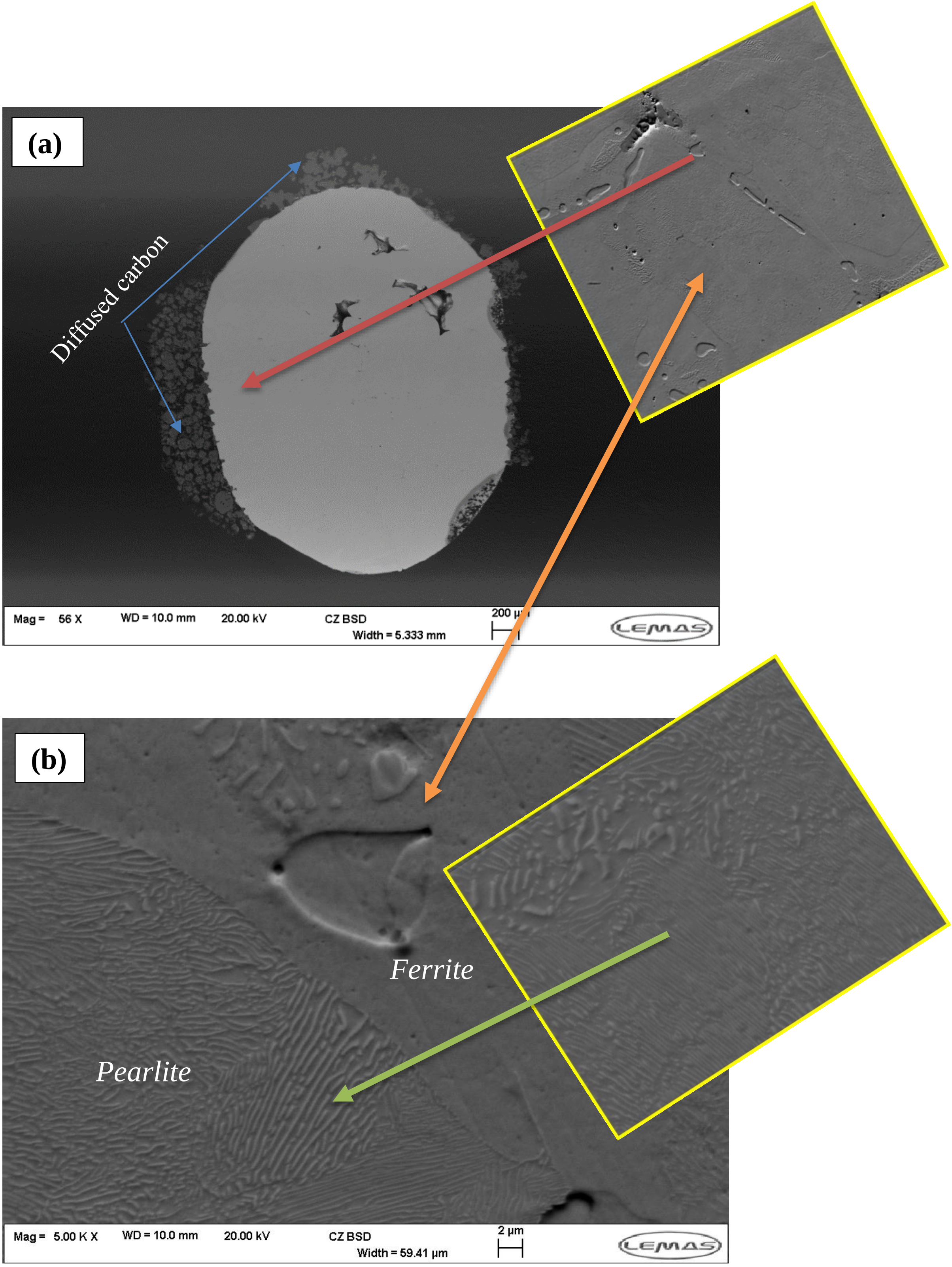

Fig. 5.38: SEM micrograph of (a) 50 – 1450 °C after 1st loop sample showing diffused carbon, making the 2nd loop starting material (morphology as inserted) to be completely different from that of initial as-cast material; (b) Enlarged microstructure of the after DTA 1st run sample confirming absence of graphite flakes which have diffused outward leaving ferrite and pearlite in irrespective of the cooling medium, i.e. similar features obtained either in N_2 or Helium gas.

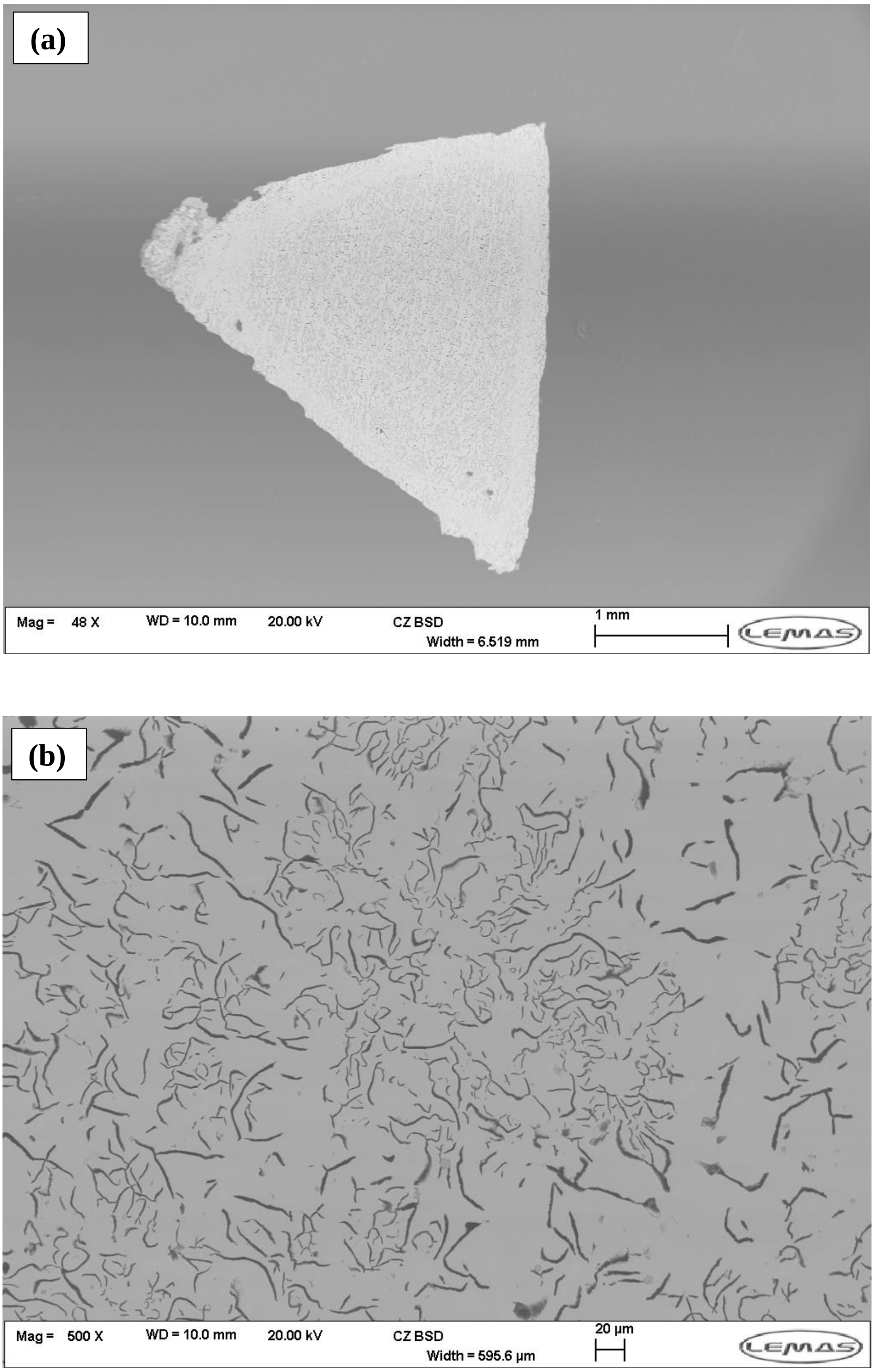

Fig. 5.39: (a) DTA of the as-cast (initial starting material) with visible randomly distributed graphite flakes; (b) Magnified microstructure of (a) above with clear contrast, showing the graphite flakes in ferrite (α-Fe) matrix.

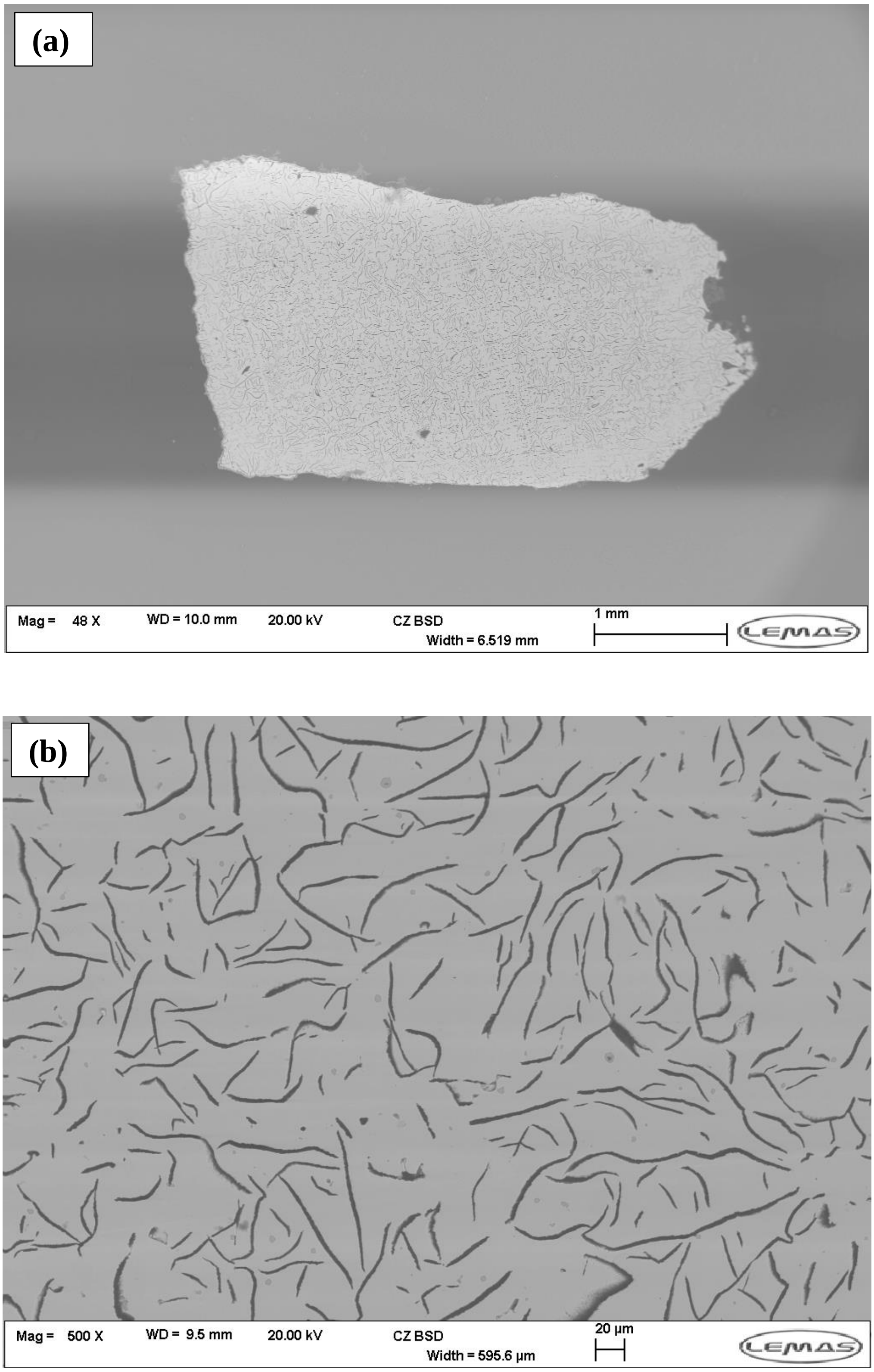

Fig. 5.40: Shows the starting material for the 2nd loop (the re-run) after 1st loop completion (i.e. 1st heating and cooling circle within 50 – 1050 °C). This was done to ensure that the randomly distributed graphite was retained to be sure that the 2nd loop starting materials is quiet similar to that of the 1st (i.e. initial starting material); although some chuck graphite were noticed as a result of slow cooling in the furnace.

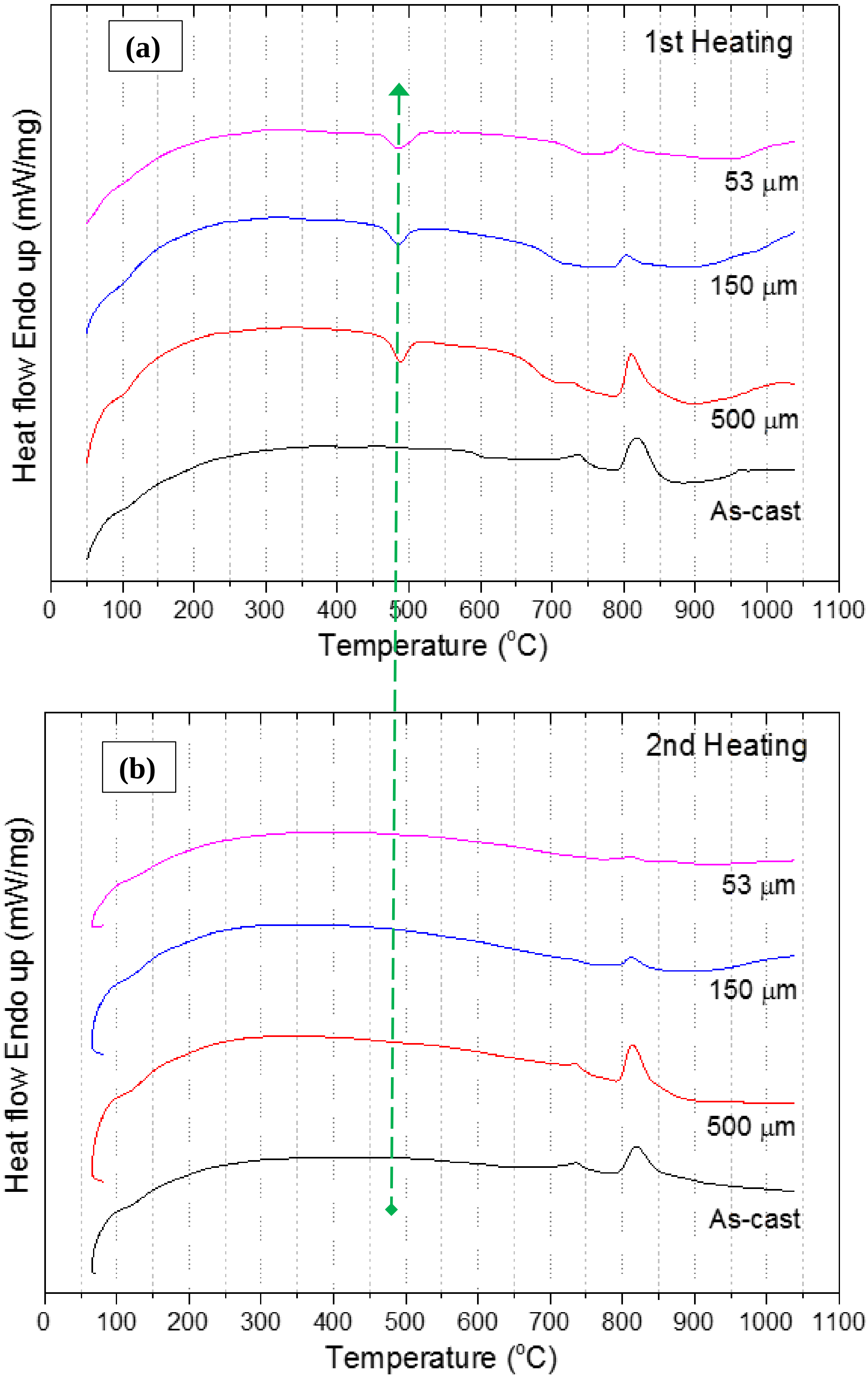

Fig. 5.41: DTA peaks profile of selected He-cooled droplets as compared to the as-cast sample. (a) 1st and (b) 2nd heating analysis. The green arrow shows metastable phase(s) presence as confirmed in the 2nd run graph in fig. 5.41 [b]; the reason for double loop heating and cooling to present difference in the thermal history as shown.

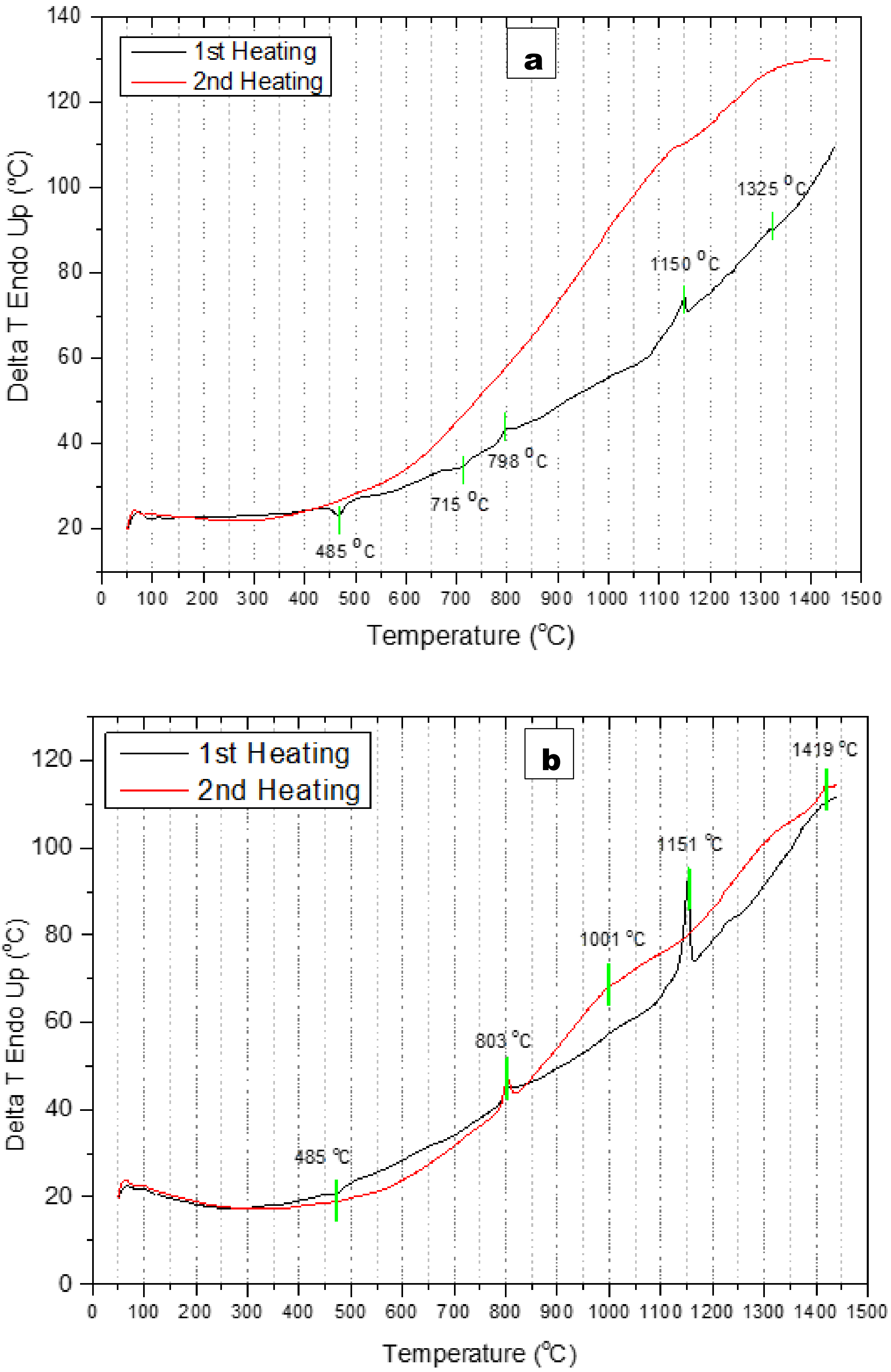

Fig. 5.42: DTA traces of the 1st and 2nd Heating runs of He cooled (a) 53 micron and (b) 500 micron sample with heating rate at 5 Kmin^{-1}. There is a pronounced exothermic peak on set at ~ 465 to °C in the first heating run which disappeared in the repeated (2nd) heating run.

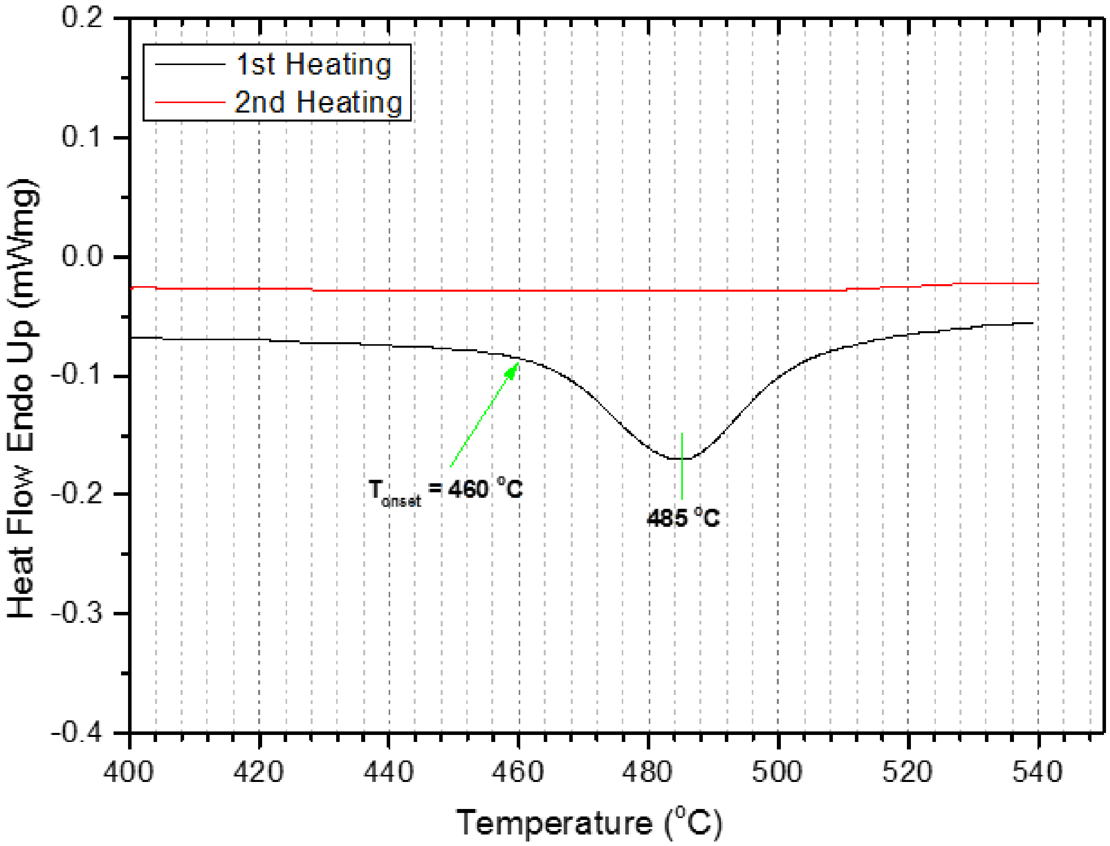

Fig. 5.43: Shows short-range slower scan over and above the noticed metastable phase in the 1st run of the droplet samples which was absent in the 2nd run. The scan rate used was 5 °C/mins and the onset temperature for this metastable phase transformation was noticed around 460 °C.

5.5.2. TEM analysis results

The transmission electron microscopy (TEM) technique used in the cause of this study was described in **section 4.5.4**. Results from this characterization technique further confirmed the x-ray diffracton identified phases in the rapidly solidified droplets with respect to increasing cooling rate. The indexing results from some selected specimens, confirmed the presence of single crystalline phase as well as the metastable polycrystalline phases in the N_2 and He cooled specimens. Again, emphasis is on very distinct selected droplet sizes, i.e. the 500 µm, 150 µm and 53 µm droplets. Hence, ***Fig. 5.43*** to ***5.51*** show series of DTA/SEM/TEM bright field micrographs and SAED patterns which reveal consisitent phase mixtures in virtually all the droplet sizes. These results are then related to the analysed XRD diffraction crystallographic data previously obtained (see ***Appendix E***) to ascertain and confirm names of the phases as found appropriate (see ***Appendix F***). Meanwhile, ***Fig. 5.44*** shows the bright field micrographs of relatively big N_2 and He cooled 500 µm droplets. The micrographs clearly show mixture of different regions of homogeneous and heterogenous phases with the former being more in proportion in the two micrographs. Similarly, ***fig. 5.44*** shows same for the 53 µm droplets cooled in the two media as well. The difference noticed here is that, there seems to be more of heterogneous region and mixture in the smaller (53 µm) droplets as compared to the big (500 µm) samples. To further analysis the different regions recognised within the specimens, Selected Area Electron Diffraction (SAED) indexing was carried out on these specimens, again thess are as displayed in ***Appendix E***.

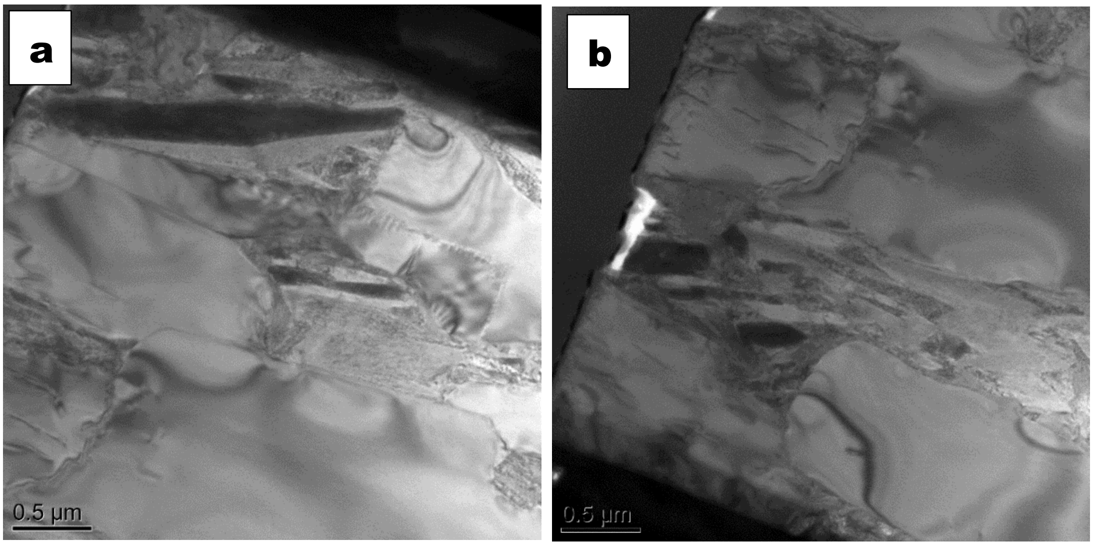

Fig. 5.44: Bright field micrographs of (a) N_2 and (b) He cooled 500 µm droplet with distinct homogeneous and heterogenous (or mixed) phases.

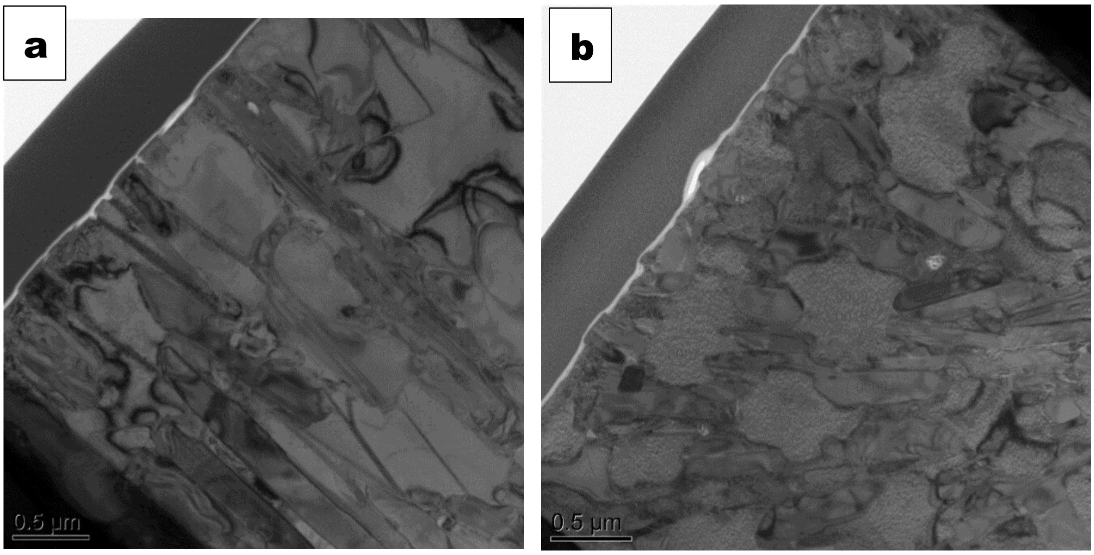

Fig. 5.45: Bright field micrograph of (a) N_2 and (b) He cooled 53 µm droplets with more mixed phase, showing higher proportion of the heterogenous or mixed phase.

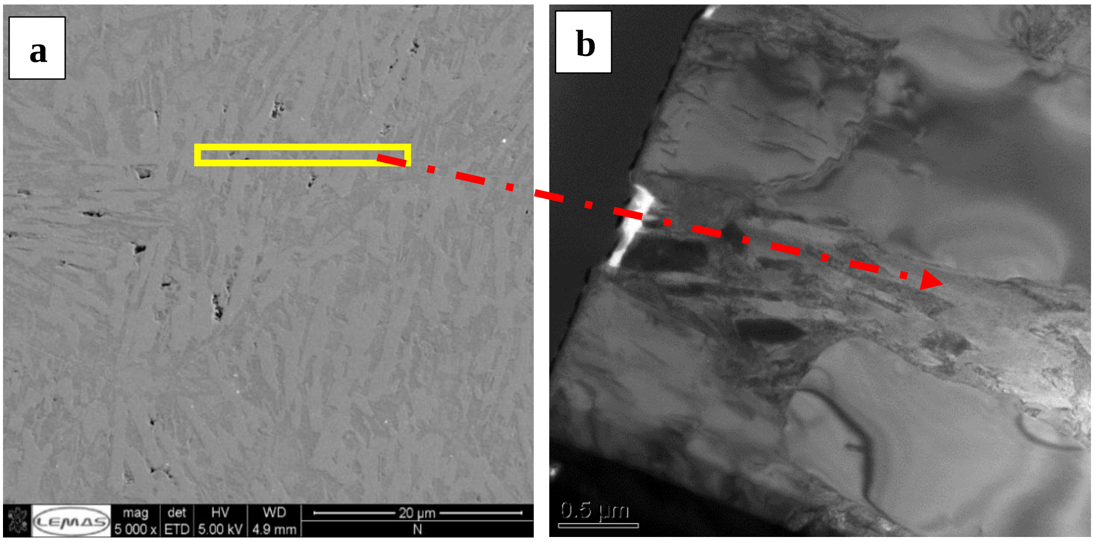

Fig. 5.46: (a) SEM micrograph of He cooled 500 µm droplet showing marked portion from where the SAED for phase analysis is taken from with corresponding TEM bright field image (b), obtained from the yellow marked area; based on the procedure describe in section 4.5.4.

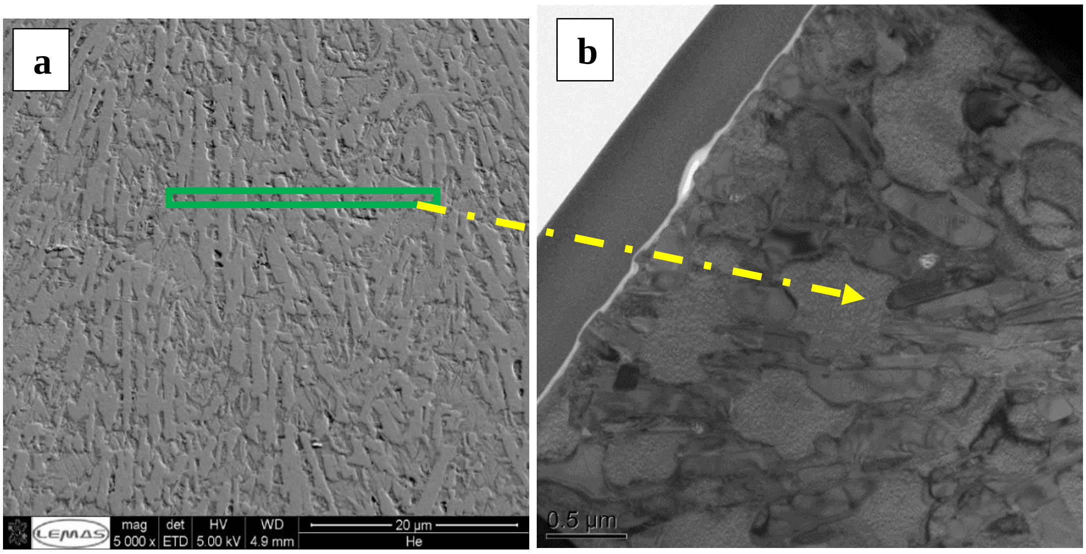

Fig. 5.47: Corresponding SEM micrograph of He cooled 53 µm droplet (a) along with TEM bright field image (b) from the green marked area showing evolved phases as in ***fig. 5.43***.

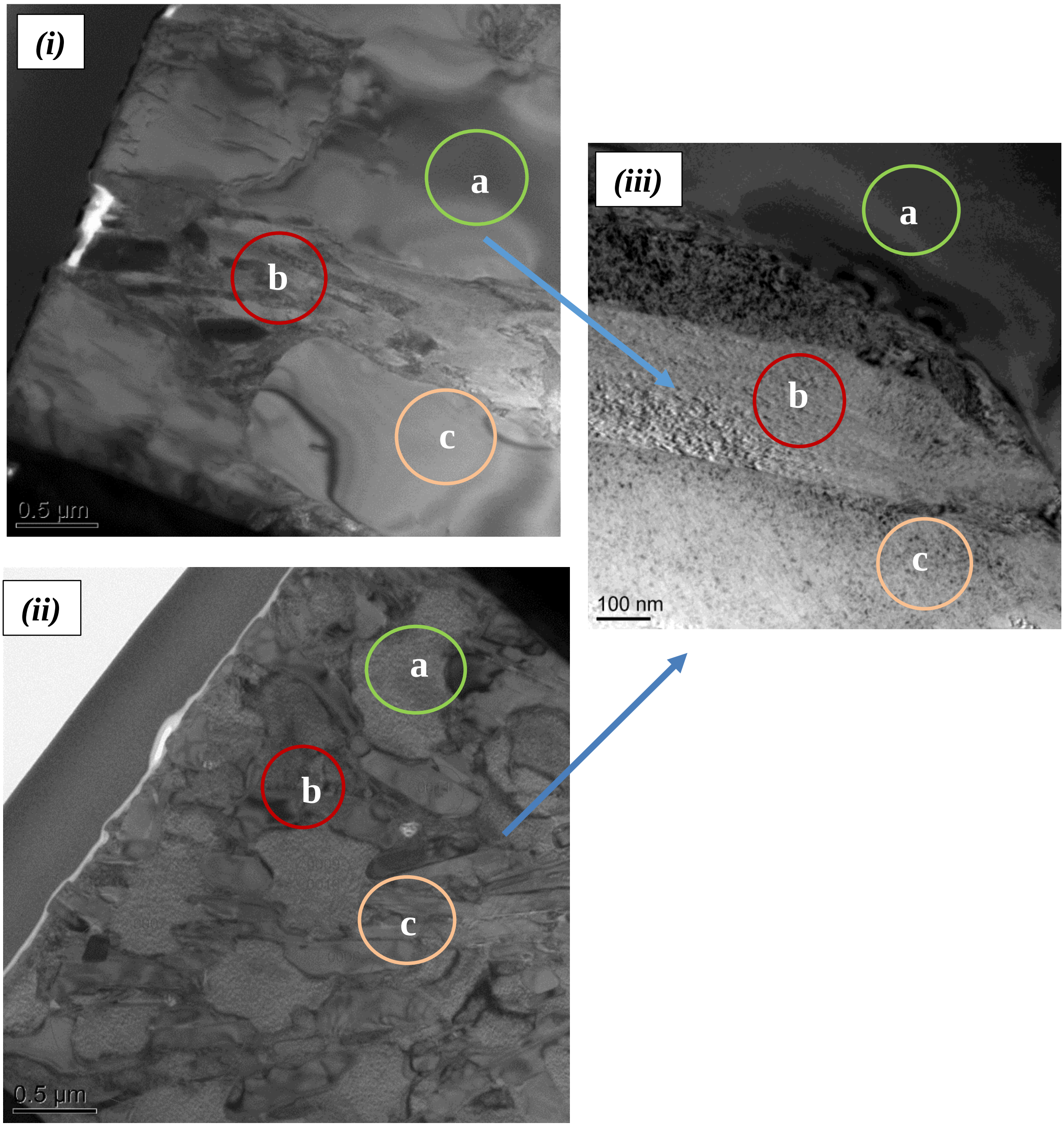

Fig. 5.48: TEM bright field images of Helium cooled (i) 500 µm and (ii) 53 µm droplets with respect to (iii) identified regions of different phases recognised by different SAED patterns as shown in *fig. 5.47* which are in accordance with corresponding XRD peaks as earlier outlined in *fig. 5.5(c)*.

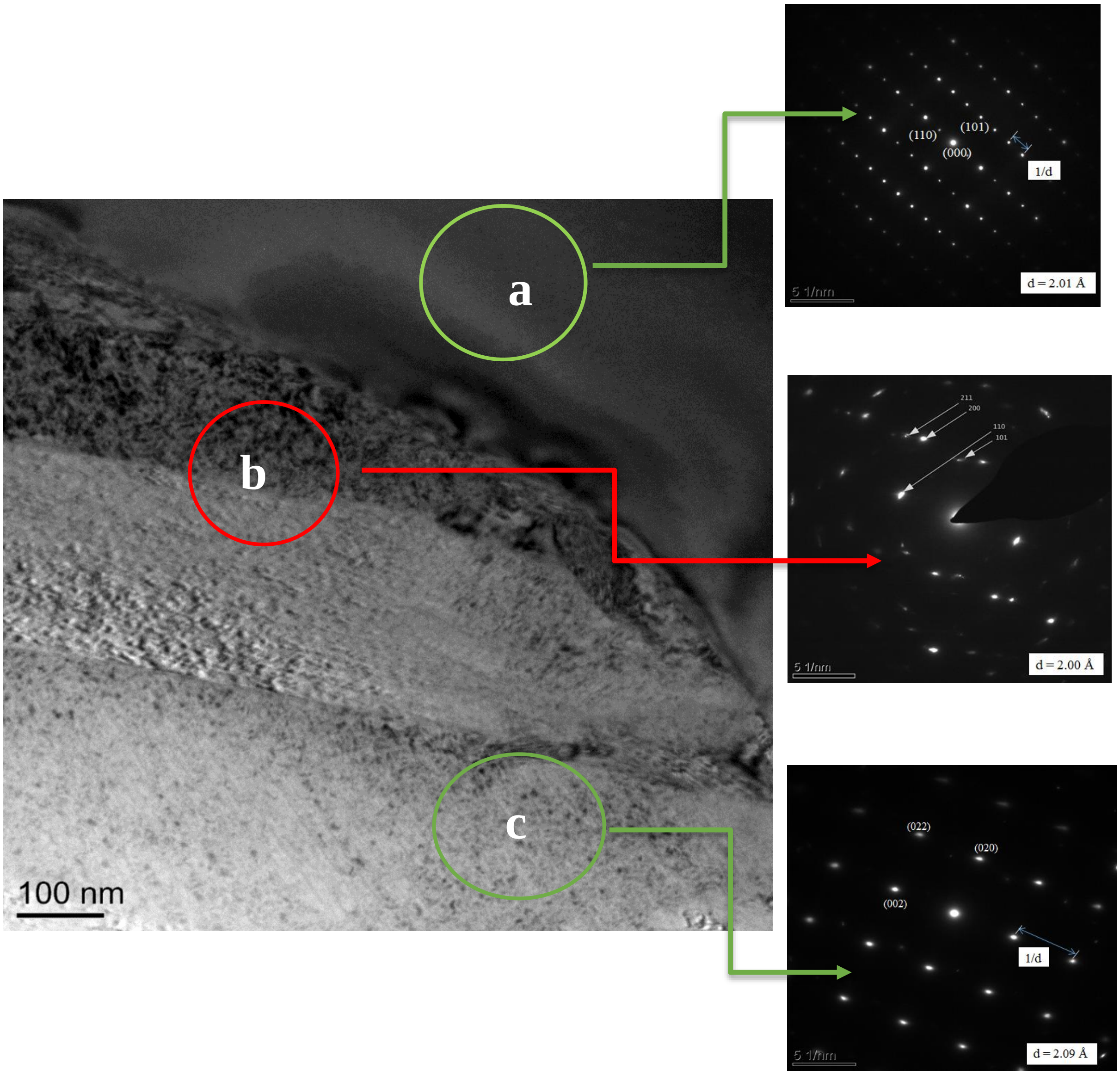

Fig. 5.49: Enlarged bright field images with indentified indexed phases from marked regions in the He cooled 53 µm droplet. The SAED patterns are as identified from each marked section.

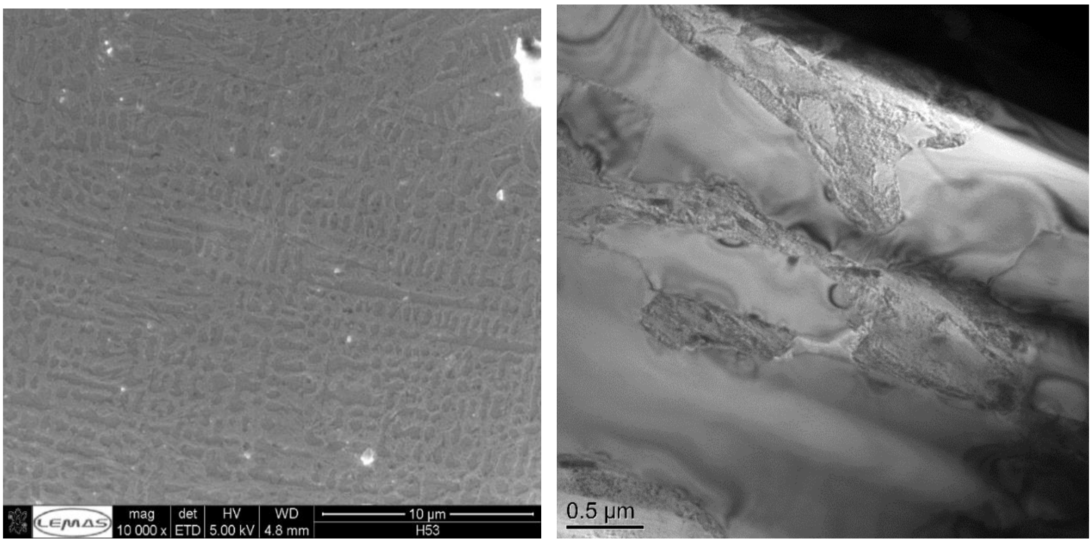

Fig. 5.50: SEM and TEM bright field image from Helium cooled 75 µm droplets, which represent the group with highest cooling rate based on their smaller size and better cooling medium. The observed evolved phases are similar to that obtained from the big and medium size samples, but obviously with more of the metastable phase due to droplet size reduction.

From the enlarged bright field images (of the fig. 5.43) shown in ***fig. 5.51 and 5.52;*** one can clearly see the different regions of the evolved phases which were earlier identified using XRD pattern in section 5.3; but now being indexed using the spot and ring TEM patterns information.

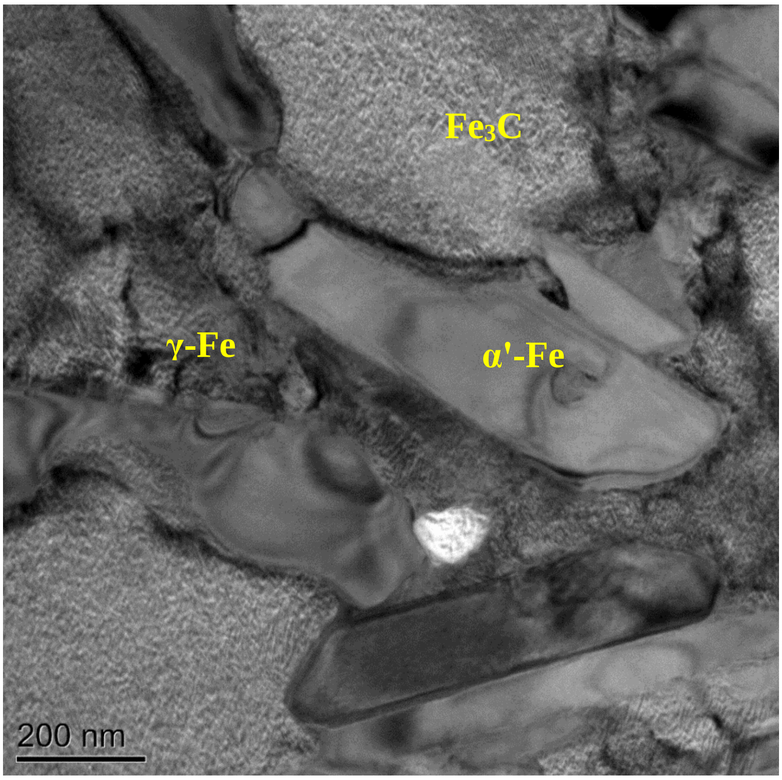

Fig. 5.51: Identified phase regions from a bright field image of a 150 µm droplets

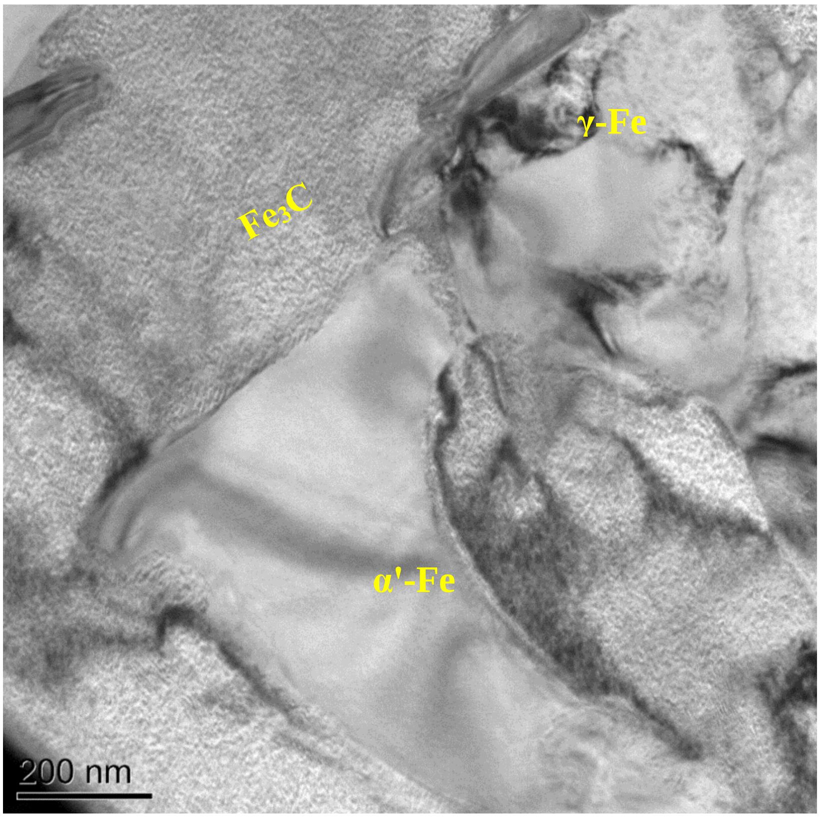

Fig. 5.52: Bright field image of a 53 µm droplets with increased α'-Fe and Fe_3C phases.

5.5.3: Result from liquid nitrogen (cryogenic) treatment

The effect of cryogenic quenching from room temperature on rapidly solidified droplets was more obvious on the big (≥ 500 µm) droplet samples. Probably as a result of relatively higher portion of retained austenite in these droplet sizes. Although there was no or very slight noticeable microstructural changes on the smaller (≤ 53 µm) droplets after the cryogenic treatment, samples cooled in either environment appear apparently alike. Meanwhile, there is obvious evidence of change from the measured microhardness values of all the droplets before and after the treatment. Therefore, the fact remains that processing influences microstructure which eventually impact on the mechanical property of the samples. ***Fig. 5.53*** and ***5.54*** show the microstructures of the N_2–cooled 850 and 53 µm samples before and after the cryogenic treatment respectively. Similar effect was noticed on the He-cooled counterparts, but the effect

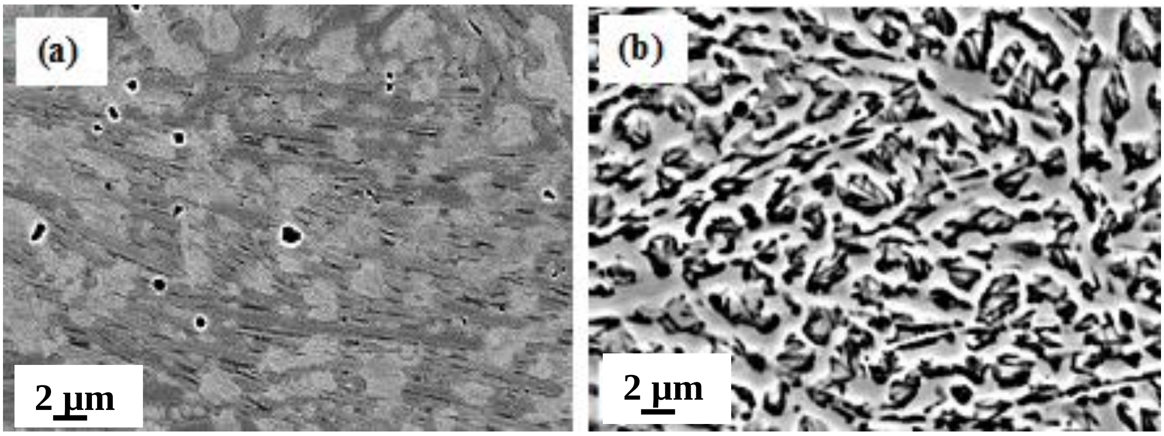

Fig. 5.53: SEM micrographs of 850 µm sample (a) before and (b) after cryogenic quenching. The observed change in the samples morphology after cryogenic treatment was reflected in its mechanical (microhardness) property.

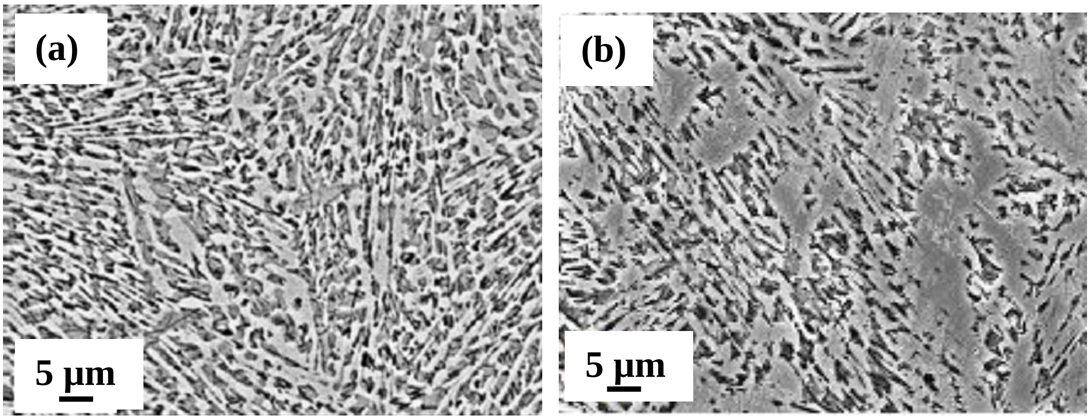

Fig. 5.54: Micrographs of 53 µm N-cooled sample (a) before and (b) after cryogenic quenching. The effect here is not as obvious as it is seen in the 850 µm droplet which also reflected on its x-ray diffraction pattern and measured microhardness values.

of this liquid nitrogen quenching was more pronounced in relatively biggest N_2-cooled droplet because there exist easily noticeable change in the morphology or microstructure of the sample and its obtained XRD patterns as shown in ***fig. 5.55*** before and after the cryogenic quenching treatment. In conclusion, the overall effect of this treatment was manifested not only on the samples' microstructure but also on the mechanical property (microhardness) as later shown in ***fig. 5.59***.

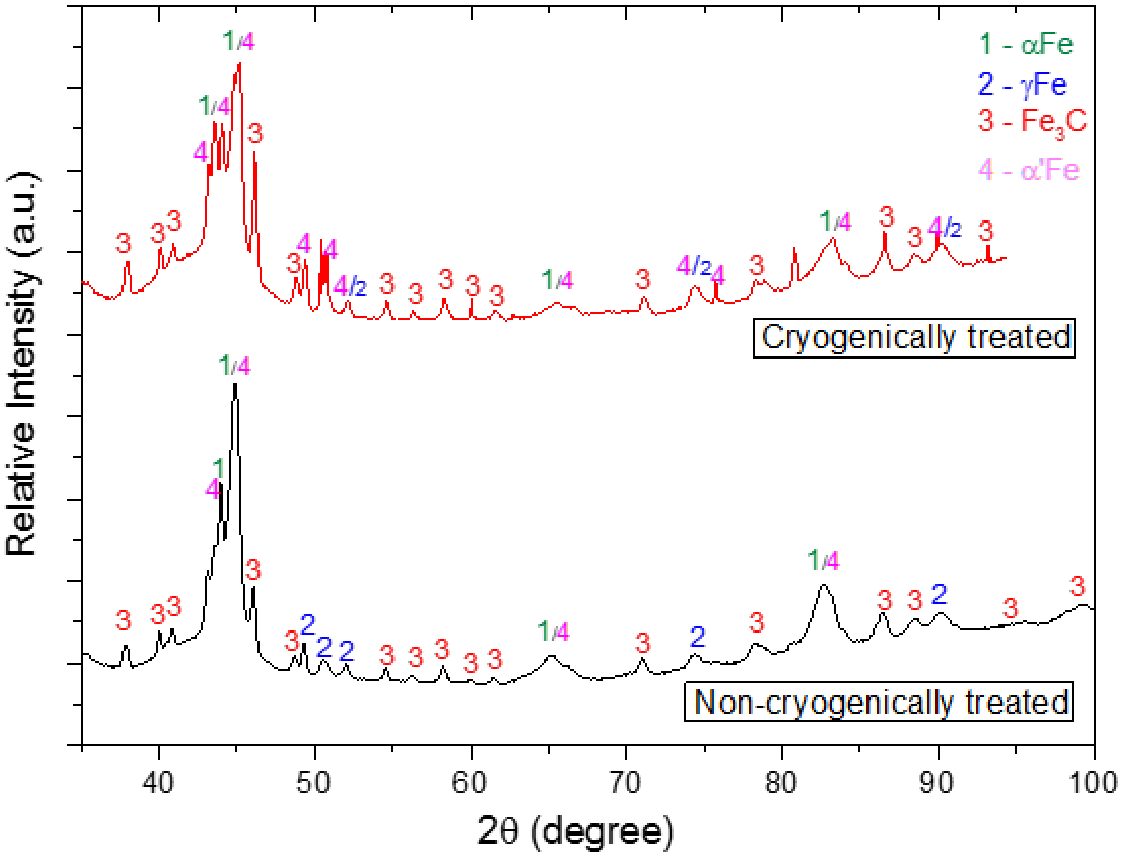

Fig. 5.55: XRD profile of N-cooled 850 µm droplet before and after cryogenic treatment.

5.6. Microhardness measurements results.

In ***fig. 5.1***, a relationship was established between cooling rate and droplets diameters in the two cooling media (N_2 and He gases) used in the course of this study. The graph simply shows an increase in cooling rate as the particle size decreases. This was established from the experimental observation; in which a power factor relates the two variables. It therefore shows the influence of particle's size in determining its cooling rate and consequently its microhardness value with every other factors being equal. ***Fig. 5.56***, shows the SEM micrographs of indented (a) as-cast sample and (b) that of a typical unetched droplet. The measured hardness value of the matrix of the control sample (as-cast) was 362 ± 3 Hv0.05. Conscious effort was made to avoid any indent impinging upon flake graphite sites in the as-cast sample. **Table 5.5** gives hardness values observed in the 2 media, with 704 ± 7 Hv0.05 and 915 ± 6 Hv0.05 as minimum values of 850 µm droplet in N_2 and He respectively; while maximum values were 1260 ± Hv0.05 for N_2 cooled and 1440 ± 4 Hv0.05 for He cooled in the 53 µm droplets. However, considering the 2 media, the thermal conductivity of Helium gas is very much higher than that of Nitrogen gas and as such it is expected that this will reflect in the higher microhardness values obtained in helium cooled samples of the same size relative to its counterpart cooled in Nitrogen as reflected in ***fig. 5.57*** in this case. Meanwhile, ***fig. 5.58*** show plotted graphs of measured Vickers microhardness values against the droplets' calculated cooling rates in the two media. It is obvious from the graph that for cooling rate < 5,000 Ks^{-1}; all the data for the N$_2$-cooled and that of He-cooled droplets aligned on the same curve. Fig. 5.59 show the martensite phase fraction in the two cooling media and this gives a definite characteristic insight into estimated microhardness values displayed in fig. 5.58. However, for cooling rates > 5,000 Ks^{-1}; the data departs from lying on a single curve such that N$_2$-cooled droplets data are now significantly lying above that of He-cooled droplets. So, the calculated hardness values and other results obtained due to effect of cooling rate and possible undercooling effect experienced by the droplets in the 2 media will be used to establish the reason for this observation and threading interdependence of processing – microstructure – property relationship (as shown in fig. 5.4 and 5.5) of this useful commercial engineering alloy in the discussion section. Meanwhile, calculated average values of each droplet measured microhardness is as shown in T***able 5.8*** shows. While ***fig. 5.60*** displays the these values as graphs obtained before and after the cryogenic treatment for each droplet size in the 2 media respectively.

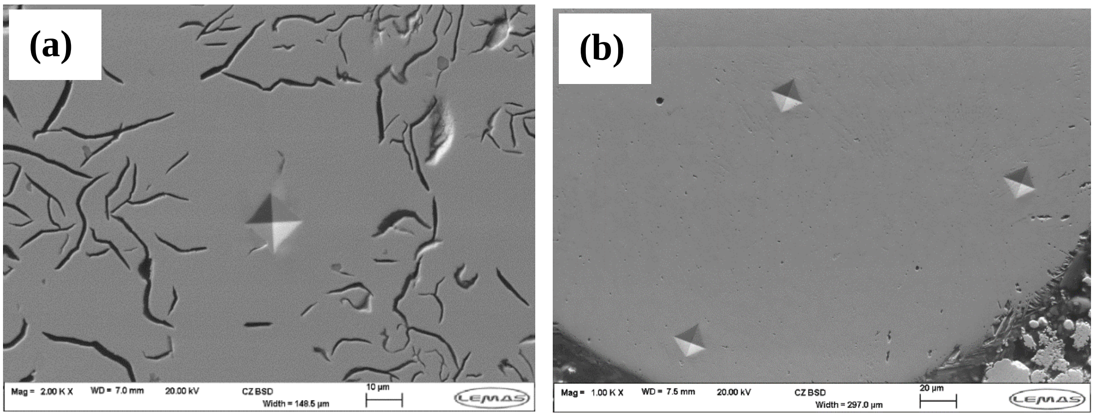

Fig. 5.56: SEM micrographs of indented (a) as-cast and (b) typical droplet samples.

Table 5.8: Calculated averange microhardness values for each droplet sample size cooled in Nitrogen and Helium environment.

D / µm	Hv0.05 (N)	yEr±	Hv0.05 (He)	yEr±
53	1259.5	3.59	1440.3	4.17
75	1121.0	9.09	1272.4	10.12
106	1070.9	7.38	1181.2	8.43
150	1043.8	11.5	1094.3	12.02
212	1010.3	12.34	1051.6	12.34
300	986.5	10.85	1041.8	9.93
500	918.9	8.67	1018.5	10.07
850	709.4	7.65	914.2	8.27

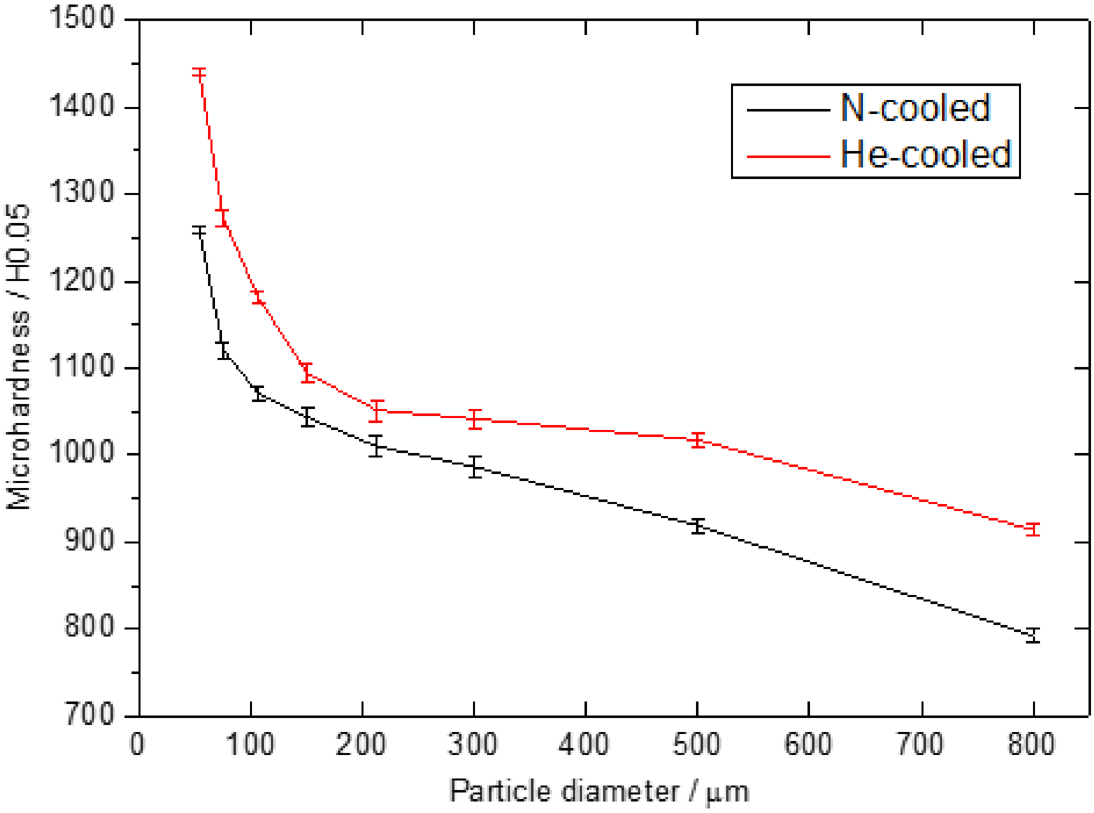

Fig. 5.57: Microhardness values (Hv0.05) as a function of droplet diameters in cooling media

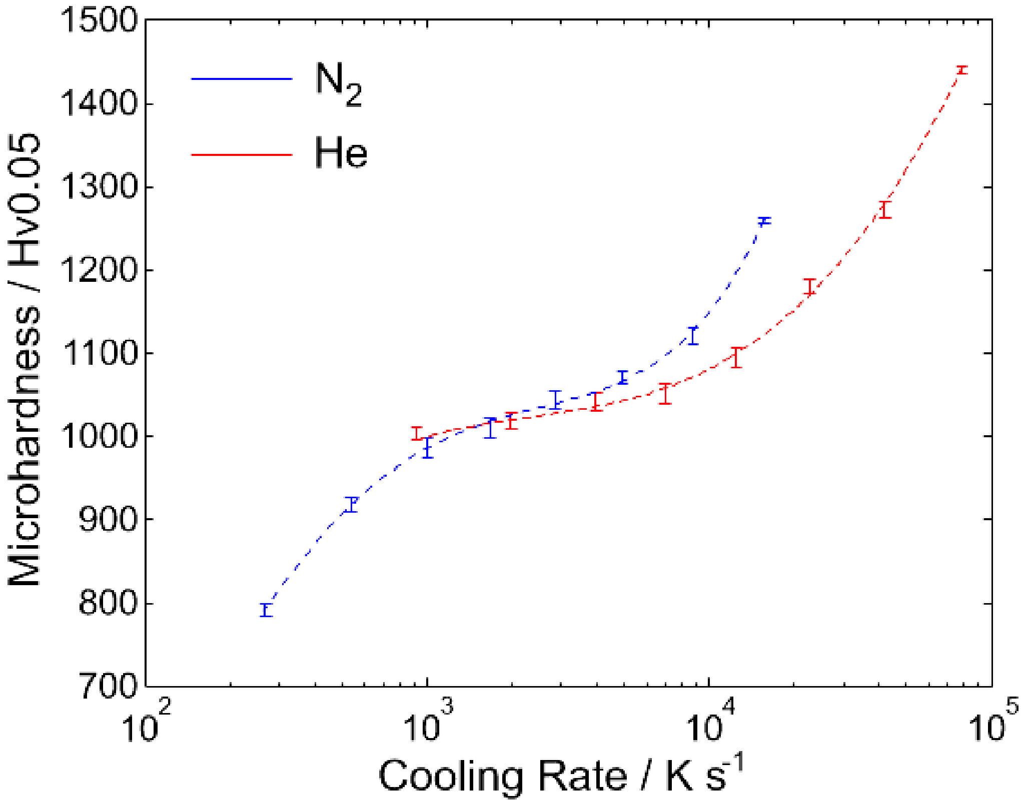

Fig. 5.58: Comparative microhardness (Hv0.05) of the droplets as a function of cooling rate.

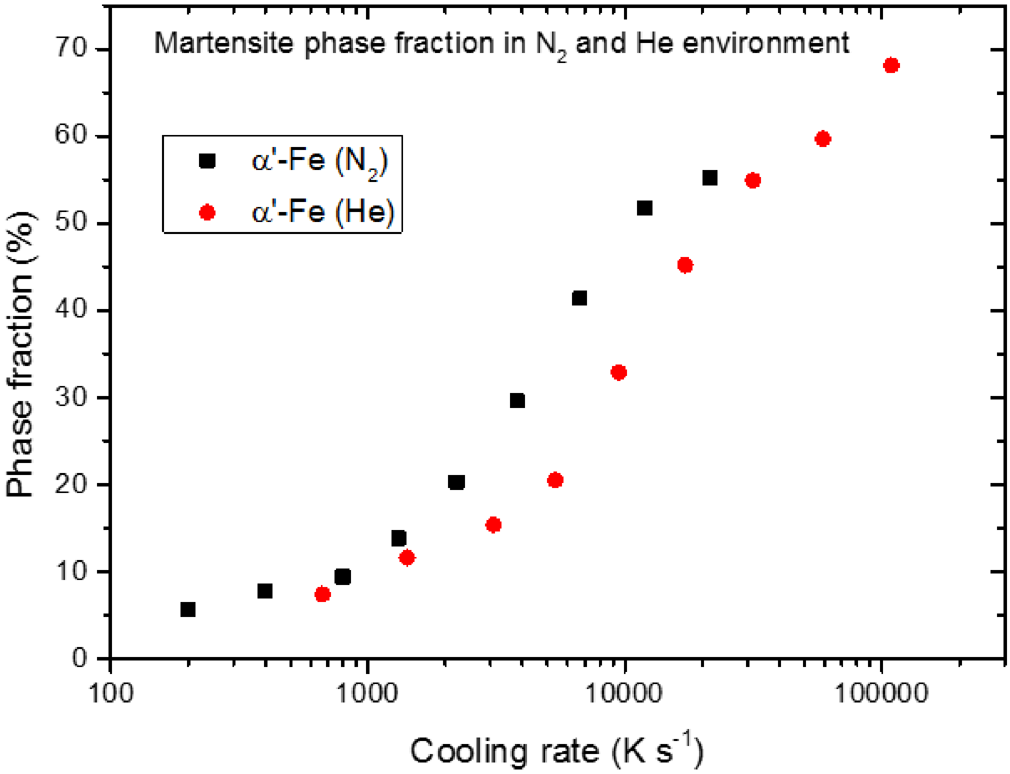

Fig. 5.59: Showing the % phase fraction of the evolved martensite against cooling rate in N_2 and He cooled droplets

Table 5.9: Microhardness values of all N_2 cooled droplets before and after the cryogenic quenching.

D (µm)	**Hv0.05 (N)** *(Before CQ)*	**yEr** ±	**Hv0.05 (H)** *(Before CQ)*	**yEr±**	**Hv0.05 (Nc)** *(After CQ)*	**yEr±**	**Hv0.05 (Nc)** *(After CQ)*	**yEr±**
53	1259.5	3.59	1440.8	4.17	1275.8	4.06	1452.3	5.01
75	1121.0	9.09	1272.4	10.12	1148.4	6.31	1288.6	10.38
106	1070.9	7.38	1181.2	8.43	1079.7	8.74	1196.5	9.41
150	1034.8	11.50	1094.3	12.02	1056.3	6.92	1099.8	11.81
212	1010.3	12.34	1051.6	12.34	1021.8	11.40	1064.1	12.47
300	986.5	10.85	1041.8	9.93	992.6	12.32	1059.3	8.34
500	918.9	8.67	1018.5	10.07	932.9	6.73	1038.4	11.34
850	792.4	7.65	1009.2	8.27	837.7	9.32	1053.8	9.82

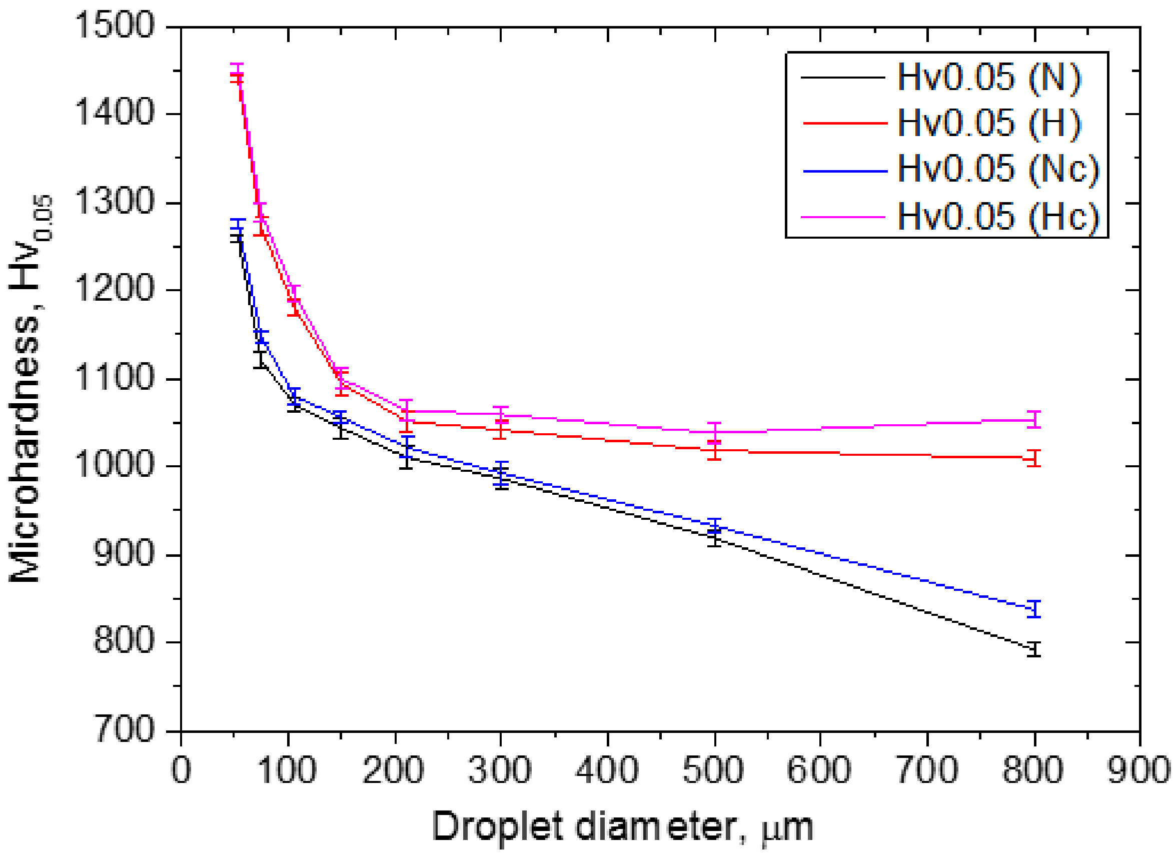

Fig. 5.60: Shows the microhardness values against droplets diameter before and after cryogenic quenching in the 2 media (Nitrogen and Helium) from room temperature.

CHAPTER SIX

DISCUSSION OF RESULTS

6.0. Discussions

This section provides basic scientific explanation on the presented experimental results and how these influenced the process – structure - property interlink that was observed. The emphasis here is on the mechanism of the phase's formation and transformation, along with other fundamental factors that might have influenced the emerged morphological changes and consequent effect on the microhardness of the samples.

6.1: Confirmation of Samples' Morphologies.

One sure outstanding fact that can be pinned down from this studies is the reality of generating new microstructure via a containerless processing without altering the alloys composition. The reverse should also be explored which is the reason I suggest this in the further work. Either way, the simple reason for this remains in the fact that there is interconnectivity between processing route, microstructure and eventually mechanical property of an alloy. Hence, for this research, droplets were produced as desired from the as-received bulk sample as stated in chapter four. Normally, a conventionally cooled grey cast iron will contain considerable graphite flakes randomly distributed in a ferritic–pearlitic matrix [89]. This is expected at equilibrium or near equilibrium as explained under ***section 3.6*** and can be confirm on any typical iron–carbon phase diagram such as presented in ***fig. 3.18*** (except that generally, the Fe-C phase diagrams do not showcase graphite). The estimated cooling rate for the control (i.e. the as-received) sample based on available information is approximately < 10 K s^{-1}. Obviously, the optical micrographs in ***fig. 5.6*** shows the graphitic nature of this starting material; while ***fig. 5.7*** reveals the evolved microstructure of the drop-tube furnace remnant (i.e. the crucible-residue).

The typical cooling rate for the crucible (hence the residue as well) is about 12 K/min. Based on the understanding of Fe – C phase diagram, graphite segregation was as expected with slow cooling. The micrographs are therefore valid and true representation of these samples conditions (as compared to ***fig. 3.15 a and c***) [76, 132]. The graphite flakes observed are not only randomly distributed in ferrite rich pearlite matrix but they also intersect one another severally thereby making it easy for crack propagation in this slowly cooled alloy (***as referred to in fig. 5.22***). This singular feature makes grey cast iron brittle and serves as one outstanding limitation of this conventionally cooled essential engineering material [6.4]. Both the as-cast and drop-tube residue micrographs contain graphite flakes but the distinction is mainly in the morphology, size and shape of the graphite in them (***compare fig. 5.6 with 5.7***). The chunky graphite, noticed in the crucible residue sample are as a result of restrained slow cooling in the furnace as compared to that of the as-cast cooled at ambient temperature. The difference in these samples microstructure is further confirmed in the backscattered mode of SEM micrographs shown in ***fig. 5.23*** for the as-cast and in ***fig. 5.24*** for the crucible residue samples. Again, it should be noted that the samples have homogenous composition and the calculated carbon equivalent (CE) by XRF technique is 3.70 as presented in ***Table 5.1***. This implies that the alloy is hypoeutectic and 2.83 % Si influenced the graphite precipitation to certain extent (compare ***fig. 3.18 a and b***, since eutectic occurs at 4.3 wt.% C) [11]. In addition to this, the XRD patterns obtained {as shown in ***fig. 5.2***} affirms to the fact that the as-cast and the drop-tube crucible residue were cooled slowly enough. Hence, the as-cast as well as the crucible residue in this study are dendritic in nature (***as shown in fig. 5.25***) with randomly distributed graphite flake in the pearlitic rich matrix (***see fig. 5.24***) as noted under primary and eutectic graphite formation in ***section 3.6.1***. The above described series of microstructures attested to the fact that the control sample is indeed typical grey iron. Therefore, the processing of slow cooling gives basic similarity between the as-cast and the drop-tube crucible residue, as both samples can be confirmed to have been cooled slowly based on the graphitic nature of their microstructures. Hence, the presence of graphite in the crucible residue indicates that little or no carbon was lost in the drop-tube furnace. Meanwhile, what happens in drop-tube products is quite different from what was obtained in the as-cast (or crucible residue sample). For instance, the estimated cooling rate for the rapidly solidified samples varies for different droplet sizes as outlined in ***Table 5.3***. Also, the two slowly cooled samples have sufficient time for separation by diffusion while droplets transformed into phases in a diffusionless manner (***as illustrated in the expression 3-6 and 3.7*** under section 3.7.1). Hence, the rate of cooling and the cooling environment affect the mechanics of phase formation in the droplets and this marks basic difference among the particle sizes and the control sample. Although elemental composition remain the same, the degree of transformed phase in each droplet size differs, hence the reason for microstructural differences as outlined in ***section 5.4*** (see ***Appendix C***) and the consequent change in their mechanical properties as reported in ***section 5.6***.

6.2: Effect of Rapid Solidification and Estimated Cooling rate.

For a phase change in Fe–C alloy having carbon equivalent as featured in ***table 5.1***, with rapid solidification processing as the major factor of the transformation; the phase transition formula expressed in ***section 3.8*** is of primary importance and must come to play. Basically, the estimated liquidus temperature for this alloy based on simple equivalent carbon calculation is about 1492 K, which is roughly about 70 K higher than the Fe – C eutectic temperature. But going by the Calphad calculation, the fact remains that; alloys of this kind of constituent shown in Table 5.1 with silicon concentration of 2.83 wt%; has its liquidus temperature as 1521 K and there is a projection that its eutectic temperature will raise by about 15 K for such % Si concentration. Meanwhile, Lacaze et al. [104], outlined major difference between the stable and metastable Fe – Si – C phase diagrams especially as it relates to the role of Si in suppressing the eutectic temperature under rapid solidification condition. For instance, during rapid cooling, based on ref. [104] estimation; it is expected that the eutectic temperature will be relatively lowered as compared to the equilibrium value for the same Si concentration.

Therefore, the summary effect of rapid solidification processing by containerless drop-tube technique used in the course of this study include: (i) drastic suppression of solid-state post solidification precipitation of graphite as confirmed in the as-cast sample and formation of supersaturated retained austenite discovered in the rapidly solidified samples. This means that in the powder particles, more C will remain in solid-solution within the γ-Fe or Fe_3C rich dendrites in as much as solid-state decomposition of $\gamma \rightarrow \alpha$ will be restrained; (ii) As a result of high % concentration of Si in the alloy, there is suppression and shift in the eutectic temperature which allows larger mixture of $L + \gamma$ region as shown in ***fig. 3.18 (b)*** under ***section 3.7.2***. Hence, for a hypereutectic alloy, it will be expected that considerable increase in microhardness will be observed as a result of more dissolved graphite in solid-solution. Again, this eventually tends to favour more of acicular ferrite phase evolution. Consequently, this is expected to increase the volume fraction of the γ retained at the expense of the predominate ledeburite (γ + Fe3C); and lastly (iii) it is expected that as a result of combined effect from high cooling rate and melt sub-division, the smaller droplets will experience melt undercooling [102]; which normally manifest at high cooling rate, which eventually favours more of martensitic transformation . Meanwhile, the effect and mechanism behind cooling rate which is a deterministic function and undercooling which is stochastic are thereby evaluated. Hence, all explanation/observation/analysis were based on morphological changes observed, the parameters of the cooling media used and the different identified evolved phases. The calculated cooling rate of this alloy in N_2 and He gases using heat balance power-law fitting in EXCEL software was given as $\dot{R}$ = 6.40 x $10^{-3}D^{-1.45}$ and 7.75 x $10^{-3}D^{-1.60}$ respectively (as shown in ***fig. 5.1***). Also the lower and upper limits of the cooling rate for the droplets rapidly solidified in N_2 and He are 200 K s^{-1} to 23,000 K s^{-1} and 700 K s^{-1} to 60,000 K s^{-1} accordingly. The cooling rate which is a function of the particle sizes is the primary factor that influences this differences. ***Table 5.3*** and ***fig. 5.1*** show values and plotted graph of estimated cooling rate (Ks^{-1}) against droplet sizes (µm) for the drop-tube particles in the two cooling media based on their peculiar thermo-physical properties shown in ***table 5.2***.

6.3: Evolved microstructure and Identified Phases.

Basically, all the droplet particles show fine microstructure and they have mainly two distinct morphologies observed throughout the various sample SEM micrographs in fig. 5.27 to 5.34 and further confirmed by TEM in figure 5.44 through to 5.47. Again as stated earlier, dendrites formation and growth from metallic melt is commonly a direct product of solid crystallization mechanism and the evolving morphology normally consist of array of fine and/or coarse dendritic structures which depend on the solidification conditions, namely cooling rate. Therefore, fast cooling such as experienced by the droplets in the drop-tube solidification technique results in fine dendrites observed in this case; which further depends on the thermophysical parameters of the cooling medium [3]. The microstructural observations of the drop-tube particle differs depending on their cooling rate, degree of fragmentation and very much clearly different from that of the as-cast (and crucible residue). To further clarify the difference between the slowly cooled and the rapidly solidified samples, ***fig. 5.35*** and ***5.36*** present elemental distribution before and after the rapid solidification processing via drop-tube. From these figures, one can clearly see that the constituent elements are well dispersed and evenly distributed in ***fig. 5.36*** (as a result of rapid solidification processing) compared to that in ***fig. 5.35*** which shows elemental segregation and its effect on the microstructure and consequently the material’s mechanical properties.

Apparently all the droplets microstructures displayed characteristic inter-connected network of dendrites with distinctive morphologies which becomes less fragmented with reduction in particle sizes (i.e. with increasing cooling rate) as seen in the observed micrographs especially in ***fig. 5.27 – 34*** and as outlined in ***Appendix C***. However, in either optical or SEM observations, there was no trace of graphite, in any of the unetched droplets even in the one with modest cooling rate (i.e. the 850 µm droplet cooled in N_2 which cooling rate is ~200 K s^{-1}) (see ***fig. 5.15 – 5.21***)*;* and the identified morphologies show a network of homogeneous single phase (denoted as M1 as seen in ***fig. 5.8***, ***5.19*** and ***5.27***). This was thereafter identified by XRD data profiles (see ***fig. 5.3, Appendix B***) and again indexed by TEM analysis (shown in ***fig. 5.44 – 5.50*** and Appendix ***E***) as retained austenite (γ-Fe) which was dendritically embedded in another polycrystalline phase (tagged M2) identified to be pearlite (in the big droplets, i.e. 850 µm ≥ x ≤ 300 µm); comprising of cementite (Fe_3C) plus ferrite (α-Fe) in the relatively big and medium size (i.e. 212 µm ≥ x ≤ 106 µm) droplets. However, α-Fe reduces considerably with droplet size reduction with more of α'-Fe identified in the smaller (75 µm ≥ x ≤ 38 µm) droplet. This shows that even at modest cooling rate, the drop-tube samples are free from graphite flake.

6.3.1: Phase confirmation and transformation progression

All the evolved phases identified were confirmed present in the powder particles albeit at different proportion as indicated by their peak intensities analysis as shown in Table 5.4 and 5.5. Hence, the morphological changes observed with increasing cooling rate are perfectly consistent with the XRD traces obtained and rim with the TEM analysis in fig. 5.48 to 5.52. Meanwhile, the % phase fraction and progressive sequence of these transformation is depends on the cooling rate, i.e. droplet sizes. For instance, at low cooling rate; the dominate phases are predicted by the equilibrium phase diagram. The observed transformation is generic and span throughout all droplet sizes with more carbide and martensitic lath evolving as cooling rate increased drastically especially in helium because of its better cooling effect (for thermophysical properties of N_2 and He gas see ***table 5.2***) [23]. The obtained XRD profiles for the smaller droplets < 106 µm show significant replacement of α-Fe by evolving α'-Fe phase with increased intensity at much higher cooling rate and these phases co-exist in the reducing fraction of retained γ-Fe matrix. At this point, the reality is that within every group sizes, there exist strong similarity which is obvious in their morphologies as well as in their mechanics of transformation. In all, there is a trend in the evolved phase formation from ferrite to retained austenite and back to acicular ferrite/martensite, a metastable phase. These analysed x-ray diffraction profiles presented in ***section 5.3*** (with full detailed in ***Appendix B***), have been further consolidated with confirmed result from transmission electron microscopy micrographs (show-cased in section 5.5.2) and differential thermal analysis (in section 5.5.1.). Therefore, these results confirmed the identified evolved phases as stated. Hence, the emphasis has always based on the selected droplet sizes. Some selected analysed x-ray result profile of few droplets traces are as displayed in ***fig. 5.3(c)*** in comparison to that of control sample as shown separately in ***fig. 5.2***). However, as a result of the level of noise in the measurement resulting from fluorescence of the Fe in the Cu K_α radiation, it was very difficult using Rietveld refinement to estimate the phase fractions present in each case. The suggestion will be to run the samples with Ag K_α radiation. Consequently, the confirmation of the evolved phases was based on other various techniques and analysis mentioned above.

Concerning the DTA results outlined in ***section 5.5.1***, a trial with higher upper temperature limit (1450 ^{o}C) resulted in what was observed in ***fig. 5.37,*** where there was significant diffusion of carbon leaving mainly α-Fe as shown in ***fig. 5.38(a).*** Meanwhile, the morphology of the sample after carbon diffused out is primarily ferritic – pearlitic as shown in ***fig. 5.38(b)***. To ensure repeatability of the DTA analysis in the 1st and 2nd run, the upper temperature limit was re-set to 1050 ^{o}C to prevent the observed carbon diffusion. Therefore, the microstructure for the start of the 1st and 2nd loop are practically the same as shown in ***fig. 5.38*** and ***5.37*** respectively. Hence, the observed DTA onset temperature of the heat treated evolved metastable phase (α'-Fe) formed (see ***fig. 5.40***) in the various powder particle sizes occurred consistently at about 460 ^{o}C at slower heating/cooling rate of 5 K min^{-1} (see ***fig. 5.41 and 5.42***) within temperature range of 50 – 1050 ^{o}C; which is in accordance with previous similar work carried out by Dutra et al. [133] and Leonhardt et al. [134] respectively. The implication of this is that austenite (retained) intensity were observed after this heat treatment process i.e. austempering. Hence, evolved martensitic phase began to decompose to austenite just above 460 ^{o}C. This is why the DTA peak at 480 ^{o}C is not observed on the second heating profile as expected. This observed metastable phase changes is still within tempered martensite formation temperature [135, 136]. Hence, high cooling rate was thereby confirmed as very essential for the evolution of this metastable phase. ***Table 5.4*** outlined the various significant reactions and their expected temperature of formation as compared to the observed temperature. Martensite transformation temperature begins at M_s (martensite start temperature) and ends at M_f (martensite finish temperature). According to Payares-Asprinco et al. [136], this vary over a wide range of temperature to well below ambient temperature until martensite finish (M_f) is reached for a tempered sample. However, the range of M_s to M_f is often within the order of 150 °C apart. It is expected that at the end of M_f temperature, most of the austenite should have been transformed to martensite, but often in reality as it is in this case, a portion of the austenite is retained even at room temperature [137]. Also, the fact remains that the higher the carbon content in any Fe-C alloy, the lower the temperature (M_f) at which the transformation of γ into martensite finishes. The presence of retained γ-Fe in those droplets with varied intensity was further confirmed by the XRD profiles in the various droplet sizes as seen in ***Appendix B***.

In line with the observed microstructures and x-ray analysis of the evolved phases, the TEM results further confirm the presence of different phases in the droplets cooled in N_2 and He. In ***fig. 5.43*** to ***5.49***, which contain series of bright field micrographs and SAD indexes; they reveal different spotted regions and identified phases in the droplets irrespective of the cooling gas used these phases have been detected in N_2 and He cooled samples. For the particles with relative cooling rate of ≤ 1000 K s^{-1} (i.e. 250 µm cooled in N_2 or 630 µm cooled in He) and 3000 K s^{-1} (120 µm N_2 cooled or 305 µm He cooled), the retained γ-Fe intensity become stronger and quite prominent. However, with increased cooling rate, say 13,000 K s^{-1} (53 µm N_2 cooled or 120 µm He cooled) and 50,000 K s^{-1} (< 38 µm cooled in N_2 or 58 µm cooled in He) respectively; the evolved metastable α'-Fe phase intensity became dominant and this is in accordance with the intensity on the XRD traces earlier described, showing that as the droplets sizes reduces drastically i.e. increasing cooling rate, the martensite formation is highly favoured. The cooling rate of 850 µm and 53 µm particles are estimated to be correspondingly 2.10 x 10^{2} and 1.29 x 10^{4} K s^{-1} in N_2 and 3.54 x 10^{2} and 5.01 x 10^{4} K s^{-1} in He. Their microstructure is as shown in ***fig. 5.27*** and ***5.31*** respectively. Consequently, it implies that, cooling rate of 5000 K s^{-1} will be experienced by a 90 µm N_2 cooled droplet and 220 µm Helium cooled droplet respectively.

In the course of rapid cooling, two fundamental post solidification mechanics will occurred; namely the inhibition of recalescence of solid-liquid and solid-solid phase transformation. Hence, the metastable phase formed was present with increasing intensity as the main dominant phase in all the droplets as cooling rate increases. Meanwhile, considering the heat released during solidification and its extraction by the cooling medium, He cooled samples have more metastable phase evolving in the relatively bigger particles. For instance, with increasing cooling rate (150 µm N_2; 500 µm He), it is obvious that retained γ-Fe (austenite) also becomes a constituent phase, along with the carbide, Fe_3C; which coexists with α in the form of pearlite (see ***fig. 5.31***). With further increase in the cooling rate (53 µm N_2, 150 µm He), more α-Fe have transformed to α' (martensite) and the observed transformation continues with more of α' replacing the α-phase in the smaller droplets (see ***fig. 31***).

6.3.2: Cooling rate and undercooling effect on measured microhardness.

Fig. 5.59 gives a comparative % phase fraction of evolved martensite in both N_2 and He gas. Hence, at any given cooling rate, one can determine the phase fraction of this metastable phase that can be obtained. The observed morphological differences especially between the ≤ 212 µm and ≤ 53 µm size droplets can mainly be attributed to the interplay of cooling rate and undercooling effects as noticed in droplets having similar cooling rate cooled in the two different media [90]. Meanwhile, particle of the same size may have approximately the same cooling rate; however small particles irrespective of the cooling medium will have high undercooling due to rapid heat extraction as a function of surface to volume ratio of the particle. As the cooling rate increases, undercooling in smaller droplets become very much prominent. Hence, undercooling is controlled by nucleation and not necessarily all particles of the same size will have the same undercooling as a result of random distribution of nucleant in the droplets due to melt sub-division. For instance, at moderate cooling say for N_2 cooled 300 µm sample (***fig. 5.28a***), the dominant microstructural feature observed is that of interconnected network of dendritic austenite with interdendritic pearlite. However, at much higher cooling rate; the microstructure of the He cooled 53 µm droplets in ***fig. 5.31(b)*** shows evidence of lath morphology of acicular ferrite or martensite. This microstructure is consistent with the identified phase; α' in the XRD patterns for this sample, having the highest cooling rate and as a result greater undercooling effect in this study as can be further deduced in ***fig. 5.31*** through ***5.34***.

Table 5.5 shows the corresponding measured values of the Vickers microhardness of each droplet size in the 2 media. This gives an insight into the effect of cooling rate on the observed microstructures and consequently upon the mechanical properties of the samples. The plotted graphs in ***fig. 5.58*** show microhardness values for helium and nitrogen cooled samples such that for same size droplet from each cooling medium will definitely as expected not have the same cooling rate. As earlier observed in ***section 5.6***, the average hardness of the matrix of the as-cast material is 362 ± 3 Hv0.05 as a result of its predominantly ferrite but randomly distributed graphite constituent was avoided. Meanwhile the hardness of each droplet size varies greatly in each medium. For instance, the minimum hardness value of 704 ± 7 Hv0.05 was observed in the 850 µm N_2 cooled droplet; while the maximum hardness value of 1440 ± 4 was obtained in the 53 µm He cooled particle. It should be noted that as a result of rapid solidification, the droplet with modest cooling rate has approximately double the microhardness value of that of the as-cast sample. The simple reason for this can be attributed to the absorption and retention of more C in the Fe rich matrix of the droplets, making them highly supersaturated with carbon. Hence, increasing cooling rate results in steady increase in the microhardness of the droplets. This observation was consistent until we reach ≤ 106 µm particle size, where a steep increase in hardness value was noticed. This sudden rise in hardness value can only be ascribed to decreasing fractions of ferrite and that of retained austenite with corresponding increasing fraction of the evolving acicular ferrite or martensite phase due to more carbon concentration in the solid solution of the sample as revealed in the accompanying morphologies of the particles as their size reduces (see droplets morphologies in ***Appendix C***).

Meanwhile, ***fig. 5.57*** shows the graph of measured Vickers microhardness values plotted against the cooling rate of the droplets in the two media. It can be noticed that for cooling rate < 5000 K s^{-1} N_2 and He cooled samples were aligned on the same curve. This is expected as cooling rate at this point is the main factor controlling the microstructure and consequently the microhardness of the droplets. Meanwhile, for cooling rate values > 5000 K s^{-1} the data departs from lying on a single curve, with the N_2 cooled samples data lying significantly above that of He cooled sample. The main reason for this is that the microhardness of the droplets is being influenced not only by the cooling rate but also by the undercooling factor prior to nucleation as shown in ***fig. 5.34***. **Fig. 5.59** shows the consistent increase of emerging martensite phase with increasing cooling rate which is more favoured with He gas because of its better thermal conductivity. Hence, the droplet size, cooling rate and undercooling effect jointly influenced the martensitic phase formation which invariably influenced observed increase in measured microhardness values of the droplets with decreasing particle size [138].

However, smaller droplets have very high probability of fewer potent heterogeneous nuclei than bigger ones; so even though the cooling rate is similar, the smaller droplets will experience a larger undercooling than the bigger ones. In which case, the N_2 cooled droplet with smaller diameter undercooled more easily than the bigger He cooled droplets at the same cooling rate. In conclusion, the eventual separation of the N_2 and He cooled microhardness curves is a reflection of higher undercooling experienced by the smaller N_2 cooled droplets. Hence, the smaller the droplets irrespective of the cooling environment, the larger the undercooling effect it will experience.

6.3.3: Influence of cryogenic treatment on Microstructure and microhardness.

Each droplet size cooled in the two media was subjected to cryogenic treatment. The effect of this was more obvious in the bigger droplets as they show substantial change in microstructure. For example, ***Fig. 5.52*** and ***5.53***; show micrographs of 850 µm N_2 cooled and 53 µm He cooled samples before and after cryogenic treatment respectively. Generally, the retained austenite in the rapidly solidified droplets seems stable at room temperature however, when this is further treated in liquid Nitrogen the M_s is lowered and then further martensitic transformation will be triggered thereby affecting both the microstructure and the mechanical property (i.e. microhardness) of the material. Meanwhile, the presence of martensite became more evident in the ≥ 300 µm samples that were subjected to this low temperature quenching (-196 ^{o}C). The big samples ($\geq$ 500 µm) rapidly solidified in any of the media have relatively lower cooling rate and as such they have higher retained austenite as indicated in the XRD peak intensities featured in ***fig. 5.3a*** for all N_2 cooled samples. ***Fig. 5.52(b)*** shows the morphology of newly generated martensite laths which tends to grow within the bigger retained austenite fields of 850 µm N_2 cooled droplet. This is as reflected in the XRD trace of the same sample before and after the treatment as shown in ***fig. 5.54***, with evolved α'-Fe peak becoming more prominent after the treatment. However, as the droplets size decreases, the effect of cryogenic quenching become less significant as seen here and in ***fig, 5.53***.

Finally, changes in the droplets were reflected in the measured Vickers microhardness values of the transformed morphologies of the samples as displayed in ***Table 5.6*** for each droplet sample cooled in N_2 and He environment. Hence, ***fig. 5.57*** shows the consistent increase in microhardness values of the droplets against their cooling rate. The measured microhardness values noticed in the cryogenically quenched samples show further evolving harder metastable phase which in this case is acicular ferrite or martensitic transformation prompted by the low temperature exposure processing as shown in ***fig. 5.58***. This change in microhardness values as a result of liquid nitrogen quenching have shown that the process has the ability to permanently transform the retained austenite fraction in the larger droplets to much harder metastable phase in this case martensite and carbide formation.

CHAPTER SEVEN

CONCLUSIONS

Conclusion Remarks

Within the set scope, aim and objectives of this study, evidence has been presented with the aid of metallography observations and % phase fraction analysis on how rapid solidification processing influenced the microstructure and microhardness of a typical commercial grey cast iron even at a constant elemental composition. Hence, the following conclusions can be drawn from this study:

1. One can confidently confirm that the elemental composition of this commercial as-cast BS1452 Grade 250 grey iron shows that it is a typical conventionally cooled hypoeutectic graphitic cast iron with estimated carbon equivalent of approximately 3.7 wt.% and having 2.83 wt.% Silicon content.

2. It was confirmed in the course of this study that the localised elemental microsegregation noticed in the SEM-EDX mapping of the as-cast sample was completely absent in the droplets due to rapid solidification effect that causes elemental redistribution (refinement) which get better with increasing cooling rate (i.e. particle size reduction).

3. Also, the initial microscopic examinations revealed the as-cast microstructure as ferritic-pearlitic dendrites with randomly distributed Type C graphite flakes in the iron matrix; the presence of which make the material relatively brittle and limits its application, but with containerless rapid solidification processing, droplets formed have the carbon in solid-solution which form give reason for improved microhardness value noticed in the droplets with increasing cooling rate.

4. The microscopic analysis shown that the as-cast and the various droplets samples have definite morphological changes in terms of microstructure and phase evolution. For instance, it has been confirmed that there are no traces of graphite in any of the droplets after rapid solidification in either Nitrogen or Helium cooled samples. Also % phase volume fraction of dendritic to interdendritic formation was favoured by increasing cooling rate.

5. The rapidly cooled droplet sizes produced range from ≥ 850 μm to ≤ 38 μm in diameter corresponding to upper and lower cooling rate of approximately

23,000 K s^{-1} to 200 K s^{-1} in Nitrogen and 60,000 K s^{-1} to 700 K s^{-1} in Helium gas environment respectively.

6. The higher the cooling rate, the less fragmented the dendritic nature of the droplets microstructure produced from the as-cast and with further increase in cooling rate, there was a progressive transformation from α-Fe to retained γ-phase and finally to α'-Fe. The observed martensitic transformation is diffusionless, hence the chemical constituent of the parent and product phases are same.

7. At constant droplet size, Helium cooled samples experienced higher cooling rate than their Nitrogen cooled counterpart because Helium gas has better thermal conductivity hence droplets cooled in it exhibit higher microhardness values than those cooled in N_2.

8. As a result of melt sub-division effect, it was noticed that at cooling rate above 5000 K s^{-1}; the N_2 cooled droplets (90 µm in diameter) display higher microhardness values than its He cooled counterpart (220 µm). This shows the dominance of droplet size effect on droplets with the same cooling rate; subsequent to higher undercooling in the smaller droplets.

9. With deep cryogenic quenching in liquid N_2 (– 196 ^{o}C) the observed retained austenite in the big rapidly solidified droplet (≥ 300 µm) were further transformed to martensite which is reflected in their morphology before and after the treatment and confirmed by further increase in their microhardness of the cryogenically treated samples.

10. Finally, the relationship between *processing*, *microstructure* and *mechanical properties* of rapidly solidified droplets is a function of cooling rate, thermal conductivity of the environment, undercooling experienced and % fraction of possible evolved phase(s) and their effect on microhardness as it is in this study.

CHAPTER EIGHT

FUTURE WORK

Suggestions for further work

The work presented in this study focused purely on the effect of rapid solidification processing on the morphological changes, accompanying phase evolution and the consequent effect on the microhardness of a standard commercial hypoeutectic grey cast iron at constant elemental composition. Based on the revealing results obtained from this present work, it will be interesting to have further research to cover the following areas:

1. Production of droplets from a typical hypereutectic cast iron alloy using drop tube technique, follow by an extensive microstructural and phase analysis investigation; in comparison to the present study. Also to find out the effect of the same conditions of rapid solidification on the mechanical property i.e. microhardness of the hypereutectic cast iron as control sample and droplets produced. This will help to ascertain the role of C wt.% variation under same processing route or solidification conditions. Of course, the effect of other elements will be minimal. For instance, % Si content is essentially meant for enhancing graphite easy formation during conventional cooling but the effect is greatly supressed during fast cooling. Likewise other elements such as Mn, S and P are considered to be minor in quantity and will at such high temperature form relatively insignificant gaseous substances, hence leaving the effect of carbon on the droplets particles more pronounced. This eventually dictates the state of the metal droplets microhardness as a measure of their mechanical property.

2. Another interesting study will be to investigate the possible effect of addition of any or combinations of popular alloying element(s) such as Cr, Al, or Ti on the morphology, phase evolution and perhaps the mechanical property of either hypo- or hyper- eutectic rapidly solidified alloyed cast iron material. The grey cast iron used in this study is a low alloyed commercial grey cast iron but if other notable alloy elements are included for further probe, the study will help to seek any supposed shift in the microstructure and microhardness of the typical commercial alloy used in this research. Also a comparative change in the usual dendritic to inter-dendritic ratio in the as-cast as well as

the droplets' microstructures can be evaluated and then compared to the values obtained in this study.

3. Also conducting cryogenic treatment on droplets formed from the hypereutectic alloy and examining their microstructures will surely be something worthwhile. Hence, analysing evolved phases of these rapidly solidified droplets further quenched in liquid N_2 or/and in ice will definitely be interesting. Such evolved phase(s) can be confirmed with DTA, TEM and EBSD (if need be). Results from this hypereutectic samples can then be compared with those obtained from the hypoeutectic samples used in this research.

4. Possible production of the rapidly solidified droplets in an Argon gas environment and consequent evaluation of cooling rate, evolved morphology and microhardness as compared to that cooled in N_2 and He gas environment.

Appendix A:

Estimated Cooling rate vs Droplets diameters in N_2 and He gases

Droplets diameter *(µm)*	***Cooling Rate in N₂*** K_T, Ks^{-1} *(N-cooled)*	***Cooling Rate in He*** K_T, Ks^{-1} *(He cooled)*	*Ratio*
15	115943.4107	632845.9683	5.45823
20	68018.6969	364609.2826	5.36043
25	45242.5458	238600.1324	5.27380
30	32563.6170	169196.4845	5.19588
35	24740.7463	126796.4056	5.12500
40	19551.5511	98930.94960	5.06001
45	15919.1921	79595.90510	5.00000
50	13268.8001	65604.81070	4.94429
55	11269.9753	55136.57700	4.89234
60	9721.44740	47087.82800	4.84371
65	8494.69550	40757.66050	4.79801
70	7504.39560	35683.07720	4.75496
75	6692.01650	31548.00700	4.71428
80	6016.27030	28130.54000	4.67574
85	5447.32270	25271.05470	4.63917
90	4963.15800	22852.28300	4.60438
95	4547.22700	20786.45530	4.57124
100	4186.88480	19006.78780	4.53960
105	3872.32660	17461.71120	4.50936
110	3595.85020	16110.87450	4.48041
115	3351.33210	14922.32450	4.45265
120	3133.85200	13870.48240	4.42602
125	2939.41670	12934.66850	4.40042
130	2764.75680	12098.01150	4.37580
135	2607.17300	11346.63240	4.35208
140	2464.41960	10669.02550	4.32922
145	2334.61530	10055.58470	4.30717
150	2216.17360	9498.236800	4.28587
155	2107.74870	8990.155100	4.26529

160	2008.19210	8525.533900	4.24538
165	1916.51890	8099.409300	4.22610
170	1831.88000	7707.516000	4.20743
175	1753.54010	7346.171400	4.18934
180	1680.85970	7012.182000	4.17178
185	1613.28010	6702.767000	4.15474
190	1550.31170	6415.495300	4.13820
195	1491.52330	6148.233800	4.12212
200	1436.53440	5899.103800	4.10648
205	1385.00780	5666.445700	4.09127
210	1336.64380	5448.788400	4.07647
215	1291.17510	5244.824000	4.06205
220	1248.36300	5053.386600	4.04801
225	1207.99330	4873.433800	4.03432
230	1169.87370	4704.031100	4.02097
235	1133.83080	4544.339000	4.00795
240	1099.70810	4393.601000	3.99524
245	1067.3641	4251.1346	3.98283
250	1036.6701	4116.3218	3.97072
255	1007.5095	3988.6027	3.95887
260	979.77580	3867.4684	3.94730
265	953.37220	3752.4556	3.93598
270	928.20990	3643.1421	3.92491
275	904.20760	3539.1419	3.91408
280	881.29100	3440.1019	3.90348
285	859.39170	3345.6984	3.89310
290	838.44650	3255.6342	3.88294
295	818.39770	3169.6360	3.87298
300	799.19150	3087.4521	3.86322
305	780.77840	3008.8504	3.85365
310	763.11290	2933.6165	3.84428
315	746.15220	2861.5523	3.83508
320	729.85720	2792.4741	3.82606
325	714.19110	2726.2119	3.81720
330	699.12010	2662.6076	3.80851
335	684.61230	2601.5145	3.79998

340	670.63830	2542.7959	3.79161
345	657.17060	2486.3247	3.78338
350	644.18320	2431.9823	3.77530
355	631.65230	2379.6578	3.76735
360	619.55520	2329.2480	3.75955
365	607.87070	2280.6559	3.75188
370	596.57920	2233.7911	3.74433
375	585.66200	2188.5686	3.73691
380	575.10160	2144.9088	3.72962
385	564.88160	2102.7371	3.72244
390	554.98660	2061.9831	3.71537
395	545.40190	2022.5810	3.70842
400	536.11380	1984.4684	3.70158
405	527.10940	1947.5870	3.69484
410	518.37650	1911.8816	3.68821
415	509.90340	1877.3002	3.68168
420	501.67940	1843.7936	3.67524
425	493.69390	1811.3154	3.66890
430	485.93730	1779.8219	3.66266
435	478.40020	1749.2715	3.65650
440	471.07390	1719.6250	3.65044
445	463.95000	1690.8451	3.64446
450	457.02070	1662.8967	3.63856
455	450.27830	1635.7462	3.63274
460	443.71570	1609.3621	3.62701
465	437.32620	1583.7141	3.62136
470	431.10330	1558.7737	3.61578
475	425.04080	1534.5136	3.61027
480	419.13280	1510.9079	3.60484
485	413.37380	1487.9322	3.59948
490	407.75840	1465.5628	3.59419
495	402.2815	1443.7775	3.58897
500	396.9384	1422.5549	3.58382
505	391.7242	1401.8748	3.57873
510	386.6348	1381.7179	3.57370
515	381.6657	1362.0656	3.56874

520	376.8129	1342.9002	3.56384
525	372.0726	1324.2049	3.55900
530	367.4411	1305.9636	3.55421
535	362.9148	1288.1608	3.54949
540	358.4903	1270.7819	3.54482
545	354.1643	1253.8126	3.54020
550	349.9338	1237.2394	3.53564
555	345.7957	1221.0495	3.53113
560	341.7472	1205.2303	3.52667
565	337.7854	1189.7700	3.52227
570	333.9078	1174.6572	3.51791
575	330.1118	1159.8810	3.51360
580	326.3949	1145.4307	3.50934
585	322.7548	1131.2964	3.50513
590	319.1892	1117.4683	3.50096
595	315.6960	1103.9371	3.49684
600	312.2731	1090.6940	3.49276
605	308.9184	1077.7302	3.48872
610	305.6300	1065.0375	3.48473
615	302.4060	1052.6079	3.48078
620	299.2446	1040.4338	3.47687
625	296.1442	1028.5077	3.47300
630	293.1029	1016.8227	3.46917
635	290.1193	1005.3718	3.46537
640	287.1917	994.14840	3.46162
645	284.3186	983.14620	3.45790
650	281.4986	972.35900	3.45422
655	278.7303	961.78100	3.45058
660	276.0124	951.40640	3.44697
665	273.3434	941.22970	3.44340
670	270.7222	931.24560	3.43986
675	268.1475	921.44900	3.43635
680	265.6182	911.83490	3.43288
685	263.1331	902.39850	3.42944
690	260.6911	893.13510	3.42603
695	258.2911	884.04040	3.42265

700	255.9322	875.11000	3.41930
705	253.6132	866.33970	3.41599
710	251.3332	857.72540	3.41270
715	249.0913	849.26320	3.40945
720	246.8866	840.94940	3.40622
725	244.7182	832.78030	3.40302
730	242.5852	824.75230	3.39985
735	240.4868	816.86200	3.39670
740	238.4223	809.10600	3.39358
745	236.3907	801.4811	3.39049
750	234.3914	793.9842	3.38743
755	232.4236	786.6123	3.38439
760	230.4867	779.3623	3.38138
765	228.5798	772.2315	3.37839
770	226.7024	765.2171	3.37543
775	224.8538	758.3164	3.37249
780	223.0334	751.5268	3.36957
785	221.2405	744.8458	3.36668
790	219.4746	738.2709	3.36381
795	217.7351	731.7996	3.36096
800	216.0213	725.4298	3.35814
805	214.3328	719.1592	3.35534
810	212.6691	712.9855	3.35256
815	211.0295	706.9067	3.34980
820	209.4136	700.9207	3.34706
825	207.8210	695.0255	3.34435
830	206.2510	689.2191	3.34165
835	204.7033	683.4996	3.33898
840	203.1775	677.8653	3.33632
845	201.6730	672.3142	3.33368
850	200.1894	666.8447	3.33107
855	198.7263	661.4550	3.32847
860	197.2834	656.1436	3.32589
865	195.8602	650.9088	3.32333
870	194.4563	645.7489	3.32079
875	193.0713	640.6626	3.31827

880	191.7050	635.6483	3.31576
885	190.3568	630.7046	3.31328
890	189.0265	625.8301	3.31081
895	187.7138	621.0233	3.30835
900	186.4183	616.2830	3.30591
905	185.1396	611.6079	3.30350
910	183.8775	606.9966	3.30109
915	182.6317	602.4479	3.29870
920	181.4018	597.9607	3.29633
925	180.1876	593.5338	3.29398
930	178.9887	589.1660	3.29164
935	177.8049	584.8561	3.28931
940	176.6360	580.6031	3.28700
945	175.4816	576.4060	3.28471
950	174.3415	572.2637	3.28243
955	173.2154	568.1751	3.28017
960	172.1031	564.1393	3.27791
965	171.0044	560.1553	3.27568
970	169.9190	556.2221	3.27345
975	168.8466	552.3389	3.27125
980	167.7871	548.5048	3.26905
985	166.7403	544.7187	3.26687
990	165.7058	540.9800	3.26470
995	164.6836	537.2878	3.26255
1000	163.6733	533.6412	3.26040

Appendix B1:

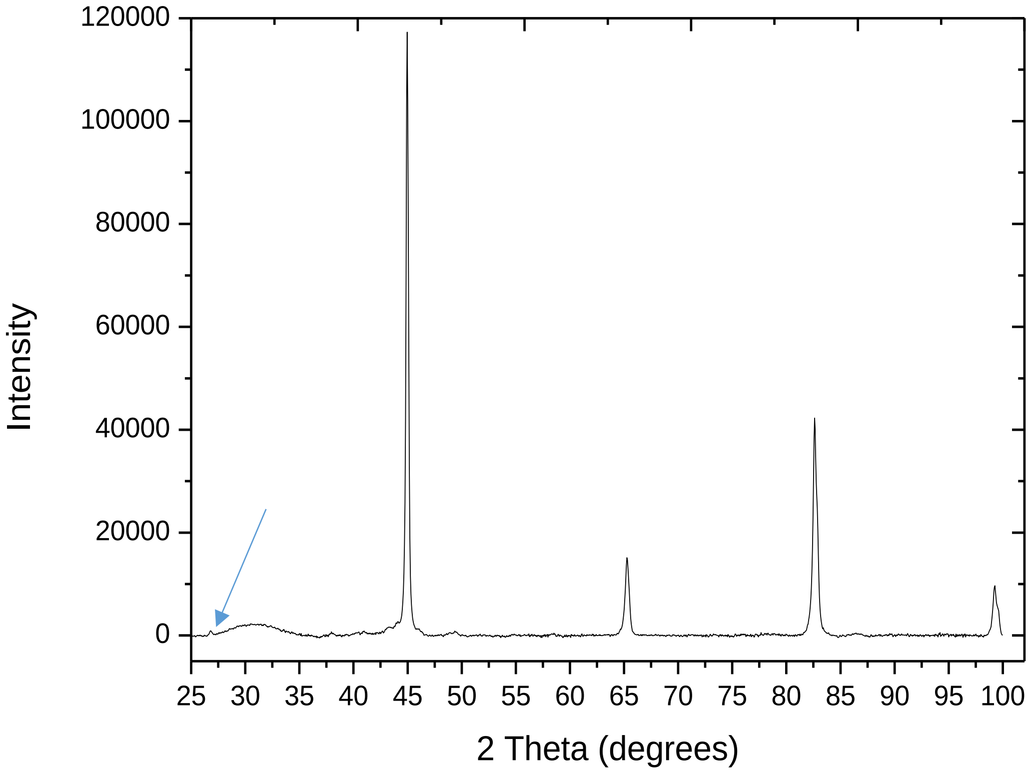

Appendix B1: XRD phases trace profiles of the as-received sample showing the graphite profile at approximately 2θ equal 26 degree with the resin hump effect.

Appendix B2:

Identified phases in XRD profile for all droplets sizes cooled in N_2 and He.

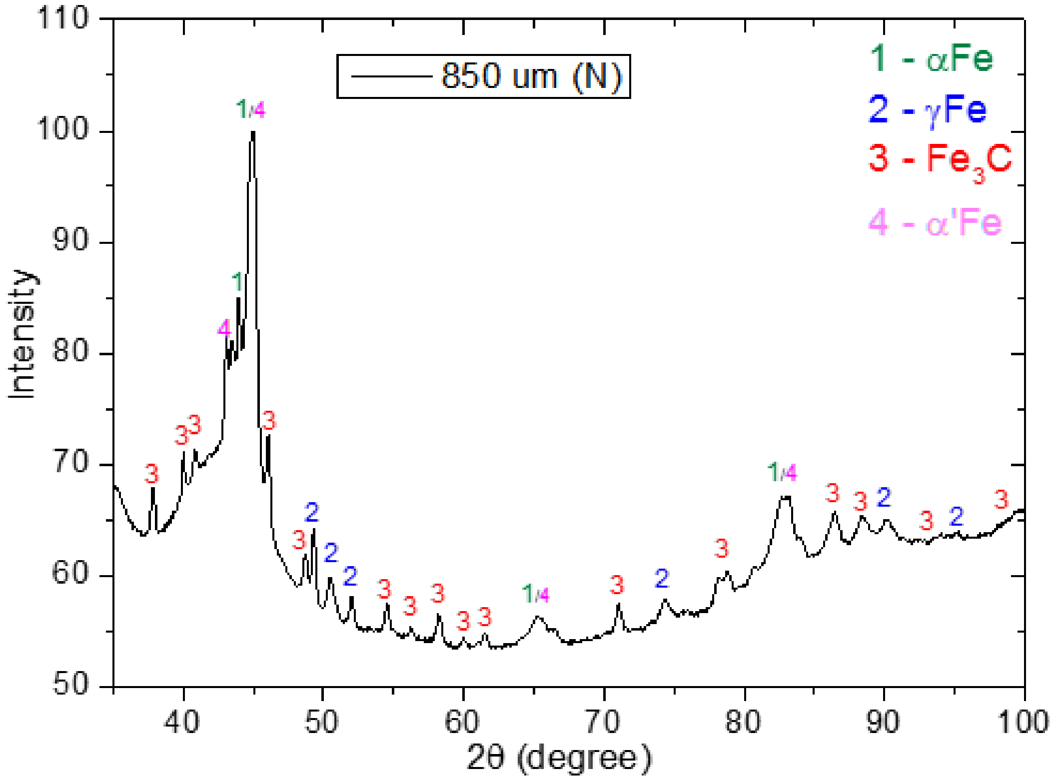

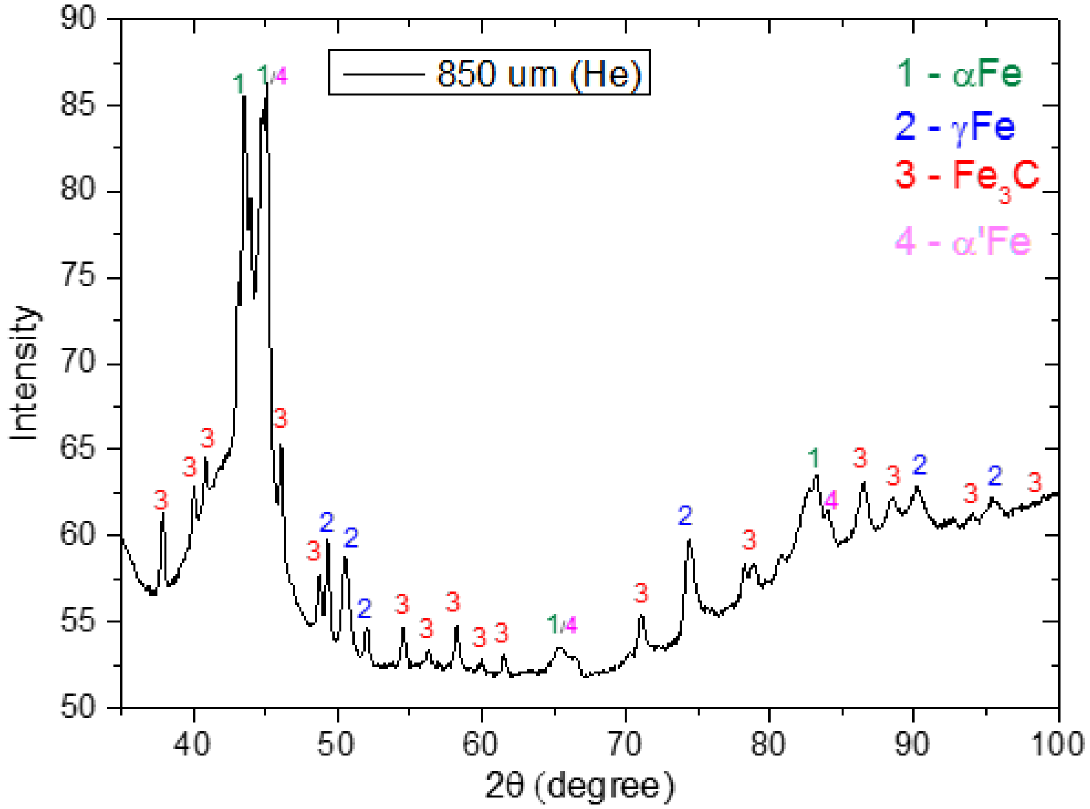

Appendix B2-2: XRD phases trace profiles identified in ***850 µm droplet*** cooled in N_2 & He.

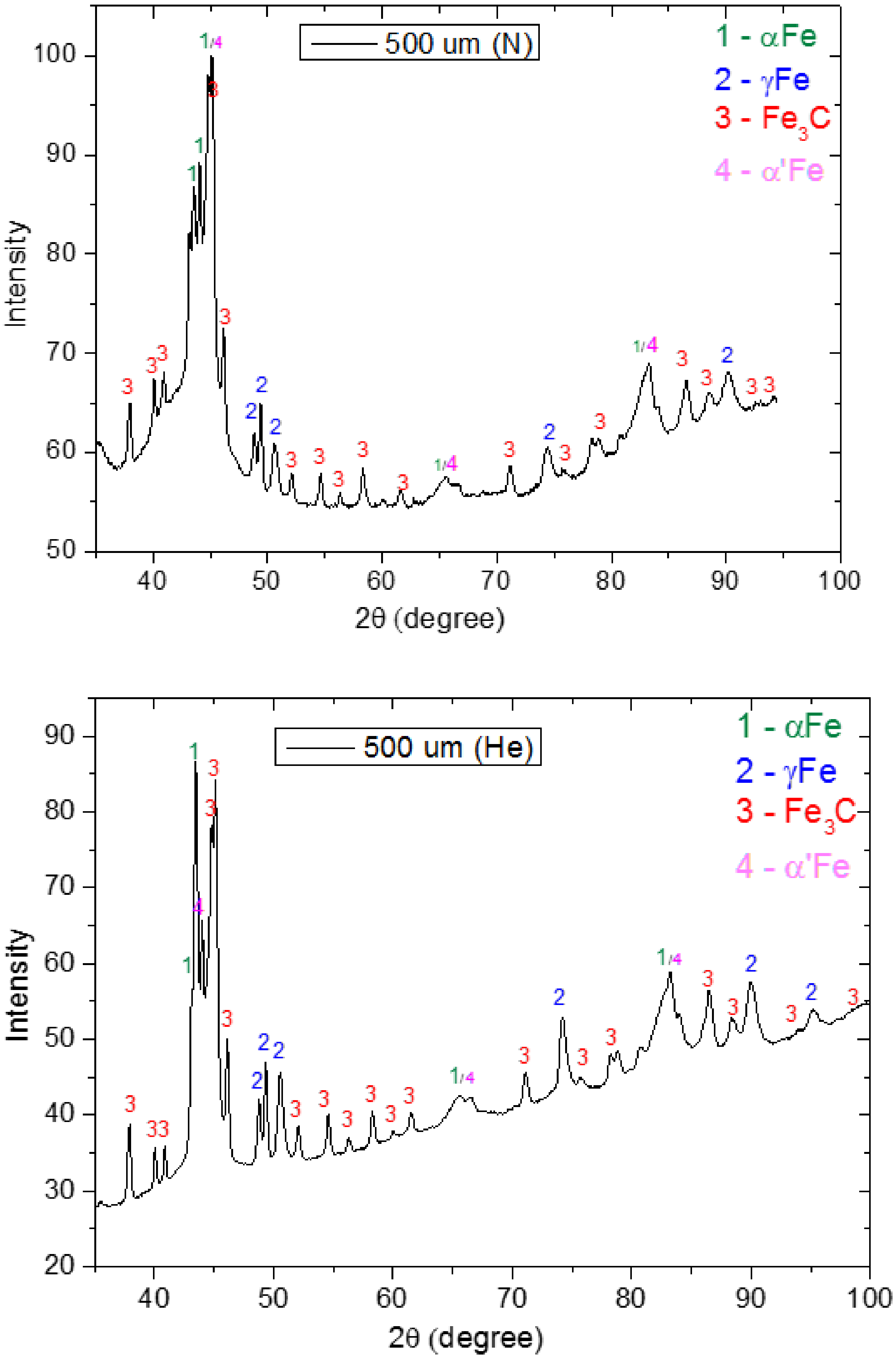

Appendix B2-2: XRD phases trace profiles identified in ***500 µm droplet*** cooled in N_2 & He.

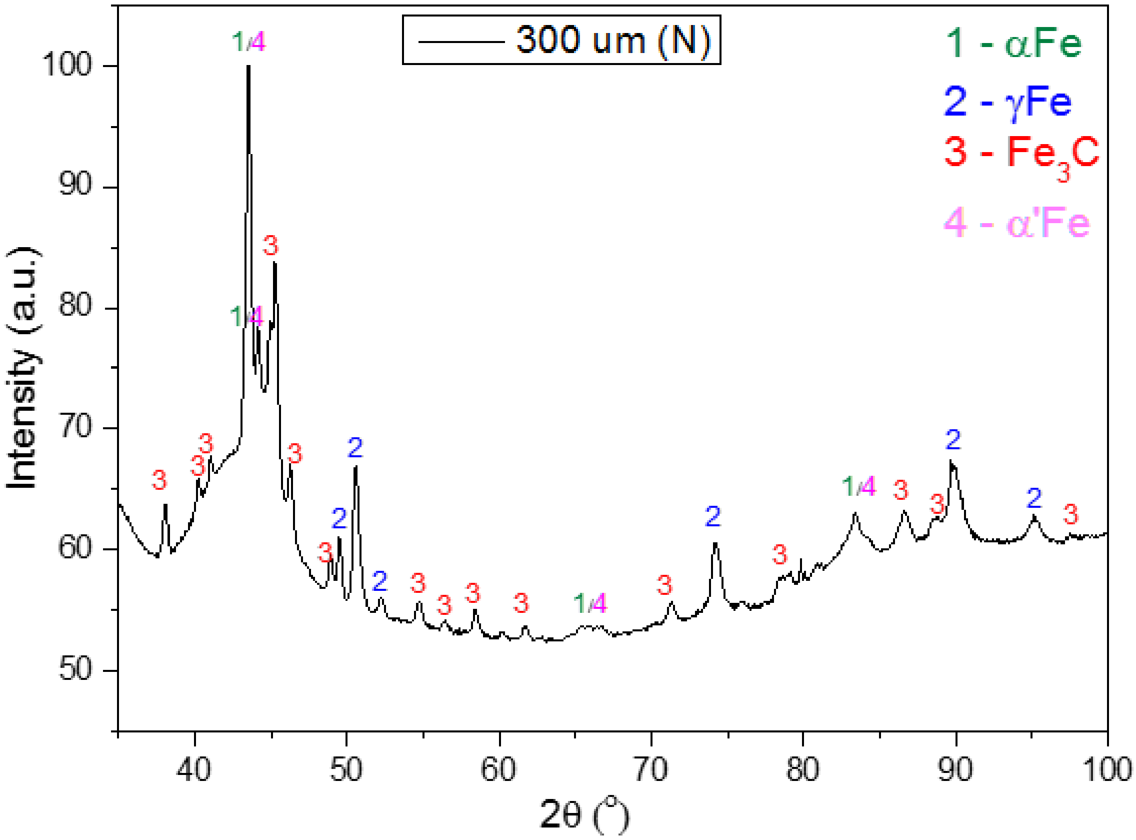

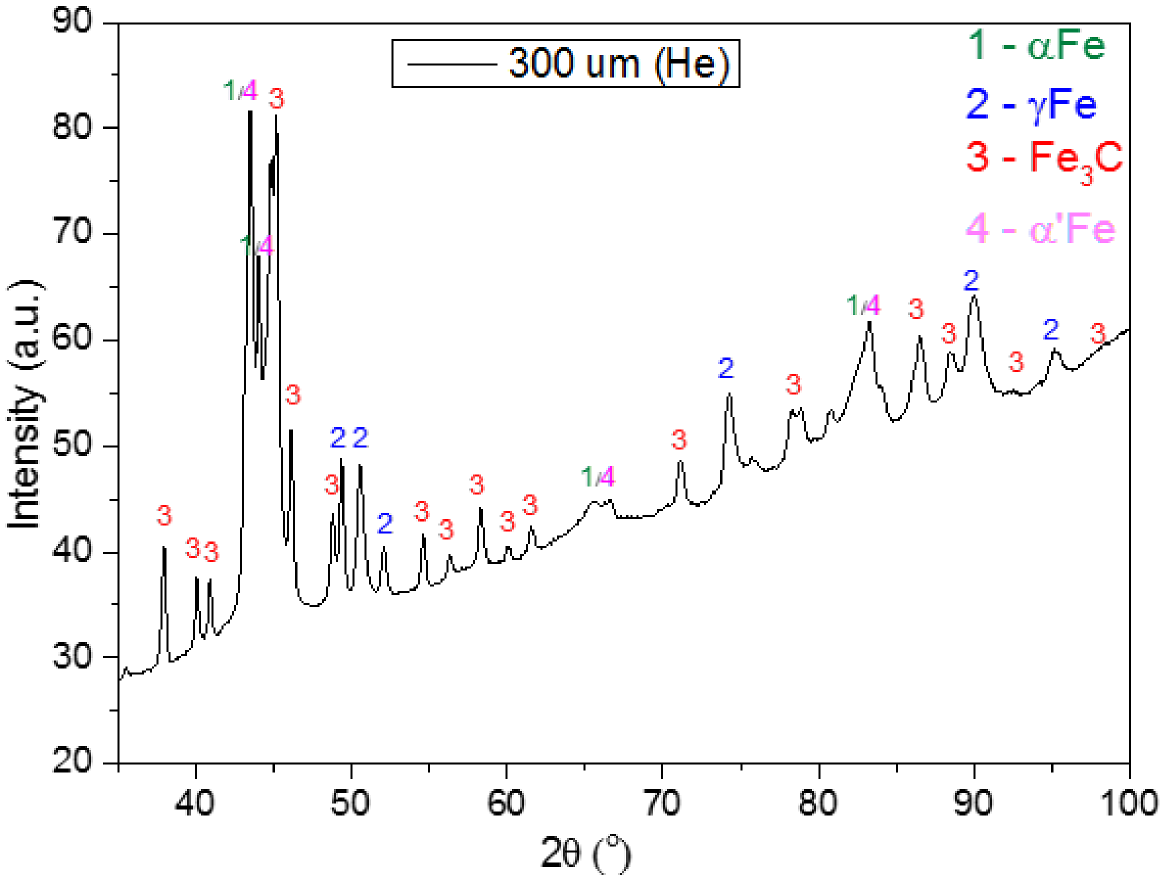

Appendix B2-3: XRD phases trace profiles identified in ***300 μm droplet*** cooled in N_2 & He.

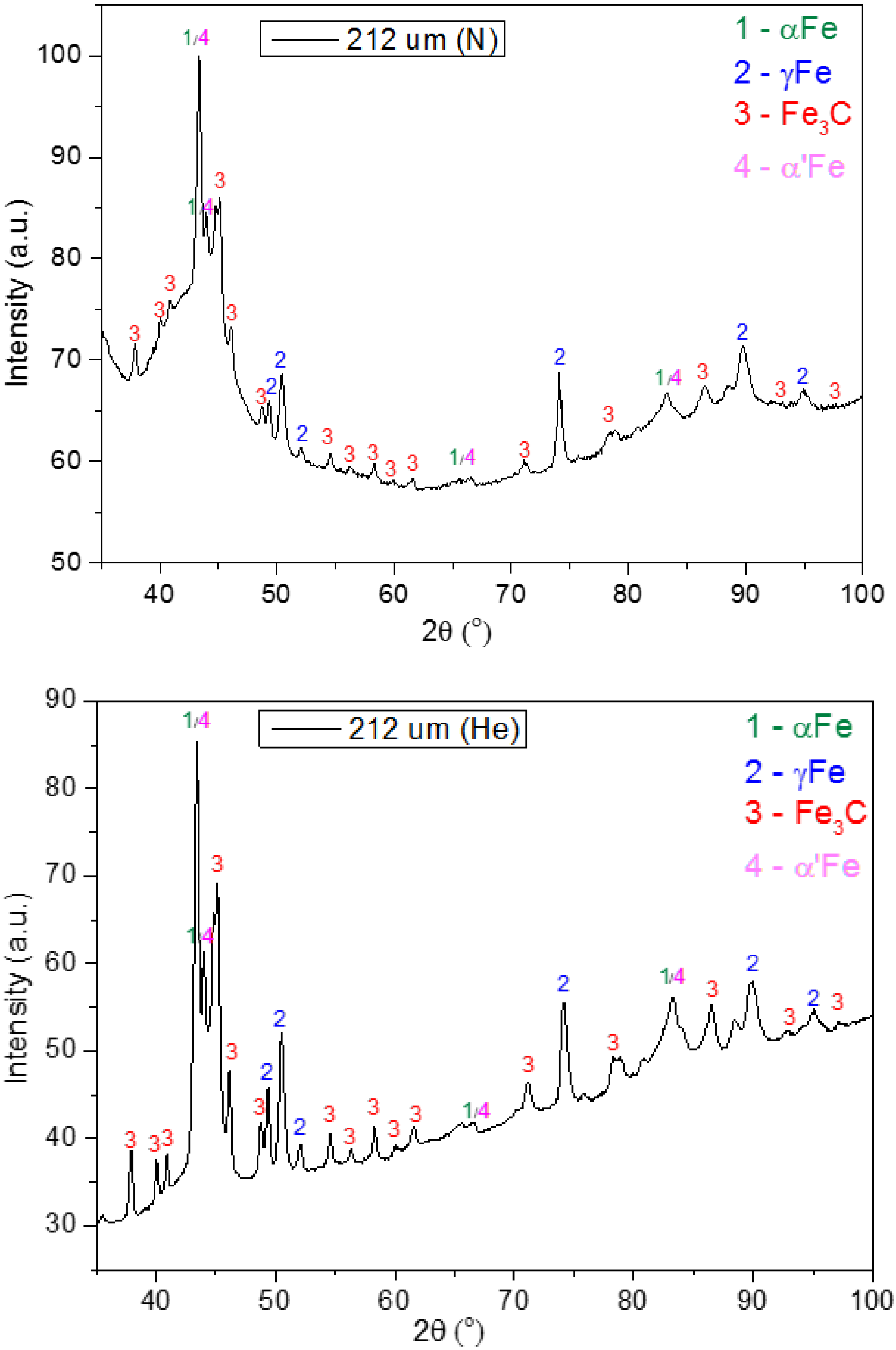

Appendix B2-4: XRD phases trace profiles identified in ***212 µm droplet*** cooled in N$_2$ & He.

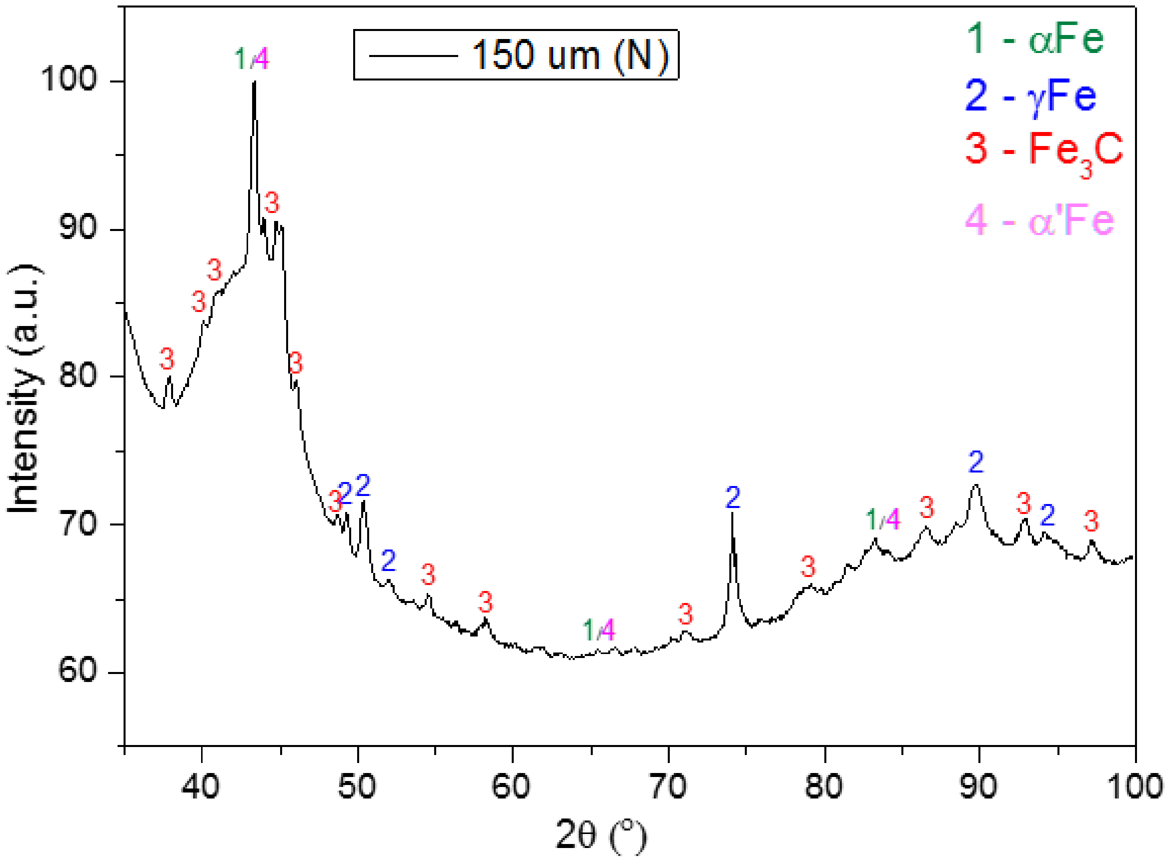

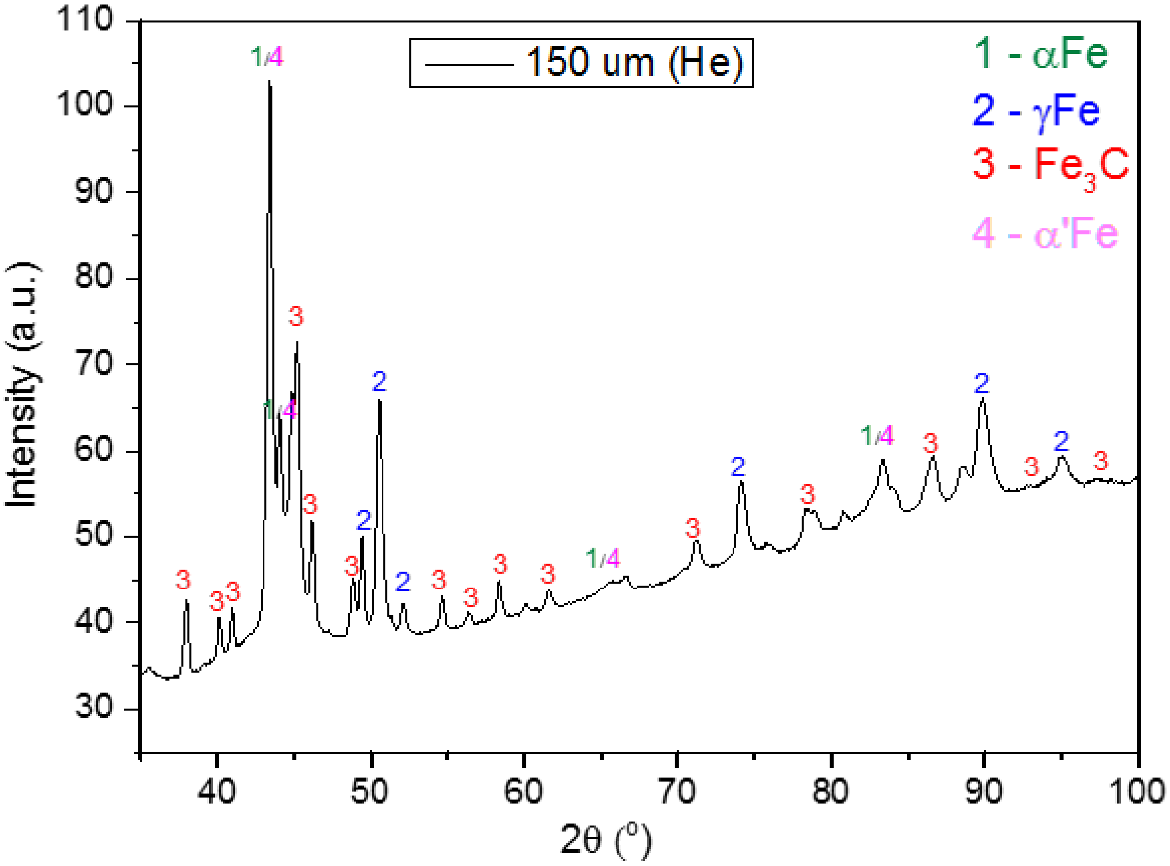

Appendix B2-5: XRD phases trace profiles identified in ***150 μm droplet*** cooled in N_2 & He.

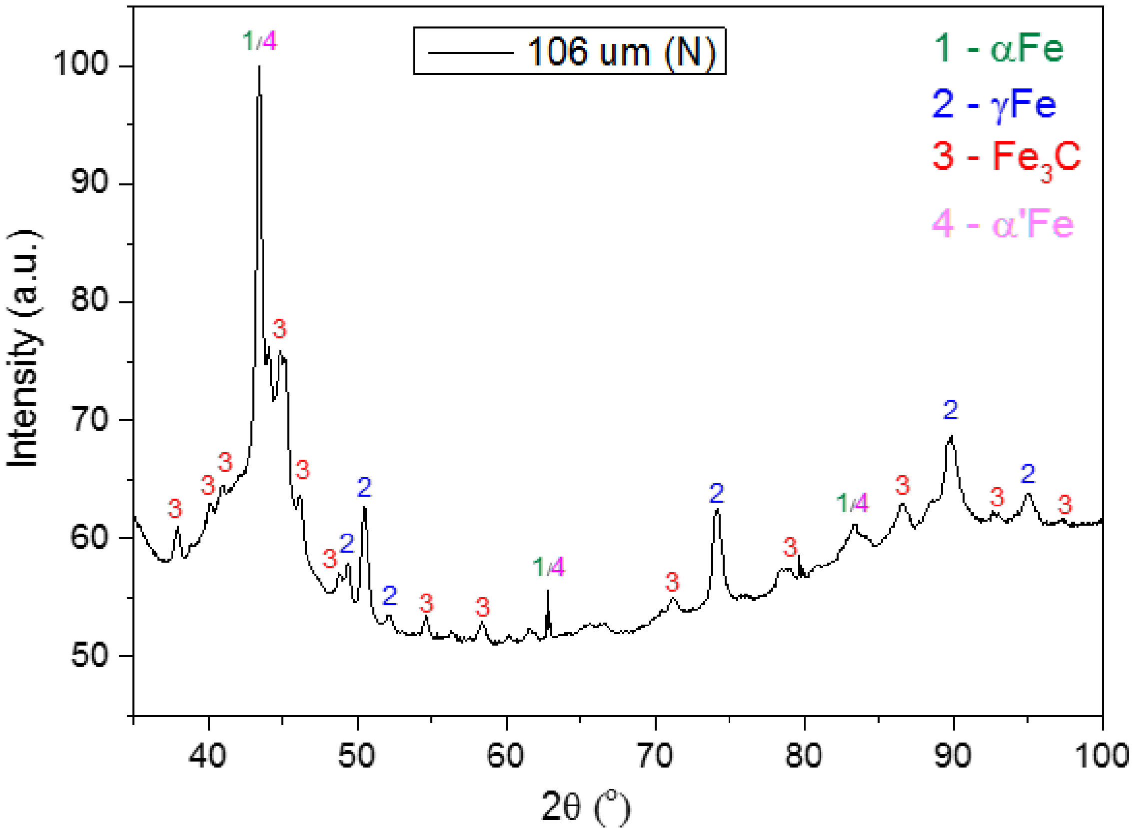

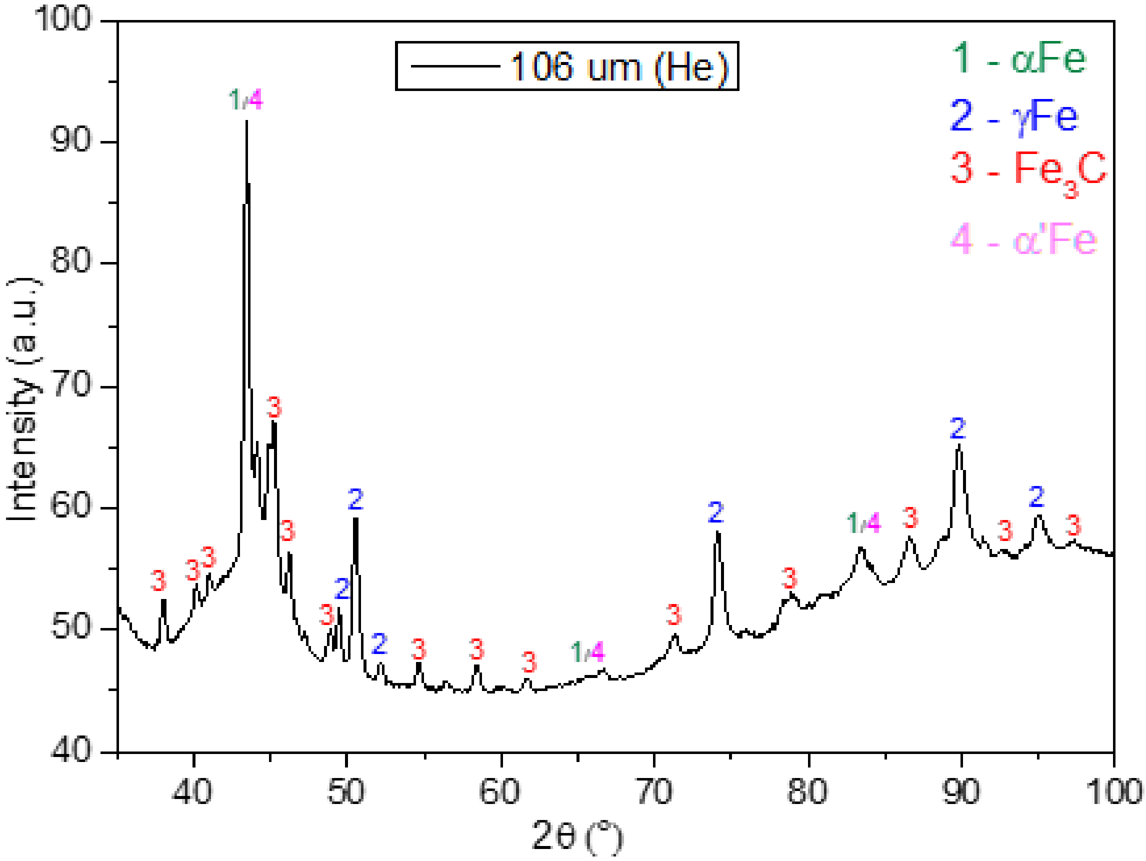

Appendix B2-6: XRD phases trace profiles identified in ***106 μm droplet*** cooled in N_2 & He.

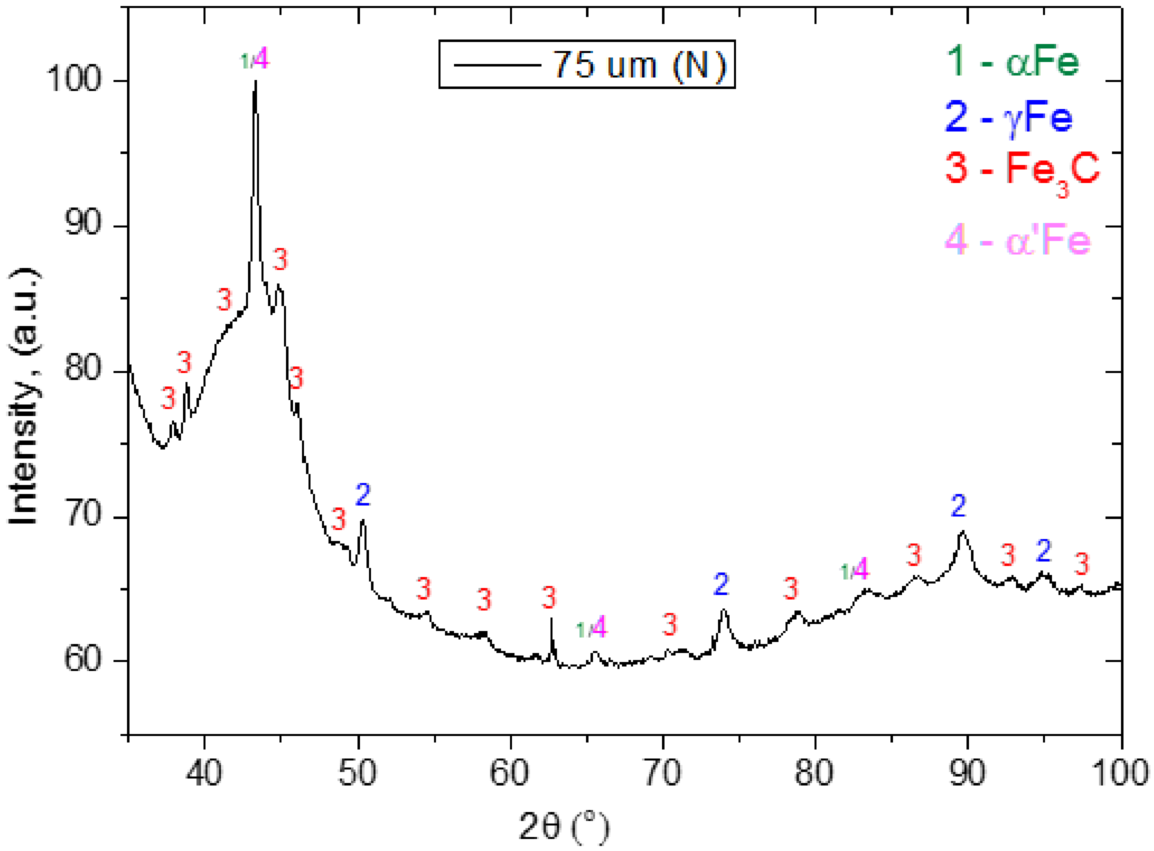

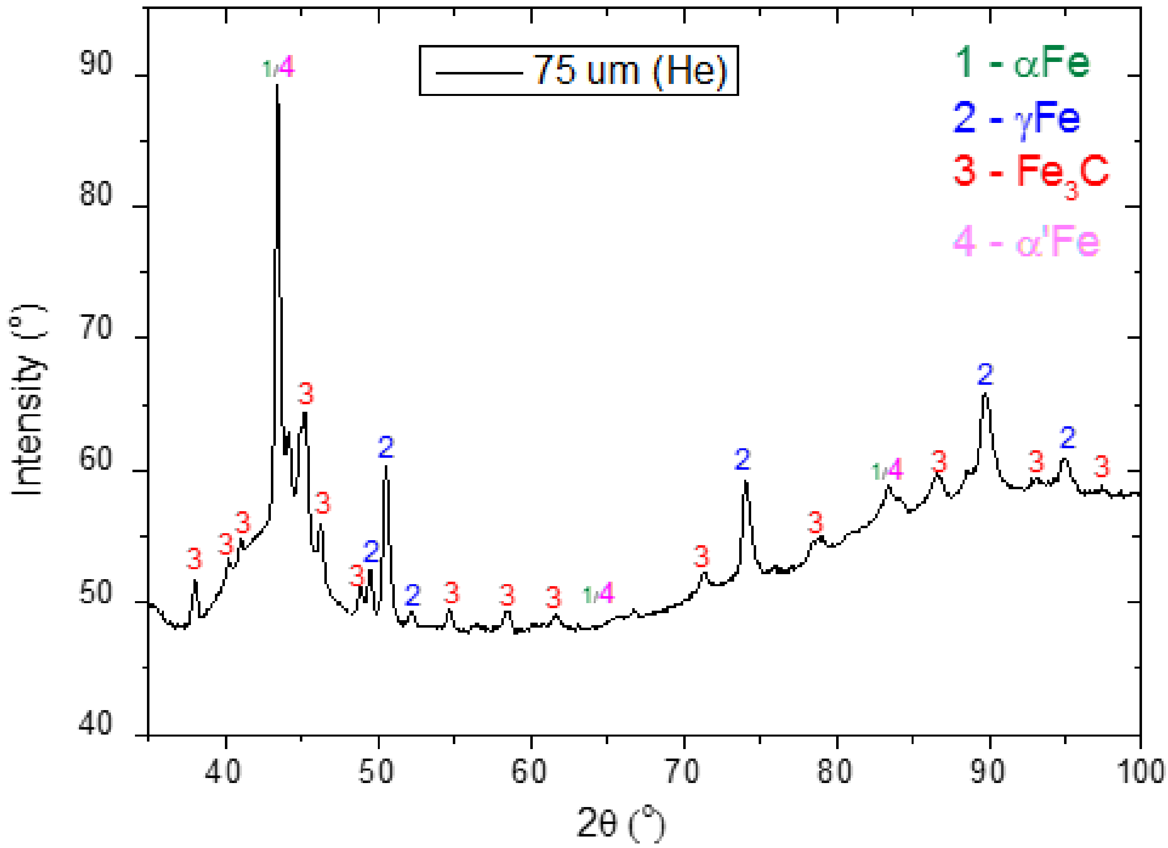

Appendix B2-7: XRD phases trace profiles identified in ***75 µm droplet*** cooled in N_2 & He.

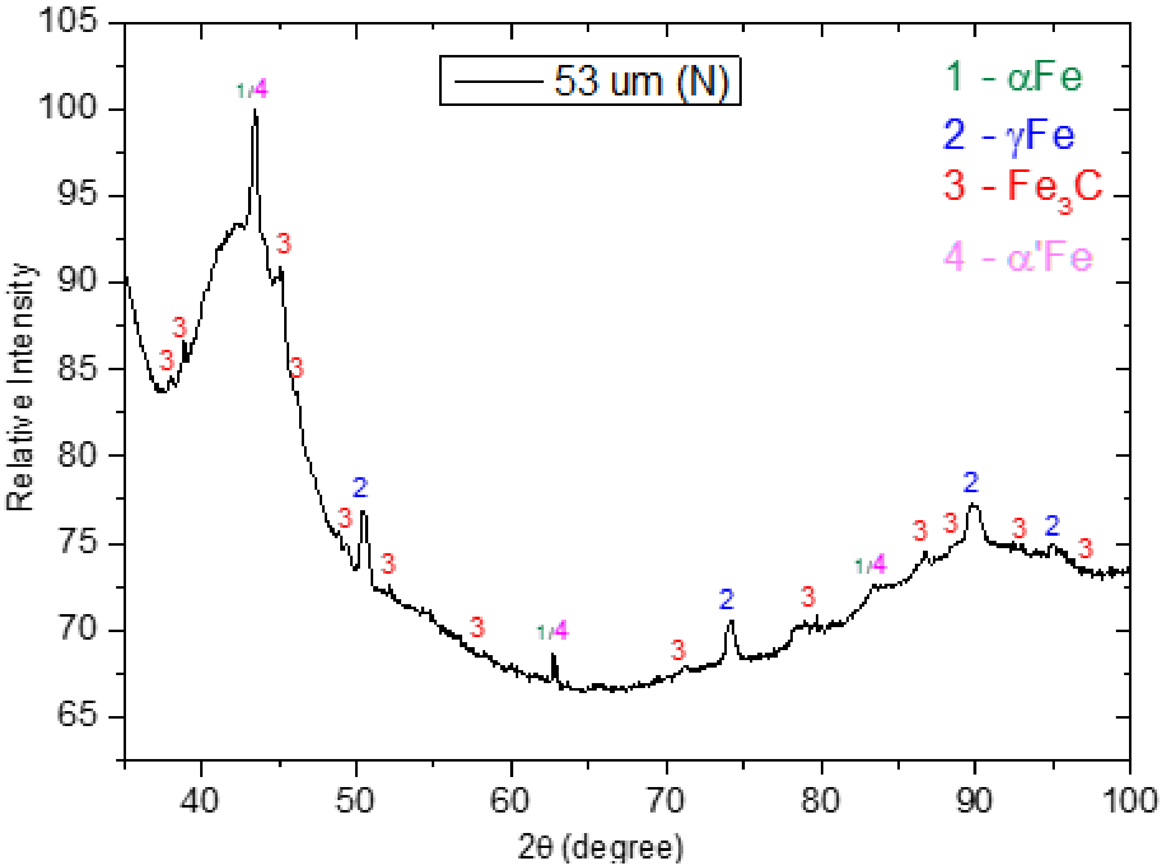

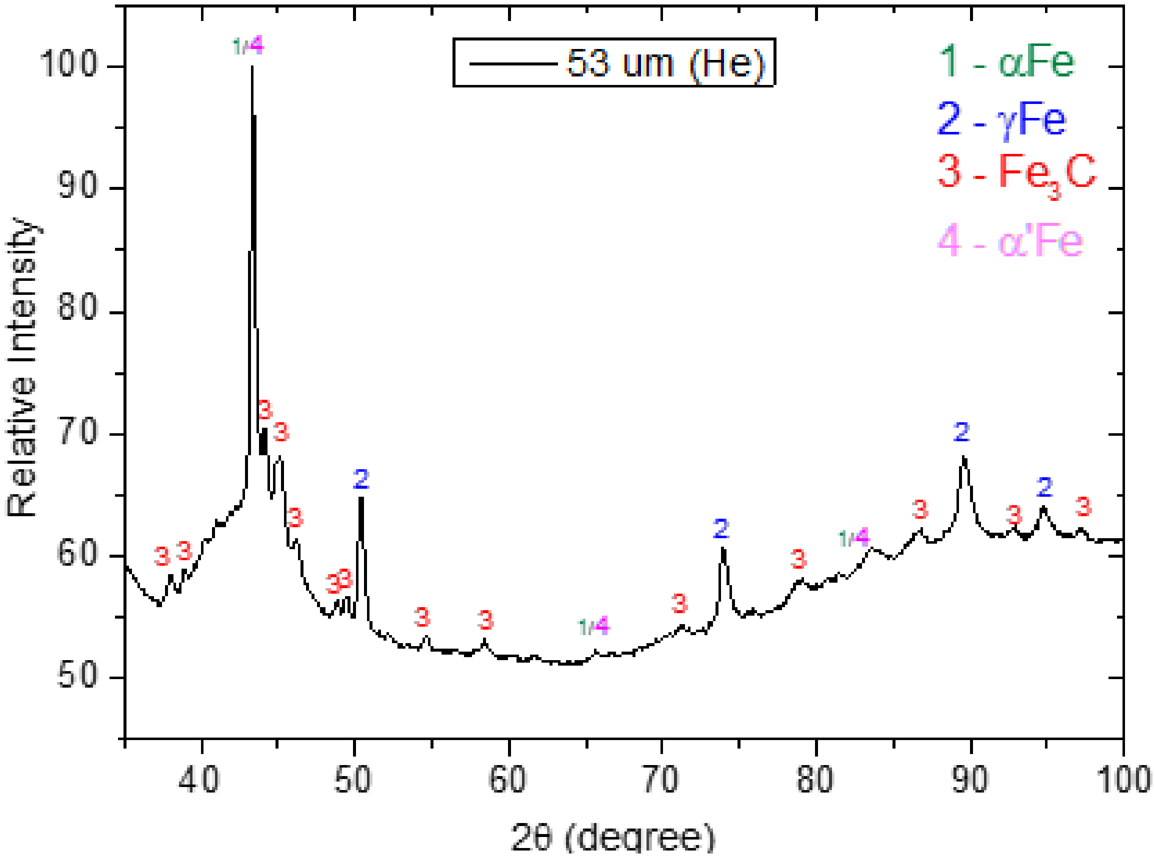

Appendix B2-8: XRD phase profiles identified in 53 µm droplet cooled in N_2 & He.

Appendix C-1:

Microstructure profiles of different droplet sizes cooled in N_2 environment.

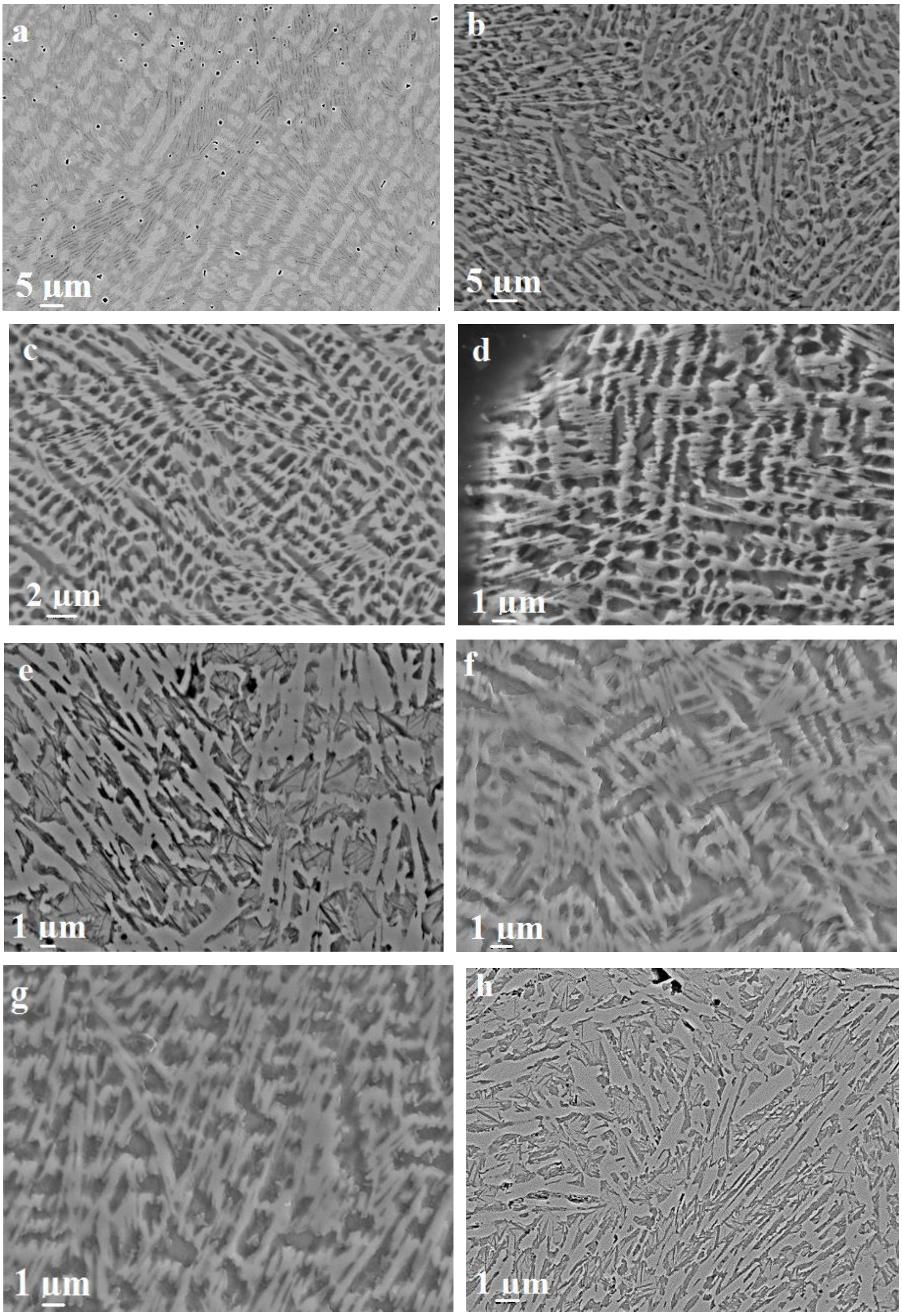

SEM micrographs of N_2 cooled droplets of different cooling rates: (a) 850 µm, (b) 500 µm, (c) 300 µm, (d) 212 µm, (e) 150 µm, (f) 106 µm, (g) 75 µm and (h) 53 µm. The morphological changes in the microstructure of droplets with diameters < 150 µm clearly show transition from dendritic to needle like structures.

Appendix C-2:

Microstructure profiles of different droplet sizes cooled in He environment.

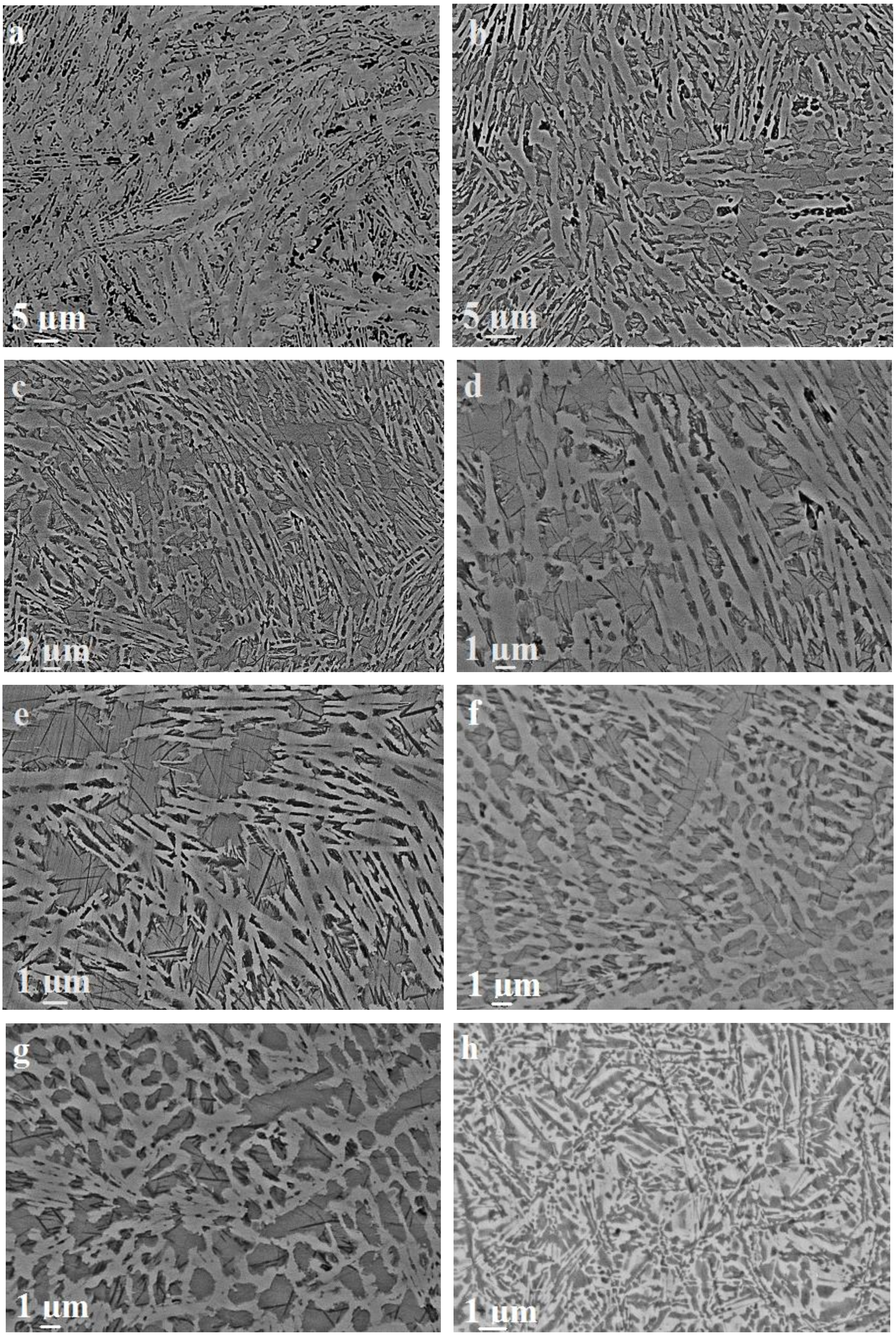

SEM micrographs of He cooled droplet sizes corresponding to different cooling rate: (a) 850 µm, (b) 500 µm, (c) 300 µm, (d) 212 µm, (e) 150 µm, (f) 106 µm, (g) 75 µm and (h) 53 µm.

Appendix D: DTA Results for some selected droplet sizes.

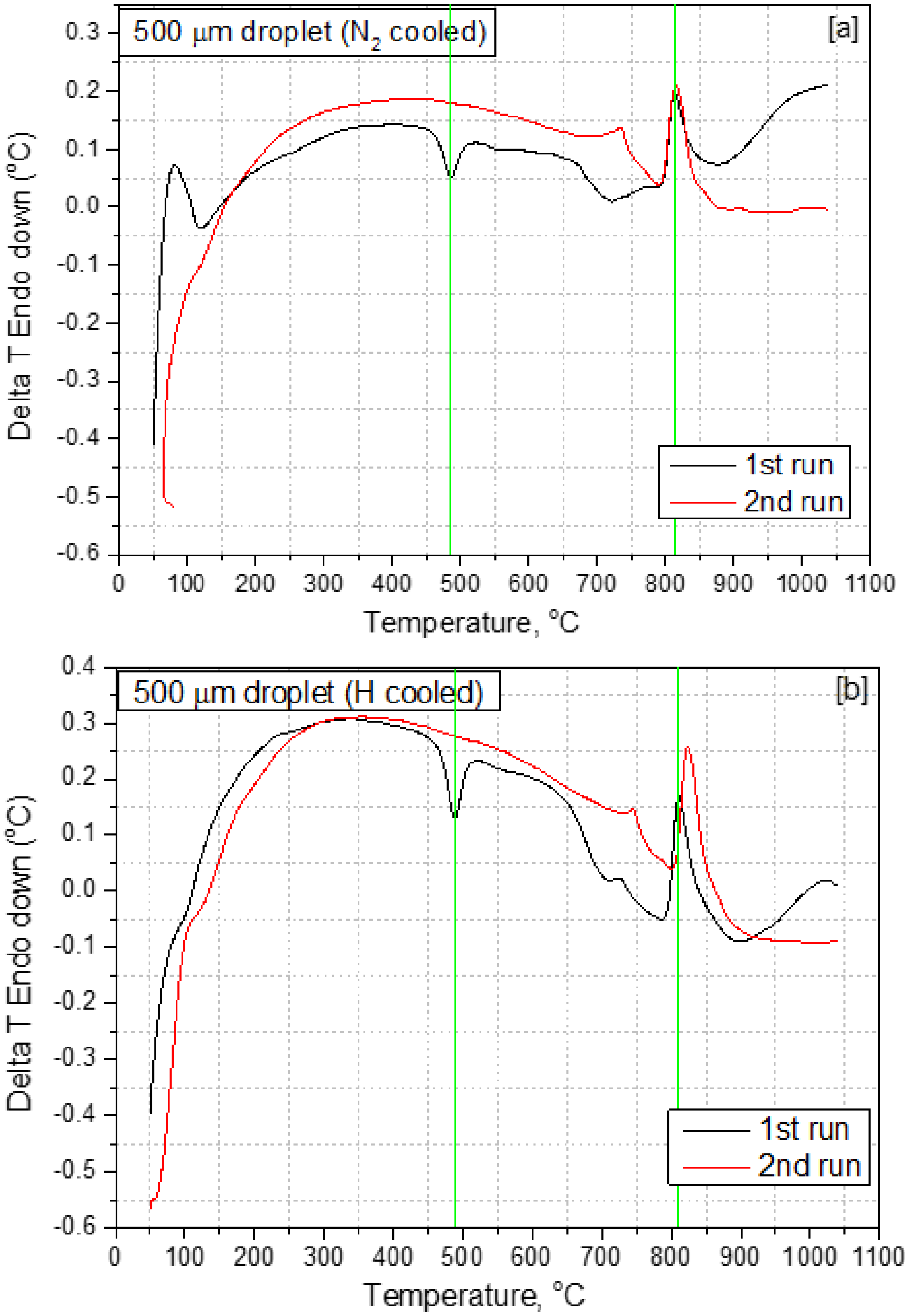

Appendix D-1: Show the DTA trace for the 500 μm droplet as a representative of the big particles (850 ≥ x ≤ 300) size group cooled in (a) Nitrogen and (b) Helium gas.

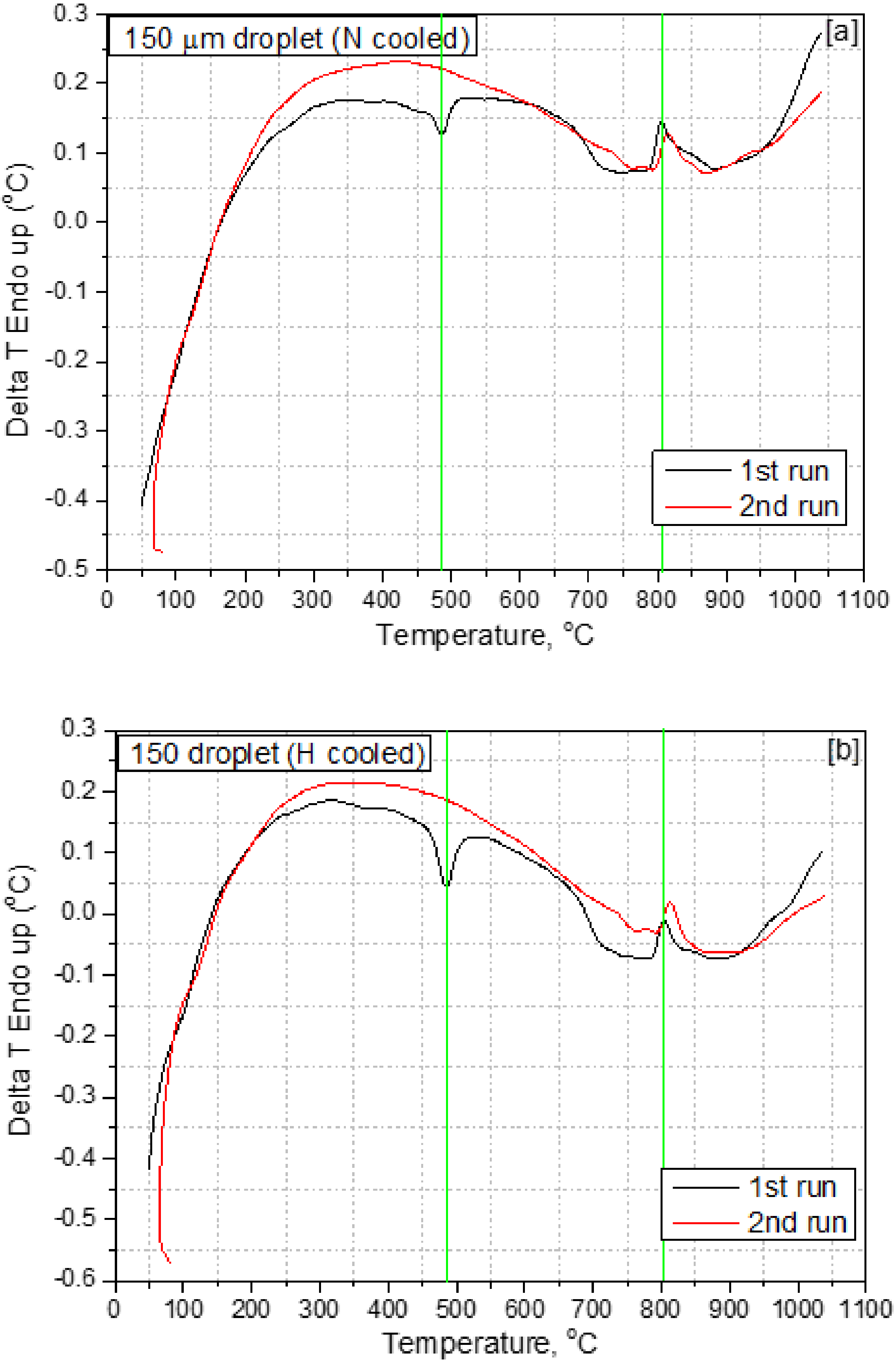

Appendix D-2: Show the DTA trace for the 150 µm droplet as a representative of medium particles (212 ≥ x ≤ 106) size group cooled in (a) Nitrogen and (b) Helium gas.

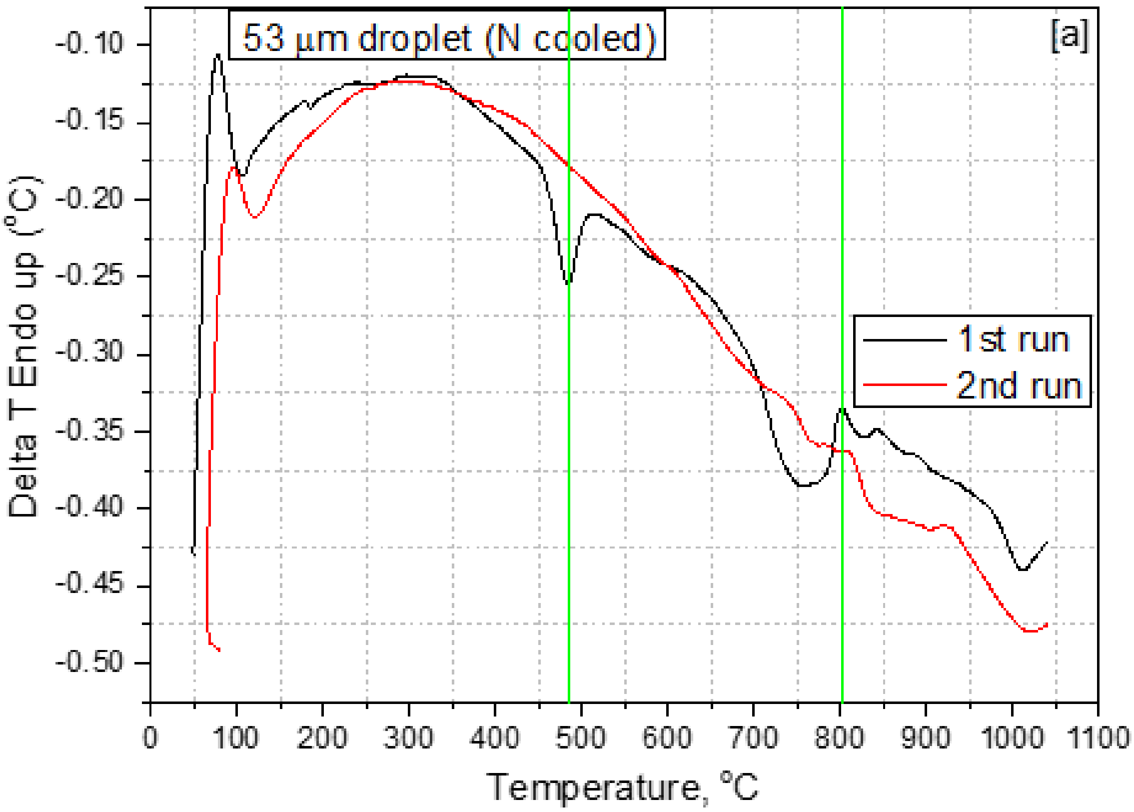

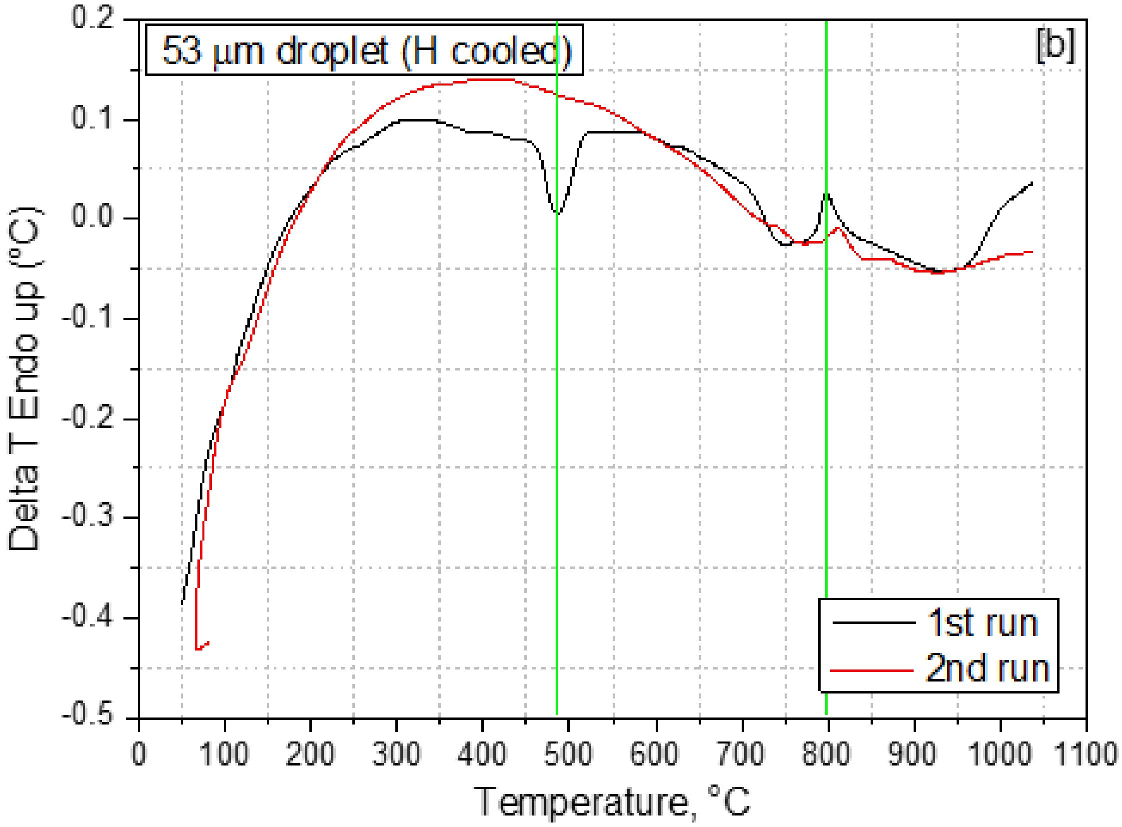

Appendix D-3: Show the DTA trace for the 53 µm droplet as a representative of medium particles (75 ≥ x ≤ 38) size group cooled in (a) Nitrogen and (b) Helium gas.

Appendix E:

Identified phases and their crystallographic parameters

Table D-1below show principal evolved phases identified in the course of this study which are mainly: Ferrite (α-Fe) phase, Retained austenite (γ-Fe), Cementite (Fe_3C) and Martensite (α'-Fe). The progressive evolution of these phases is irrespective of the cooling medium. This ranges from the α-Fe rich as-cast to the retained γ in big droplets and finally to α'-Fe in the smaller droplets. Listed in the table are derived parameters that define each phase obtained from XRD diffraction database including peculiar crystal parameters, the diffraction peak list as well as standard diffraction angel 2θ (°C) and the value of phase percentage intensity (I%).

The tables below show standard crystallographic parameters of the evolved phases' standard intensity data obtained from XRD peak list.

α-Fe phase: (ferrite)

Reference code:	04-011-9042	*Space group number:*	229
Compound:	Iron	*Common name:*	α-Fe
Empirical formula:	Fe	*Chemical formula:*	Fe
Crystal system:	Cubic	*Space group:*	Im-3m

a = b = c = 2.8660 Å and α = β = γ = 90°

No.	h	k	l	d [A]	2Theta[deg]	I [%]
1	1	1	0	2.02660	44.679	100.0
2	2	0	0	1.43300	65.033	11.6
3	2	1	1	1.17000	82.352	17.8
4	2	2	0	1.01330	98.962	4.6
5	3	1	0	0.90630	116.410	6.4
6	2	2	2	0.82730	137.214	1.7

γ-Fe phase: (austenite)

Reference code:	04-016-6641	*Space group number:*	225
Compound:	Iron	*Common name:*	γ-Fe
Empirical formula:	Fe	*Chemical formula:*	Fe

Crystal system: Cubic *Space group:* Fm-3m

a = b = c = 3.6200 Å and α = β = γ = 90°

No.	h	k	l	d [A]	2Theta[deg]	I [%]
1	1	1	1	2.09000	43.254	100.0
2	2	0	0	1.81000	50.375	43.0
3	2	2	0	1.27990	74.004	18.2
4	3	1	1	1.09150	89.776	17.2
5	2	2	2	1.04500	94.975	4.7
6	4	0	0	0.90500	116.676	2.1
7	3	3	1	0.83050	136.101	7.0
8	4	2	0	0.80950	144.193	6.8

Fe_3C phase: (cementite)

Reference code:	04-013-2473	*Space group number:*	62
Compound:	Iron	*Common name:*	Fe_3C
Empirical formula:	Fe_3C	*Chemical formula:*	Fe_3C
Crystal system:	Orthorhombic	*Space group:*	Pnma

a = 5.0580 Å; b = 6.7030 Å; c = 4.5060 Å and α = β = γ = 90°

No.	h	k	l	d [A]	2Theta[deg]	I [%]
1	0	1	1	3.73960	23.774	0.5
2	1	0	1	3.36450	26.470	0.6
3	0	2	0	3.35150	26.575	0.6
4	1	1	1	3.00700	29.686	1.9
5	2	0	0	2.52900	35.467	1.8
6	1	2	1	2.37450	37.859	29.0
7	2	1	0	2.36620	37.997	26.7
8	0	0	2	2.25300	39.985	23.2
9	2	0	1	2.20540	40.886	20.9
10	2	1	1	2.09490	43.148	57.0
11	1	0	2	2.05810	43.959	51.1
12	2	2	0	2.01880	44.861	50.1

13	0	3	1	2.00180	45.263	100.0
14	1	1	2	1.96740	46.100	49.4
15	0	2	2	1.86980	48.657	2.0
16	1	3	1	1.86130	48.894	28.8
17	2	2	1	1.84230	49.432	43.8
18	1	2	2	1.75380	52.108	15.7
19	2	0	2	1.68230	54.501	0.6
20	0	4	0	1.67440	54.780	13.9
21	2	3	0	1.67440	54.780	13.9
22	2	1	2	1.63170	56.339	6.2
23	3	0	1	1.57910	58.393	13.6
24	2	3	1	1.56960	58.781	0.8
25	3	1	1	1.53700	60.155	2.8
26	1	3	2	1.51380	61.175	0.5
27	2	2	2	1.50350	61.639	7.1
28	1	4	1	1.50000	61.799	2.5
29	0	1	3	1.46560	63.416	0.1
30	1	0	3	1.43990	64.683	0.1
31	3	2	1	1.42850	65.263	0.2
32	1	1	3	1.40770	66.351	2.4
33	2	4	0	1.39690	66.931	4.1
34	3	0	2	1.34990	69.589	0.1
35	0	4	2	1.34390	69.945	1.4
36	2	3	2	1.34390	69.945	1.4
37	2	4	1	1.33430	70.523	2.2
38	3	1	2	1.32290	71.222	14.3
39	1	2	3	1.32290	71.222	14.3
40	1	4	2	1.29950	72.707	0.1
41	2	0	3	1.29140	73.237	0.1
42	3	3	1	1.28950	73.363	0.3
43	0	5	1	1.28490	73.668	1.1
44	2	1	3	1.26810	74.810	0.1
45	4	0	0	1.26450	75.060	0.1
46	3	2	2	1.25210	75.934	2.1
47	1	5	1	1.24540	76.416	1.2
48	0	3	3	1.24540	76.416	1.2

49	4	0	1	1.21750	78.498	10.4
50	1	3	3	1.21030	79.056	13.0
51	2	2	3	1.20500	79.472	0.2
52	4	1	1	1.19790	80.038	2.1
53	2	4	2	1.18720	80.908	1.0
54	2	5	0	1.18450	81.131	4.6
55	3	3	2	1.15540	83.625	14.5
56	3	4	1	1.14920	84.179	0.6
57	2	5	1	1.14560	84.505	7.8
58	0	0	4	1.12650	86.283	1.7
59	1	5	2	1.12330	86.589	7.0
60	3	0	3	1.12150	86.762	9.6
61	2	3	3	1.11720	87.180	5.1
62	0	6	0	1.11720	87.180	5.1
63	3	1	3	1.10610	88.279	1.4
64	1	0	4	1.10050	88.847	8.8
65	4	3	0	1.10050	88.847	8.8
66	1	4	3	1.09210	89.714	2.9
67	1	1	4	1.08510	90.452	2.3
68	4	3	1	1.06910	92.194	0.1
69	0	2	4	1.06780	92.339	0.1
70	3	2	3	1.06350	92.822	0.6
71	3	4	2	1.05120	94.240	0.6
72	2	5	2	1.04840	94.570	2.0
73	1	2	4	1.04480	94.999	1.0
74	2	0	4	1.02900	96.937	0.1
75	2	6	0	1.02200	97.827	0.6
76	3	5	1	1.02200	97.827	0.6
77	2	1	4	1.01710	98.462	0.5
78	4	4	0	1.00940	99.481	0.2
79	0	5	3	1.00090	100.637	1.1
80	0	6	2	1.00090	100.637	1.1
81	2	6	1	0.99660	101.235	0.8
82	4	3	2	0.98880	102.343	2.5
83	1	3	4	0.98700	102.603	0.3
84	5	0	1	0.98700	102.603	0.3

85	4	4	1	0.98500	102.894	0.5
86	2	2	4	0.98370	103.084	1.3
87	1	6	2	0.98180	103.364	3.5
88	1	5	3	0.98120	103.452	3.3
89	5	1	1	0.97650	104.154	0.6
90	4	1	3	0.95740	107.138	0.1
91	3	5	2	0.95120	108.157	0.9
92	5	2	1	0.94680	108.895	0.8
93	3	0	4	0.93670	110.642	0.8
94	0	7	1	0.93670	110.642	0.8
95	2	3	4	0.93470	110.998	0.4
96	0	4	4	0.93470	110.998	0.4
97	3	4	3	0.93200	111.482	0.3
98	4	2	3	0.92940	111.954	0.1
99	3	1	4	0.92760	112.284	0.1
100	5	0	2	0.92280	113.178	0.1
101	1	7	1	0.92120	113.480	0.4
102	4	4	2	0.92120	113.480	0.4
103	1	4	4	0.91990	113.728	0.4
104	4	5	0	0.91990	113.728	0.4
105	5	1	2	0.91420	114.830	0.8
106	3	6	1	0.91200	115.264	2.0
107	3	2	4	0.90210	117.276	0.9
108	4	5	1	0.90130	117.443	1.1
109	2	7	0	0.89550	118.676	0.1
110	0	1	5	0.89320	119.175	0.1
111	5	2	2	0.88970	119.948	2.9
112	4	3	3	0.88770	120.396	0.1
113	1	0	5	0.88770	120.396	0.1
114	1	6	3	0.88260	121.562	0.1
115	1	1	5	0.87960	122.265	0.1
116	2	7	1	0.87830	122.574	0.4
117	2	4	4	0.87690	122.908	0.4
118	1	7	2	0.86820	125.056	0.7
119	3	3	4	0.86380	126.190	5.7
120	3	6	2	0.86020	127.143	0.8

121	3	5	3	0.86020	127.143	0.8
122	1	2	5	0.85770	127.819	0.6
123	5	3	2	0.85300	129.123	0.9
124	4	5	2	0.85160	129.521	0.3
125	1	5	4	0.85020	129.923	1.9
126	5	4	1	0.85020	129.923	1.9
127	2	0	5	0.84890	130.300	0.7
128	2	6	3	0.84490	131.484	0.1
129	6	0	0	0.84300	132.061	1.1
130	2	1	5	0.84220	132.306	1.5
131	5	0	3	0.83900	133.305	0.6
132	0	8	0	0.83790	133.654	0.2
133	4	4	3	0.83790	133.654	0.2
134	0	3	5	0.83580	134.332	3.4
135	2	7	2	0.83250	135.423	2.1
136	5	1	3	0.83250	135.423	2.1
137	6	0	1	0.82860	136.758	0.1
138	1	3	5	0.82460	138.182	0.9
139	2	2	5	0.82310	138.733	4.7
140	4	6	1	0.82310	138.733	4.7
141	3	7	1	0.81880	140.362	0.2
142	6	2	0	0.81750	140.870	0.9
143	3	4	4	0.81750	140.870	0.9
144	4	2	4	0.81630	141.347	0.8
145	2	5	4	0.81630	141.347	0.8
146	5	2	3	0.81390	142.322	1.7
147	1	8	1	0.81300	142.696	0.7
148	5	4	2	0.80840	144.679	0.9
149	6	2	1	0.80440	146.515	1.2

α'-phase: (martensite)

Reference code:	04-014-0361	*Space group number:*	139
Compound:	α'-Fe	*Common name:*	α'-Fe
Empirical formula:	α'-Fe	*Chemical formula:*	α'-Fe
Crystal system:	Tetragonal	*Space group:*	14/mm

a = b = c = 2.8232 Å and α = β = γ = 90°

No.	h	k	l	d [A]	2Theta[deg]	I [%]
1	1	0	1	2.01190	45.023	100.0
2	1	1	0	1.99630	45.395	49.5
3	0	0	2	1.43390	64.987	6.1
4	2	0	0	1.41160	66.144	11.3
5	1	1	2	1.16460	82.818	9.1
6	2	1	1	1.15550	83.616	17.3
7	2	0	2	1.00590	99.953	4.7
8	2	2	0	0.99820	101.012	2.3
9	1	0	3	0.90540	116.594	3.3
10	3	0	1	0.89420	118.957	3.3
11	3	1	0	0.89280	119.263	3.3
12	2	2	2	0.81920	140.207	2.7

Appendix F:

TEM indexing for confirmation of identified phases

Phase confirmation by TEM indexing based on XRD identified phase peak list and parameters peculiar to each phase.

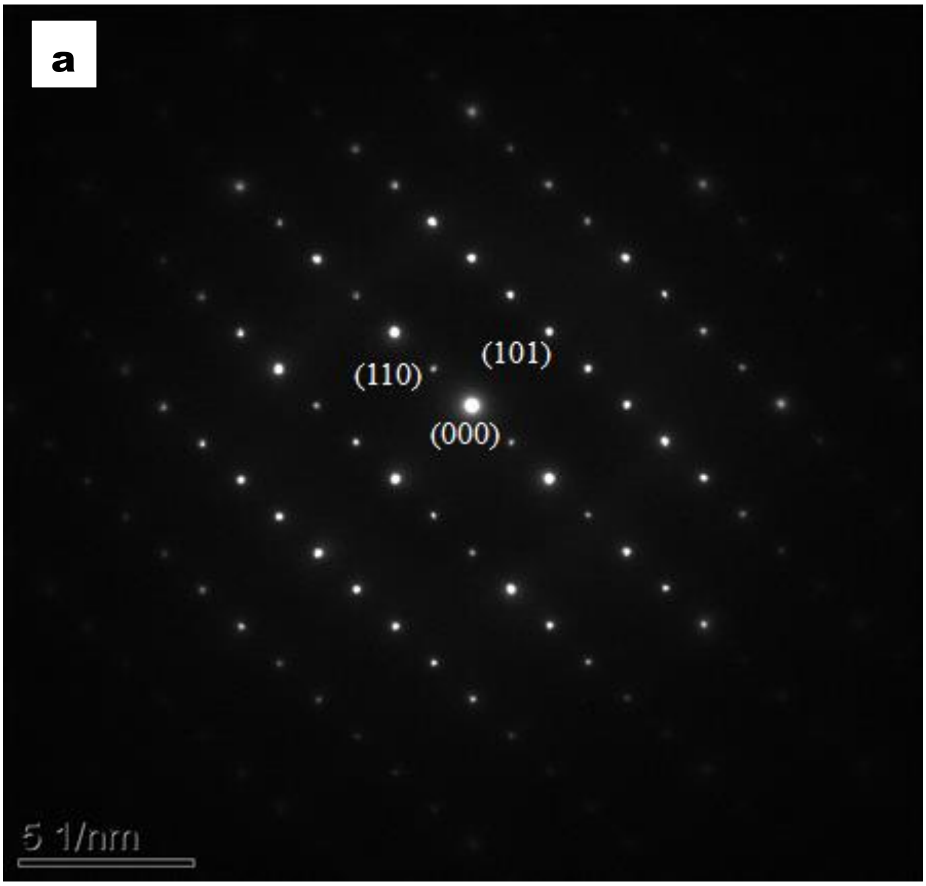

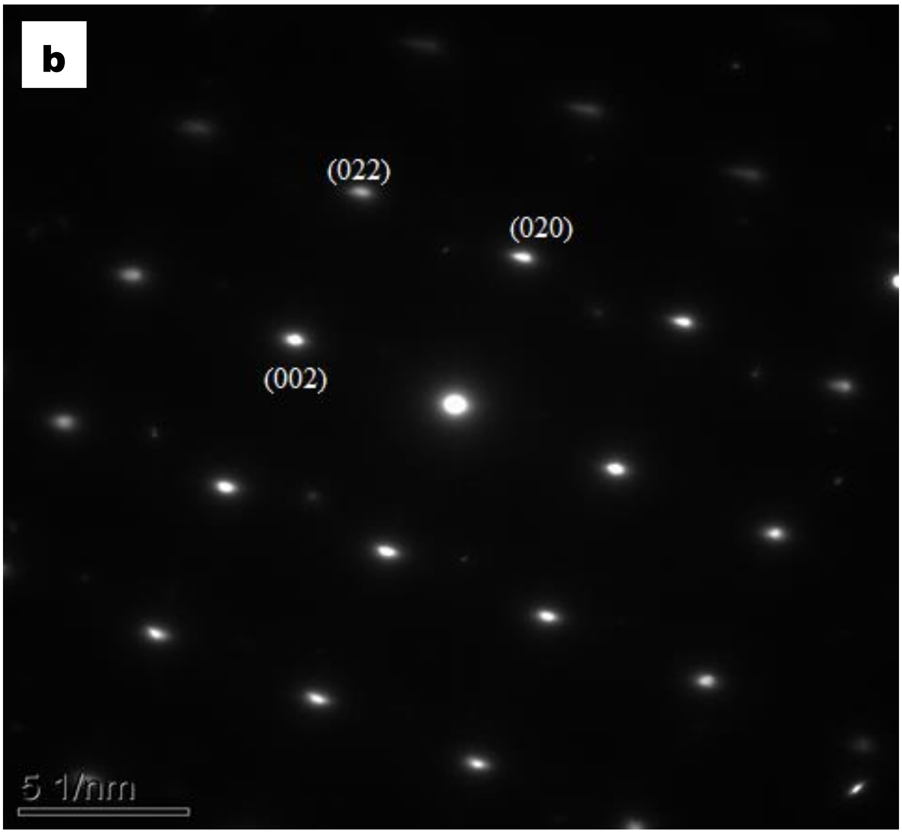
b
(022)
(020)
(002)
5 1/nm

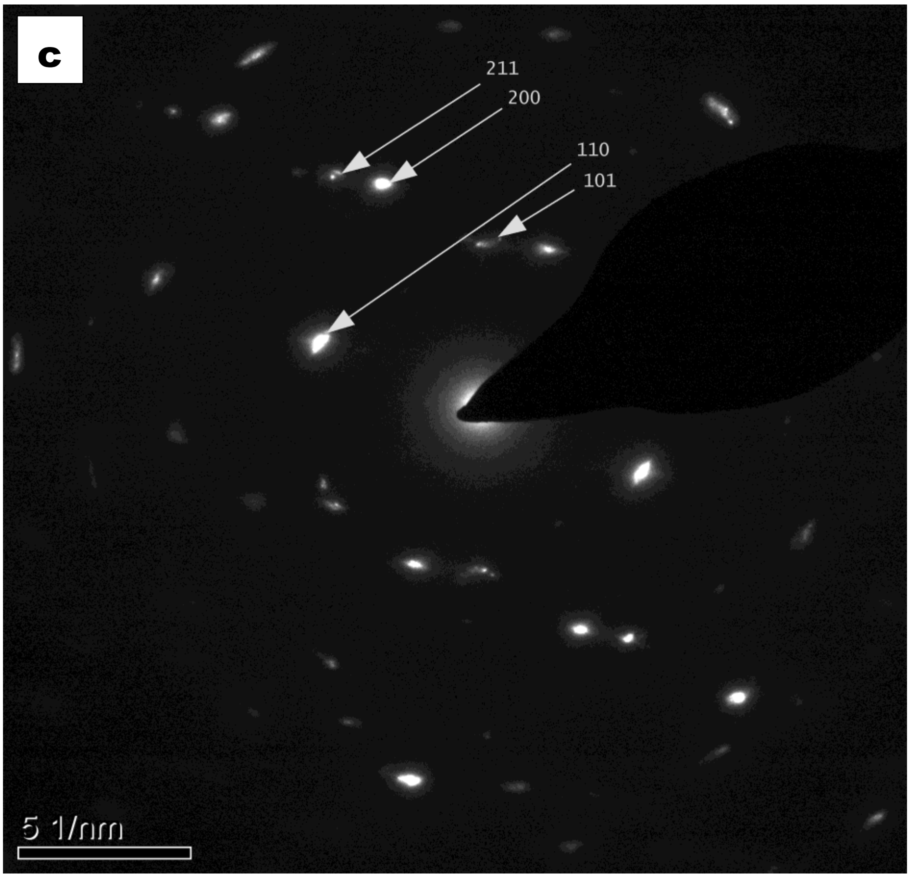
c
211
200
110
101
5 1/nm

Picture Attachments

Some micrographs of the As-cast, Crucible residue & drop-tube samples

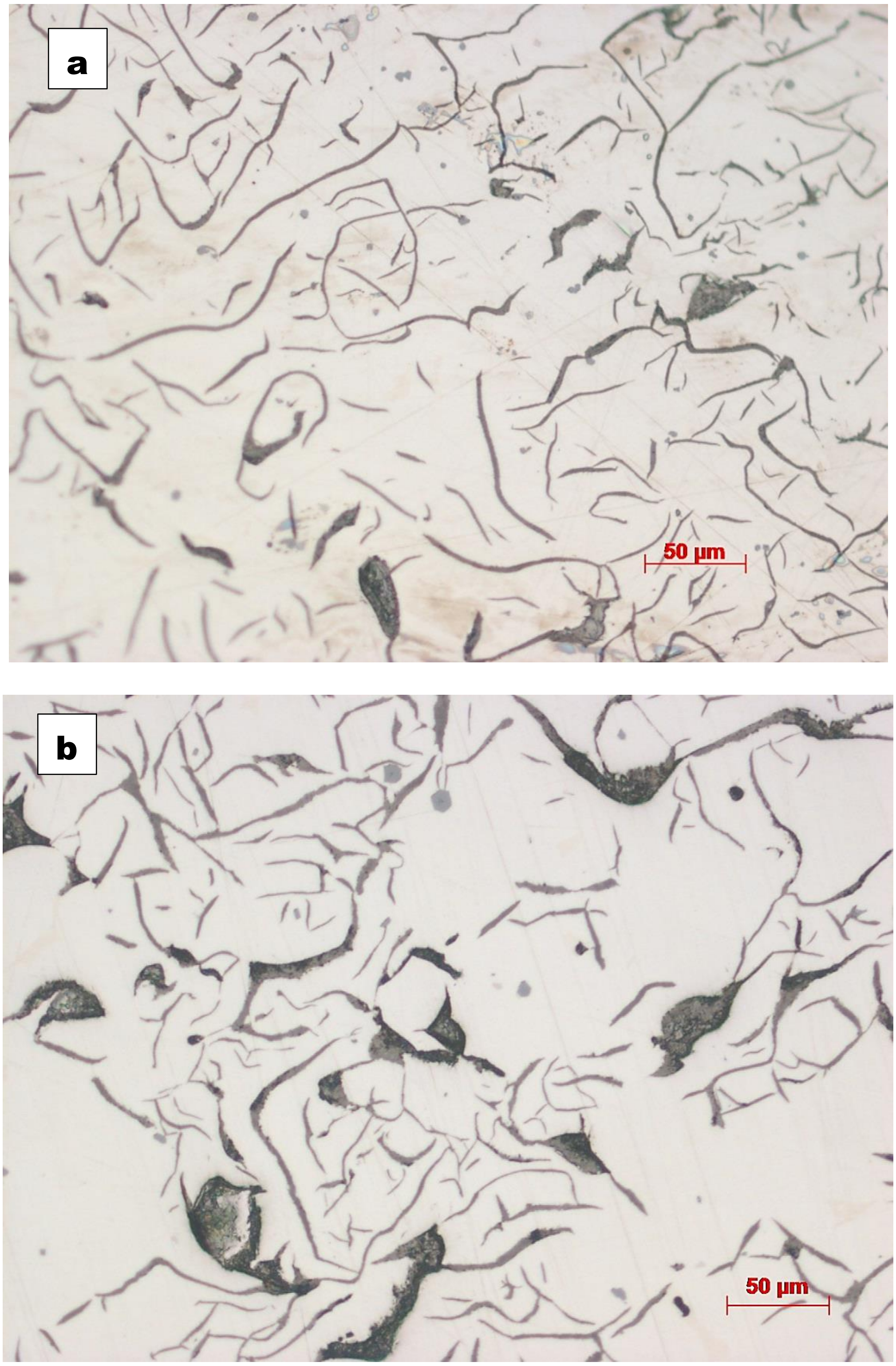

Picture 1: Optical micrographs of the unetched (a) as-cast and (b) Crucible residue samples of the same composition under same magnification; showing randomly well distributed type A graphite flakes which is typical of grey cast iron but with more chucky graphite noticed in (b) as a result of constrained cooling in the furnace.

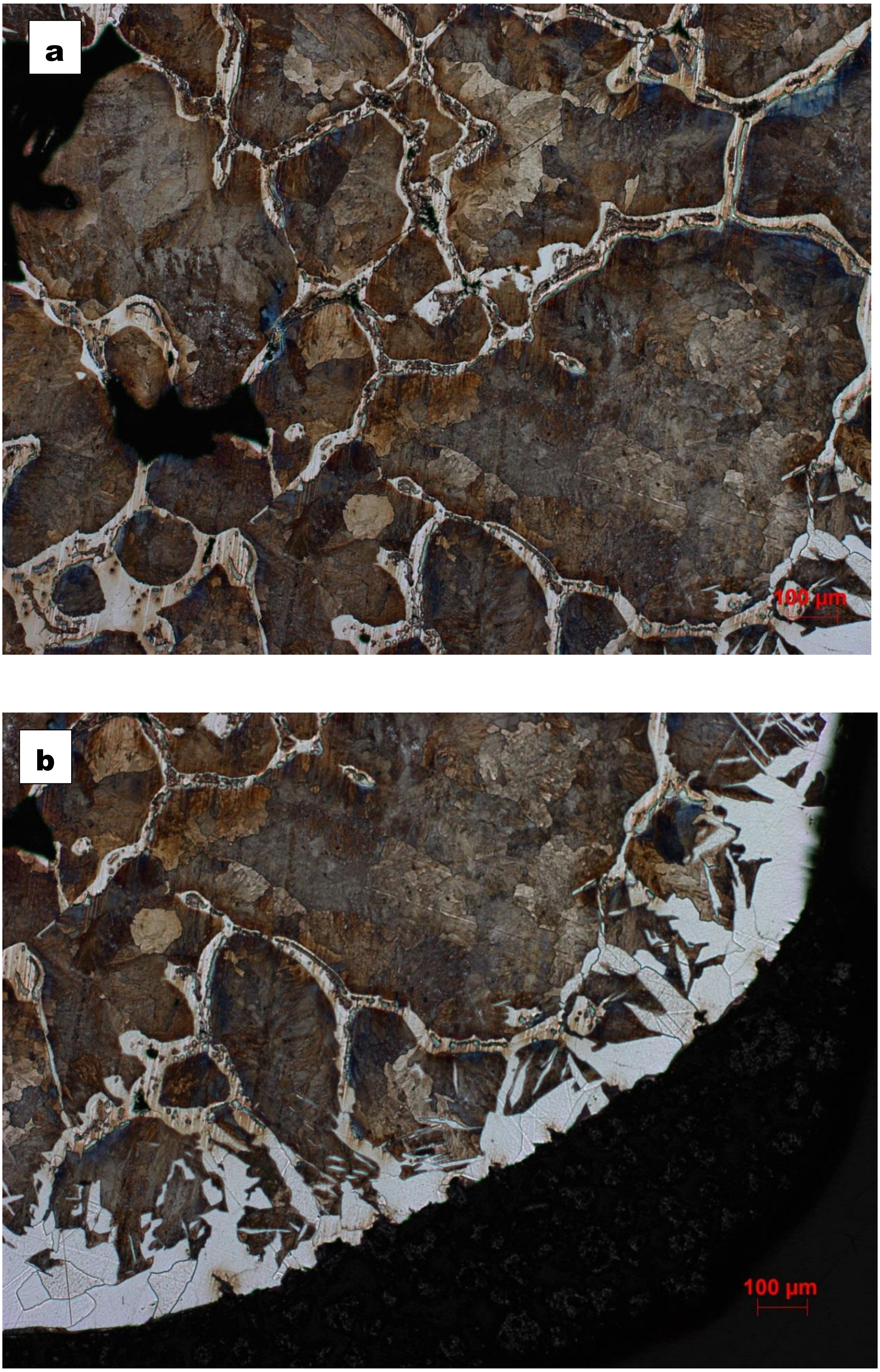

Picture 2: Optical micrograph of 4% Picral etched as-cast sample at (a) the center and (b) near the edge; showing the free ferrite (white) in pearlite (dark brown) matrix.

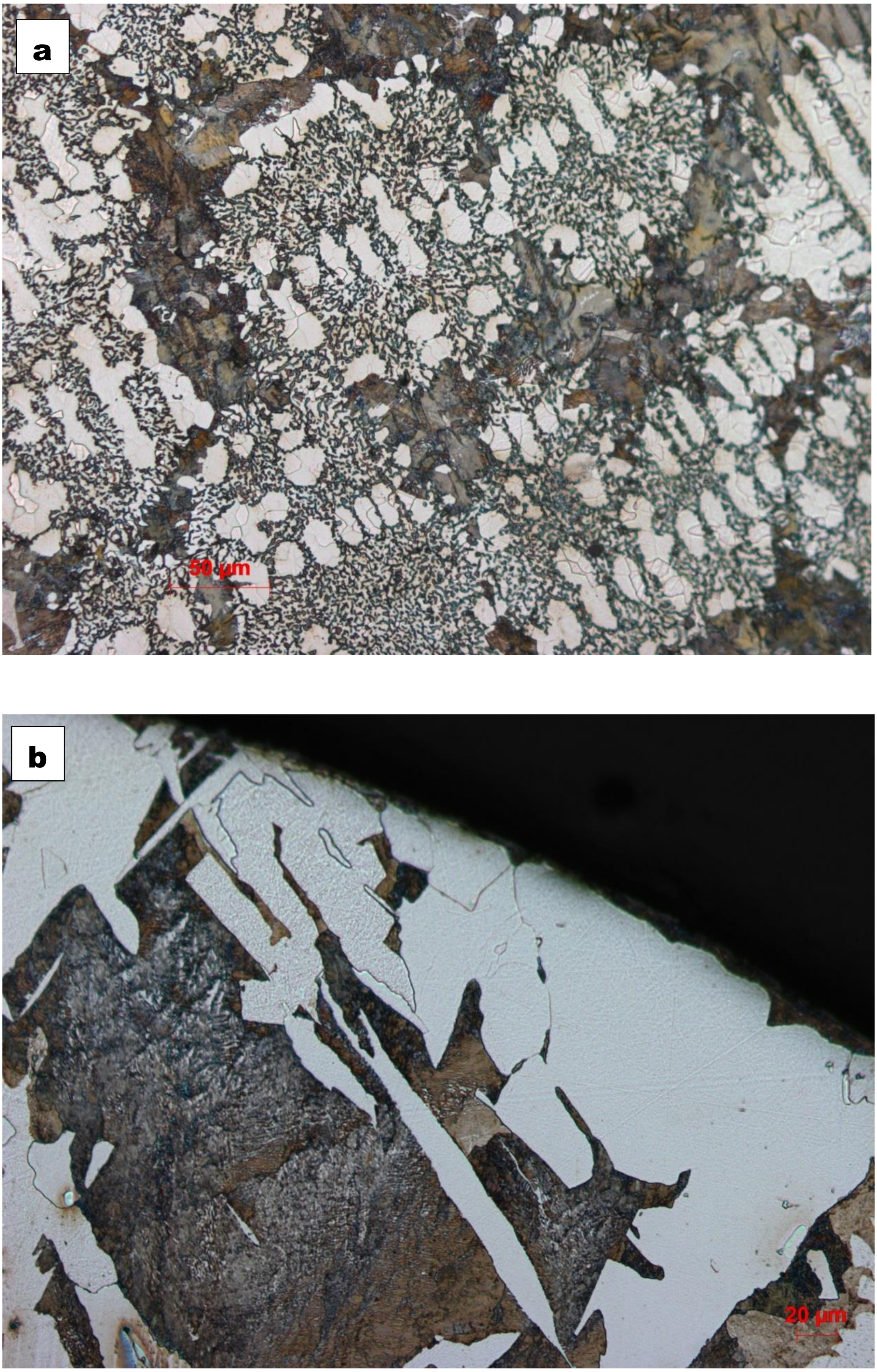

Picture 3: Enlarged sections of the (a) central portion and (b) edge of the 4% Picral etched sample to show the ferrite segregation and the pearlitic nature of the matrix.

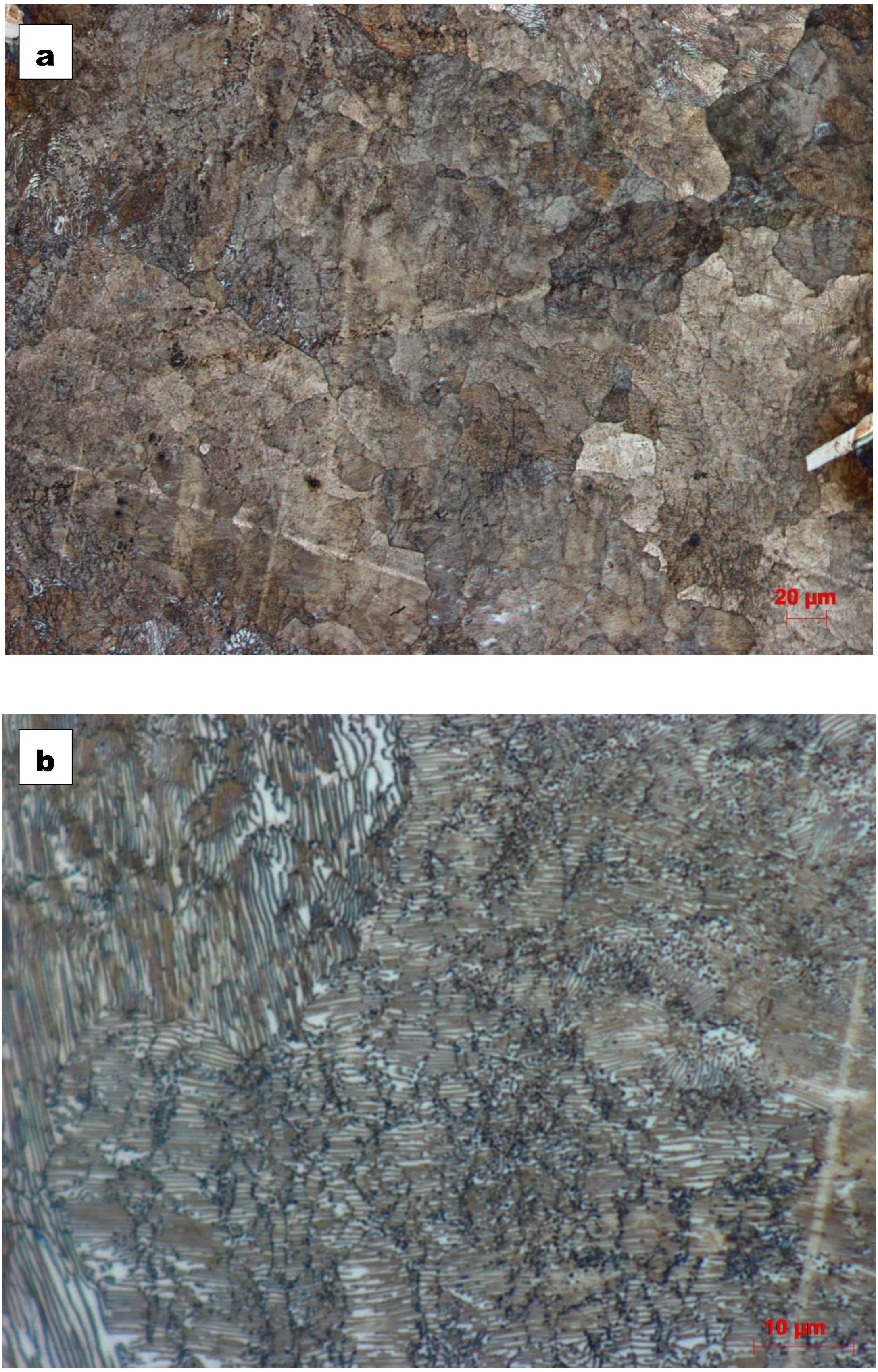

Picture 4: Further magnification of the optical micrographs focused on (a) the center and (b) edge portion of the as-cast sample; the revealing colony of lamellar pearlitic nature of the samples' matrix.

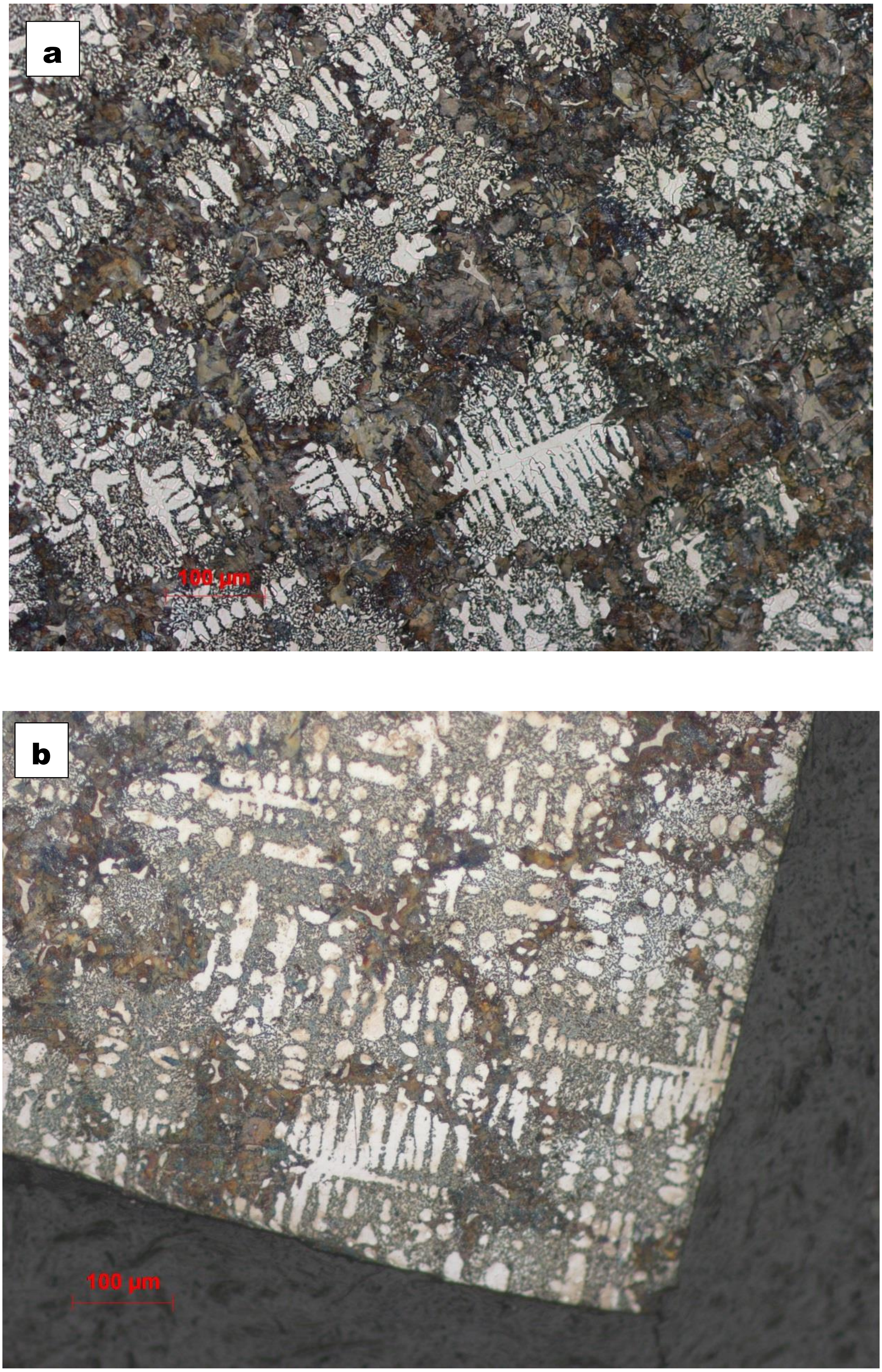

Picture 5: Microstructure of the edge zone of the as-cast sample which consist of (a) type D and (b) type B graphite mixed with ferrite; the dark zones are pearlitic (2% Nital etched; 20 sec.).

Picture 6: Micrograph of observed Rosette groupings (type B) in the middle-section of the as-cast sample as typically specified by ASTM A247 (2% Picral etched;15 sec.)

Picture 7: Micrograph of uniformly distributed observed graphite flakes with random orientation in the ferrite rich pearlite matrix classified as Type C graphite by ASTM A247 (4% Nital etched; 20 sec.).

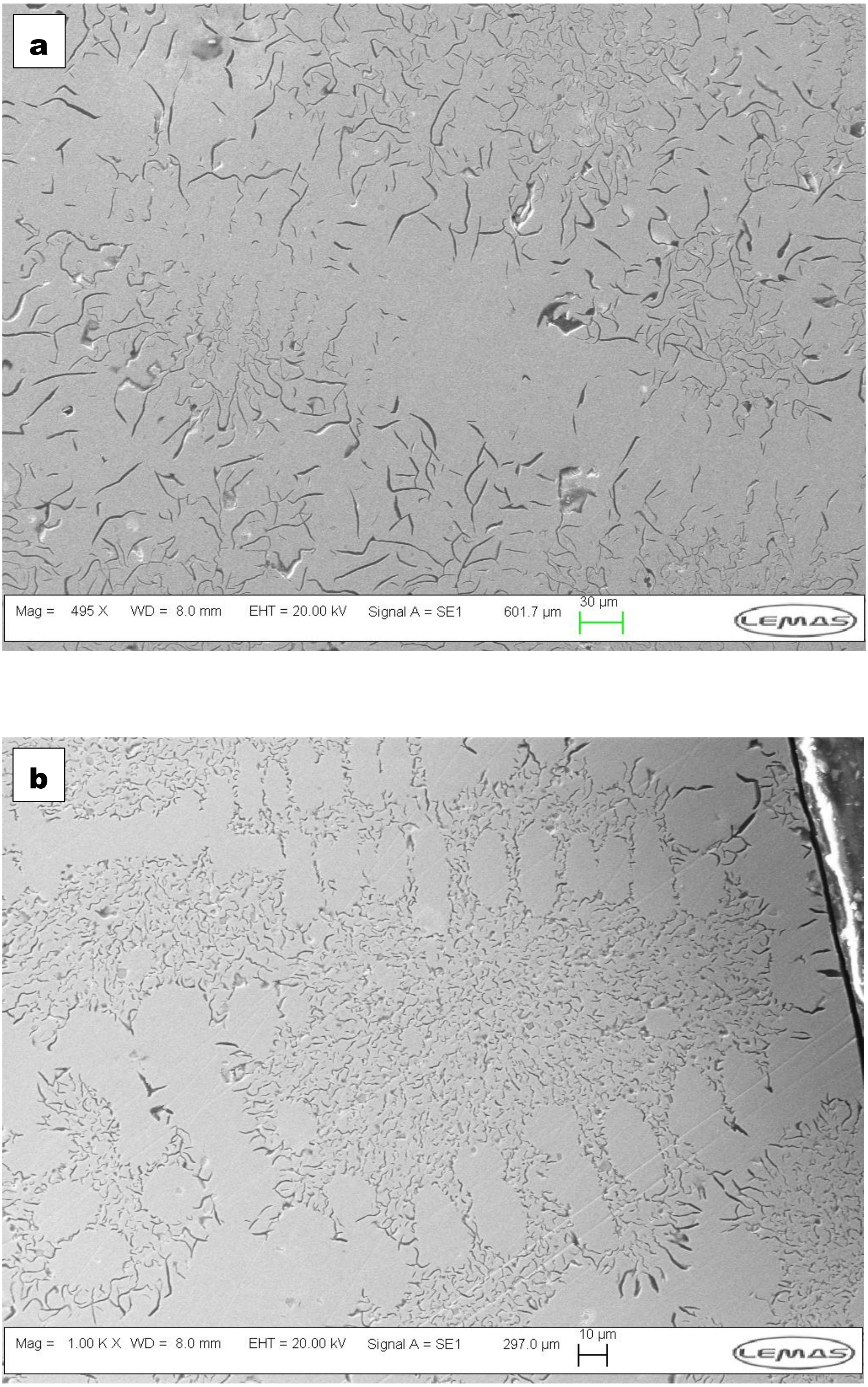

Picture 8: SEM micrographs of the as cast sample at (a) the center and (b) the edge of the sample showing the dendritic – graphitic nature of the sample.

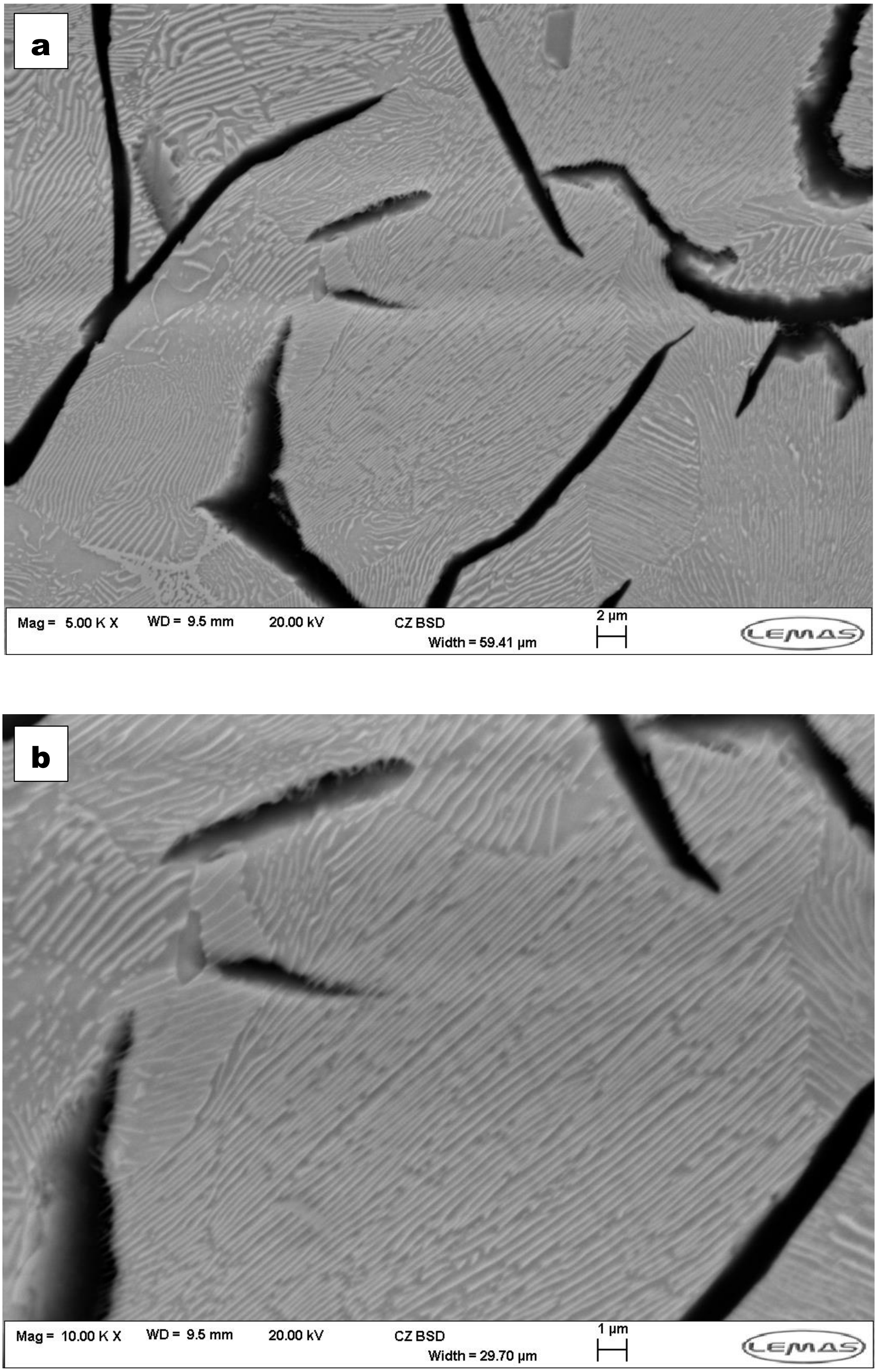

Picture 9: Enlarged SEM micrograph of the as-cast sample (a) showing the thick graphite tips and (b) fine lamellar ferrites in its pearlitic matrix (2% picral etched, 30 sec.).

Some micrographs of typical unetched, etched and colour etched droplet.

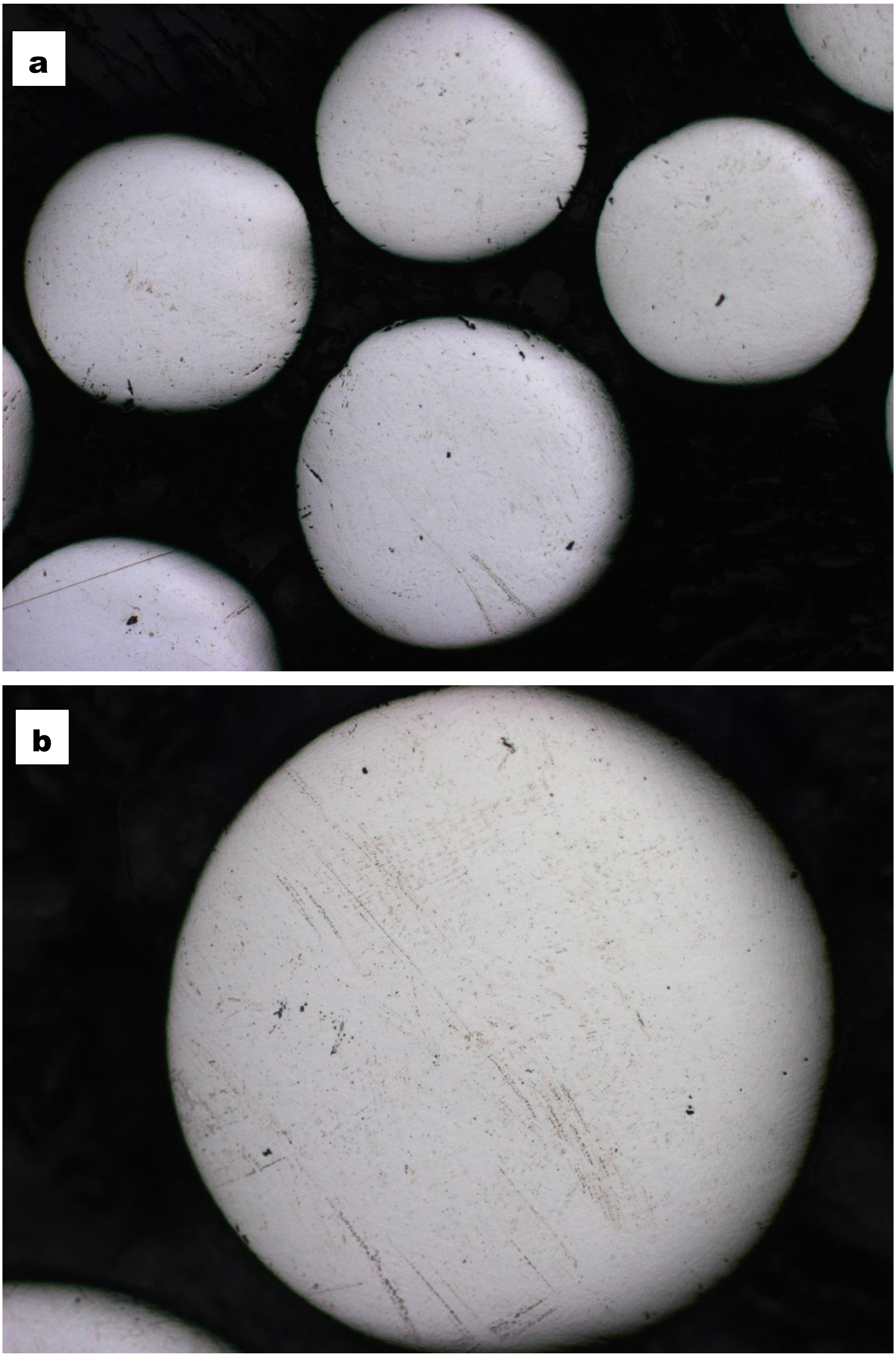

Picture 10: Optical micrographs of metallographically well prepared unetched (a) small and (b) relatively big droplets; the morphology show nothing important until such is properly etched.

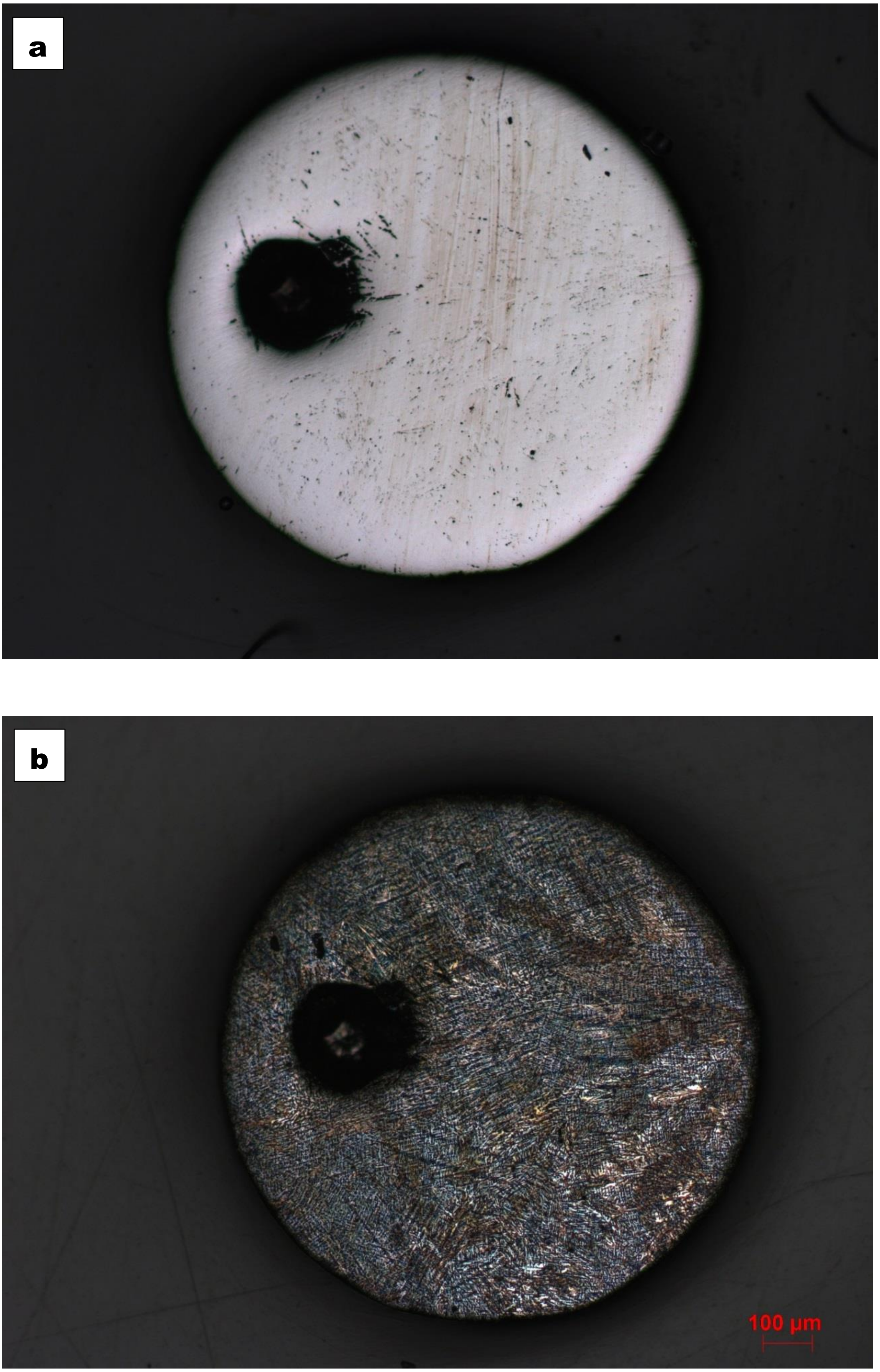

Picture 11: Difference between unetched and etched small droplet samples. (a) unetched and (b) etched (4% Picral, 20 sec. only)

Picture 12: Micrographs of (targeted) relatively big droplet (a) unetched and (b) pre-etched in 4% Picral for 20 sec. and then etched in 10% aqueous solution of Sodium Metabisulfite ($Na_2S_2O_5$) for 15 sec. with vigorous stirring. (Better than picral only).

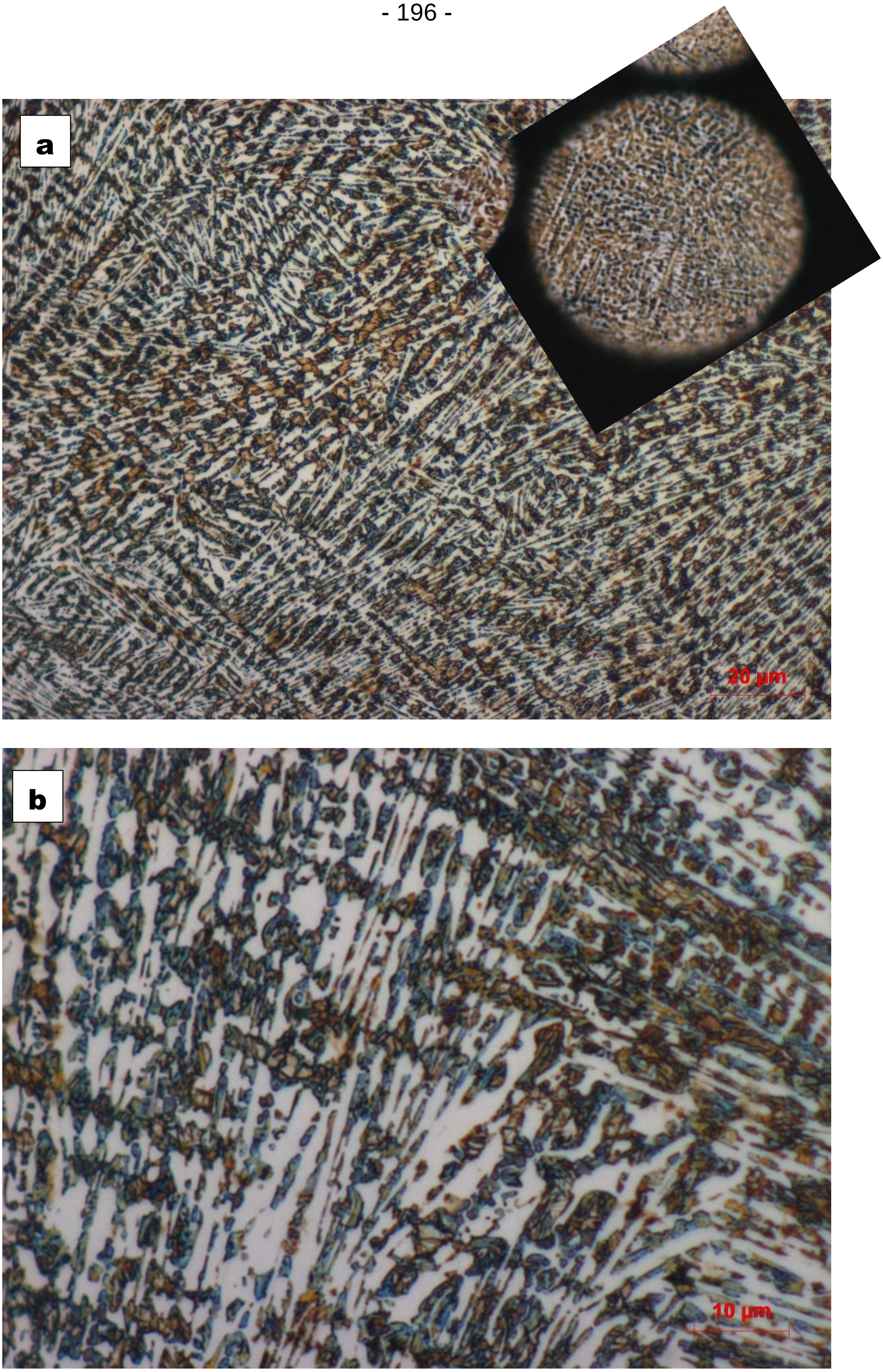

Picture 13: Enlarged micrographs (a) to (b) from *picture 12* revealing the evolved phases in the microstructure of the droplet by combined effect of 4% Picral and 10% Sodium Metabisulfite etching.

References

1. Callister, W.D.a.R.D.G., *Materials Science and Engineering: An Introduction*. 2007, New York, USA: John Wiley & Sons Inc.
2. Kurz, W. and D.J. Fisher, *Fundamentals of Solidification*. Third ed. 1992, Switzerland: Trans Tech Publications Ltd. 305.
3. Flemings, M.C., *Solidification Processing.* Metallurgical Transactions, 1974. **5**(10): p. 2121-2134.
4. William F., S.a.H., J.,, *Foundations of Materials Science and Engineering*. Fourth Edition ed. 2011: McGraw-Hill.
5. Kreith, F., Manglik, R.M. and Bohn, M.S., *Principle of Heat Transfer*. Seventh Edition ed. 2012, Stamford, USA: Cengage Learning, Global Engineering.
6. Sobota, T., *Fourier's Law of Heat Conduction. In Encyclopedia of Thermal Stresses*. 2014, Netherlands: Spinger.
7. Debenedetti, P.G., *Metastable liquids: concepts and principles*. 1996, USA: Princeton University Press.
8. Wolynes, P., *The concept of Nucleation*. Vol. 3. 1998: Folding and Design.
9. Behnam, M.M.J., P. Davami, and N. Varahram, *Effect of cooling rate on microstructure and mechanical properties of gray cast iron.* Materials Science and Engineering a-Structural Materials Properties Microstructure and Processing, 2010. **528**(2): p. 583-588.
10. Meyrick, G.a.P., G.W., *Phase transformation in metals and alloys.* Annual Review of Materials Science, 1973. **3**(1): p. 327-362.
11. Kurz, W., B. Giovanola, and R. Trivedi, *Theory of Microstructural Development During Rapid Solidification.* Acta Metallurgica, 1986. **34**(5): p. 823-830.
12. Liebermann, H.H., *Rapidly Solidified Alloys: Process, Structure, Properties and Applications.* 1993, 270 Madison Ave., New York 10016, USA: Marcel Dekker, Inc.
13. A., P.D. and E.K. E., *Phase Transformations in Metals and Alloys*. 2nd Edition ed. 2009, London, UK: Chapman & Hall. 513.
14. Dragnevski, K.I., *Microstructure evolution during solidification into undercooled Cu-based melts*, 2002, The University of Leeds, UK.

15. Levi, C.G. and R. Mehrabian, *Heat Flow during Rapid Solidification of Undercooled Metal Droplets.* Metallurgical Transactions A, 1982. **13**(2): p. 221-234.
16. Battersby, S.E., R.F. Cochrane, and A.M. Mullis, *Microstructural evolution and growth velocity-undercooling relationships in the systems Cu, Cu-O and Cu-Sn at high undercooling.* Journal of Materials Science, 2000. **35**(6): p. 1365-1373.
17. Willnecker, R., Herlach, D. M. and Feuerbacher B. . *Microgravity effect on Solidification*. in *7th European Symposium on materials and fluid science in Microgravity*. 1989. ESA special publication.
18. Erol, M., et al., *Containerless solidification of Ag-Al and Ag-Cu eutectic alloys in a drop tube.* Journal of Alloys and Compounds, 2013. **575**: p. 96-103.
19. Herlach, D.M., *Solidification and Crystallization*. 2004, Weinheim KGaA: Wiley-VCH Verlag GmbH & Co. .
20. Dragnevski, K., et al., *Mechanical deformation of dendrites by fluid flow during the solidification of undercooled melts.* Acta Materialia, 2002. **50**(14): p. 3743-3755.
21. Papon, P., Leblond, J. and Meijer, P. H., *The Physics of Phase transisitions* 2002, Berlin Heidelberg, Germany
    Springer-Verlag.
22. Lavernia, E.J. and T.S. Srivatsan, *The rapid solidification processing of materials: science, principles, technology, advances, and applications.* Journal of Materials Science, 2010. **45**(2): p. 287-325.
23. Cao, L., R.F. Cochrane, and A.M. Mullis, *Microstructural Evolution and Phase Formation in Rapidly Solidified Ni-25.3 At. Pct Si Alloy.* Metallurgical and Materials Transactions A, 2015. **46**(10): p. 4705-4715.
24. Morris, D.G., *Rapid-Solidification Phenomena.* Metal Science, 1982. **16**(10): p. 457-464.
25. Jacobson, L.A. and J. McKittrick, *Rapid Solidification Processing.* Materials Science & Engineering R-Reports, 1994. **11**(8): p. 355-408.
26. Turnbull, D., *Kinetics of Heterogeneous Nucleation.* The Journal of Chemical Physics, 1950. **18**: p. 198-202.

27. Sundquist B. E. and Mondolfo, L.E., *Heterogeneous nucleation in the liquid-to-solid transformation in alloys.* . Transaction of Metallurgical Society of AiME, 1961. **1**(221): p. 157-164.
28. Cochrane, R.F., P.V. Evans, and A.L. Greer, *Containerless Solidification of Alloys in a Drop-Tube.* Materials Science and Engineering, 1988. **98**: p. 99-103.
29. Cochrane, R.F., S.E. Battersby, and A.M. Mullis, *Dendrite growth velocity-undercooling relationships and microstructural evolution in highly undercooled dilute Cu-Sn alloys*. Solidification 1998, ed. S.P. Marsh, et al. 1998. 245-254.
30. Perepezko, J.H., et al., *Undercooling and solidification of atomized liquid droplets.* Materials Science and Engineering: A, 2002. **326**(1): p. 144-153.
31. Cohen, M., Kear, B. H. and Mehrabian R., *Rapid Solidification Processing: Principle and Technologies II.* 1989, Baton Rouge, LA: Claitor Publishing Division.
32. Oloyede, O., et al., *Microstructure evolution and mechanical properties of drop-tube processed, rapidly solidified grey cast iron.* Materials Science and Engineering: A, 2016. **654**: p. 143-150.
33. Willnecker, R., D.M. Herlach, and B. Feuerbacher, *Nucleation in bulk undercooled nickel-base alloys.* Materials Science and Engineering, 1988. **98**: p. 85-88.
34. Wang, C.X. and G.W. Yang, *Thermodynamics of metastable phase nucleation at the nanoscale.* Materials Science and Engineering: R: Reports, 2005. **49**(6): p. 157-202.
35. Wang, D., Li, Y., Sun, B. B., Sui, M. L., Lu, K. and Ma, E., *Bulk metallic glass formation in the binary Cu-Zr system.* . Applied Physics Letters, 2004. **84**(20): p. 4029-4031.
36. Cochrane, R.F., D.M. Herlach, and B. Feuerbacher, *Grain-Refinement in Drop-Tube-Processed Nickel-based Alloys.* Materials Science and Engineering a-Structural Materials Properties Microstructure and Processing, 1991. **133**: p. 706-710.
37. Kenney, C.S.a.K., G. C., *The equilibrum boundary between graphite and diamond.* Journal of Geophysical Research, 1976. **81**(14): p. 2467-2470.

38. Davis, G.J., *Solidification and Casting*. 1973, New York: Halsted Press, Wiley Publishing.

39. Cohen, M., *The status of selected scientific and technical areas*. Advancing Materials Research, ed. N.R. Council. 1987, Waswhington, DC: The National Academies Press.

40. Herlach, D.M., *Nonequilibrum Solidification of Undercooled Metallic Melts.* Materials Science & Engineering R-Reports, 1994. **12**(4-5): p. 177-272.

41. Gillessen, F., D.M. Herlach, and B. Feuerbacher, *Glass-Formation by Containerless Solidification of Metallic Droplets in Drop Tube Experiment.* Journal of the Less-Common Metals, 1988. **145**(1-2): p. 145-152.

42. Esaka, H., Daimon, H., Natsume, Y., Ohsasa, K. and Tamura, M., *Growth Direction of Cellular and Dendritic Interface in a Constrained Growth Condition.* Materials Transactions, 2002. **43**(6): p. 1312-1317.

43. Zhao, X., et al., *Influence of directional solidification variables on the microstructure and crystal orientation of AM3 under high thermal gradient.* Journal of Materials Science, 2010. **45**(22): p. 6101-6107.

44. Zhang, Z., X. Bian, and Y. Wang, *Growth of dendrites in a rapidly solidified Al-23 Sr alloy.* Journal of Crystal Growth, 2002. **243**(3–4): p. 531-538.

45. El Din, A.M.S. and G. Wranglén, *Dendrite formation and electrocrystallization of silver from molten salts.* Electrochimica Acta, 1962. **7**(1): p. 79-90.

46. Coriell, S.R. and D. Turnbull, *Relative Roles of Heat-Transport and Interface Rearrangement Rates in the Rapid Growth of Crystals in Undercooled Melts.* Acta Metallurgica, 1982. **30**(12): p. 2135-2139.

47. Kang, S.-H. and Y.-T. Im, *Three-dimensional finite-element analysis of the quenching process of plain-carbon steel with phase transformation.* Metallurgical and Materials Transactions A, 2005. **36**(9): p. 2315-2325.

48. Koster, U., *Phase transformations in rapidly solidified alloys.* Key Engineering Materials, 1993. **81**: p. 647-662.

49. Mehrabia.R, D.R. Geiger, and M.C. Flemings, *Refining by Partial Solidification.* Metallurgical Transactions, 1974. **5**(3): p. 785-787.

50. Yadav, T., Dirstine, R. and Pfaffenbach, K., *High purity fine metal powders & methods to produce such powder*, N.P. Corporation, Editor 2004: USA.

51. McCoy, J.K., et al., *Cooling and solidification of liquid-metal drops in a gaseous atmosphere.* Journal of Materials Science, 1992. **27**(3): p. 761-766.
52. Lekan, J., *Microgravity research in NASA ground-based facilities*, in *27th Aerospace Sciences Meeting*, A.S. Meetings, Editor 1989, NASA, Lewis Research Center, Cleveland, OH: Reno,NV,U.S.A.
53. Herlach, D.M., et al., *Containerless Processing in the Study of Metallic Melts and Their Solidification.* International Materials Reviews, 1993. **38**(6): p. 273-347.
54. Hofmeister, W.H.R., M. B. and Bayuzick, R. J. , *Undercooling of pure metals in a containerless, microgravity environment.* AIP Applied Physics Letters, 1986. **49**(20): p. 1342-1344.
55. Giessen, B.C., Paik, J. S., Kear, B. H. and Cohen, M., *Rapidly solidified amorphous and crystalline alloys.* MRS Bulletin, 1982. **7**(2): p. 5.
56. Lavernia, E.J.A., J. D. & Srivatsan, T. S., *Rapid solidification processing with specific application to aluminium alloys.* International Materials Reviews, 1992. **37**(1): p. 1-44.
57. Inoue, A.a.G., J. S., *Fe-Based Ferromagnetic Glassy Alloys with Wide Supercooled Liquid Region.* Materials Transactions, JIM, 1995. **36**(9): p. 1180-1183.
58. Flemings, M.C. and Y. Shiohara, *Solidification of Undercooled Metals.* Materials Science and Engineering, 1984. **65**(1): p. 157-170.
59. Perepezko, J.H., *Nucleation in undercooled liquids.* Materials Science and Engineering, 1984. **65**(1): p. 125-135.
60. Paradis, P.F., Ishikawa, T., Yu, J. and Yoda, S. , *Hybrid electrostatic–aerodynamic levitation furnace for the high-temperature processing of oxide materials on the ground.* AIP Review of Scientific Instruments, 2001. **72**(6): p. 2811-2815.
61. Winborne, D.A., et al., *Aerodynamic levitation technique for containerless high temperature studies on liquid and solid samples.* Metallurgical Transactions B, 1976. **7**(4): p. 711-713.
62. Castle, E.G., A.M. Mullis, and R.F. Cochrane, *Evidence for an extensive, undercooling-mediated transition in growth orientation, and novel dendritic seaweed microstructures in Cu-8.9 wt.% Ni.* Acta Materialia, 2014. **66**: p. 378-387.

63. Mathiak, G., et al., *Aerodynamic Levitation and Inductive Heating – A New Concept for Structural Investigations of Undercooled Melts.* International Journal of Thermophysics, 2005. **26**(4): p. 1151-1166.

64. Toda, R., Takeda, N., Murakoshi, T., Nakamura, S. and Esashi, M., *Electrostatically levitated spherical 3-axis accelerometer,* in *Micro Electro Mechanical Systems, 2002. The Fifteenth IEEE International Conference* A. Ball Semicond. Inc., PA, USA, Editor 2002, IEEE.

65. Yu, J., et al., *Containerless solidification of oxide material using an electrostatic levitation furnace in microgravity.* Journal of Crystal Growth, 2001. **231**(4): p. 568-576.

66. Jayawant, B.V., *Electromagnetic Levitation and Suspension Techniques*. 1981: The National Academics of Sciences, Engineering & Medicine.

67. Okress E. C., W., D. M., Comenetz, G., Brace, P. H. and Kelly, J. C. R., *Electromagnetic Levitation of Solid and Molten Metals.* Journal of Applied Physics, 1952. **23**(5): p. 545-552.

68. Egry, I., et al., *Containerless Processing in Space—Thermophysical Property Measurements Using Electromagnetic Levitation.* International Journal of Thermophysics, 2001. **22**(2): p. 569-578.

69. Flemings, M.C., *Solidification of Castings.* Scientific American, 1974. **231**(6): p. 88-95.

70. Barth, M., B. Wei, and D.M. Herlach, *Crystal growth in undercooled melts of the intermetallic compounds FeSi and CoSi.* Physical Review B, 1995. **51**(6): p. 3422-3428.

71. Dragnevski, K.I., A.M. Mullis, and R.F. Cochrane, *The effect of experimental variables on the levels of melt undercooling.* Materials Science and Engineering: A, 2004. **375–377**: p. 485-487.

72. Clopet, C.R., R.F. Cochrane, and A.M. Mullis, *Spasmodic growth during the rapid solidification of undercooled Ag-Cu eutectic melts.* Applied Physics Letters, 2013. **102**(3).

73. Clopet, C.R., R.F. Cochrane, and A.M. Mullis, *The origin of anomalous eutectic structures in undercooled Ag-Cu alloy.* Acta Materialia, 2013. **61**(18): p. 6894-6902.

74. Birol, Y., *Microstructural characterization of a rapidly-solidified Al-12 wt% Si alloy*. Journal of Materials Science, 1996. **31**(8): p. 2139-2143.

75. Uzun, O., et al., *Hardness and microstructural characteristics of rapidly solidified Al–8–16 wt.%Si alloys.* Journal of Alloys and Compounds, 2004. **376**(1–2): p. 149-157.
76. Lora, R., A. Dioszegi, and L. Elmquist, *Solidification Study of Gray Cast Iron in a Resistance Furnace,* in *Science and Processing of Cast Iron Ix*, A. Nofal and M. Waly, Editors. 2011, Trans Tech Publications Ltd: Stafa-Zurich. p. 108-113.
77. Gameiro, M., K. Mischaikow, and T. Wanner, *Evolution of pattern complexity in the Cahn–Hilliard theory of phase separation.* Acta Materialia, 2005. **53**(3): p. 693-704.
78. Seppecher, P., *Moving contact lines in the Cahn-Hilliard theory.* International Journal of Engineering Science, 1996. **34**(9): p. 977-992.
79. Gao, J.R. and B.B. Wei, *Containerless solidification of undercooled NdFeZrB alloy droplets in a drop tube.* Journal of Alloys and Compounds, 1999. **285**(1-2): p. 229-232.
80. Reuter, K.B., D.B. Williams, and J.I. Goldstein, *Determination of the Fe−Ni phase diagram below 400°C.* Metallurgical Transactions A, 1989. **20**(4): p. 719-725.
81. Stephens, P.W.G., A.I., *The structure of quasicrystals.* Scientific American, 1991. **264**(4).
82. Kimura, H.M., Sasamori, K. and Inoue, A., *Al–Fe-based bulk quasicrystalline alloys with high elevated temperature strength.* Journal of Materials Research, 2000. **15**(12): p. 2737-2744.
83. Shen, B., Kimura, H., Inoue, A., Omori, M. and Okubo, A., *Preparation of Fe65Co10Ga5P12C4B4 Bulk Glassy Alloy with Good Soft Magnetic Properties by Spark-Plasma Sintering of Glassy Powder.* Materials Transactions, 2002. **43**(8): p. 1961-1965.
84. Egami, T., *Universal criterion for metallic glass formation.* Materials Science and Engineering: A, 1997. **226**: p. 261-267.
85. Telford, M., *The case for bulk metallic glass.* Materials Today, 2004. **7**(3): p. 36-43.
86. Aziz, M.J., *Model for Solute Redistribution during Rapid Solidification.* Journal of Applied Physics, 1982. **53**(2): p. 1158-1168.

87. Taub, A.I. and F. Spaepen, *The kinetics of structural relaxation of a metallic glass.* Acta Metallurgica, 1980. **28**(12): p. 1781-1788.

88. Wagner, D.B., *Science and Civilization in China*. Vol. vol. 5. 2008: Cambrdge University Press.

89. Davis, J.R., *ASM specialty handbook: case irons*. 1996: ASM international.

90. Oloyede, O.R., Bigg, T. and Mullis, A.M. *Effect of Cooling Rate on Drop-Tube Processed Commercial Grey Cast Iron*. in *ASME 2015 International Mechanical Engineering Congress and Exposition*. 2015. Houston, Texas, USA: ASME International.

91. Kenney, M.P., Courtois, J.A., Evans, R.D., Farrior, G.M., Kyonka, C.P., Koch, A.A. and Young, K.P., *Metal Handbook*. Vol. 15. 1988, Metals Park, OH: ASM International.

92. Durand-Charre, M., *Microstructure of steels and cast irons*. 2004: Springer Science & Business Media.

93. Eiselstein, L.E., O.A. Ruano, and O.D. Sherby, *Structural Characterization of Rapidly Solidified White Cast-Iron Powders.* Journal of Materials Science, 1983. **18**(2): p. 483-492.

94. Chaus, A.S., *Special Features of the Microstructure of Cast Iron with Spheroidal Graphite.* Metal Science and Heat Treatment, 2015. **57**(7): p. 419-427.

95. Jones, D.R.a.A., M.F., *Engineering materials 2: an introduction to microstructures, processing and design*. Third ed. 2005: Butterworth-Heinemann.

96. Rivera, G.L., R.E. Boeri, and J.A. Sikora, *Solidification of gray cast iron.* Scripta Materialia, 2004. **50**(3): p. 331-335.

97. Alp, T., A.A. Wazzan, and F. Yilmaz, *Microstructure-property relationships in cast irons.* Arabian Journal for Science and Engineering, 2005. **30**(2B): p. 163-175.

98. Yescas-Gonzalez, M.A. and H. Bhadeshia, *Cast Iron.*

99. Geier, G.F., et al., *Microstructure transition from lamellar to compacted graphite using different modification agents.* Materials Science and Engineering: A, 2005. **413–414**: p. 339-345.

100. Roviglione, A.N. and J.D. Hermida, *From flake to nodular: A new theory of morphological modification in gray cast iron.* Metallurgical and Materials Transactions B, 2004. **35**(2): p. 313-330.
101. Predel, B., Hoch, M. and Pool, M.J., *Phase diagrams and heterogeneous equilibria: a practical introduction*. 2013, New York, USA: Springer Science & Business Media.
102. Battezzati, L., M. Baricco, and S. Curiotto, *Non-stoichiometric cementite by rapid solidification of cast iron.* Acta Materialia, 2005. **53**(6): p. 1849-1856.
103. Nishiyama, Z., *Martensitic transformation*. 2012, New York: Elsevier, Academic Press.
104. Lacaze, J. and B. Sundman, *An assessment of the Fe-C-Si system.* Metallurgical Transactions A, 1991. **22**(10): p. 2211-2223.
105. Vejman, K.M., *Diffusionless phase transformations*. Physical metallurgy. V. 2. Vol. 19. 1987.
106. Mehl, R.F. and W.C. Hagel, *The austenite: Pearlite reaction.* Progress in Metal Physics, 1956. **6**: p. 74-134.
107. Handbook, A., *Metallography and Microstructures*. Vol. 9. 2004, Materials Park, OH.
108. Stefaneseu, D.M., *Solidification and modeling of cast iron - A short history of the defining moments.* Materials Science and Engineering a-Structural Materials Properties Microstructure and Processing, 2005. **413**: p. 322-333.
109. Kiani-Rashid, A.R., et al., *The Effect of Cooling Rate on Bainite Phase Formation in Austempered Nickel-Molybdenum Gray Cast Iron.* International Scholarly Research Network, 2011. **2011**: p. 5 pages.
110. Roviglione, A. and J.D. Hermida, *X-Ray-Diffraction Characterization of Flake and Compacted Graphite in Cast-Iron.* Materials Characterization, 1994. **32**(2): p. 127-137.
111. Yang, M., et al., *Microstructure evolution of grey cast iron powder by high pressure gas atomization.* Journal of Materials Processing Technology, 2010. **210**(2): p. 351-355.
112. Yi, P., Xu, P., Fan, C., Yang, G., Liu, D., & Shi, Y., *Microstructure Formation and Fracturing Characteristics of Grey Cast Iron Repaired Using Laser.* The Scientific World Journal, 2014. **2014**: p. 10.

113. Ebrahimnia, M., et al., *Effect of cooling rate and powder characteristics on the soundness of heat affected zone in powder welding of ductile cast iron.* Materials & Design, 2012. **33**: p. 551-556.

114. Wei, F., Deng Qilin, Cao Peng, and Chen Dianbing, *Experimental Research and Engineering Application of Laser Cladding Reparations,* in *International Conference on Mechatronics, Electronic, Industrial and Control Engineering (MEIC 2014)*2014, Atlantis Press. p. 1055-1059.

115. Cao, L., *Rapid solidification of Ni-Si-Fe intermetallics in drop tube*, 2014, University of Leeds, UK: White Rose.

116. Goodhew, P.J., Humphreys, J. and Beanland, R., *Electron microscopy and analysis*. 3rd ed. ed. 2001, London: Taylor & Francis.

117. Sidney, H.A., *Introduction to Physical Metallurgy*. 1964, USA: McGraw-Hill Book Company.

118. Cullity, B.D.a.S., S. R., *Element of X-ray Diffraction.* . 3rd ed. 2001, Prentice Hall, New Jersy: Upper Saddle River.

119. Williams, D.B. and C.B. Carter, *Scattering and Diffraction*, in *Transmission Electron Microscopy: A Textbook for Materials Science*. 2009, Springer US: Boston, MA. p. 23-38.

120. Cao, G., *Nanostructures & nanomaterials: synthesis, properties & applications*. 2004, London, UK: Imperial College Press.

121. Mackenzie, R.C., *Differential thermal analysis*. 1970, London and New York: Academic Press.

122. Haines, P.J., *Thermal Methods of Analysis: Principles, Applications and Problems*. 1995, Glasgow, UK.: Springer Science and Business Media.

123. Yun, D., Xiaoping L. & Hongshen X., *Deep cryogenic treatment of high-speed steels and its mechanism,.* Heat Treatment Mat. , 1998. **3**: p. 55.

124. Thornton, R., et al., *The effects of cryogenic processing on the wear resistance of grey cast iron brake discs.* Wear, 2011. **271**(9–10): p. 2386-2395.

125. Molinari, A., Pellizzari, M., Gialanella, S., Straffelini, G. and Stiasny, K.H., *Effect of deep cryogenic treatment on the mechanical properties of tool steels.* Journal of materials processing technology, 2001. **118**(1): p. 350-355.

126. Huang, J.Y., et al., *Microstructure of cryogenic treated M2 tool steel.* Materials Science and Engineering: A, 2003. **339**(1–2): p. 241-244.

127. Moore, K., and Collins, D. N., *Cryogenic treatment of three heat treated tool steel.* Key Eng. Materials, 1993. **86-87**: p. 47-54.

128. Zurecki, Z., *Cryogenic quenching of steel revisited*, in *Air Products and Chemicals Inc.*2005.

129. Çadırlı, E., D.M. Herlach, and T. Volkmann, *Characterization of rapidly solidified Ni–Si and Co–Al eutectic alloys in drop tube.* Journal of Non-Crystalline Solids, 2010. **356**(9–10): p. 461-466.

130. Lee, E.-S. and S. Ahn, *Solidification progress and heat transfer analysis of gas-atomized alloy droplets during spray forming.* Acta Metallurgica et Materialia, 1994. **42**(9): p. 3231-3243.

131. Herlach, D.M.a.M., D.M., *Solidification of Containerless Undercooled Melts*. 2012: John Wiley & Sons.

132. Collini, L., G. Nicoletto, and R. Konecna, *Microstructure and mechanical properties of pearlitic gray cast iron.* Materials Science and Engineering a-Structural Materials Properties Microstructure and Processing, 2008. **488**(1-2): p. 529-539.

133. Dutra, A.T., et al., *Microstructure and metastable phase formation in a rapidly solidified Ni–Si eutectic alloy using a melt-spinning technique.* Journal of Alloys and Compounds, 2004. **381**(1–2): p. 72-76.

134. Leonhardt, M., W. Löser, and H.G. Lindenkreuz, *Metastable phase formation in undercooled eutectic Ni78.6Si21.4 melts.* Materials Science and Engineering: A, 1999. **271**(1–2): p. 31-37.

135. Zhirafar, S., A. Rezaeian, and M. Pugh, *Effect of cryogenic treatment on the mechanical properties of 4340 steel.* Journal of Materials Processing Technology, 2007. **186**(1–3): p. 298-303.

136. Payares-Asprino, M.C., Katsumoto, H. and Liu, S., *Effect of martensite start and finish temperature on residual stress development in structural steel welds.* Welding Journal, Research Supplement, 2008. **87**: p. 279s-289s.

137. Edmonds, D.V., et al., *Quenching and partitioning martensite—A novel steel heat treatment.* Materials Science and Engineering: A, 2006. **438–440**: p. 25-34.

138. Cao, L., R.F. Cochrane, and A.M. Mullis, *Solidification morphology and phase selection in drop-tube processed Ni–Fe–Si intermetallics.* Intermetallics, 2015. **60**: p. 33-44.